

A Search for an
Electron Antineutrino Signal
in the
Sudbury Neutrino Observatory

John Laurence Orrell

A dissertation submitted in partial fulfillment
of the requirements for the degree of

Doctor of Philosophy

University of Washington

2004

Program Authorized to Offer Degree: Physics

University of Washington
Graduate School

This is to certify that I have examined this copy of a doctoral dissertation by

John Laurence Orrell

and have found that it is complete and satisfactory in all respects,
and that any and all revisions required by the final
examining committee have been made.

Chair of Supervisory Committee:

John F. Wilkerson

Reading Committee:

Wick C. Haxton

R. G. Hamish Robertson

John F. Wilkerson

Date:

In presenting this dissertation in partial fulfillment of the requirements for the Doctoral degree at the University of Washington, I agree that the Library shall make its copies freely available for inspection. I further agree that extensive copying of this dissertation is allowable only for scholarly purposes, consistent with "fair use" as prescribed in the U.S. Copyright Law. Requests for copying or reproduction of this dissertation may be referred to Bell and Howell Information and Learning, 300 North Zeeb Road, Ann Arbor, MI 48106-1346, to whom the author has granted "the right to reproduce and sell (a) copies of the manuscript in microform and/or (b) printed copies of the manuscript made from microform."

Signature_____

Date_____

University of Washington

Abstract

A Search for an
Electron Antineutrino Signal
in the
Sudbury Neutrino Observatory

by John Laurence Orrell

Chair of Supervisory Committee:

Professor John F. Wilkerson
Department of Physics

The Sudbury Neutrino Observatory (SNO) is capable of detecting electron antineutrinos, $\bar{\nu}_e$, through the charged-current weak interaction $\bar{\nu}_e + d \rightarrow e^+ + n + n$ denoted as $\overline{\text{CC}}$. SNO registers electron antineutrino interactions with deuterons, d , via a time coincidence of detector events produced by any of the three product particles. Historically, proposals have suggested conversion of solar electron neutrinos into electron antineutrinos as either a solution to the “solar neutrino problem” or a signature of time-varying neutrino interactions with strong solar magnetic fields. This dissertation introduces the SNO detector via a brief overview of the main scientific objective of the SNO experiment. The potential sources of electron antineutrinos are enumerated and evaluated for their detection potential. The core of the analysis presented here investigates how to maximize SNO’s sensitivity to an electron antineutrino signal in the ^8B solar neutrino energy range. Backgrounds that can mimic event coincidences similar to the electron antineutrino signal are identified and addressed. Finally, 90% confidence level limits of $(\Phi_{\bar{\nu}_e}^{8\text{B}})_{\text{D}_2\text{O}} \leq 2.4 \times 10^4 \text{ cm}^{-2}\text{s}^{-1}$ and $(\Phi_{\bar{\nu}_e}^{8\text{B}})_{\text{Salt}} \leq 2.8 \times 10^4 \text{ cm}^{-2}\text{s}^{-1}$ are set on the solar electron antineutrino flux for the Pure D_2O and Salt phases of the SNO experiment, where a ^8B energy spectrum is assumed for solar electron antineutrinos. These limits correspond to less than 0.47% and 0.56% of the total standard solar model ^8B neutrino flux, respectively.

TABLE OF CONTENTS

List of Figures	vi
List of Tables	ix
Glossary	xii
I Introduction	1
Chapter 1: The Sudbury Neutrino Observatory (SNO)	2
1.1 Purpose	2
1.2 Design	3
1.3 An Experiment in Three Phases	3
1.4 Understanding Event Analysis at SNO	5
1.5 Data Reduction and Event Selection	6
Chapter 2: Electron Antineutrinos - A Brief Introduction	9
2.1 Measuring Electron Antineutrinos at SNO	9
2.2 Electron Antineutrino Physics Topics	10
Chapter 3: Analysis Outline	12
3.1 Dissertation Focus	12
3.2 Plan	12
3.3 Implementation and Organization	12
II Motivation	13
Chapter 4: Solar Electron Antineutrinos	14
4.1 The Standard Solar Model	14
4.2 Models of Electron Antineutrino Production in the Sun	14
4.3 Experimental Limits on the Solar Electron Antineutrino Flux	21
4.4 Calculating the Solar Electron Antineutrino Induced Event Rate in SNO	24
4.5 Other Derived Measurements	26

Chapter 5:	Atmospheric Electron Antineutrinos	29
5.1	Cosmic Rays and Atmospheric Neutrino Production	29
5.2	Atmospheric Electron Antineutrinos	29
Chapter 6:	Nuclear Reactor Electron Antineutrinos	34
6.1	Nuclear Reactor Properties	34
6.2	Calculating the Reactor $\bar{\nu}_e$ Flux Spectrum, $N_i^{\bar{\nu}_e}(E)$	35
6.3	Calculating the Total Number of \overline{CC} Events from Reactors	38
Chapter 7:	The Diffuse Supernova Neutrino Background	42
7.1	The Diffuse Supernova Neutrino Background Flux Spectrum	42
7.2	Event Rates from the Diffuse Supernova Neutrino Background	43
Chapter 8:	Terrestrial Electron Antineutrino Sources	44
8.1	Naturally Occurring, Terrestrial Radioisotopes	44
8.2	Hypothetical Geo-Fission Reactor at the Earth's Core	44
Chapter 9:	Electron Antineutrino Summary	46
9.1	Summary of Electron Antineutrino Sources	46
9.2	Electron Antineutrino Physics Topics at SNO	46
III	Supporting Analysis	48
Chapter 10:	Muon Followers and Muon Predecessors	49
10.1	Muons at SNO	49
10.2	Muon Identification and Fitting	50
10.3	Muon Selection	57
10.4	Defining Muon Followers & Muon Predecessors	59
10.5	Muon Follower & Muon Predecessor Selection	59
10.6	Conclusions from the Muon Follower Analysis	64
Chapter 11:	Neutron Capture Times	67
11.1	Neutron Monte Carlo and Capture Times	67
11.2	Choice of the Coincidence Time Windows	68
Chapter 12:	Pulse Global Trigger Followers	70
12.1	Analysis Parameters and Accidental Coincidence Backgrounds	70
12.2	Selecting m in $N_{\text{hit}}(R_{\text{fit}}) \geq m(R_{\text{fit}}/R_{\text{AV}})^3 + N_{\text{hit}}(0)$	70
12.3	Data Used in the Pulse Global Trigger Follower Analysis	73

Chapter 13:	Accidental Coincidence Background	74
13.1	Accidental Coincidences	74
13.2	The Theory of Accidental Coincidences	74
13.3	Determining the Accidental Coincidence Rate and Selecting $N_{\text{hit}}(0)$	75
13.4	Conclusions	80
Chapter 14:	Additional Analysis Cuts	84
14.1	A Maximum N_{hit} Value — $N_{\text{hit}} < 150$	84
14.2	The Choice of R_{fit} — $R_{\text{fit}} < 550$ cm and $R_{\text{fit}} < 600$ cm	84
14.3	“High-Level” Cuts — ITR, θ_{ij} , and β_{14}	85
Chapter 15:	$\overline{\text{CC}}$ Detection Efficiency - Theory	87
15.1	Introduction	87
15.2	Radius Dependent Detection Efficiencies	87
15.3	The Outcome Equation	88
Chapter 16:	$\overline{\text{CC}}$ Signal Monte Carlo	93
16.1	The Monte Carlo Program	93
16.2	Detector Response to $\overline{\text{CC}}$ Products	94
16.3	$\overline{\text{CC}}$ Detection Efficiencies	97
Chapter 17:	Detection Efficiency for Non-Solar Sources of Electron Antineutrinos	101
17.1	Review of Electron Antineutrino Sources	101
17.2	Efficiencies to Detect Non-Solar Sources of Electron Antineutrinos	101
Chapter 18:	Spontaneous Fission Backgrounds	104
18.1	Spontaneously Fissioning Isotopes in SNO	104
18.2	Spontaneous Fission Products	109
18.3	Efficiency to Detect Spontaneous Fission in SNO	111
Chapter 19:	Atmospheric Neutrino Induced Backgrounds	115
19.1	Introduction and Review of Early Calculations	115
19.2	NUANCE and SNO’s Monte Carlo Extension	116
Chapter 20:	Backgrounds from (α, n) Reactions	124
20.1	$^{13}\text{C} (\alpha, n) ^{16}\text{O}$	124
20.2	$^{17,18}\text{O} (\alpha, n) ^{20,21}\text{Ne}$	129
Chapter 21:	Secondary Neutrons	131
21.1	Secondary Neutrons	131

Chapter 22:	Other Backgrounds	134
22.1	“Sacrifice and Contamination”	134
22.2	Yet More Minor Backgrounds	134
22.3	A List of Other Potential Backgrounds Not Yet Addressed	135
 IV Electron Antineutrino Analysis		136
Chapter 23:	Candidate \overline{CC} Event Selection	137
23.1	Data Sets Used	137
23.2	Extracting Candidate \overline{CC} Coincidences	137
Chapter 24:	Statistical Treatment and Physics Results	142
24.1	The Feldman & Cousins Method	142
24.2	Background Counts	143
24.3	Limits on the Solar Electron Antineutrino Flux	143
 V Conclusion		145
Chapter 25:	Concluding Remarks	146
25.1	Strengths and Weaknesses of the Analysis Presented	146
25.2	My Contributions to the SNO Experiment	147
25.3	The Career Development Organization for Physicists and Astronomers	149
 VI Bibliography and Appendices		151
Bibliography		152
Appendix A:	Defining the Data Sets Used	168
A.1	The Pure D ₂ O Phase and Salt Phase Data Sets	168
A.2	Runs Used in the Pure D ₂ O Phase and Salt Phase	169
Appendix B:	Instrumental Noise and Cuts	171
B.1	Instrumental Noise and Cuts	171
B.2	Muon and Muon Spallation Cuts	172
B.3	Blindness “Cuts”	173
Appendix C:	Reactor Thermal to Electrical Efficiency Determination	174
C.1	Reactor Thermal to Electrical Efficiency	174

Appendix D:	More on Muon Followers	175
D.1	Measured Neutron Production Rate	175
D.2	Muon Follower Multiplicities	176
D.3	Muons Followed by High-Energy Čerenkov Rings	176

LIST OF FIGURES

1.1 Schematic design of the Sudbury Neutrino Observatory (SNO)	4
1.2 Example visualization of a SNO event	7
1.3 Data reduction from instrumental cuts.	8
4.1 The Standard Solar Model pp-chain	15
4.2 <i>CPT</i> properties of Dirac and Majorana neutrinos	17
4.3 Hypothetical solar $\bar{\nu}_e$ flux spectrum	25
4.4 Energy integrated \overline{CC} event rate	26
5.1 Calculated atmospheric neutrino fluxes	30
5.2 Low energy atmospheric electron antineutrino spectra	31
5.3 Ratios of atmospheric neutrinos to atmospheric antineutrinos	32
6.1 Nuclear reactor production of plutonium	35
6.2 Reactor $\bar{\nu}_e$ flux-spectrum	37
6.3 Normalized \overline{CC} yield from reactor $\bar{\nu}_e$'s	39
7.1 The diffuse supernova $\bar{\nu}_e$ background	43
10.1 Calculated muon incident direction at SNO	50
10.2 Example of a through-going muon	51
10.3 Muon N_{hit} spectrum in the Pure D ₂ O phase	52
10.4 Muon N_{hit} spectrum in the Salt phase	53
10.5 Impact parameter for clean, selected muons	54
10.6 Example of the routine that identifies high-energy muon followers	56
10.7 Classes of neutron producing, muon spallation processes	60
10.8 The N_{hit} vs. R_{fit} of muon followers in the Pure D ₂ O phase	61
10.9 The N_{hit} vs. R_{fit} of muon predecessors in the Pure D ₂ O phase	61
10.10 The N_{hit} vs. R_{fit} of muon followers in the Salt phase	63
10.11 The N_{hit} vs. R_{fit} of muon predecessors in the Salt phase	63
10.12 Pure D ₂ O phase N_{hit} distribution of muon followers & predecessors and MC neutrons	65
10.13 Pure D ₂ O phase Δt distribution of muon followers & predecessors and MC neutrons	65
10.14 Salt phase N_{hit} distribution of muon followers & predecessors and MC neutrons	66
10.15 Salt phase Δt distribution of muon followers & predecessors and MC neutrons	66

11.1	Monte Carlo neutron capture time in the Pure D ₂ O and Salt phases	67
12.1	Choosing the energy and volume event selection region	71
12.2	Choice of the slope parameter, m , in the Pure D ₂ O phase	72
12.3	Choice of the slope parameter, m , in the Salt phase	73
13.1	Fitting the mean event rate in the Pure D ₂ O phase Standard window	81
13.2	Fitting the mean event rate in the Pure D ₂ O phase e^+ -Enlarged window	81
13.3	Fitting the mean event rate in the Pure D ₂ O phase n -Enlarged window	82
13.4	Fitting the mean event rate in the Salt phase Standard window	82
13.5	Fitting the mean event rate in the Salt phase e^+ -Enlarged window	83
13.6	Fitting the mean event rate in the Salt phase n -Enlarged window	83
15.1	Example radius-dependent, single-particle detection efficiencies	88
15.2	Coincidence detection and radius-dependent detection efficiencies	89
16.1	Monte Carlo N_{hit} response to $\overline{\text{CC}}$ products in the Pure D ₂ O phase	94
16.2	Monte Carlo N_{hit} response to $\overline{\text{CC}}$ products in the Salt phase	95
16.3	Monte Carlo positron detection efficiency in the Pure D ₂ O and Salt phases	96
16.4	Monte Carlo neutron capture separation distances in the Pure D ₂ O phase	97
16.5	Monte Carlo neutron capture separation distances in the Salt phase	98
18.1	The ²³² Th, ²³⁵ U, and ²³⁸ U decay chains	106
18.2	The ²⁴⁹ Cf, ²⁵⁰ Cf, and ²⁵² Cf decay chains	107
18.3	The U and Th concentrations in the Pure D ₂ O phase	108
18.4	Prompt gamma-ray spectra from spontaneous fission	110
18.5	Monte Carlo of the prompt gamma-ray spectrum from spontaneous fission of ²³⁸ U	111
18.6	Monte Carlo of the prompt gamma-ray spectrum from spontaneous fission of ²⁵² Cf	112
18.7	Monte Carlo of the detector response to spontaneous fission, prompt gamma-rays	113
19.1	Raw NUANCE multiplicities for atmospheric neutrino interactions	117
19.2	The N_{hit} response to the first particle from an atmospheric neutrino interaction	118
19.3	The N_{hit} response to secondary particles from an atmospheric neutrino interaction	119
20.1	N_{hit} response to e^+e^- pairs in the Pure D ₂ O phase	126
20.2	N_{hit} response to e^+e^- pairs in the Salt phase	127
20.3	Radial fit position of e^+e^- pairs produced at $r = 600$ cm	128
20.4	Radial fit position of neutrons produced at $r = 600$ cm	129
20.5	Capture time for neutrons produced at $r = 600$ cm	130
21.1	Monte Carlo of the reduced N_{hit} response of 6.25 MeV γ -rays that $d(n, \gamma)t$	132

21.2	Monte Carlo of the reduced N_{hit} response to ^{36}Cl cascade γ -rays that $d(n, \gamma)t$	133
23.1	Radial fit position of first event in 2-fold Salt coincidences	141
D.1	Muon follower multiplicities in a Pure D_2O phase Standard analysis	177
D.2	Muon follower multiplicities in a Pure D_2O phase Enlarged analysis	177
D.3	Muon follower multiplicities in a Salt phase Standard analysis	178
D.4	Muon follower multiplicities in a Salt phase Enlarged analysis	178

LIST OF TABLES

4.1	Limits on the neutrino magnetic moment	18
4.2	Measured limits on the solar electron antineutrino flux	21
4.3	Parameters for the calculation of the $\overline{\text{CC}}$ rate induced by solar $\bar{\nu}_e$	25
4.4	The $\overline{\text{CC}}$ rate for a given solar $\bar{\nu}_e$ flux	26
5.1	The low energy atmospheric electron antineutrino induced $\overline{\text{CC}}$ rate	31
6.1	Calculation factors in determining the total $\bar{\nu}_e$ flux from nuclear reactors	36
6.2	Neutrino mixing parameters used in reactor $\bar{\nu}_e$ flux calculations	39
6.3	The $\bar{\nu}_e$ flux from nuclear reactors and induced $\overline{\text{CC}}$ rate	40
6.4	Expected $\overline{\text{CC}}$ interactions from nuclear reactor $\bar{\nu}_e$ in the Pure D ₂ O phase	40
6.5	Expected $\overline{\text{CC}}$ interactions from nuclear reactor $\bar{\nu}_e$ in the Salt phase	41
6.6	North American nuclear reactors used in calculating expected $\overline{\text{CC}}$ rates	41
8.1	Electron antineutrino producing terrestrial radioisotopes	44
8.2	Geo-reactor electron antineutrino flux calculation parameters	45
8.3	Hypothetical geo-reactor $\bar{\nu}_e$ induced $\overline{\text{CC}}$ rate	45
9.1	Summary of expected yearly $\overline{\text{CC}}$ rates from $\bar{\nu}_e$ sources	46
10.1	Classes of muon events at the Sudbury Neutrino Observatory	50
10.2	Q. R. Ahmad's distinctive AV-going events compared to this muon analysis	57
10.3	Muon selection criterion	57
10.4	Runs excluded from the muon and muon follower analysis in the Pure D ₂ O phase	58
11.1	The coincidence time windows chosen for the electron antineutrino analysis	69
13.1	Event selection criterion for accidental coincidence rates in the Pure D ₂ O phase	77
13.2	Number of events satisfying the selection criterion in the Pure D ₂ O phase	77
13.3	Mean event rates in the Pure D ₂ O phase	78
13.4	Accidental coincidence rates in the Pure D ₂ O phase.	78
13.5	Event selection criterion for accidental coincidence rates in the Salt phase	78
13.6	Number of events satisfying the selection criterion in the Salt phase	79
13.7	Mean event rates in the Salt phase	79
13.8	Accidental coincidence rates in the Salt phase	79

16.1	Monte Carlo detection efficiency for $\bar{\nu}_e$ with a ^8B spectral shape in the Pure D_2O phase	98
16.2	Monte Carlo detection efficiency for $\bar{\nu}_e$ with a ^8B spectral shape in the Salt phase	99
17.1	Review of electron antineutrino sources	101
17.2	Nuclear reactor $\bar{\nu}_e$ induced $\overline{\text{CC}}$ detection efficiencies	102
17.3	Estimated positron detection efficiency for $14 < E_{\bar{\nu}_e} \text{ (MeV)} < 23$	103
17.4	Total positron and $\overline{\text{CC}}$ detection efficiencies for diffuse supernova background $\bar{\nu}_e$	103
18.1	Spontaneous fission nuclei	105
18.2	Concentrations of U and Th in the Pure D_2O and Salt phases	105
18.3	Number of spontaneous fissions of ^{232}Th , ^{235}U , and ^{238}U	107
18.4	Neutron multiplicity probabilities for spontaneous fission of ^{238}U and ^{252}Cf	109
18.5	Characteristics of prompt gamma-rays from spontaneous fission	110
18.6	Monte Carlo detection efficiency for ^{238}U spontaneous fission in the Pure D_2O phase	113
18.7	Monte Carlo detection efficiency for ^{252}Cf spontaneous fission in the Pure D_2O phase	114
18.8	Monte Carlo detection efficiency for ^{238}U spontaneous fission in the Salt phase	114
18.9	Monte Carlo detection efficiency for ^{252}Cf spontaneous fission in the Salt phase	114
19.1	Calculated atmospheric neutrino quasi-elastic interaction rate	115
19.2	NUANCE settings for atmospheric neutrino simulations	116
19.3	Breakdown of Monte Carlo errors and output	118
19.4	<i>A priori</i> elimination of atmospheric neutrino events as background contributors	120
19.5	$\overline{\text{CC}}$ backgrounds in the Pure D_2O phase from atmospheric neutrino interactions	121
19.6	$\overline{\text{CC}}$ backgrounds in the Salt phase from atmospheric neutrino interactions	122
19.7	Estimated $\overline{\text{CC}}$ backgrounds from 100 years of atmospheric neutrino interactions	123
20.1	Elemental and mass fractions of isotopes in the acrylic vessel	124
20.2	Coincidence detection efficiencies for a e^+e^- pair and neutron	126
20.3	Backgrounds from $^{13}\text{C} (\alpha, n) ^{16}\text{O}$	129
20.4	Backgrounds from $^{13}\text{C} (\alpha, n) ^{16}\text{O}$ after photo-disintegration subtraction	130
21.1	Secondary neutrons in the Pure D_2O and Salt phases	132
22.1	Other backgrounds taken from the Antineutrino Unified Document	135
23.1	Pure D_2O phase, Enlarged region electron antineutrino candidate coincidences.	138
23.2	Short list of Pure D_2O phase, Standard region $\overline{\text{CC}}$ candidate coincidences	138
23.3	Salt phase, Enlarged region $\overline{\text{CC}}$ candidate coincidences – I	139
23.4	Salt phase, Enlarged region $\overline{\text{CC}}$ candidate coincidences – II	140
23.5	Short list of Salt phase, Standard region $\overline{\text{CC}}$ candidate coincidences	141

24.1	Summary of expected background counts in the Pure D ₂ O and Salt phases	143
24.2	Uncertainties on the \overline{CC} background estimates	144
24.3	Limits on the flux of solar electron antineutrinos, $\Phi_{\nu_e}^{8B}$	144
A.1	Runs used for the Pure D ₂ O analysis	169
A.2	Runs used for the Salt analysis	170
C.1	US nuclear reactor thermal to electric conversion efficiencies	174
D.1	Muons failing the muon decay ring test in the Pure D ₂ O & Salt phases	179

GLOSSARY

PURE D₂O PHASE: The first phase of the SNO experiment where the neutrino target volume is composed solely of pure heavy water.

SALT PHASE: The second phase of the SNO experiment in which 2 tonnes of table salt (NaCl) is mixed into the heavy water target volume for added neutron sensitivity.

NCD PHASE: The third phase of the SNO experiment in which ³He proportional counts are inserted into the pure heavy water region for added neutron sensitivity.

AV: Acrylic vessel. Contains the heavy water target volume and is optically transparent. The acrylic vessel has a 12 m diameter.

\overline{CC} : The charge-current weak interaction of an electron antineutrino, $\bar{\nu}_e$, with a deuterium nucleus, d , producing a positron, e^+ and two neutrons, n , written as $\bar{\nu}_e + d \rightarrow e^+ + n + n$.

DETECTOR INNER VOLUME: The region inside the PMT Support Structure.

DETECTOR OUTER VOLUME: The region outside the PMT Support Structure.

FTM: The muon fitter routine used in the SNO Monte Carlo program, SNOMAN.

PMT: Photomultiplier tube. Used to detect optical Čerenkov photons.

PSUP: The geodesic PMT Support Structure located ≈ 8.5 m from the detector's center.

NAFTA: North American Free-Trade Agreement.

NCD: Neutral Current Detector. A ³He proportional counter used in the third phase of SNO.

SNO: The Sudbury Neutrino Observatory

SNOMAN: The SNO Monte carlo and ANalysis program. The primary simulation and data analysis program used in the SNO experiment.

ACKNOWLEDGMENTS

The enduring support of my parents has allowed me to pursue my interests for over a quarter century. This is great a gift and I count myself as extremely fortunate to have received it.

Likewise, the work represented by this dissertation would not have been possible without the help and support of my colleagues at the University of Washington and at the other SNO Collaboration member institutions.

Thank you.

Part I

Introduction

Chapter 1

THE SUDBURY NEUTRINO OBSERVATORY (SNO)

Electron antineutrino physics is one of many topics that can be studied by the Sudbury Neutrino Observatory experiment. In fact, the primary objective of SNO is to study neutrinos produced by the Sun. Chapter 1 briefly introduces SNO's primary physics topic and detection capabilities. Chapter 2 then introduces antineutrino physics, the focus of this dissertation. Chapter 3 then closes the Introduction by concisely restating the focus, plan, and organization of this dissertation.

1.1 Purpose

The Sudbury Neutrino Observatory was designed for the implementation of a novel detection technique aimed at measuring both the solar electron neutrino flux and the flux of *all* weakly interacting flavors of neutrinos coming from the Sun. Beginning in the mid-1960's with the solar electron neutrino studies of R. Davis [78], forty years of solar electron neutrino measurements returned a consistent result: The flux of solar electron neutrinos is less than the number predicted by models of the fusion processes occurring in the core of the Sun. This situation is known as the solar neutrino problem. One hypothetical solution to the solar neutrino problem was that the electron neutrinos produced in the core of the Sun could quantum mechanically oscillate (see Ref. [61] for an introduction) into neutrinos of another flavor before arriving at detectors on Earth. This flavor changing neutrino oscillation would then account for the reduced number of electron neutrinos measured. Thus, the flux of *all* weakly interacting flavors of neutrinos (succinctly referred to as the flux of all active neutrinos) is the crucial measurement to test the neutrino oscillation hypothesis. SNO's primary purpose was to address the neutrino oscillation hypothesis by measuring both the solar ^8B electron neutrino flux and the flux of all active neutrinos coming from the Sun.

SNO's novel detection technique uses the deuterium nuclei contained in heavy water molecules, D_2O . As originally suggested by H. H. Chen [74], a volume of D_2O , monitored by light detecting photomultiplier tubes, provides a suitable deuteron target for solar neutrinos. Additionally, the atomic electrons bound in the D_2O provide a second target for solar neutrinos. Thus, SNO is able to study solar neutrinos through three distinct interactions:

$$\nu_e + d \rightarrow e^- + p + p \quad Q = -1.44 \text{ MeV} \quad (\text{CC})$$

$$\nu_\ell + d \rightarrow \nu_\ell + p + n \quad Q = -2.23 \text{ MeV} \quad (\text{NC})$$

$$\nu_\ell + e^- \rightarrow \nu_\ell + e^- \quad (\text{ES})$$

The CC reaction is a charged-current interaction of an electron neutrino, ν_e , with a deuterium nucleus, d . The product electron, e^- , will then pass through the water and Čerenkov radiate optical photons making it

detectable by the photomultiplier tubes monitoring the D_2O volume. The NC reaction is a neutral-current interaction of *any* weakly interacting flavor of neutrino, ν_ℓ , with a deuterium nucleus. The product neutron, n , liberated in the neutral-current interaction may capture on another deuterium nucleus producing a 6.25 MeV gamma-ray through the reaction $n + d \rightarrow t + \gamma$. This mono-energetic gamma-ray will then Compton scatter atomic electrons which will Čerenkov radiate optical photons and thus be detectable by the monitoring photomultiplier tubes. The protons produced by solar neutrinos participating in either the CC or NC reactions will not produce a detectable signal in the SNO detector. The ES reaction is the elastic scattering of a neutrino and an atomic electron. Once again, the scattered electron will Čerenkov radiate optical photons and be detectable by the monitoring photomultiplier tubes. In both the NC and ES reactions, it is *extremely* unlikely that the outgoing neutrinos will interact a second time in the SNO detector.

Each of the three reactions, CC, NC, and ES, ultimately rely upon Čerenkov radiating electrons to produce detectable optical photons. Each of the three reactions, however, generates Čerenkov radiating electrons with characteristic energies and momenta. The characteristic energies, momenta, and reconstructed positions provide a means by which the CC, NC, and ES reactions can be distinguished. In this way, SNO is capable of using the three neutrino reactions, CC, NC, and ES, to achieve the goal of determining both the solar electron neutrino flux and the flux of all active neutrinos coming from the Sun above the given reaction thresholds.

1.2 Design

The Sudbury Neutrino Observatory [62] is located 2 km underground in INCO Ltd.'s Creighton mine outside of Sudbury, Ontario, Canada. The detector consists of a main volume of D_2O contained in a transparent, spherical acrylic vessel. The acrylic vessel is suspended in ultra-pure light water, H_2O , and is viewed by 9456 submerged photomultiplier tubes (PMTs). The photomultiplier tubes are situated on a geodesic support structure surrounding the acrylic vessel. Figure 1.1 is a schematic of the detector's construction and geometry. The acrylic vessel holds approximately 1 kilotonne¹ of D_2O and is 12 meters in diameter. The photomultiplier support structure (PSUP) is 17 meters in diameter. The primary PMT array is augmented by several additional set's of PMTs used as veto triggers. These PMTs include:

- 23 PMTs on the Berkeley Underwater Tube Testing Sled (BUTTS) located above and outside the PSUP
- 4 tubes located inside the neck of the acrylic vessel (NECK tubes).
- 96 outward looking (OWL) tubes attached to the exterior of the photomultiplier support structure.

1.3 An Experiment in Three Phases

In an effort to make conclusive measurements of the flux of all active neutrinos coming from the Sun, three phases were proposed for the SNO experiment. Each phase of the experiment uses a different method for

¹The tonne (t) is the SI unit designating 1000 kilograms (kg). This dissertation will use the following units and abbreviations for large masses: 10,000 kilograms = 10,000 kg = 10 tonnes = 10 t = 0.010 kilotonnes = 0.010 kt. In a number of cases, published scientific papers use the term "ton". While it is often clear the author(s) intend the SI tonne, if a published value is written using the "ton" as a unit, it is left this way if reported in this dissertation. In other words, the use of the term "ton" should alert the reader.

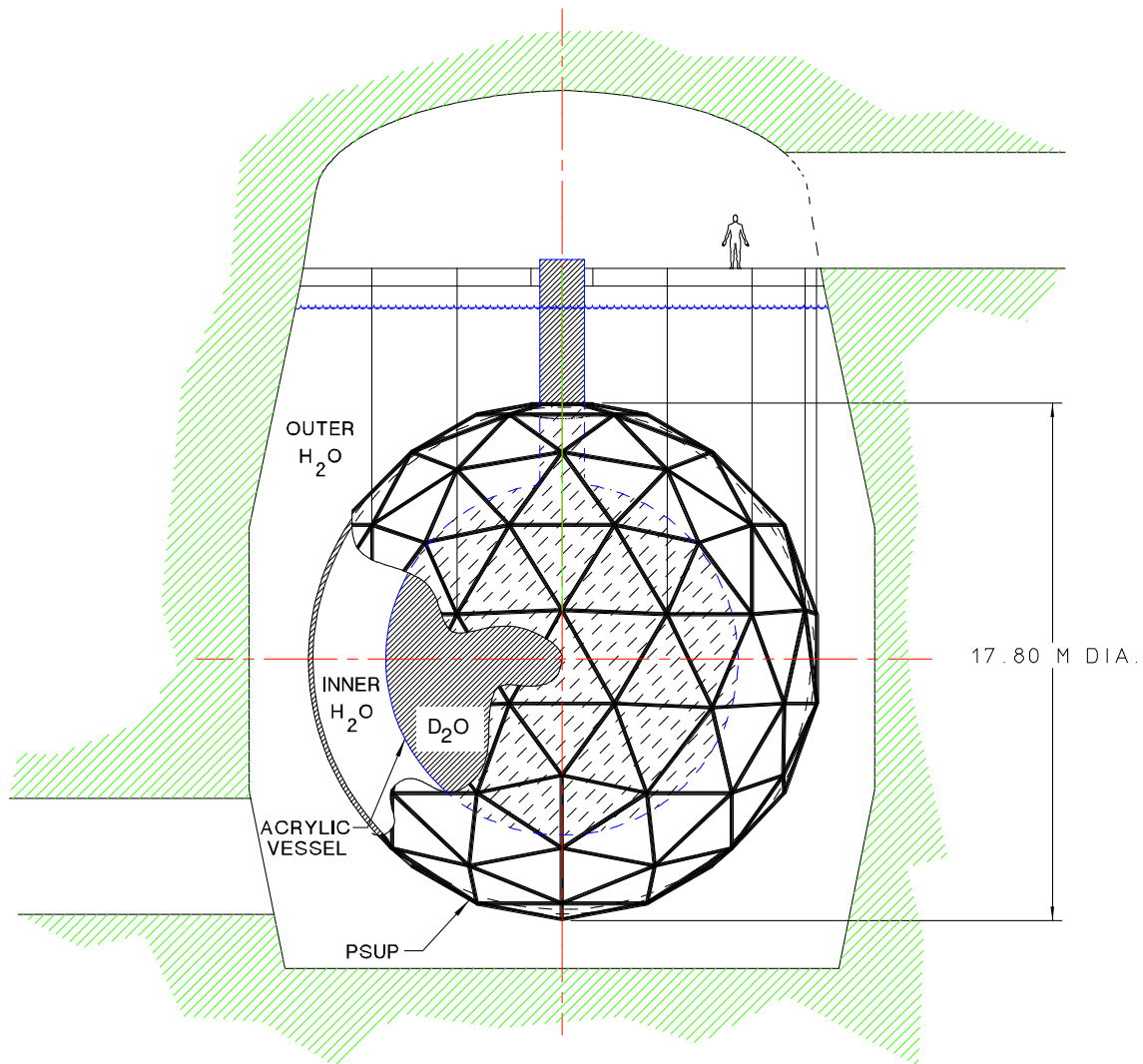


Figure 1.1: Schematic design of the Sudbury Neutrino Observatory (SNO). The neutrino target volume is the most central D₂O region. Optical Čerenkov light detecting photomultiplier tubes are mounted on the inside of geodesic sphere (PSUP) surrounding the D₂O volume. The rest of the cavity is filled with ultra-pure light water.

determining the NC reaction rate in the SNO detector. The NC reaction provides the least ambiguous measurement of the flux of all active neutrinos because it is equally sensitive to all active neutrinos. As already described in Section 1.1, the neutron liberated in the NC reaction can capture on deuterium nuclei producing a single detectable gamma-ray. The first phase of the SNO experiment uses this method for measuring the NC

reaction rate in SNO. Since this phase of the experiment uses only D_2O , it is called the **Pure D_2O phase**. The Pure D_2O phase of the SNO experiment was completed in June 2001 and the solar neutrino analysis results have been published in Physical Review Letters [9, 10, 11].

One way to augment the measurement of the NC reaction rate in the SNO detector is to dissolve ordinary table salt, NaCl, in the D_2O . The neutron liberated in the NC reaction has an approximately 100 times greater cross-section for capturing on ^{35}Cl (75% natural abundance) than on deuterium nuclei. Once a neutron captures on a ^{35}Cl nucleus, the excited ^{36}Cl nucleus produces a cascade of de-excitation gamma-rays whose energy totals 8.6 MeV. Thus, neutron capture on ^{35}Cl will produce a detectable signal in the SNO detector. The greatest affect of the addition of salt to the D_2O volume is the increased efficiency with which the NC reactions occurring in the SNO detector are measured. This second phase of the SNO experiment is obviously called the **Salt phase**. The Salt phase of the SNO experiment was completed in September of 2003 with initial results submitted to Physical Review Letters [12].

By inserting 3He proportional counters into the D_2O volume, it is possible to provide a third, and most importantly, independent measurement of the neutron production rate in the SNO detector. The 3He proportional counters are sensitive to neutrons liberated in the NC reaction, but are insensitive to the CC and ES reactions. The 3He proportional counters are named neutral-current detectors or NCDs for short. Thus the third phase of the SNO experiment is called the **NCD phase**. Similar to the Salt phase, the NCD phase also benefits from increased neutron measurement efficiency. More importantly though, the NCDs detect neutrons without the production of Čerenkov light. Thus the NCDs provide the greatest separation between the NC (via NCDs) and CC (via PMTs) signals. The NCD phase of the SNO experiment is scheduled to begin in 2004.

1.4 Understanding Event Analysis at SNO

1.4.1 The Trigger System

The SNO detector is a neutrino detector sensitive to physics events in real-time. Light generated in the detector's inner volume will fire photomultiplier tubes which are tuned to respond at a charge threshold crossing equivalent to 0.25 photo-electrons generated on the photo-cathode. The analog charge from all firing tubes is continually summed in a master trigger card. The master trigger card monitors the summed charged and if the summed charged crosses a preset threshold value, a global trigger is generated². The generation of a global trigger initiates a readout of all fired PMTs. The readout from all PMTs forms a data packet which is identified as a single event. A more detailed description of the SNO trigger system is given in References [130, 165].

1.4.2 SNO Events

A single event in SNO is a record of all PMTs that fired during a 485 ns period around the time at which the global trigger was generated. The information contained in the event is a list of PMTs each specified

²There are actually three separate charge indicators, each with several levels of charge thresholds. Furthermore, there are 6 classes of PMTs. In combination, these make the SNO trigger system significantly more complex than described in this introduction.

by a PMT identifying number, time-to-analog converter values, and three separate measures of the charge deposited in the individual PMTs.

Event Visualization

The known position of each PMT on the PMT support structure allows SNO events to be visualized as a set of PMTs that have fired. Figure 1.2 is an example of event visualization in the SNO experiment. The PMT support structure (PSUP) is represented by the black geodesic sphere. Inside the PSUP, the acrylic vessel is shown as a gray (spherical) flask shape. The fired PMTs are represented by colored circles located on the PSUP. Solid circles represent fired PMTs located on the near-side hemisphere and hollow circles represent fired PMTs located on the far-side hemisphere. The color is used to represent either early or late times or high or low charge. True physics (or background) events will appear as either rings of fired PMTs or, in the case of Figure 1.2, clusters of fired PMTs.

SNO Events and Energy Determination

The amount of Čerenkov light produced by a charged particle passing through the detector provides a measure of the particle's kinetic energy. This dependence is via the particle's velocity, v , in the equation for the number of Čerenkov photons emitted, $N_\gamma^{\check{\text{Cerenkov}}}$, at wavelength, λ :

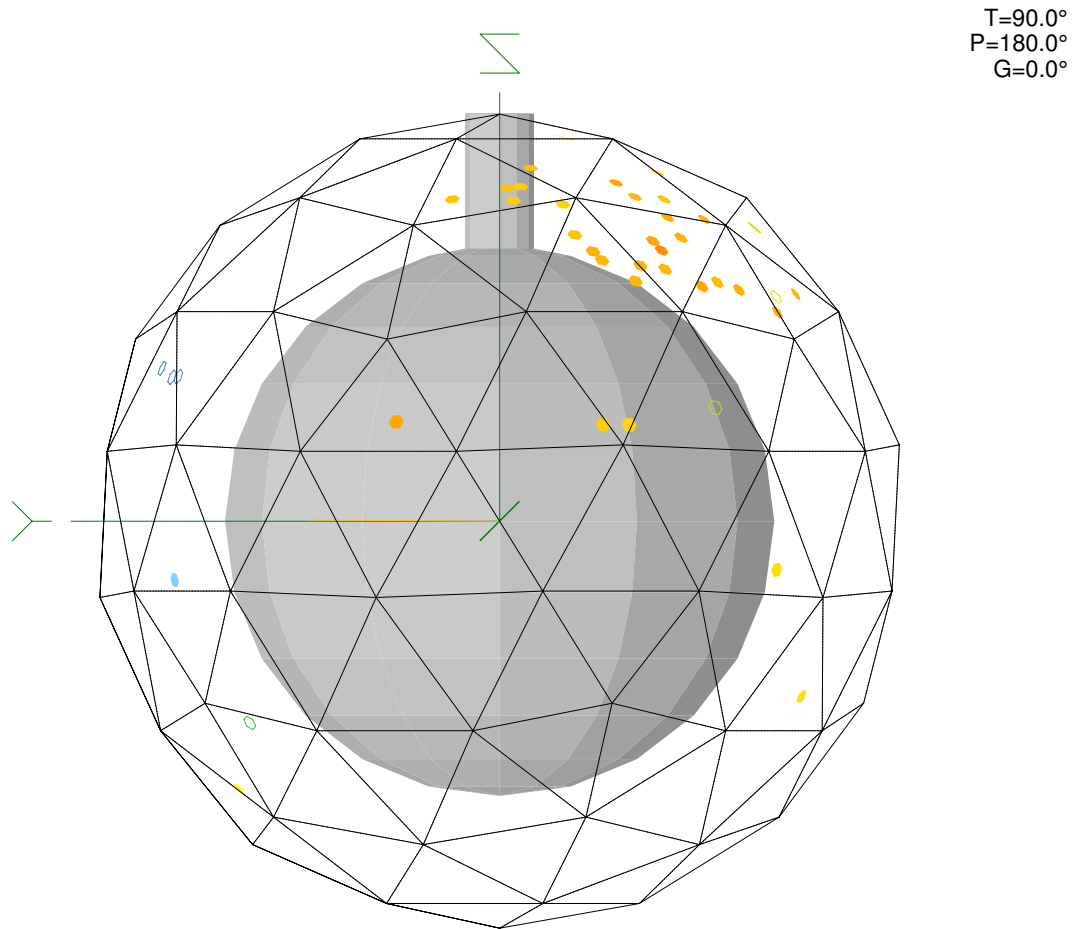
$$\frac{dN_\gamma^{\check{\text{Cerenkov}}}}{d\lambda} = 2\pi\alpha L \left(\frac{z}{\lambda}\right)^2 \left[1 - \left(\frac{1}{\beta n(\lambda)}\right)^2\right] \quad \text{with } \beta n(\lambda) > 1 \quad (1.1)$$

where $\beta = v/c$, $n(\lambda)$ is a wavelength dependent index of refraction, α is the fine structure constant, z is charge in units of electron charge, and L is the length of the particle's track. The crudest measure of a particle's kinetic energy is thus given by the total number of PMTs fired during an event. This crude measure is known as N_{hit} . A number of additional energy measures have been developed for use in SNO analysis. Most of these rely on the event's prompt light, defined as only those PMTs that have fired within several to a few tens of nanoseconds around the zero-time set by the instant of the generation of a global trigger in the master trigger card. More detailed information on energy measures in the SNO experiment are given in References [64, 116, 165].

Although, N_{hit} is the crudest measure of a particle's kinetic energy, it provides an accessible and intuitive method for comparing the energies of SNO events. Furthermore, it makes the fewest number of assumptions regarding the events physical origin and the optical properties of the detector. Since the analysis presented in this dissertation is intended as a demonstration of a technique that is not closely connected to a particular choice of energy measure the N_{hit} energy measure is used.

1.5 Data Reduction and Event Selection

There are approximately two dozen analysis cuts which are applied to the data set to remove known instrumental backgrounds as well as cosmic ray muons and the spallation products those muons may create in the detector. These cuts are individually detailed in a technical format in N. McCauley's dissertation [157].



Run: 10000 GTID: 5189

Figure 1.2: A visualization of a SNO event. The black geodesic sphere represents the PMT support structure. The inner, gray Florence flask shape is the acrylic vessel that contains the D_2O . The small colored circles represent PMTs which have fired; yellow and blue representing early and late times, respectively, during the event.

1.5.1 Instrumental Noise Cuts

The work presented in this dissertation uses those analysis cuts designed to flag (and hence remove) instrumental noise. These instrumental noise cuts are algorithms designed to identify events which are produced by features of the electronics and PMTs that are *not* indicative of true Čerenkov light inside the detector volume. Figure 1.3 shows the progression of instrumental cuts. Appendix B provides a brief description of

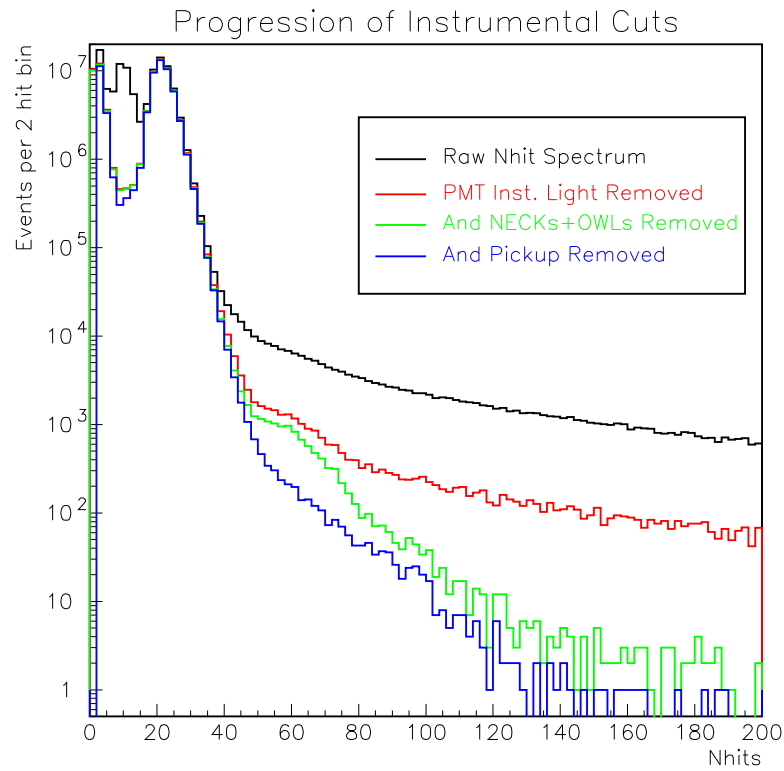


Figure 1.3: Data reduction from instrumental cuts. This figure is representative of the analysis presented in the SNO Collaboration's first Physical Review Letter [9] and is data from the Pure D_2O phase of the experiment.

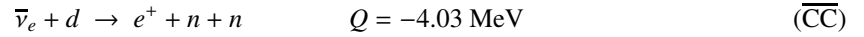
those cuts of primary importance to the electron antineutrino analysis. Again, a complete treatment of these instrumental analysis cuts is presented in N. McCauley's dissertation [157].

Chapter 2

ELECTRON ANTINEUTRINOS - A BRIEF INTRODUCTION

2.1 Measuring Electron Antineutrinos at SNO

Electron antineutrinos can interact with deuterium nuclei in D₂O via a charged-current weak interaction¹



Each of the three products of the $\overline{\text{CC}}$ reaction can produce a detectable signal in the SNO detector. First, the positron, e^+ , can generate a prompt Čerenkov signal analogous to the CC reaction's product electron. Second, the two neutrons, n , can capture on nuclei and generate measurable signals. The particular capture site of the neutrons depends on the phase of the SNO experiment, as described in Section 1.3. The salient point is that the $\overline{\text{CC}}$ reaction produces multiple, signal generating particles that will occur in a time coincidence. This time coincident, multi-particle signal provides a unique way to measure the rate of $\overline{\text{CC}}$ reactions in the SNO detector.

Measuring $\overline{\text{CC}}$ in the Pure D₂O Phase

For any phase of the SNO experiment, the positron measurement efficiency is determined by the energy threshold used in the analysis. For a positron total energy of 1 or 2 MeV, there are radioactive backgrounds at the same energy which dominant the number of events observed in the detector. At a positron total energy around 5 MeV, the radioactive backgrounds inherent in the detector's construction materials contribute significantly fewer observed events. This dissertation considers measurement of electron antineutrinos in the energy range 4 - 15 MeV so positron measurement efficiencies will range from 90% to 50% depending on a choice of the analysis energy threshold.

During the Pure D₂O phase, neutrons produced in the heavy water region will capture on the a deuterium nucleus $\approx 30\%$ of the time. Thus ≈ 9 out of every 100 $\overline{\text{CC}}$ interactions will have a chance of being measured as a triple coincidence. Inclusion of the positron detection efficiency will further lower the efficiency for detecting $\overline{\text{CC}}$ interactions via a triple coincidence. Thus, during the Pure D₂O phase the dominate measured signal of a $\overline{\text{CC}}$ interaction will be a positron-neutron, (e^+, n), coincidence.

The coincidence timing used in the electron antineutrino analysis hinges upon the capture time for the neutrons produced in the $\overline{\text{CC}}$ reaction. In the pure heavy water, neutrons can random walk several meters from their production point before capturing on either a deuteron or a proton. The average time a neutron spends random walking is ≈ 40 ms. The distance a neutron can travel partially explains the low capture efficiency

¹There is also a neutral-current weak interaction, $\bar{\nu}_e + d \rightarrow \bar{\nu}_e + p + n, \overline{\text{NC}}$. However, the single neutron produced in the $\overline{\text{NC}}$ reaction is indistinguishable from the single neutron produced in the NC reaction.

noted above. Neutrons that reach the acrylic vessel are highly likely to capture on a proton contained in the acrylic since the proton's neutron capture cross-section is ≈ 100 times that of a deuteron's. Neutron capture on protons produces a 2.2 MeV γ -ray, which, again, is at an energy where natural radioactive impurities in the detector's materials dominate the event rate.

Measuring \overline{CC} in the Salt Phase

During the Salt phase of the experiment, neutrons will predominantly capture on ^{35}Cl , that is, $\approx 80\%$ of the time. In contrast to the Pure D_2O phase, during the Salt phase more than half of all \overline{CC} interactions in the detector will have *both* neutrons capture on ^{35}Cl . Therefore, in the Salt phase the triple coincidence signature, (e^+, n, n) , from \overline{CC} interactions will dominate. Along with the increased neutron capture efficiency, during the Salt phase the neutron capture time is reduced to ≈ 5 milliseconds and the distance the neutron will travel from the point of origin is on average less than a meter.

Measuring \overline{CC} in the NCD Phase

It is expected that during the NCD phase of the experiment the neutron capture characteristics (efficiency for capture on the ^3He in the NCDs, mean time till capture, and distance of capture from production location), will be between the values noted above for the Pure D_2O and Salt phases. The NCD phase however provides a definitive detection of neutrons. Unlike in the Pure D_2O and Salt phases that must detect *all* particles through Čerenkov photons, the NCDs are primarily sensitive to neutrons and have backgrounds which are uncorrelated with the Čerenkov activity in the detector. Thus, during the NCD phase the detection of a prompt Čerenkov ring from a positron followed ≈ 15 milliseconds later by two NCD neutron detections, is by far the most unambiguous \overline{CC} identification SNO will have.

2.2 Electron Antineutrino Physics Topics

There are several reasons to consider studying electron antineutrinos at the Sudbury Neutrino Observatory:

- Detect or limit the $\bar{\nu}_e$ component of the solar neutrino flux.
- Make a first measurement of the atmospheric ν_e to $\bar{\nu}_e$ ratio.
- Detect or limit the $\bar{\nu}_e$ flux from a geo-reactor in the Earth's core.
- Detect or limit the flux of the diffuse background of supernova $\bar{\nu}_e$'s.
- Study one of the backgrounds to SNO's primary solar neutrino analysis.

A detection or limit on the electron antineutrino component of the solar neutrino flux provides information about neutrino properties (e.g. Dirac or Majorana type, magnetic moment strength, and neutrino decay) as well as solar properties (e.g. solar magnetic field strength). Measuring the ratio of the flux of atmospheric ν_e 's

to the flux of atmospheric $\bar{\nu}_e$'s, would be a ground breaking measurement providing a new test of atmospheric neutrino models. Recent suggestions [119, 122, 182] that there is a uranium based fission geo-reactor active in the Earth's core is testable via electron antineutrino studies at SNO. A detection or limit on the diffuse supernova neutrino background (via $\bar{\nu}_e$ detection) is a long awaited measurement by the astrophysics community. Finally, an electron antineutrino study will, at minimum, supply a measure of a class of events that are a background to the primary goal of the Sudbury Neutrino Observatory, to measure the total active flux of neutrinos coming from the Sun. In Part II of this dissertation, each of these possible topics is examined in detail. In the end it is found that placing a limit on the electron antineutrino component of the solar neutrino flux is the outstanding physics objective. The remaining physics topics in the above list are shown to have low rates and are thus difficult to address on the ≈ 5 year time scale that SNO is expected to be operational.

Chapter 3

ANALYSIS OUTLINE

3.1 *Dissertation Focus*

This dissertation focuses on placing an upper limit on the flux of solar electron antineutrinos. Part II demonstrates, in the solar neutrino energy range, the expected electron antineutrino interaction rate from all other sources is smaller than the rate allowed by current limits on the solar electron antineutrino flux. Thus, measuring an electron antineutrino signal at the expected background level will place a stricter upper limit on the electron antineutrino component of the solar neutrino flux.

3.2 *Plan*

The analysis presented here is designed to optimize the sensitivity and robustness of an electron antineutrino result generated from the Salt phase of the SNO experiment. To develop the analysis strategy and tools, the data from the Pure D₂O phase is used *in toto*. The goal of this plan is to determine how to implement a $\overline{\text{CC}}$ detection scheme optimized with respect to backgrounds of both known and unknown origins. Using the less efficient Pure D₂O phase to tune the analysis, a convincing blind electron antineutrino analysis of the Salt phase is possible. This analysis is blind in the sense that the answer is obtained without any prior inspection of the Salt phase data, thus eliminating human bias.

3.3 *Implementation and Organization*

Determining the rate of $\overline{\text{CC}}$ events from all potential sources of electron antineutrinos is paramount to motivating the solar electron antineutrino search. Part II of this dissertation calculates these expected $\overline{\text{CC}}$ interaction rates. Part III uses other physics analyses or Monte Carlo studies to develop the set of analysis parameters used in the extraction of the candidate set of $\overline{\text{CC}}$ events. Part IV applies these analysis parameters, extracts the candidate set of $\overline{\text{CC}}$ events, and then places a limit on the solar electron antineutrino flux. Finally, Part V discusses this electron antineutrino analysis scheme in relation to other suggested methods of electron antineutrino analysis of the SNO data.

Part II

Motivation

Chapter 4

SOLAR ELECTRON ANTINEUTRINOS

4.1 *The Standard Solar Model*

The standard solar model (SSM) describes the energy production, energy transport, thermodynamic properties, and evolution of stars. J. N. Bahcall's book, *Neutrino Astrophysics* [37] is an extensive introduction to the SSM and solar neutrino physics. The major neutrino producing reactions in the Sun produce electron neutrinos and *not* electron antineutrinos. Figure 4.1 shows what is referred to as the pp-chain, the dominant energy producing nuclear reaction chain in the Sun and the main source of solar electron neutrinos. The standard solar model is based upon four primary physics principles:

- Stars are in hydrostatic equilibrium.
- Energy transport is by photons and/or mass convection.
- Energy is generated by nuclear fusion reactions.
- Initial isotopic homogeneity and evolution solely by nuclear reactions.

These principles and the action of gravity determine the evolution of stars. The primary success of the standard solar model is accurately producing the observed distribution of star. That is to say, the SSM correctly models the observed distribution of stars on the Hertzsprung-Russell diagram of stellar luminosity verse temperature. Additionally, the SSM accurately predicts the observed oscillations of the Sun (i.e. helioseismology). To simplify things tremendously one might say that the Sun shines because nuclear processes are equivalent to the short hand equation, $4\text{H} \rightarrow {}^4\text{He} + e^- + e^+ + 2\nu_e + 25.7 \text{ MeV}$, where the 25.7 MeV released is shared among photons and the particles shown.

4.2 *Models of Electron Antineutrino Production in the Sun*

This section presents theoretical suggestions for how electron neutrinos produced in the Sun could be converted into electron antineutrinos. All these proposals assume neutrinos are massive particles. The primary class of models assume a large neutrino magnetic moment which interacts with the Sun's (unknown) internal magnetic fields inducing a spin flip. A second class is decay of massive neutrinos. The discussion begins by distinguishing between Dirac and Majorana neutrino types followed by a discussion of the differences between the magnetic moments of Dirac and Majorana type neutrinos. The neutrino magnetic moment discussion naturally leads into a presentation of the primary class of solar neutrino conversion models. Finally, neutrino decay is briefly discussed.

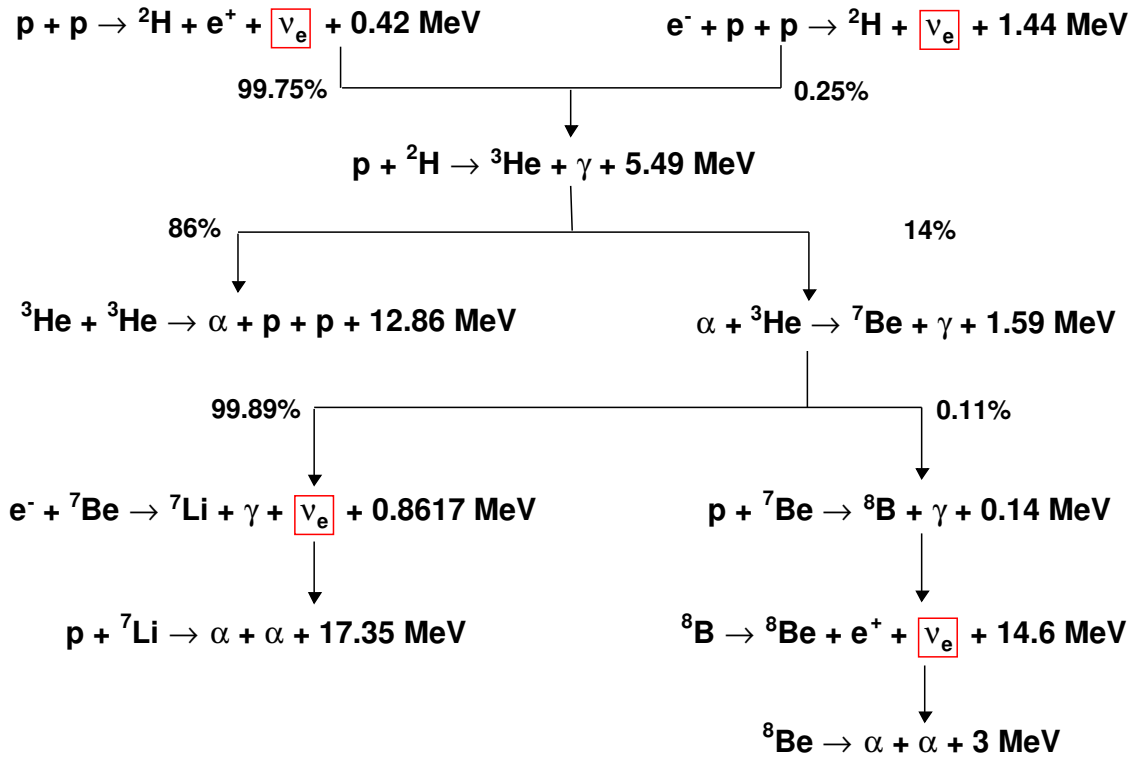


Figure 4.1: The Standard Solar Model pp-chain. Note that there are only electron neutrinos (boxed) produced in these reactions.

4.2.1 Dirac vs. Majorana Massive Neutrinos

In this section the properties distinguishing Dirac and Majorana massive neutrinos are presented. The presentation will begin with a mathematical treatment, although the more intuitive *CPT* treatment of the second section is perhaps a better introduction. The goal is to develop a precise language for discussing these particle types while fleshing out the guiding mantra: “Majorana neutrinos are their own anti-particles.”

Dirac and Majorana Mathematical Treatment

This subsection compares and contrasts the mathematical description of Dirac and Majorana massive neutrinos and closely follows the arguments of Ref. [61]. The Dirac-Pauli representation of the 4×4 gamma matrices is given by $\vec{\gamma} = \begin{pmatrix} 0 & -i\vec{\sigma} \\ i\vec{\sigma} & 0 \end{pmatrix}$, $\gamma_4 = \begin{pmatrix} 1 & 0 \\ 0 & -1 \end{pmatrix}$, and $\gamma_5 = \begin{pmatrix} 0 & 1 \\ 1 & 0 \end{pmatrix}$ where $\vec{\sigma} = (\sigma_1, \sigma_2, \sigma_3)$ are the standard 2×2 Pauli spin matrices. In the following, ϕ^\dagger is the adjoint of a complex matrix, ϕ , defined as $\phi^\dagger \equiv (\phi^*)^T$ where $*$ denotes taking the complex conjugate and T denotes forming the transposed matrix.

Define ψ as a four component column vector representing a massive fermion field. The corresponding

row vector for this field is given by $\bar{\psi} = \psi^\dagger \gamma_4$. Charge conjugation of these fields are denoted by c

$$\psi \xrightarrow{^c} \psi^c \qquad \bar{\psi} \xrightarrow{^c} \bar{\psi}^c \quad (4.1)$$

and changes the sign of all additive quantum numbers of the fields. Note that the structure of the fermion fields imply ψ and $\bar{\psi}$ have opposite parities [61]. For a single, massive fermion field the Dirac equation determines the free field Lagrangian:

$$\mathcal{L}_\psi = -\frac{1}{2} \int (\bar{\psi} \gamma_\mu \partial_\mu \psi + \bar{\psi} m_D \psi) d^4x \quad (4.2)$$

The mass term is $\bar{\psi} m_D \psi$. Mass terms are the focus of the following deliberations and, thus, are presented separated of the full Lagrangian formalism. A Lorentz invariant free field theory describing two fermions of equal mass but conjugated additive quantum numbers has two mass terms

$$\mathcal{L}_{\text{Dirac}} = \bar{\psi} m_D \psi + \bar{\psi}^c m_D \psi^c \quad (4.3)$$

In general, $\psi \neq \psi^c$ and $\bar{\psi} \neq \bar{\psi}^c$ so the terms in 4.3 are not redundant. This situation is labeled the Dirac particle case.

The neutrino is an electrically neutral, massive fermion field. In this case is not clear what distinction is made by the two mass terms in 4.3. That is, the charge conjugation does not obviously distinguish between particle types as, for example, it does for electrons and positrons. Thus one can postulate the following equalities:

$$\psi = \psi^c \qquad \bar{\psi} = \bar{\psi}^c \quad (4.4)$$

This attribution is the defining property of Majorana fields. This is in sharp contrast to the Dirac case. When the Majorana condition holds, ψ and $\bar{\psi}$ are charge conjugation eigenstates. New mass terms are now allowed (retaining the requirement of Lorentz invariance). These Majorana mass terms have the form

$$\mathcal{L}_{\text{Majorana}} = \bar{\psi} m_M \psi^c + \bar{\psi}^c m_M^* \psi \quad (4.5)$$

where $m_M = m_1 + im_2$ and $|m_M| = |m_M^*|$. The parity of Majorana fields is imaginary ($\pm i$).

The most general form of the mass terms describing a neutrino and its charge conjugate states is the sum of the Dirac and Majorana mass terms

$$\mathcal{L}_\nu = \mathcal{L}_{\text{Dirac}} + \mathcal{L}_{\text{Majorana}} \quad (4.6)$$

$$= [\bar{\psi} m_D \psi + \bar{\psi}^c m_D \psi^c]_{\text{Dirac}} + [\bar{\psi} m_M \psi^c + \bar{\psi}^c m_M^* \psi]_{\text{Majorana}} \quad (4.7)$$

The Dirac mass terms in (4.7) are no longer distinguishable under the Majorana conditions on the ψ fields, but are retained to expose the underlying formalism. The mass eigenvalues of this most general case are $m_D \pm |m_M|$.

CPT Treatment of Dirac and Majorana Particles

A discussion of the *CPT* ($C =$ charge, $P =$ parity, and $T =$ time symmetries [65]) properties of Dirac and Majorana neutrinos augments the mathematical discussion of the previous section. Figure 4.2 presents the intuitive *CPT* relations of massive neutrinos, taking into account the fact that the Standard Model weak interactions include left-handed neutrinos and right-handed antineutrinos. Note that the two Dirac states $\bar{\nu}_L$

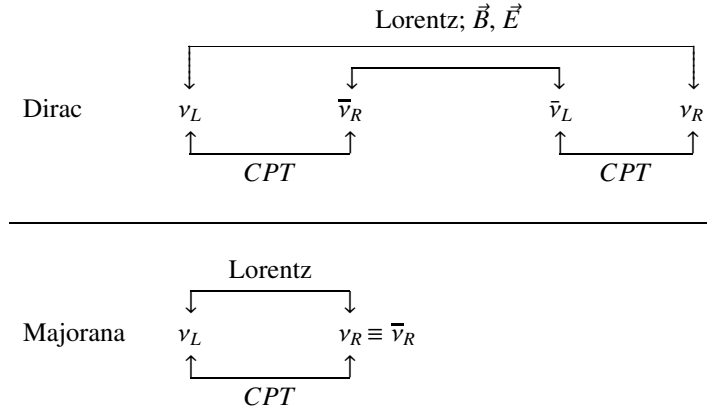


Figure 4.2: *CPT* properties of Dirac and Majorana neutrinos as presented in Ref. [61]. There are 4 distinct Dirac states and 2 distinct Majorana states.

and ν_R are effectively sterile in the Standard Model which includes only left-handed particle interactions and right-handed antiparticle interactions. Extensions to the Standard Model can allow for right-handed particle interactions, but are severely constrained experimentally [88, 196, 197]. Figure 4.2 shows that a massive left-handed neutrino will transform under *CPT* into right-handed antineutrinos.

To make a connection to the mathematical treatment of the previous section define the chiral projections of the ψ fields:

$$\psi_L = \frac{1 - \gamma_5}{2} \psi \quad (\psi_L)^c = \frac{1 + \gamma_5}{2} \psi^c = (\psi^c)_R \quad (4.8)$$

$$\psi_R = \frac{1 + \gamma_5}{2} \psi \quad (\psi_R)^c = \frac{1 - \gamma_5}{2} \psi^c = (\psi^c)_L$$

These definitions and the property that $(1 + \gamma_5)(1 - \gamma_5) = 0$ allows the Lagrangian mass terms, \mathcal{L}_ν , to be rewritten as

$$\mathcal{L}_\nu = \left[(\bar{\psi}_R m_D \psi_L + \bar{\psi}_L m_D \psi_R)_{\nu_L \leftrightarrow \nu_R} + ((\bar{\psi}_R)^c m_D (\psi_L)^c + (\bar{\psi}_L)^c m_D (\psi_R)^c)_{\bar{\nu}_L \leftrightarrow \bar{\nu}_R} \right]_{\text{Dirac}} \quad (4.9)$$

$$+ \left[(\bar{\psi}_R m_M (\psi_L)^c + \bar{\psi}_L m_M (\psi_R)^c)_{\bar{\nu}_L \leftrightarrow \bar{\nu}_R} + ((\bar{\psi}_R)^c m_M^* \psi_L + (\bar{\psi}_L)^c m_M^* \psi_R)_{\nu_L \leftrightarrow \nu_R} \right]_{\text{Majorana}} \quad (4.10)$$

As already mentioned, the two terms in the Dirac portion are identical when the Majorana condition is imposed. The terms are not combined to highlight their relation to the information presented in Figure 4.2 and to show the distinct terms present when the Dirac condition (instead of the Majorana condition) holds. Note that when the Dirac condition holds, it must also be the case that $|m_M| = 0$ to maintain the Lagrangian's Lorentz invariance.

4.2.2 The Neutrino Magnetic Moment

Massive neutrinos allow a non-zero neutrino magnetic moment. The electroweak standard model of leptons provides for only a very small Dirac neutrino magnetic moment,

$$\mu_{\nu_e} \simeq 3.1 \times 10^{-19} \mu_B \cdot \left(\frac{m_{\nu_e}}{1 \text{ eV}} \right), \quad (4.11)$$

where μ_B is the Bohr magneton and m_{ν_e} is the mass of the electron neutrino measured in electron volts, eV. Refer to Section 11.3 of Ref. [162] for a discussion of how this value is derived or see the Particle Data Group's review of particle physics [113].

The experimental situation, however, is quite different as demonstrated in the following. There are several ways in which limits on the neutrino magnetic moment have been set. Each of these ways has a different level of "trust" for the derived limit - lab experiments are the most trusted while arguments based on astrophysical grounds are less trusted. Table 4.1 lists a number of limits on the neutrino magnetic moment, providing a reference and stating the method used to set the limit.

Table 4.1: Limits placed on the magnitude of the neutrino magnetic moment, μ_{ν_e} , by different techniques. This table is a selected listing of the Particle Data Group's μ_{ν_e} table [113].

$ \mu_{\nu_e} /\mu_B \times 10^{-10}$	Year	Ref.	Method or Group
≤ 1.3	2003	[113]	Particle Data Group value
≤ 1.3	2003	[142]	Reactor $\bar{\nu}_e + e \rightarrow \bar{\nu}_e + e$
≤ 2	2002	[112]	Fit solar + reactor oscillation data (Majorana ν)
$\leq 0.01-0.04$	1999	[36]	$\nu_L \rightarrow \nu_R$ in SN 1987A
≤ 1.1	2004	[146]	Super-K solar ν spectrum shape
≤ 0.03	1999	[181]	Red giant luminosity
≤ 4	1999	[181]	Solar cooling
≤ 0.62	1999	[90]	Depolarization in early universe plasma

Dirac Neutrino Magnetic Moments

In the case of Dirac neutrinos, the magnetic moment is "diagonal". That is, in the Dirac case, the matrix describing the neutrinos' magnetic moments does not have any non-zero off diagonal elements which would connect neutrinos of different flavors. This means that if one considers *only* a magnetic moment interaction with a transverse magnetic field, there can only be a spin-flip interaction, $\nu_{x,L} \rightarrow \nu_{x,R}$. There can not be any

induced neutrino flavor transition. This does not preclude flavor oscillation via the well known vacuum and MSW processes.

Phenomenologically, if a left-handed Dirac neutrino with a non-zero magnetic moment has its spin flipped due to an interaction with a magnetic field, it becomes a right-handed Dirac neutrino which, in the absence of right-handed interactions, does not interact in the electroweak standard model. The implication is, if neutrinos are Dirac particles and under go a spin-flip process in magnetic fields, then the resulting right-handed neutrino state is not detectable or at least only detectable through right-handed weak interactions.

Majorana Neutrino Magnetic Moments

In the case of pure Majorana neutrinos, the magnetic moment is exactly zero on the diagonal and can only exist via non-zero off diagonal elements. That is, in the Majorana case, the matrix describing the neutrinos' magnetic moments can have non-zero off diagonal elements which connect neutrinos of different flavors. This allows for a spin-flavor transition of the type $\nu_{x,L} \rightarrow \bar{\nu}_{y,R}$ where $x \neq y$. The spin-flip only transition, $\nu_{x,L} \rightarrow \bar{\nu}_{x,R}$, is allowed in conjunction with MSW effects but only via second order perturbations in the interaction [25].

4.2.3 Spin-Flavor Precession

For over 20 years, physicists have considered the possibility of electron neutrino conversion in solar magnetic fields. The hypothesis of solar magnetic field induced conversion of solar $\nu_{e,L}$ to sterile $\nu_{e,R}$ was first proposed as a solution to the neutrino deficit measured by the Homestake ^{37}Cl experiment [76]. Later, it was proposed to account for an apparent time (*anti*)correlation between the ^{37}Cl experiment's neutrino signal and solar magnetic field activity as quantified by Sun spot number [216, 170]. It was realized the combination of matter enhanced neutrino flavor oscillation (MSW) and spin precession (SP) (Dirac case) or spin-flavor precession (SFP) (Majorana case) could provide a single description including both significant ν_e depletion and a time varying signal [218]. The combination of these effects is known as *resonant* conversion schemes (RSP & RSFP) [20, 143, 40]. More realistic descriptions include a varying magnetic field direction along the neutrino's path [213, 200, 207, 33, 39, 138, 204]. Current conversion schemes have five characteristics:

- Focus on Majorana neutrino signature rather than Dirac sterile admixture.
- Matter enhanced flavor oscillations (MSW).
- Hypothetical solar magnetic field configurations with varying field direction.
- Consideration of two conversion scenarios: $\nu_e \xrightarrow{\text{SFP}} \bar{\nu}_x \xrightarrow{\text{Osc}} \bar{\nu}_e$ OR $\nu_e \xrightarrow{\text{Osc}} \nu_x \xrightarrow{\text{SFP}} \bar{\nu}_e$
- Two experimentally unconfirmed assumptions:
 - A neutrino magnetic moment on the order of $\mu_\nu \approx 10^{-10} \mu_B$.
 - Solar magnetic field strengths of 10-100 kGauss. The actual interior field strength is not known. Predictions range from 10-10⁶ Gauss. See Ref. [68] and the references there-in.

Complete analytic treatments of the combined matter enhanced and spin-flavor precession models exist in the literature [143, 25, 149]. The importance of these results is the ability to study the conditions for resonant transitions defined as the case when the matter enhanced oscillations and the spin-flavor transitions occur in the same region of the Sun. The evolution equation that describes these combined affects to neutrinos is [25, 149]

$$i \frac{d}{dt} \begin{pmatrix} \nu_{e,L} \\ \nu_{\mu,L} \\ \bar{\nu}_{e,R} \\ \bar{\nu}_{\mu,R} \end{pmatrix} = \left(\begin{pmatrix} H_L & 0 \\ 0 & H_R \end{pmatrix} + \mu_{e\mu} B_{\perp}(t) \begin{pmatrix} 0 & -D^* \\ D & 0 \end{pmatrix} \right) \begin{pmatrix} \nu_{e,L} \\ \nu_{\mu,L} \\ \bar{\nu}_{e,R} \\ \bar{\nu}_{\mu,R} \end{pmatrix} \quad (4.12)$$

where $\mu_{e\mu}$ is the magnitude of the Majorana neutrino transition magnetic moment and $B_{\perp}(t)$ is the time-varying magnitude of the magnetic field perpendicular to the direction of the neutrino's momentum. The sub-matrices $H_{L,R}$ and D are

$$H_{L,R} = \begin{pmatrix} \pm \frac{G_F}{\sqrt{2}} (2N_e - N_n) - \frac{\Delta m^2}{4E_\nu} \cos 2\theta & \frac{\Delta m^2}{4E_\nu} \sin 2\theta \\ \frac{\Delta m^2}{4E_\nu} \sin 2\theta & \pm \frac{G_F}{\sqrt{2}} (-N_n) + \frac{\Delta m^2}{4E_\nu} \cos 2\theta \end{pmatrix} \quad D = e^{-i\phi(t)} \begin{pmatrix} 0 & -1 \\ 1 & 0 \end{pmatrix} \quad (4.13)$$

where $H_{L,R}$ describes matter enhanced neutrino oscillations for left- and right-handed Majorana neutrinos in the two-flavor neutrino oscillation approximation represented by $\begin{pmatrix} \nu_e \\ \nu_\mu \end{pmatrix} = \begin{pmatrix} \cos \theta & \sin \theta \\ -\sin \theta & \cos \theta \end{pmatrix} \begin{pmatrix} \nu_1 \\ \nu_2 \end{pmatrix}$. The magnetic field direction matrix, D , describes the time-varying direction of the magnetic field in the plane perpendicular to the direction of the neutrino's momentum. The factors in the two equations 4.13 are:

G_F The Fermi constant.

N_e The local electron density.

N_n The local neutron density.

E_ν The energy of the neutrino.

Δm^2 The difference of the squares of the neutrino masses: $\Delta m^2 = m_2^2 - m_1^2$.

θ The neutrino vacuum mixing angle describing neutrino flavor oscillations.

$\phi(t)$ The parameterization of the time-varying direction of the magnetic field.

Ref. [25] provides a graphical representation of the energy level crossings under various conditions in addition to pointed discussions of the phenomenology for specific scenarios. The above comments are the latest ideas, in a wealth of proposals for solar electron neutrino conversion to electron antineutrinos¹.

¹An attempt at a definitive list of articles discussing $\nu_e \rightarrow \bar{\nu}_e$ conversion in solar magnetic fields: [5, 14, 15, 16, 17, 18, 19, 20, 21, 22, 23, 24, 25, 26, 27, 28, 32, 33, 39, 40, 41, 43, 44, 52, 60, 71, 72, 73, 76, 90, 95, 100, 108, 112, 134, 136, 138, 143, 144, 149, 158, 159, 160, 161, 167, 170, 178, 179, 184, 186, 192, 193, 195, 198, 200, 203, 204, 207, 213, 216, 217, 218]

4.2.4 Massive Neutrino Decay

If neutrinos are massive particles they may decay. There are two models of neutrino decay widely considered. The first model assumes neutrinos are Dirac type particles and have a decay of the form, $\nu \rightarrow \nu' + \phi$, where ϕ is a scalar particle and ν' is a right-handed “sterile” neutrino. The second model assumes neutrinos are Majorana type particles and has a decay of the form, $\nu \rightarrow \nu' + J$, where J is a pseudo-scalar particle (Majoron) and $\nu' \equiv \bar{\nu}$ is an active, right-handed antineutrino.

In the early 1990’s, one group studied both of these decay models in the context of the experimental results from the available solar neutrino experiments. A generalization of these results is presented in Ref. [2] referencing the authors’ specific decay models for Dirac [4, 3] and Majorana [1] neutrinos. More recent neutrino decay studies that include solar neutrino data from SNO and Super-Kamiokande demonstrate solar neutrino decay is not a dominant phenomenon, however, the models are not restrictive enough to place strong limits on specific neutrino lifetimes [54, 127, 42, 75]. These more recent papers also perpetuate the possible models of neutrino decay mentioned in the previous paragraph.

4.3 Experimental Limits on the Solar Electron Antineutrino Flux

Table 4.2 lists experimental limits set on the solar electron antineutrino flux. Each limit listed in Table 4.2 is discussed in detail below.

Table 4.2: Measured limits on the solar electron antineutrino flux, $\Phi_{\bar{\nu}_e}^{8\text{B}}$. The quoted confidence level is given in the column titled C.L. Note that, SNO is capable of detecting electron antineutrinos of any energy above the $\bar{\nu}_e$ reaction threshold of 4.03 MeV.

Year	$\Phi_{\bar{\nu}_e}^{8\text{B}} \left(\frac{10^5}{\text{cm}^2\text{s}} \right)$	C.L.	Reference	Data used	$E_{\bar{\nu}_e}$ (MeV)
2004	≤ 0.014	90%	K. Eguchi <i>et al.</i> [87]	KamLAND	8.3 \rightarrow 14.8
2003	≤ 0.11	95%	E. Torrente-Lujan [73]	KamLAND	6.0 \rightarrow 8.125
2002	≤ 0.404	90%	Y. Gando <i>et al.</i> [111]	Super-Kamiokande	9.3 \rightarrow 21.3
2000	≤ 1.8	95%	E. Torrente-Lujan [205]	Super-Kamiokande	6.5 \rightarrow 20.0
1997	≤ 1.98	95%	G. Fiorentini <i>et al.</i> [96]	Super-Kamiokande	$>$ 8.3
1996	≤ 1.0	90%	M. Aglietta <i>et al.</i> [6]	Liquid Scintillation Detector	7.0 \rightarrow 17.0
1991	≤ 3.03	99%	R. Barbieri <i>et al.</i> [44]	Kamiokande	\geq 10.6

4.3.1 K. Eguchi *et al.* [87]

Under the assumption of a ${}^8\text{B}$ energy spectrum, the KamLAND Collaboration places an upper limit on the total solar electron antineutrino flux of $\Phi_{\bar{\nu}_e}^{8\text{B}} \leq 1.4 \times 10^3 \text{ (cm}^{-2}\text{s}^{-1}\text{)}$ at a 90% confidence level. This equals 2.8×10^{-4} of the SSM total ${}^8\text{B}$ electron neutrino flux. The KamLAND experiment is similar in design to the Sudbury Neutrino Observatory in that it is a spherical liquid neutrino target observed by photomultiplier tubes. KamLAND is sensitive to electron antineutrinos via inverse beta-decay of protons, $\bar{\nu}_e + p \rightarrow e^+ + n$, contained in a liquid scintillator solution. The positron, e^+ , can then generate scintillation light as it passes

through the scintillator and finally produces two photons upon annihilation with an atomic electron. The free neutron, n , produces a second (coincident) signal when it captures on a proton in the solution. The KamLAND experiment is designed to study electron antineutrinos produced by nuclear reactors. Reactor electron antineutrino's energy spectra is predominately below 8 MeV. Thus, the upper limit on the solar electron antineutrino flux is determined by searching for inverse beta decay reactions indicative of electron antineutrinos in the energy range $8.3 < E_{\bar{\nu}_e}$ (MeV) < 14.8 . No candidate events are found in a 185.5 day (0.28 kton-year) KamLAND data set, hence setting the limit noted above. In the current detector configuration, KamLAND will continue to lower the upper limit by accumulating an increased set data (i.e. exposure time). However, future upgrades to the KamLAND detector are expected. These upgrades are intended to reduce the intrinsic radioactive backgrounds in the detector materials as well as increasing the light collection efficiencies via the addition of new photomultiplier tubes. These improvements will likely give KamLAND a significant improvement in electron antineutrino detection efficiency, thus allowing for further lowering of the upper limit set on the solar electron antineutrino flux.

4.3.2 E. Torrente-Lujan [73]

Using reactor neutrino results from KamLAND [86], E. Torrente-Lujan *et al.* set two upper limits on the total solar electron antineutrino flux. The KamLAND experiment observes electron antineutrinos produced by nuclear reactors using a coincidence signature from $\bar{\nu}_e + p \rightarrow e^+ + n$ in liquid scintillator. The first limit set by E. Torrente-Lujan *et al.* is based upon assuming values for the neutrino oscillation parameters ($\Delta m^2 = 6.9 \times 10^{-5} \text{ eV}^2$ and $\sin^2 2\theta = 1$) and then doing a maximum likelihood fit of an expected reactor $\bar{\nu}_e$ spectra plus a variable ^8B solar $\bar{\nu}_e$ spectra to the measured KamLAND data. This method sets a limit of $\Phi_{\bar{\nu}_e}^{8\text{B}} \leq 1.1 \times 10^4 \text{ (cm}^{-2}\text{s}^{-1}\text{)}$ at a 95% confidence level. The second method uses the fact that KamLAND reports zero events in the 6 – 8.125 MeV energy range. The lack of signal in this energy range also sets an upper limit on the solar electron antineutrino flux, $\Phi_{\bar{\nu}_e}^{8\text{B}} \leq 3.5 \times 10^4 \text{ (cm}^{-2}\text{s}^{-1}\text{)}$ at a 95% confidence level. Note that KamLAND had not presented results for energies above 8.125 MeV when this article was written.

4.3.3 Y. Gando *et al.* [111]

The Super-Kamiokande detector is a soda-can shaped cavity filled with 50,000 tons of pure light water, viewed by 11,200 photomultiplier tubes². Super-Kamiokande is sensitive to solar electron neutrinos via elastic scattering of atomic electrons in the detector's water. The atomic electrons are forward scattered and emit Čerenkov radiation. This forward scattering appears in the analysis of Super-Kamiokande data via the parameter $\cos \theta_\odot$, where θ_\odot is the angle between the direction *away* from the Sun and the fit direction of $\approx 5 - 20$ (MeV) events.

The Super-Kamiokande Collaboration uses a muon spallation background subtraction method to statistically determine the number of potential electron antineutrino events occurring in their detector. This analysis focuses on the $\cos \theta_\odot < 0.5$ data above 6 MeV. These events are directed into a Sun-side hemisphere and are

²On November 12, 2001 an accidental implosion of a photomultiplier tube caused a chain reaction of photomultiplier tube implosions. After redistributing the remaining operational photomultiplier tubes, Super-Kamiokande continues to take data, however with a reduced light sensitivity.

dominated by the isotropic decay of spallation products from muons. The spallation event rate is estimated for this data sample and subtracted from the data set. The remaining number of events (statistical) is considered the antineutrino candidate sample because an electron produced in the $\bar{\nu}_e + p \rightarrow e^+ + n$ reaction is predominantly directed away from the $\bar{\nu}_e$'s incoming direction. A simulation of an electron antineutrino flux equal in magnitude to the total solar neutrino flux was used to determine the number of expected events in the region analyzed. The ratio of candidate events to expected events sets a limit of $\Phi_{\bar{\nu}_e}^{8\text{B}} \leq 4.04 \times 10^4 \text{ (cm}^{-2}\text{s}^{-1}\text{)}$ at a confidence level of 90%. This limit is based upon 1496 days of data. The Super-Kamiokande Collaboration will be able to improve upon these results by simply increasing the size of their data set. There are no planned detector upgrades that will significantly improve the solar electron antineutrino sensitivity, however a recent proposal to dissolve Gd in the water *would* make Super-Kamiokande very sensitive to $\bar{\nu}_e$ through the coincidence detection of the positron and a neutron capture on Gd [55].

4.3.4 E. Torrente-Lujan [205]

Using a Doctoral dissertation from Super-Kamiokande [125], E. Torrente-Lujan presents a limit on the total solar ^8B electron antineutrino flux, $\Phi_{\bar{\nu}_e}^{8\text{B}} \leq 1.8 \times 10^5 \text{ (cm}^{-2}\text{s}^{-1}\text{)}$ at a 95% confidence level. The limit is determined by analyzing the ‘‘flatness’’ of the flat background of Super-Kamiokande’s $\cos \theta_\odot$ neutrino-electron scattering data. The reaction of interest is $\bar{\nu}_e + p \rightarrow e^+ + n$. The positron will look just like a scattered electron in the Super-K detector. The signature of an electron antineutrino component of the total solar neutrino flux is a backward scattering of positrons from the $\bar{\nu}_e + p$ interactions. The $\bar{\nu}_e + p$ reaction is peaked backward in the lab frame for energies less than 13 MeV. Thus the limit is derived by comparing the slope of a linear fit to the $\cos \theta_\odot \lesssim 0.4$ data to the expectation of a slope equal to zero for an isotropic background.

4.3.5 G. Fiorentini *et al.* [96]

G. Fiorentini *et al.* were the first to exploit the angular distribution of the out-going positron in the $\bar{\nu}_e + p \rightarrow e^+ + n$ reaction (see Section 4.3.4). They used Super-Kamiokande data to set a limit on the solar ^8B electron antineutrino flux above an electron antineutrino energy of $E_{\text{limit}} = 8.3 \text{ MeV}$, $\Phi_{\bar{\nu}_e}^{8\text{B}}(E_{\bar{\nu}_e} > 8.3\text{MeV}) < 6 \times 10^4 \text{ (cm}^{-2}\text{s}^{-1}\text{)}$. A simple ratio is used to scale this limit to the total solar ^8B electron antineutrino flux,

$$\frac{\Phi_{\text{SSM}}^{8\text{B}}(E_{\nu_e} \geq E_{\text{limit}})}{\Phi_{\text{SSM}}^{8\text{B}}} = \frac{\Phi_{\bar{\nu}_e}^{8\text{B}}(E_{\bar{\nu}_e} \geq E_{\text{limit}})}{\Phi_{\bar{\nu}_e}^{8\text{B}}}, \quad (4.14)$$

where the left-hand side of the equation is the ratio of solar ^8B electron neutrino fluxes and the right-hand side of the equation is the ratio of solar electron antineutrino fluxes with an assumed ^8B energy spectrum. $\Phi_{\text{SSM}}^{8\text{B}}$ is the SSM total integrated solar ^8B electron neutrino flux. $\Phi_{\text{SSM}}^{8\text{B}}(E_{\nu_e} \geq E_{\text{limit}})$ is the SSM integrated solar ^8B electron neutrino flux above a specific energy, E_{limit} , taken from the G. Fiorentini *et al.* analysis. $\Phi_{\bar{\nu}_e}^{8\text{B}}(E_{\bar{\nu}_e} \geq E_{\text{limit}})$ is exactly the limit placed on the solar ^8B electron antineutrino flux in the paper. The flux is then $\Phi_{\bar{\nu}_e}^{8\text{B}}(E_{\bar{\nu}_e} \geq E_{\text{limit}}) = 1.53 \times 10^5 \text{ (cm}^{-2}\text{s}^{-1}\text{)}$ for a BP2000 model with $\Phi_{\text{SSM}}^{8\text{B}} = 5.05 \times 10^5 \text{ (cm}^{-2}\text{s}^{-1}\text{)}$. Solving equation 4.14, the G. Fiorentini *et al.* limit on the total solar ^8B electron antineutrino flux is $\Phi_{\bar{\nu}_e}^{8\text{B}} = 1.98 \times 10^5 \text{ (cm}^{-2}\text{s}^{-1}\text{)}$ at the 95% confidence level.

4.3.6 M. Aglietta *et al.* [6]

M. Aglietta *et al.* determine an upper limit on the solar ^8B electron antineutrino flux using data from the Liquid Scintillation Detector (LSD) in the Mont Blanc Laboratory. LSD is sensitive to electron antineutrinos through the $\bar{\nu}_e + p \rightarrow e^+ + n$ reaction and is capable of detecting the e^+ and n in coincidence, greatly reducing the background. Using data from a 93.9 ton-yr exposure of the 86.4 tonne detector, M. Aglietta *et al.* compare the number of coincidences counted to the number of expected accidentals and there-by determine a limit on the number of electron antineutrino interactions occurring in LSD. Using a Monte Carlo simulation of supposed solar ^8B electron antineutrinos, they determine LSD's expected number of counts above accidentals assuming complete $\nu_e \rightarrow \bar{\nu}_e$ conversion. Comparing the measured limit on the number of counts to the expected number of counts for full conversion, they set the limit, $\Phi_{\bar{\nu}_e}^{8\text{B}} \leq 1.0 \times 10^5 \text{ (cm}^{-2}\text{s}^{-1}\text{)}$ at a 90% confidence level on the total solar ^8B electron antineutrino flux.

4.3.7 R. Barbieri *et al.* [44]

R. Barbieri *et al.* use Kamiokande data to set a limit on the solar ^8B electron antineutrino flux. They state, incorrectly, that positrons are produced isotropically in the reaction $\bar{\nu}_e + p \rightarrow e^+ + n$. Using this premise, they state that the total number of events in the isotropic background of the $\cos \theta_\odot$ data, sets a bound on the number of solar electron antineutrinos interaction occurring in the Kamiokande detector. Since the data analyzed is above 9.3 MeV, this solar electron antineutrino flux would be due to ^8B electron neutrinos converting to electron antineutrinos. It's interesting to note the incorrect premise of isotropic positron production does not invalidate their flux limit because the produced positron is actually slightly back scattered (see Section 4.3.4).

R. Barbieri *et al.* present a model independent limit on the solar electron antineutrino flux, $\Phi_{\bar{\nu}_e}(E_{\bar{\nu}_e} \geq 10.6 \text{ MeV}) \leq 6.1 \times 10^4 \text{ (cm}^{-2}\text{s}^{-1}\text{)}$. They state that "A more stringent limit can be derived if one assumes, as above, the spectrum to be the same as for ν_e " - namely the ^8B spectrum. They give the relation,

$$A\langle P(\bar{\nu}_e) \rangle_{88-89} \leq 6\% \quad (\text{at } 99\% \text{ C.L.}), \quad (4.15)$$

where A defines the error bars ($A = [0.7, 1.3]$) and $\langle P(\bar{\nu}_e) \rangle_{88-89}$ is the average $\nu_e \rightarrow \bar{\nu}_e$ conversion probability averaged over the data taking done in 1988 and 1989. Setting A equal to 1 gives the central value of the error range quoted. Thus, 6% of the BP2000 total solar ^8B electron neutrino flux ($5.05 \times 10^6 \text{ (cm}^{-2}\text{s}^{-1}\text{)}$) gives the R. Barbieri *et al.* limit on the total integrated solar ^8B electron antineutrino flux of $\Phi_{\bar{\nu}_e}^{8\text{B}} \leq 3.03 \times 10^5 \text{ (cm}^{-2}\text{s}^{-1}\text{)}$ at a 99% confidence level.

4.4 Calculating the Solar Electron Antineutrino Induced Event Rate in SNO

For each case in Section 4.3 the upper limit on the solar electron antineutrino flux was set assuming a SSM ^8B electron neutrino spectrum. Thus in calculating the electron antineutrino interaction rate in SNO, the SSM ^8B energy spectrum will be assumed. Table 4.3 lists the various parameters used in this calculation. This calculation is integrated over the entire ^8B energy spectrum for the $\bar{\nu}_e + d \rightarrow e^+ + n + n$ reaction from

Table 4.3: Factors or parameters used in the calculation of the solar electron antineutrino rate. The total flux is taken from measured limits as explained in the text.

Parameter or Factor	Source or Value
^8B energy spectrum	BP2000 [38]
Total $\bar{\nu}_e$ flux	$1.0 \times 10^5 \text{ (cm}^{-2}\text{s}^{-1}\text{)}$
$\overline{\text{CC}}$ cross-section	NSGK+ [163]
Target mass	1 kilotonne D_2O
Integration time	365.25 days

threshold at $E_{\bar{\nu}_e} = 4.03 \text{ MeV}$ to above the 14.06 MeV end point.³ Figures 4.3 & 4.4 show the results of this calculation. Table 4.4 presents the number of expected $\overline{\text{CC}}$ interactions in SNO for a range of electron antineutrino fluxes having a solar ^8B neutrino energy spectra, specifically, if the flux limits of Table 4.2 are taken as the actual total flux.

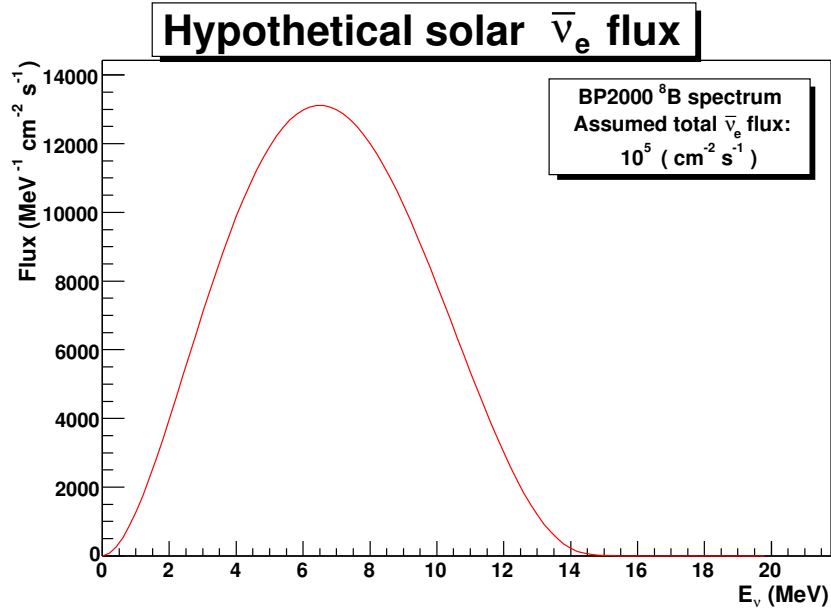


Figure 4.3: A hypothetical flux spectrum for electron antineutrinos converted from ^8B electron neutrinos. The shape is given by the Bahcall-Pinsonneault-Basu (BP2000) [38] ^8B standard solar model (SSM) flux-spectra since an energy independent conversion mechanism is assumed.

³A neutrino reaction and integration package provided by a SNO Collaborator, F. Duncan, was used in these calculations. The $\overline{\text{CC}}$ cross-section from Ref. [163] was added to this package for the calculations of this section.

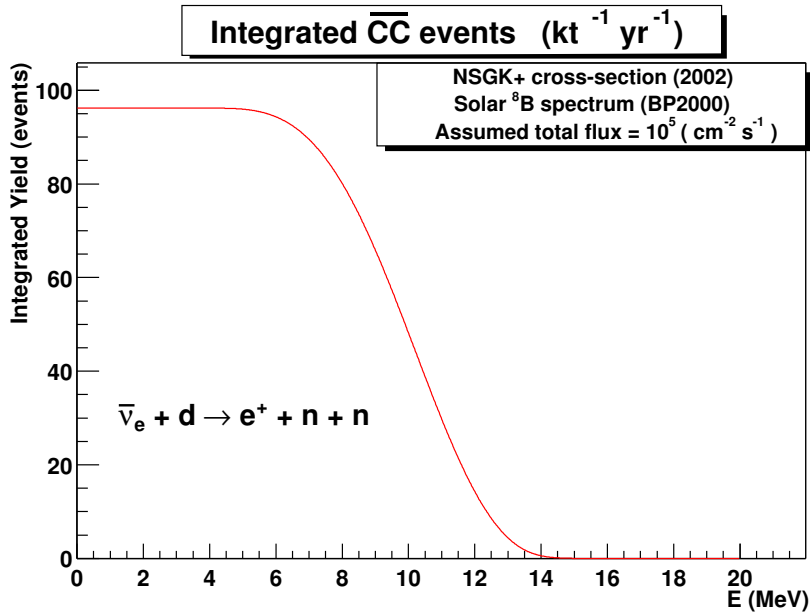


Figure 4.4: The expected energy integrated number of \overline{CC} interactions.

Table 4.4: The number of expected \overline{CC} interactions for one kt-yr for various values of a total electron antineutrino flux, $\Phi_{\nu_e}^{8B}$, having solar 8B spectral shape.

$\Phi_{\nu_e}^{8B}$ ($\text{cm}^{-2}\text{s}^{-1}$)	$\overline{CC}/\text{kt} \cdot \text{yr}$
1.4×10^3	1.3
1.1×10^4	11
4.04×10^4	39
1.0×10^5	96
1.8×10^5	173
1.98×10^5	190
3.03×10^5	291

4.5 Other Derived Measurements

There are additional quantities which SNO can address using the results of a solar electron antineutrino analysis. This section lists these additional possibilities for electron antineutrino analysis in the SNO experiment,

however each of these topics must assume further model-dependent details not currently constrained by experiment. Thus, these topics are mentioned for completeness but exact values are left for others to infer from the SNO electron antineutrino search results.

4.5.1 *Limiting the Electron Neutrino Magnetic Moment*

A null result for the solar electron antineutrino flux translates into an upper limit on the magnitude of the electron neutrino's magnetic moment. However, this translation depends significantly on the model of the magnetic structure of the Sun. Several recent papers [180, 56, 128, 27, 206] place limits on the neutrino magnetic moment or, in an attempt to remove some of the model dependence, place limits on the product of the maximum strength of the solar magnetic field and the neutrino magnetic moment. It is for these reasons that this dissertation will not use the results of the electron antineutrino search to make any statements regarding the neutrino magnetic moment or the magnetic field strength of the Sun.

4.5.2 *Limiting Right-Handed Currents*

It may be possible to use limits on the flux of solar electron antineutrinos to limit right-handed current contributions to the decay of solar ^8B if one assumes neutrinos are Majorana type particles. Measurements of the total ^8B flux [10, 12] determine the rate of ^8B decay in the Sun. A right-handed decay of ^8B produces a right-handed electron antineutrino and, in the case of Majorana neutrinos, this neutrino is detectable on Earth as an electron antineutrino. This should be distinguished from the case when the normal Standard Model left-handed current produces an electron neutrino in a positive helicity state. In the Majorana neutrino case, these neutrinos are detectable as electron antineutrinos but this left-handed current production of positive helicity electron neutrinos is suppressed by a factor $(m_{\nu_e}/2E_{\nu_e})^2$ [140]. Right-handed currents, not suppressed by the above factor, are experimentally limited by neutrinoless double beta decay searches [177, 88], unless neutrinos are "light" particles [214] (e.g. $m_\nu < 10$ eV). Using right-handed current corrections [209] to the mixed Fermi and Gamow-Teller ^8B beta decay⁴, it may be possible to provide a new method for limiting right-handed currents.

4.5.3 *Electron Antineutrino Flux and Sun Spot Activity*

From the mid-1980's there was interest in whether or not there is an anti-correlation between the number of Sun spots and the magnitude of the neutrino flux measured on Earth. This interest was generated by reports of an anti-correlation [58] observed in Ray Davis's now famous neutrino-chlorine experiment located in the Homestake mine [79]. This result was largely refuted by the combined results of Kamiokande II and III [102] which showed no statistically significant correlation (anti- or otherwise) between the number of Sun spots and the measured neutrino flux.

However, if one were to expand upon this "Sun spot" hypothesis despite of the lack of supporting evidence, the first supposition to make is that the neutrinos are interacting with the Sun's magnetic field's generally rather than being correlated to Sun spot number. Interested readers are referred to Ref. [138] for details

⁴The ^8B beta decay is mixed Fermi and Gamow-Teller however the two branches are distinguishable because the Fermi transition only produces electron neutrinos with energies below ≈ 4 MeV. Thus, SNO is only sensitive to the Gamow-Teller branch of the decay.

on the solar magnetic fields which were hypothesized to create the anti-correlation reported in the Homestake experiment. Invoking electron neutrino interactions with solar magnetic fields returns the discussion to the RSFP hypothesis of Section 4.2. Thus, if one had a reason to believe the solar neutrino flux⁵ is varying and that neutrinos are Majorana particles, then it is a general expectation for there to be variation in any electron antineutrino flux coming from the Sun. These considerations show that SNO should minimally supply the community the time stamps of the electron antineutrino candidates extracted from the data sets. If desired, a correlation between the candidate SNO electron antineutrino signal and solar cycle would then be possible. Unfortunately, as has already been shown, the expected number of solar electron antineutrino induced $\overline{\text{CC}}$ events in the SNO detector events is at best small (i.e. on the order of a few per year).

⁵Discussions of time varying solar neutrino flux have a tendency to fail to state that it is not the total flux of neutrinos which is varying with time, it is the relative flavor fraction arriving at the Earth which is hypothesized to vary.

Chapter 5

ATMOSPHERIC ELECTRON ANTINEUTRINOS

5.1 Cosmic Rays and Atmospheric Neutrino Production

Cosmic rays (composed of protons, helium nuclei, and a small fraction of more massive nuclei) interact with the Earth's atmosphere and generate neutrinos [124]. Initially the cosmic ray particles, A_{cr} , interact with atmospheric nuclei, A_{air} , generating pions (π^\pm), kaons (K^\pm), and a small fraction of more massive particles.

$$A_{\text{cr}} + A_{\text{air}} \longrightarrow \pi^\pm, K^\pm, K^0, \dots$$

The kaons decay into states of pions, leptons (μ^\pm or e^\pm) and neutrinos, or a mixture of pions, leptons, and neutrinos [113]. The dominant charged pion decay chain is:

$$\pi^\pm \longrightarrow \begin{array}{l} \mu^\pm + \nu_\mu(\bar{\nu}_\mu) \\ \downarrow \\ e^\pm + \nu_e(\bar{\nu}_e) + \bar{\nu}_\mu(\nu_\mu) \end{array}$$

The atmospheric neutrino spectrum extends over several decades of energies as shown in Figure 5.1. The flux maximum occurs around ~ 35 MeV, just above the mean energy of neutrinos emitted from pions at rest. At neutrino energies below 10 GeV the absolute flux is sensitive to solar activity. For instance, at solar maximum, the solar wind increases and inhibits the primary cosmic ray flux from reaching the Earth's atmosphere. At the SNO site the solar modulation affects the flux by as much as 20% [109].

5.2 Atmospheric Electron Antineutrinos

The atmospheric electron antineutrino flux is specifically produced by decays of cosmic ray induced pions and kaons:

$$\pi^- \longrightarrow \begin{array}{l} \mu^- + \bar{\nu}_\mu \\ \downarrow \\ e^- + \bar{\nu}_e + \nu_\mu \end{array} \quad \left| \quad \begin{array}{l} K^- \longrightarrow \pi^0 + e^- + \bar{\nu}_e \\ K_L^0 \longrightarrow \pi^+ + e^- + \bar{\nu}_e \end{array}$$

Considering the atmospheric neutrino spectrum, it is natural to divide electron antineutrino studies into two energy ranges. Above ~ 50 MeV only atmospheric electron antineutrinos are present. All other electron antineutrino sources discussed in Part II of this dissertation, have energies below 50 MeV. It is also important to note that up to 50 MeV the $\overline{\text{CC}}$ reaction remains dominant over other processes, for instance neutrino deep-inelastic scattering [145, 172].

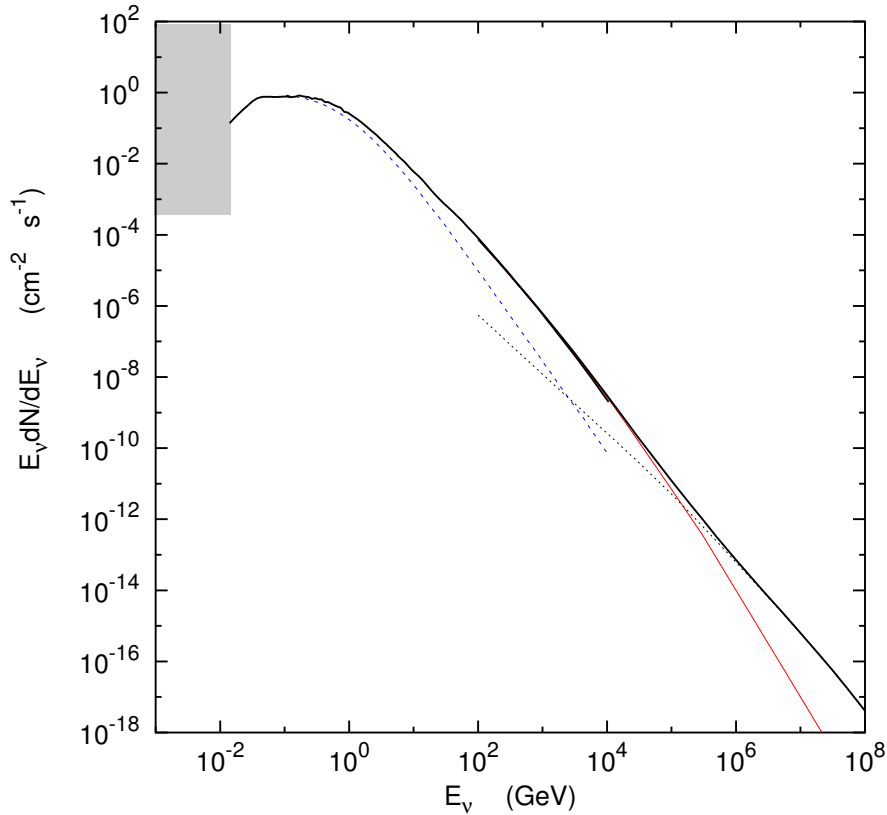


Figure 5.1: Plot of calculated atmospheric neutrino fluxes taken from Ref. [109]. Solar neutrinos dominate the atmospheric flux by several orders of magnitude in the gray box region. Heavy solid black line: $\nu_\mu + \bar{\nu}_\mu$. Dashed blue line: $\nu_e + \bar{\nu}_e$. Dotted gray line: Prompt neutrinos from charmed particle decay. Thin solid red line: $\nu_\mu + \bar{\nu}_\mu$ from pions and kaons.

5.2.1 Low Energy Atmospheric Electron Antineutrinos

There are only a few reported calculations of the atmospheric electron antineutrino flux at energies below 100 MeV [141, 110, 51, 124, 173]. Two flux spectra, shown in Figure 5.2, were constructed from these calculations that extended below 100 MeV. Both calculations were done for the IMB experiment located in Cleveland, Ohio. The red and lowest energy portion of the flux spectra is at maximum solar activity (minimum neutrino flux¹). The blue and higher energy portion of the flux spectra is at solar middle (mean neutrino flux). Both calculations are done using one dimensional Monte Carlo routines (all produced particles go in the same direction as the primary cosmic ray). Note that the year 2000 was a year of solar maximum. It has been noted that one dimensional calculations over estimate the flux at the low neutrino energies by approximately a factor

¹The solar maximum increases the solar wind's strength and volume of influence. The cosmic rays creating neutrinos are extra-solar-system particles. Thus at solar maximum *fewer* extra-solar-system particles make it to Earth to interact in the Earth's atmosphere.

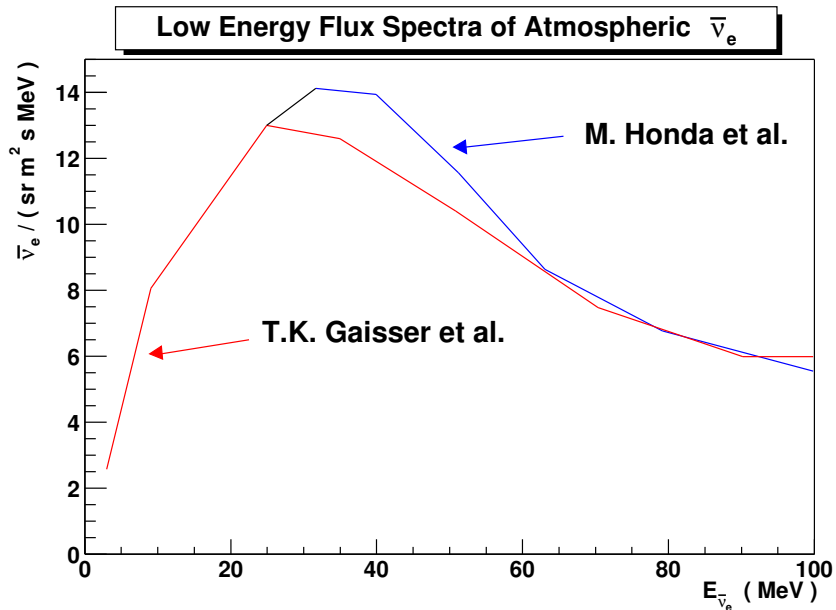


Figure 5.2: The low energy portion of the atmospheric electron antineutrino spectrum. Full energy range, red line is Refs. [110, 51]. The high energy range only, blue line is Ref. [124].

of two [141, 124] in comparison to full three dimensional calculations. A direct application of the constructed flux spectra of Figure 5.2 gives the expected number of $\overline{\text{CC}}$ interactions, listed in Table 5.1.

Table 5.1: The low energy atmospheric electron antineutrino induced $\overline{\text{CC}}$ rate. Note that these values are intended to represent the rate at solar mid, but are perhaps a factor of 2 too large.

$\bar{\nu}_e$ Energy Range (MeV)	$\overline{\text{CC}}/\text{kt} \cdot \text{yr}$
4 \rightarrow 14.5	2.9×10^{-4}
4 \rightarrow 20	1.2×10^{-3}
4 \rightarrow 50	3.7×10^{-2}
4 \rightarrow 100	1.7×10^{-1}

5.2.2 Atmospheric Electron Antineutrinos Above 100 MeV

There are two related, interesting studies of atmospheric electron antineutrinos. However, as shown in Chapter 19, the event rate is so low in SNO that these measurements are unrealistic objectives. First, there has never been a measurement of the atmospheric neutrino to antineutrino ratio even while atmospheric neutrino production models provide predictions for this ratio's value [210, 123, 148, 223, 124]. An example

ratio calculation is presented in Figure 5.3. Through the distinguishable CC and $\overline{\text{CC}}$ reactions SNO could

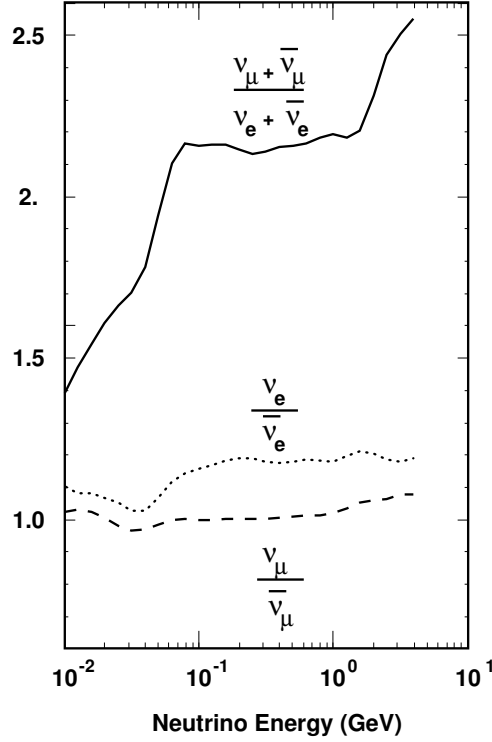


Figure 5.3: Ratios of atmospheric neutrinos to atmospheric antineutrinos from Ref. [110].

make such an electron flavor neutrino to antineutrino measurement for the first time. Second, this ratio becomes particularly interesting in light of recent suggestions that CPT may be violated in the neutrino sector [49, 50, 183, 126, 46, 45, 47, 199, 48]. These suggestions invoke CPT violation because it provides a model where by all neutrino oscillation experimental results are retained. In these models the atmospheric electron flavor neutrino to antineutrino ratio is modified by oscillation physics.

LSND proposed $\bar{\nu}_\mu \rightarrow \bar{\nu}_e$ oscillation with an L/E that is comparable to that of atmospheric neutrinos [34]. However, Super-Kamiokande shows atmospheric $\nu_\mu \rightarrow \nu_\tau$ oscillation. To keep both the LSND and Super-Kamiokande results without introducing sterile neutrinos, one has to violate CPT so that the neutrinos and antineutrinos can have different oscillation properties. In this CPT violating case atmospheric neutrinos would have to oscillate as:

$$\begin{aligned} \nu_\mu &\rightarrow \nu_\tau \\ \bar{\nu}_\mu &\rightarrow \bar{\nu}_e \end{aligned}$$

From normal production mechanisms (i.e. not including any oscillation physics), there are simple $\nu_e / \bar{\nu}_e$

ratios one can calculate. This is given roughly as $\nu_{e\text{prod}} / \bar{\nu}_{e\text{prod}} \approx 1.2$ and is plotted in Figure 5.3.

In the presence of *CPT* violating neutrinos, there are additional $\bar{\nu}_e$'s through $\bar{\nu}_\mu \rightarrow \bar{\nu}_e$ oscillation, thus modifying the $\nu_e / \bar{\nu}_e$ ratio. Comparing the $\nu_e / \bar{\nu}_e$ ratio derived from *production* to the measured ratio becomes a test of the *CPT* properties of neutrinos and tests the LSND result.

A “back of the envelope” calculation shows what might be expected in a maximal mixing case with *CPT* violating neutrinos. Neutrino production mechanisms give the following rough relations:

$$\begin{aligned}\nu_{e\text{ prod}} &\equiv \text{fixed, no oscillation} \\ \bar{\nu}_{e\text{ prod}} &\simeq \frac{1}{1.2} \nu_{e\text{ prod}} \\ \bar{\nu}_{\mu\text{ prod}} &\simeq 2\bar{\nu}_{e\text{ prod}}\end{aligned}$$

The factor of 2 in the third equation is the standard muon to electron production ratio. Assuming maximal mixing, $\bar{\nu}_\mu \leftrightarrow \bar{\nu}_e$, then after oscillation:

$$\begin{aligned}\bar{\nu}_{e\text{ osc}} &= \frac{1}{2} \bar{\nu}_{e\text{ prod}} + \frac{1}{2} \bar{\nu}_{\mu\text{ prod}} \\ &= \frac{1}{2} \bar{\nu}_{e\text{ prod}} + \frac{1}{2} (2 \bar{\nu}_{e\text{ prod}}) \\ &= \frac{3}{2} \bar{\nu}_{e\text{ prod}} \\ &= \frac{3}{2} \left(\frac{1}{1.2} \nu_{e\text{ prod}} \right)\end{aligned}$$

The result of this rough calculation is that $\nu_e / \bar{\nu}_e \approx 0.8$ rather than the expected 1.2.

Chapter 6

NUCLEAR REACTOR ELECTRON ANTINEUTRINOS

6.1 Nuclear Reactor Properties

Commercial, electric power generating, nuclear reactors produce copious numbers of electron antineutrinos. However, due to SNO's location, reactor $\bar{\nu}_e$'s are a small signal and act as a small background to the measurement of solar neutrinos. There are three basic types of nuclear reactors used for commercial electric power generation in North America: boiling (light) water reactors (BWR), pressurized (light) water reactors (PWR), and CANDU pressurized heavy water reactors. Each reactor type represents a different method for generating and converting the thermal energy produced by the nuclear fissioning occurring in the nuclear reactor core into electrical energy.

All three reactor types use ^{235}U as the main fissile fuel component. Additionally, listed in decreasing significance, ^{239}Pu , ^{238}U , and ^{241}Pu contribute to the thermal output of the reactor cores [57]. Both light water reactor types use enriched uranium ($\approx 3.5\%$ ^{235}U) fuel while the heavy water reactor type uses unenriched uranium (natural abundance: 0.7% ^{235}U). This difference between the light and heavy water reactors produces a different relative composition between the four main fissile uranium and plutonium isotopes. This study derives the $\bar{\nu}_e$ flux spectrum produced by light water reactors. While strictly incorrect (due to the composition differences outlined above), the derived light water reactor $\bar{\nu}_e$ flux spectrum is taken as representative of the heavy water reactors in the following calculation of the total reactor $\bar{\nu}_e$ induced $\overline{\text{CC}}$ interacts in SNO.

During reactor operation ^{235}U is burned by thermal neutron induced fission. The fissioning produces additional free neutrons and fission fragments whose kinetic energy constitutes the thermal energy of the reactor core. Thus ^{235}U 's contribution to the thermal energy decreases as the reactor operates because ^{235}U is being consumed in the burning process. A similar situation describes the burning of ^{238}U , though ^{238}U requires fast neutrons to induce fissioning. Thermal neutrons can capture on ^{238}U forming ^{239}U which can then be transmuted to ^{239}Pu through two beta decays. Similarly, thermal neutron captures and beta decays can transmute ^{238}U to ^{241}Pu , the last of the four main fissile isotopes in reactor fuel. Figure 6.1 illustrates the formation of the plutonium isotopes during reactor operation. The net result of these fission and transmutation processes is that the fissile fuel composition evolves during reactor operation. This fuel evolution affects not only the relative proportion of the thermal energy produced by each fissile isotope, it also affects the $\bar{\nu}_e$ flux spectrum. Given a beginning fuel composition, it is not difficult to model the time evolution of the fuel composition. However, in this study a constant, average fuel composition is assumed because of a lack of the detailed refueling schedules for each reactor in North America.

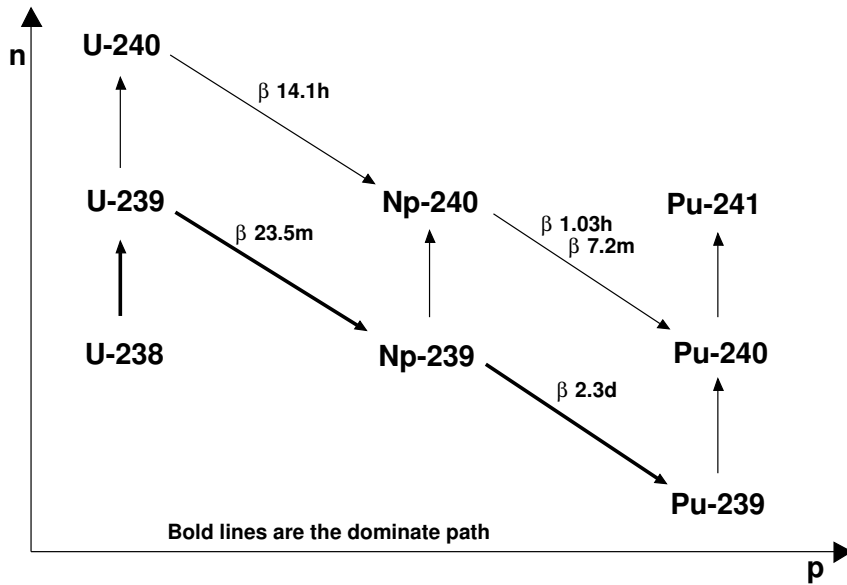


Figure 6.1: The steps in creating ^{239}Pu and ^{241}Pu from ^{238}U in nuclear reactors.

6.2 Calculating the Reactor $\bar{\nu}_e$ Flux Spectrum, $N_i^{\bar{\nu}_e}(E)$

The reactor $\bar{\nu}_e$ flux spectrum, $N_i^{\bar{\nu}_e}(E)$, is the number of $\bar{\nu}_e$ produced by a reactor core, i , at a given $\bar{\nu}_e$ energy, E and is determined by the individual isotope properties and the total thermal energy output of the reactor core. The individual isotope properties are defined as:

- w_j - The fraction of the total number fissions in a reactor core of isotope j .
- E_j^{fission} - The total mean thermal energy from the fission and subsequent decays of isotope j .
- $\lambda_j(E)$ - The individual $\bar{\nu}_e$ flux spectrum from the fission and subsequent decays of isotope j .

The values used for w_j , E_j^{fission} , and $\lambda_j(E)$ are listed in Table 6.1. To determine the total thermal energy output of the reactor core, define three quantities:

- P_i - The electrical energy output by reactor i measured in MWh.
- $f = 2.247 \times 10^{22} \frac{\langle \text{MeV} \rangle}{\text{MWh}}$ - A conversion factor. $\langle \text{MeV} \rangle$ is the *thermal* energy in MeV.
- $\epsilon = 0.325 \pm 0.008$ - The thermal to electrical conversion efficiency. See Appendix C.1.

The (monthly) net electrical energy output [171], P_i , for each reactor i was provided by the US Nuclear Regulatory Commission [69] and Canada's Chalk River Laboratory [67]. Define $E_i^{\text{thermal}} = (fP_i/\epsilon)$ as the total thermal energy output of a reactor core measured in units of $\langle \text{MeV} \rangle$.

Table 6.1: Factors in calculating the total number electron antineutrinos produced by a nuclear reactor core. The values for w_j and E_j^{fission} are taken from Ref. [185] and [80], respectively.

Isotope	w_j	$E_j^{\text{fission}} \left(\frac{\langle \text{MeV} \rangle}{\text{fission}} \right)$	Reference for $\lambda_j(E) \left(\frac{\bar{\nu}_e}{\text{fission} \cdot \text{MeV}} \right)$
^{235}U	0.556	201.8 ± 0.5	K. Schreckenbach <i>et al.</i> [194]
^{239}Pu	0.326	210.3 ± 0.6	A. A. Hahn <i>et al.</i> [114]
^{238}U	0.071	205.0 ± 0.7	P. Vogel <i>et al.</i> [215] (0.5 MeV neutrons)
^{241}Pu	0.047	212.6 ± 0.7	A. A. Hahn <i>et al.</i> [114]

The reactor $\bar{\nu}_e$ flux spectrum, $N_i^{\bar{\nu}_e}(E)$, is equal to the sum over isotopes of the number of fissions of an isotope j times the individual flux spectrum of each isotope j ,

$$N_i^{\bar{\nu}_e}(E) = \left(\sum_j^{\text{isotope}} N_j^{\text{fission}} \lambda_j(E) \right)_i = \left(N^{\text{fission}} \sum_j^{\text{isotope}} w_j \lambda_j(E) \right)_i \quad (6.1)$$

where the relation $N_j^{\text{fission}} = w_j N^{\text{fission}}$ is used in the last step. The total number of fissions, N^{fission} , is determined by the total thermal energy output of the reactor core in the following way. The total thermal energy output is equal to the sum of the contributions to the thermal energy from each isotope:

$$E_i^{\text{thermal}} = \left(\frac{fP_i}{\epsilon} \right) = \left(\sum_j^{\text{isotope}} E_j^{\text{fission}} N_j \right)_i = \left(N^{\text{fission}} \sum_j^{\text{isotope}} E_j^{\text{fission}} w_j \right)_i \quad (6.2)$$

Solving (6.2) for N^{fission} in terms of known quantities and then substituting into (6.3), the final form of the reactor $\bar{\nu}_e$ flux spectrum from a reactor i is

$$N_i^{\bar{\nu}_e}(E) = \frac{fP_i}{\epsilon} \left(\sum_j^{\text{isotope}} \frac{w_j \lambda_j(E)}{\sum_k^{\text{isotope}} w_k E_k^{\text{fission}}} \right) \quad (6.3)$$

The summation term in parenthesis in (6.3) is plotted in Figure 6.2.

6.2.1 Estimated Uncertainty on $N_i^{\bar{\nu}_e}(E)$

The estimated uncertainty for each of the inputs to the nuclear reactor electron antineutrino flux calculation is listed below.

- w_j - These values are an average over one burning cycle. It is probably possible to estimate the errors on these values from the plotted time evolution of the fissile material in Figure 6 of Ref. [57].

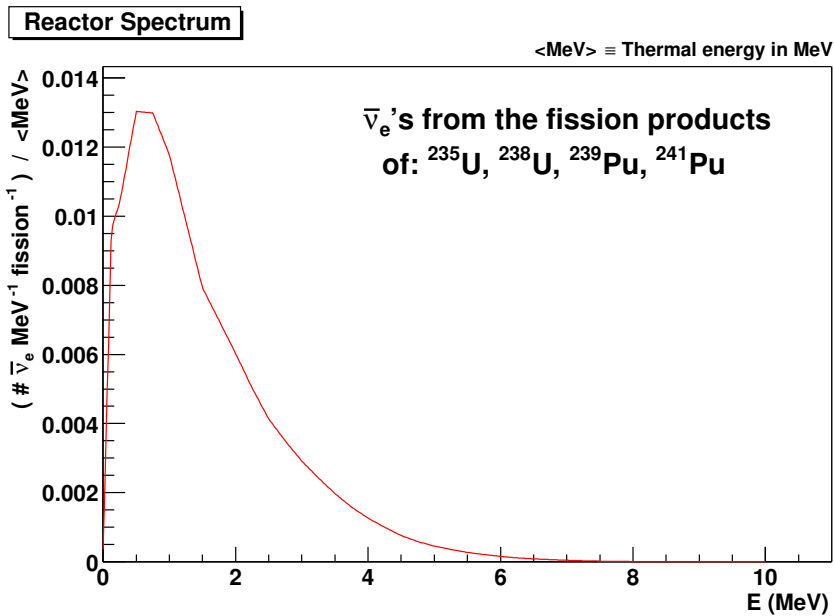


Figure 6.2: The reactor $\bar{\nu}_e$ flux-spectrum per MeV of thermal energy generated. This flux-spectrum is the weighted combination of the $\bar{\nu}_e$ flux-spectra from ^{235}U , ^{239}Pu , ^{238}U , and ^{241}Pu .

- E_j^{fission} - The errors on these values are given in Table 6.1.
- $\lambda_j(E)$ - KamLAND uses the same method as presented here and claims 2.5% error on all four combined [86]. For the spectra themselves: ^{235}U at 3.5% [194], ^{239}Pu and ^{241}Pu both at 4% [114], and ^{238}U at $\approx 4\%$ [215]. In reality, it is the high energy portion of the spectrum that is important in the SNO experiment. At $E_{\bar{\nu}_e} = 6$ MeV the uncertainties become 4.3% for ^{235}U [194], 6.8% for ^{239}Pu and 5.6% for ^{241}Pu [114], and probably $\approx 6\%$ for ^{238}U [215].
- Reported monthly reactor energy outputs, P_i , are expected to have an error of less than 1% [117].
- f - An exact conversion factor.
- $\epsilon = 0.325 \pm 0.008$ - The problem here is that using an average is only fair if all the reactors are the same distance away. A close reactor with a significant deviation from the average will dominate the total flux. Since the flux is directly proportional to the inverse of this efficiency, a shift of ± 0.017 (the greatest seen deviation) would change the derived flux by $\approx 5.25\%$. This 5.25% is an extreme deviation and the error due to the efficiency is likely significantly less than this.
- The error on the distance to the reactors is not known. The exact longitude and latitude of nuclear reactors could give precision distances to within hundreds of meters, however, this information is no

longer available to the general public. The distances reported here are probably good to within 2 km. A 2 km error amounts to a 1.6% error on the flux at 250 km and a 0.8% error on the flux at 500 km.

- Composition related uncertainty introduced in using light water reactors as representative of CANDU reactors. The author is not aware of any references that address this issue though it is clear the contributing spectra are the same and that the numerical order of the relative contribution to the flux from each isotope is the same. It is merely a change in the relative weightings, w_j , from light water reactors to CANDU reactors.

In practice, a precise determination of the error on the flux of electron antineutrinos from nuclear reactors would amount to treating each reactor core separately, rather than using a set of average properties as is done here. Thus, a conservative uncertainty of 10% is assigned to the flux of electron antineutrinos from nuclear reactors.

6.3 Calculating the Total Number of $\overline{\text{CC}}$ Events from Reactors

Reactor cores are treated as point sources of isotropic electron antineutrinos. Furthermore, the large physical separation of SNO from any reactor makes the flux effectively constant over the size of the detector volume. These two assumptions are used in the calculation of the total number of charged-current electron antineutrino interactions with deuterium, $N_{\overline{\text{CC}}}$, in SNO:

$$N_{\overline{\text{CC}}} = \sum_i^{\text{reactors}} \int_{E_{\text{thresh}}}^{E_{\text{max}}} N^d \left(\frac{N_i^{\overline{\nu}_e}(E)}{4\pi r_i^2} \right) \sigma_{\overline{\text{CC}}}(E) dE \quad (6.4)$$

The summation is over all reactor cores and the integration is over the number of target deuterons, N^d , multiplied by the electron antineutrino's flux-spectrum from the $\overline{\text{CC}}$ threshold, $E_{\text{thresh}} = 4.03$ MeV, to the maximum reactor electron antineutrino energy, E_{max} . Practically, E_{max} is set to 10 MeV. The reactor electron antineutrino flux spectrum at SNO is calculated from $N_i^{\overline{\nu}_e}(E)$ and the geometrical factor $1/4\pi r_i^2$ which depends upon the line-of-site distance, r_i , to the reactor i . The cross-section for the $\overline{\text{CC}}$ reaction is given by $\sigma_{\overline{\text{CC}}}(E)$ [163]. Figure 6.3 shows the normalized integrand of (6.4) as a function of $\overline{\nu}_e$ energy.

6.3.1 Including Neutrino Oscillations

The KamLAND experiment located in Japan has reported observation of a deficit of observed reactor electron antineutrinos attributed to the phenomenon of neutrino oscillations [86]. The formalism describing neutrino oscillations is presented in Ref. [61] and amounts to a reduction in the measured electron antineutrino interaction rate given by the probability equation

$$P_{\overline{\nu}_e \rightarrow \overline{\nu}_e} = 1 - \sin^2 2\theta \sin\left(\frac{1.27\Delta m^2 L}{E_{\overline{\nu}_e}}\right) \quad (6.5)$$

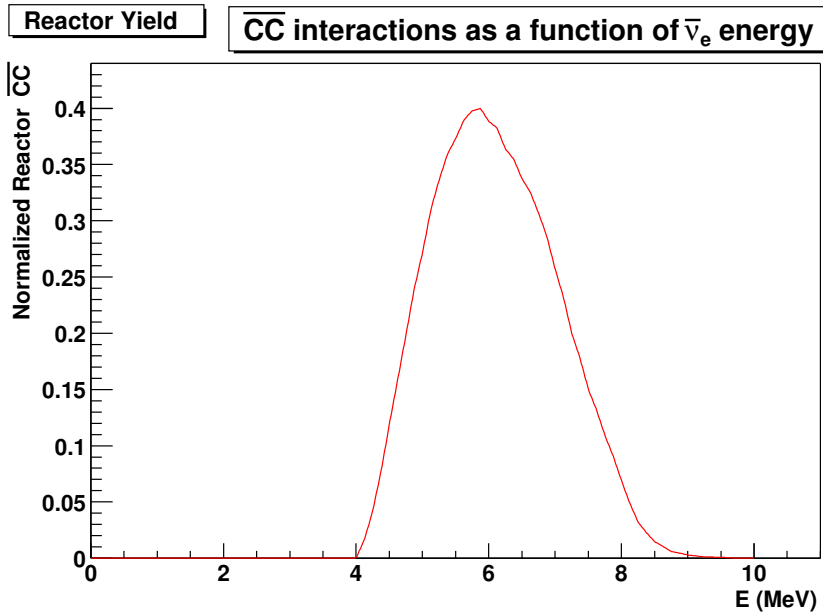


Figure 6.3: The normalized $\overline{\text{CC}}$ yield from reactor $\bar{\nu}_e$'s as a function of $\bar{\nu}_e$ energy, E .

for a produced $\bar{\nu}_e$ to be detected as a $\bar{\nu}_e$. In (6.5) L is the straight line distance from the reactor to the detector in meters, $E_{\bar{\nu}_e}$ is the energy of the $\bar{\nu}_e$ in MeV, and $\sin^2 2\theta$ and Δm^2 are fundamental neutrino mixing parameters. Table 6.2 gives the world data best fit values for $\sin^2 2\theta$ and Δm^2 used in this calculation.

Table 6.2: The neutrino mixing parameters used in the calculation of oscillations for reactor $\bar{\nu}_e$'s [12].

Parameter	Value
$\sin^2 2\theta$	0.833
Δm^2	$7.1 \times 10^{-5} \text{ eV}^2$

6.3.2 Predicting the $\overline{\text{CC}}$ Interaction Rate in SNO

A review of the literature and SNO reports reveals several predictions of the flux and/or $\overline{\text{CC}}$ rate at SNO due to electron antineutrinos created in commercial nuclear reactors. Table 6.3 gives a summary of various calculations. The calculations presented in Table 6.3 all assume that neutrinos do not oscillate. Tables 6.4 & 6.5 show the results of the calculation done for this study. The SNO live fraction is the fraction of the time that the SNO detector was actively taking data [156, 107]. The $\overline{\text{NC}}$ interaction rate is included here even though it

Table 6.3: Flux and/or \overline{CC} event rate of electron antineutrinos at SNO from nuclear reactors. All calculations are the integral flux above threshold ($E_{\overline{\nu}_e} > 4.02\text{MeV}$), unless noted otherwise.

Author(s)	Ref.	Flux ($\frac{10^6 \overline{\nu}_e}{\text{cm}^2 \cdot \text{s}}$)	$\frac{\overline{CC}}{\text{kt}\cdot\text{yr}}$	Notes
Oblath <i>et al.</i>	[169]	-	1.4	Their own “from scratch” calculation.
Dunmore <i>et al.</i>	[85]	-	5.3	Based on Rothschild <i>et al.</i> flux.
Rothschild <i>et al.</i>	[189]	1.3	-	
Balantekin <i>et al.</i>	[41]	-	2.3	$E_{\overline{\nu}_e} > 6\text{MeV}$, Estimated from plot.

is not a background to the electron antineutrino analysis. The \overline{NC} calculation only differs from the \overline{CC} calculation in energy threshold ($E_{\text{thresh.}} = 2.225 \text{ MeV}$) and the \overline{NC} cross-section taken from Ref. [163]. Table 6.6 gives the details of the reactors used in this calculation.

Table 6.4: The number of \overline{CC} events per month during the Pure D₂O phase as determined by the calculation described in this chapter. The Totals row is the sum of the above column corresponding to the entire period November 1999 to May 2001.

Year	Month				SNO live fraction	live fraction #'s		
		# \overline{CC}	# \overline{NC}	# $\overline{CC}_{\text{Osc.}}$		# \overline{CC}	# \overline{NC}	# $\overline{CC}_{\text{Osc.}}$
1999	11	0.12	0.35	0.062	0.59	0.07	0.21	0.036
1999	12	0.14	0.41	0.072	0.76	0.1	0.31	0.055
2000	1	0.14	0.43	0.075	0.78	0.11	0.33	0.059
2000	2	0.12	0.37	0.065	0.63	0.079	0.23	0.041
2000	3	0.12	0.35	0.061	0.92	0.11	0.32	0.056
2000	4	0.1	0.31	0.053	0.67	0.069	0.2	0.036
2000	5	0.12	0.35	0.061	0.29	0.035	0.1	0.018
2000	6	0.12	0.37	0.065	0.63	0.079	0.23	0.041
2000	7	0.15	0.44	0.077	0.59	0.087	0.26	0.045
2000	8	0.14	0.42	0.075	0.2	0.028	0.084	0.015
2000	9	0.12	0.34	0.06	0.39	0.045	0.13	0.024
2000	10	0.11	0.32	0.057	0.43	0.047	0.14	0.025
2000	11	0.12	0.36	0.064	0.34	0.042	0.12	0.022
2000	12	0.15	0.43	0.076	0.57	0.084	0.25	0.044
2001	1	0.16	0.46	0.081	0.49	0.076	0.23	0.04
2001	2	0.14	0.41	0.073	0.45	0.063	0.19	0.033
2001	3	0.14	0.4	0.07	0.22	0.029	0.086	0.015
2001	4	0.12	0.35	0.062	0.69	0.082	0.24	0.042
2001	5	0.12	0.37	0.065	0.63	0.078	0.23	0.041
Totals		2.45	7.24	1.28		1.32	3.90	0.69

Table 6.5: The number of \overline{CC} events per month during the Salt phase as determined by the calculation described in this chapter. The bottom Totals row is the sum of the above column corresponding to the entire period July 2001 to October 2002.

Year	Month	\overline{CC}			SNO live fraction	live fraction #'s		
		# \overline{CC}	# \overline{NC}	# $\overline{CC}_{Osc.}$		# \overline{CC}	# \overline{NC}	# $\overline{CC}_{Osc.}$
2001	7	0.15	0.43	0.076	0.087	0.013	0.038	0.0066
2001	8	0.14	0.43	0.075	0.44	0.063	0.19	0.033
2001	9	0.12	0.35	0.062	0.43	0.052	0.15	0.027
2001	10	0.12	0.36	0.064	0.63	0.078	0.23	0.041
2001	11	0.12	0.36	0.063	0.42	0.051	0.15	0.027
2001	12	0.13	0.39	0.069	0.69	0.09	0.27	0.047
2002	1	0.14	0.4	0.071	0.52	0.071	0.21	0.037
2002	2	0.12	0.37	0.065	0.65	0.08	0.24	0.042
2002	3	0.14	0.41	0.071	0.74	0.1	0.3	0.053
2002	4	0.12	0.36	0.063	0.67	0.082	0.24	0.042
2002	5	0.13	0.39	0.068	0.61	0.08	0.24	0.041
2002	6	0.13	0.39	0.069	0.59	0.078	0.23	0.04
2002	7	0.14	0.42	0.073	0.45	0.063	0.19	0.033
2002	8	0.14	0.41	0.073	0.67	0.093	0.28	0.049
2002	9	0.14	0.4	0.07	0.74	0.1	0.29	0.052
2002	10	0.12	0.37	0.065	0.022	0.0027	0.0081	0.0014
Totals		2.11	6.22	1.1		1.1	3.24	0.57

Table 6.6: The North American nuclear reactors used in calculating expected \overline{CC} rates.

Reactor	Location	Mean Thermal Power (MW)	Distance from SNO (km)	Reactor Type
Bruce	Tiverton, ON	10320	281	CANDU
Pickering	Pickering, ON	6192	330	CANDU
Darlington	Bowmanville, PQ	10572	340	CANDU
R. E. Ginna	Ontano, NY	1410	455	PWR
James A. Fitzpatrick	Scriba, NY	2340	488	BWR
Nine Mile Point	Scriba, NY	5070	488	BWR
Perry	North Perry, OH	3615	530	BWR
Enrico Fermi	Detroit, MI	3255	559	BWR
Kewaunee	Carlton, WI	1509	568	PWR
Davis-Besse	Oak Harbor, OH	2531	588	PWR
Point Beach	Two Rivers, WI	2910	589	PWR
Palisades	South Haven, MI	2340	617	PWR
Gentilly	Gentilly, PQ	1914	648	CANDU
Beaver Valley	Shippingport, PA	4929	657	PWR
Donald C. Cook	Benton Harbor, MI	3060	685	PWR

Chapter 7

THE DIFFUSE SUPERNOVA NEUTRINO BACKGROUND**7.1 The Diffuse Supernova Neutrino Background Flux Spectrum**

There is a great wealth of literature on neutrino production and radiation during the core collapse and explosive phases of supernovae; Ref. [162] serves as an introduction. The continual explosion of stars throughout the lifetime of the universe creates a diffuse background of supernova neutrinos, ever present and awaiting detection. This chapter reviews the literature regarding the diffuse supernova neutrino background and the estimated interaction rate in the Sudbury Neutrino Observatory.

To estimate the diffuse supernova neutrino background, it is assumed that using one set of average neutrino emission properties for all type II supernova is a reasonable approximation. That is, all supernova radiate a given number of neutrinos with the same relative proportions of neutrino flavors and the same relative proportions of particles to anti-particles. It is also often assumed that all neutrino species have the same energy spectrum, further simplifying the calculation of the diffuse supernova neutrino background. These approximations make dealing with individual supernova simple. Only the details of the summation of all supernova is left to determine the flux of diffuse supernova background neutrinos.

Calculating the summation over all supernova to obtain the flux-spectrum of the diffuse supernova neutrino background, focuses on two facts. First, the expansion of the universe red-shifts neutrinos emitted from cosmologically distant supernova. It is fairly accurate to say, the greater a supernova's red-shift, the greater its distance from Earth, and thus the lower the emitted neutrinos' energies will be, as detected here on Earth. For massless particles (a good approximation for neutrinos), this relationship is written as:

$$z = \frac{\lambda - \lambda_0}{\lambda_0} = \frac{1/E - 1/E_0}{1/E_0} = \frac{E_0 - E}{E} \quad (7.1)$$

$$\longrightarrow E = \frac{E_0}{1 + z} \quad (7.2)$$

The red-shift, z (for $z > 0$)¹, is a measure of the stretching of the particle's emission wavelength, λ_0 , to the wavelength at the Earth, λ . A massless particle's energy is defined as, $E = h\nu$ (here ν is a frequency). Equation (7.2) shows that the detected energy, E , of a massless particle with initial energy, E_0 , is lessened by its travel over a cosmological distance through the expanding universe.

Second, the rate of type II supernova explosions over the life-time of the universe is not constant. This is the most challenging aspect for calculating the diffuse supernova neutrino background. A number of different approaches to this problem have been proposed [129, 115, 150, 208] and are not discussed here in depth.

¹ $z < 0$ is a *blue-shift* due to movement toward the observer.

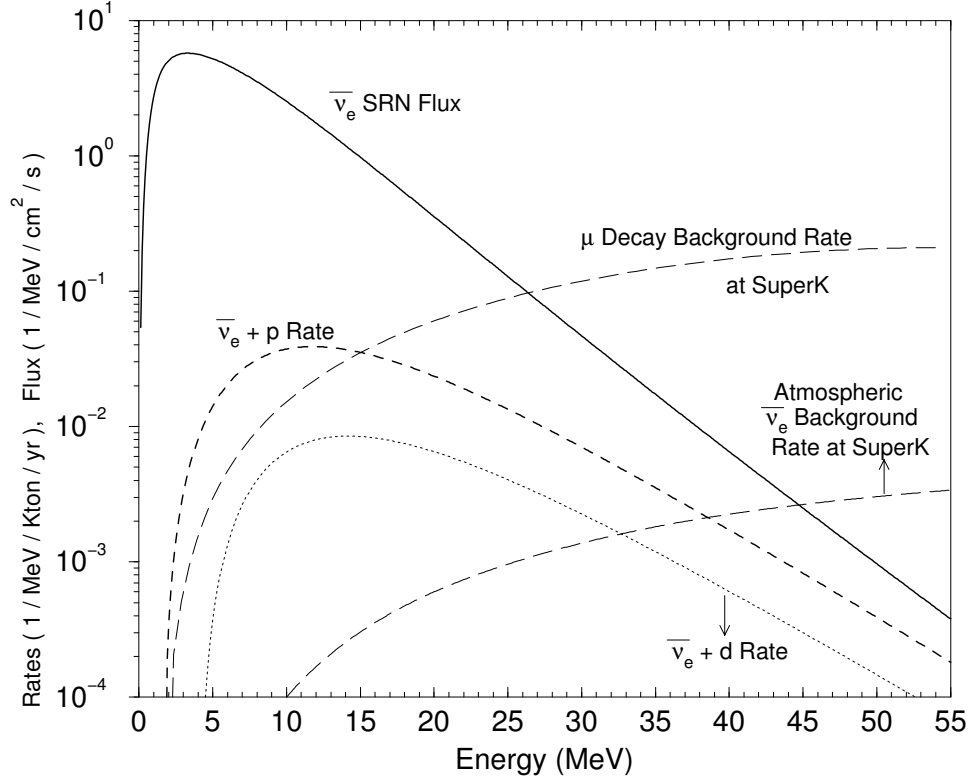


Figure 7.1: A figure from Ref. [129] showing the diffuse supernova electron antineutrino flux-spectrum and the expected event rate of charged-current $\bar{\nu}_e + d$ events in SNO.

7.2 Event Rates from the Diffuse Supernova Neutrino Background

A review paper [129] of estimates on the diffuse supernova neutrino background includes a calculation of the $\overline{\text{CC}}$ event rate in SNO. This review paper deliberately estimated the *maximum* possible flux of diffuse supernova background neutrinos. Figure 7.1 shows the results of this upper limit calculation. The integrated upper bound on the number of $\overline{\text{CC}}$ events in the SNO detector is 0.1 for one kt · yr above a $\bar{\nu}_e$ energy of 10 MeV. An estimation from Figure 7.1 of the $\overline{\text{CC}}$ rate from 4.03 to 10 MeV yields 0.02 per kt · yr for a total event rate of 0.12 $\overline{\text{CC}}$ /kt · yr. A second paper [31] attempts to predict the true flux of diffuse supernova neutrinos. This second paper estimates the diffuse supernova neutrino background induced $\overline{\text{CC}}$ rate as 0.03 per kt · yr for $\bar{\nu}_e$ energies below 23 MeV. This latter calculation is taken as the definitive value to use in the forthcoming electron antineutrino analysis and is acceptable given the current experimental findings. The Super-Kamiokande Collaboration reports [151] limiting the flux of diffuse supernova background $\bar{\nu}_e$ ($E_{\bar{\nu}_e} > 19.3$ MeV) to $< 1.2 \text{ cm}^{-2}\text{s}^{-1}$ at a 90% confidence level. The prediction from Ref. [31], the model used here, predicts a diffuse supernova background $\bar{\nu}_e$ flux of $0.43 \text{ cm}^{-2}\text{s}^{-1}$ for $E_{\bar{\nu}_e} > 19.3$ MeV.

Chapter 8

TERRESTRIAL ELECTRON ANTINEUTRINO SOURCES

8.1 Naturally Occurring, Terrestrial Radioisotopes

Naturally occurring radioisotopes residing in the Earth's lithosphere contribute to the electron antineutrino flux at the Sudbury Neutrino Observatory. Several articles [35, 137, 189, 185] have discussed the possibility of using the electron antineutrino flux to study the Earth's total radioisotope content. Table 2 of Ref. [189] gives the predicted total integrated electron antineutrino flux above 1.804 MeV at SNO as $6.8 \times 10^6 \text{ cm}^{-2} \text{ s}^{-1}$. Table 8.1 shows the highest energy electron antineutrinos produced by the major naturally occurring radioisotopes are all below the threshold energy for the $\overline{\text{CC}}$ reaction, $E_{\overline{\text{CC}},\text{thres.}} = 4.03 \text{ MeV}$. Thus SNO is neither capable of detecting terrestrial electron antineutrinos through the $\overline{\text{CC}}$ interaction nor do terrestrial antineutrinos induce a background to the $\overline{\text{CC}}$ signal.

Table 8.1: The naturally occurring terrestrial radioisotopes that produce $\overline{\nu}_e$ above 2.0 MeV.

^{232}Th decay chain products		^{238}U decay chain products	
Nuclei	$E_{\overline{\nu}_e,\text{max}}$ (MeV)	Nuclei	$E_{\overline{\nu}_e,\text{max}}$ (MeV)
^{228}Ac	2.08	^{234}Pa	2.19
^{212}Bi	2.25	^{214}Bi	3.27
^{208}Tl	1.8		

8.2 Hypothetical Geo-Fission Reactor at the Earth's Core

It has been suggested [182] that a measurement of electron antineutrino flux in the fission reactor energy range can distinguish between competing models of the thermal energy production in the core of the Earth. The preferred model posits that the Earth's inner core is composed of a nickel-iron metal, free from significant concentrations of Actinide Series elements. Thermal energy is produced by additional gravitational accretion of nickel and iron in the mantle onto the inner core. A second proposed model states that the Earth's core is composed of a nickel silicate that allows heavy elements in the Actinide Series to accumulate at the very center of the Earth [118]. This accumulation allows for a concentration of uranium to the extent that a sustained fission chain reaction can occur producing thermal energy. Both of these models are supposed to provide an explanation for the Earth's magnetic field. However, the preferred model fails to account for the measured rate of Earth's magnetic field reversals because the nickel and iron accretion should be a slow and

constant process relative to the time scale of the magnetic field reversals. The geo-reactor can account for the variability of the magnetic field through a uranium cycle of accumulation, burning, accumulation, burning, etc. As an additional piece of evidence, magma flows have a high measured ${}^3\text{He}$ to ${}^4\text{He}$ ratio that is possibly indicative of fission processes occurring inside the Earth [122].

The hypothesized geo-fission reactor located at the Earth's center would produce between 1 - 10 Terra-Watts (TW) of thermal power and a potentially measurable flux of electron antineutrinos [182]. Additionally, the electron antineutrino spectrum is nearly identical to that of commercial power generating nuclear reactors¹. Using the reactor $\bar{\nu}_e$ flux calculation tools of Chapter 6 and the parameters listed in Table 8.2, the number of $\overline{\text{CC}}$ events in SNO is estimated for 1, 3, and 10 TW geo-reactor thermal power outputs. Reference [182] states that a 10 TW geo-reactor would produce an electron antineutrino flux at the surface of

Table 8.2: The parameters used to calculate the number of $\overline{\text{CC}}$, $\overline{\text{NC}}$, and $\overline{\text{CC}}_{\text{Osc.}}$ in the SNO detector from a hypothetical fission based geo-reactor.

Parameter	Value
$\frac{\text{Thermal energy}}{\text{month of 1 TW core power}}$	7.305×10^8 (MWh/(month·TW))
Earth's mean radius	637101000 ± 2000 (cm)
Δm^2	7.1×10^{-5} (eV ²)
$\sin^2 2\theta$	0.833

the Earth of $\approx 3 \times 10^5$ (cm⁻² s⁻¹). The calculation employed here gives a flux at SNO of 3.33×10^5 (cm⁻² s⁻¹). The results of the calculation are presented in Table 8.3.

Table 8.3: The number of $\overline{\text{CC}}$ events expected from geo-fission electron antineutrinos. **Pure D₂O**: November 1999 to May 2001, **Salt**: July 2001 to October 2002. "Live" results take into account the SNO detector data taking live time fractions.

Power:	1 TW	3 TW	10 TW	Power:	1 TW	3 TW	10 TW
Pure D₂O				Salt			
$\overline{\text{CC}}$	0.175	0.526	1.753	$\overline{\text{CC}}$	0.148	0.443	1.476
$\overline{\text{NC}}$	0.518	1.553	5.177	$\overline{\text{NC}}$	0.436	1.308	4.360
$\overline{\text{CC}}_{\text{Osc.}}$	0.096	0.321	0.963	$\overline{\text{CC}}_{\text{Osc.}}$	0.081	0.243	0.811
Pure D₂O Live				Salt Live			
$\overline{\text{CC}}$	0.093	0.285	0.948	$\overline{\text{CC}}$	0.077	0.231	0.771
$\overline{\text{NC}}$	0.280	0.840	2.801	$\overline{\text{NC}}$	0.228	0.683	2.276
$\overline{\text{CC}}_{\text{Osc.}}$	0.052	0.156	0.521	$\overline{\text{CC}}_{\text{Osc.}}$	0.042	0.127	0.423

¹The *nearly* caveat is merely to distinguish the fact that the geo-fission reactor would burn only unenriched uranium, similar to CANDU Canadian reactors. See Chapter 6 for details.

Chapter 9

ELECTRON ANTINEUTRINO SUMMARY**9.1 Summary of Electron Antineutrino Sources**

The primary sources of interest and concern in an electron antineutrino search at the Sudbury Neutrino Observatory are listed in Table 9.1. The estimated rates in Table 9.1 are collected from the analyses of the preceding chapters of Part II with only the following noted modifications. In the case of $\overline{\text{CC}}$ reactions induced by electron antineutrinos produced by nuclear reactors, the approximate symbol merely signifies that the reactor electron antineutrino flux is known on a month-by-month basis (Chapter 6) and that, in detailed calculations, the month-by-month values are used rather than the yearly average. The hypothetical geo-reactor induced rate is the $\overline{\text{CC}}_{\text{Osc.}}$ value from the 10 TW column of the **Pure D₂O Live** portion of Table 8.3, scaled to one year.

Table 9.1: Summary of expected yearly $\overline{\text{CC}}$ rates from $\bar{\nu}_e$ sources.

Sources of Electron Antineutrinos		
Source	$\overline{\text{CC}}/\text{kt} \cdot \text{yr}$	Note
Atmospheric	0.0012	$4 < E_{\bar{\nu}_e} \text{ (MeV)} < 20$
Reactor	≈ 0.72	Includes oscillations
Diffuse Supernova Neutrinos	0.03	$4 < E_{\bar{\nu}_e} \text{ (MeV)} < 23$
Terrestrial Isotopes	0.0	Below $\overline{\text{CC}}$ threshold
Hypothetical Source	$\overline{\text{CC}}/\text{kt} \cdot \text{yr}$	Note
Solar	1.3	$\Phi_{\bar{\nu}_e}^{\text{SB}} = 1.4 \times 10^3 \text{ (cm}^{-2} \text{ s}^{-1}\text{)}$
Geo-reactor	0.61	10 TW core power

9.2 Electron Antineutrino Physics Topics at SNO

Recall the electron antineutrino physics topics proposed in Part I:

- Detect or limit on the $\bar{\nu}_e$ component of the solar neutrino flux.
- First measurement of the atmospheric ν_e to $\bar{\nu}_e$ ratio.
- Detect or limit the $\bar{\nu}_e$ flux from a geo-reactor in the Earth's core.

- Detect or limit the flux of the diffuse background of supernova $\bar{\nu}_e$'s.
- Study one of the minor backgrounds to SNO's primary solar neutrino analysis.

At less than a tenth of an interaction expected per year, the atmospheric and diffuse supernova background electron antineutrinos are not practical to study since SNO (as currently funded) will acquire approximately 5 years of analyzable data. Likewise, the expected interaction rate of electron antineutrinos from a hypothetical geo-reactor is low and, as Chapter 17 will show, the detection efficiency is less than 10%. However, studying backgrounds to SNO's primary solar neutrino analysis is always a useful exercise.

The results from the KamLAND Collaboration discussed in Section 4.3.1 were published in February 2004 as the work in this dissertation was being finalized. KamLAND's results establish an upper limit on the solar electron antineutrino flux below what the Sudbury Neutrino Observatory is capable of detecting. This is unfortunate as the work on this dissertation topic began 3.5 years earlier, before either KamLAND or Super-Kamiokande had reported their solar electron antineutrino analyses. However, this assessment hinges upon the assumed energy independent $\nu_e \rightarrow \bar{\nu}_e$ conversion mechanism. This assumption is equivalent to assuming a ${}^8\text{B}$ spectrum for solar electron antineutrinos. This assumption is used by most authors to report results for comparison between experiments. In this light, an electron antineutrino analysis of SNO data is still relevant because SNO can detect $\overline{\text{CC}}$ interactions induced by $\bar{\nu}_e$'s greater than 4.03 MeV. This is 4.27 MeV lower in $\bar{\nu}_e$ energy than reported by KamLAND. Thus, SNO covers 82.8% of the ${}^8\text{B}$ spectrum while KamLAND is only sensitive to the upper 30.3%. SNO's sensitivity to lower energy $\bar{\nu}_e$'s provides a rigorous test of the energy independent conversion mechanism usually assumed in searches for solar electron antineutrinos.

Part III

Supporting Analysis

Chapter 10

MUON FOLLOWERS AND MUON PREDECESSORS

Muons and the free neutrons they produce through spallation processes provide a way to determine the cut criterion for an optimized electron antineutrino analysis. This chapter introduces the topic of muons at the Sudbury Neutrino Observatory. Previous work on muons is reviewed and then a refinement on the sorting of muon event classes is added. The goal of this chapter is to extract a sample of muon induced neutrons. The study of muon induced neutrons along with a comparison to a “signal off” period immediately preceding the muon, provides a proof of principle for the cut criterion used in the electron antineutrino analysis presented in this dissertation.

10.1 Muons at SNO

There are two primary sources of muons that reach the SNO detector. First, there are *atmospheric muons* generated in cosmic-ray interactions with the Earth’s atmosphere. Second, there are *neutrino induced muons* generated in atmospheric muon neutrino interactions in the Earth’s interior. The atmospheric muon neutrinos that generate this second class are also originally produced in cosmic-ray interactions with the Earth’s atmosphere. The production of both the atmospheric muons and atmospheric muon neutrinos was described in Section 5.1.

Atmospheric muons detected at SNO come from above the detector’s horizon line, dominating near the vertical. Neutrino induced muons, on the other hand, come from all directions. As a function of angle from the horizon, Figure 10.1 shows these two contributions to the expected muon flux at SNO.

Muons’ distinctive signal in the SNO detector is their copious production of Čerenkov light. An immediate qualitative comparison of Figures 1.2 & 10.2 shows how the latter muon creates a much larger Čerenkov signal in the SNO detector. Figures 10.3 & 10.4 show the N_{hit} spectrum for a sample of through-going muons as defined below.

10.1.1 Muon Event Classes at SNO

There are several different muon event classes at SNO. This chapter selects through-going muons with the goal of isolating muon spallation processes from other muon event classes. A through-going muon is defined as a muon which passes completely through the interior of the SNO detector, intersecting the PSUP at two locations. The geometry of a through-going muon and the definition of the muon impact parameter, b_{μ} , is shown in Figure 10.2 while other classes of muons are described in Table 10.1. It should be noted that it is not currently possible to reliably distinguish each of the muon event classes described in Table 10.1, however, it is possible to select a sub-set of muons that are adequate for the extraction of muon induced neutrons.

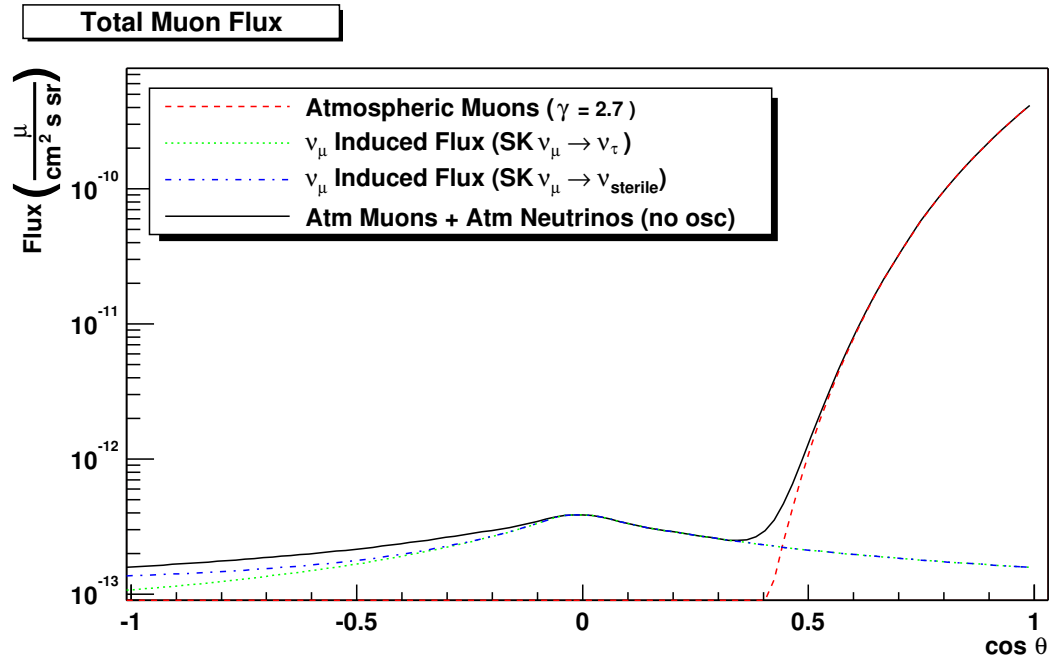


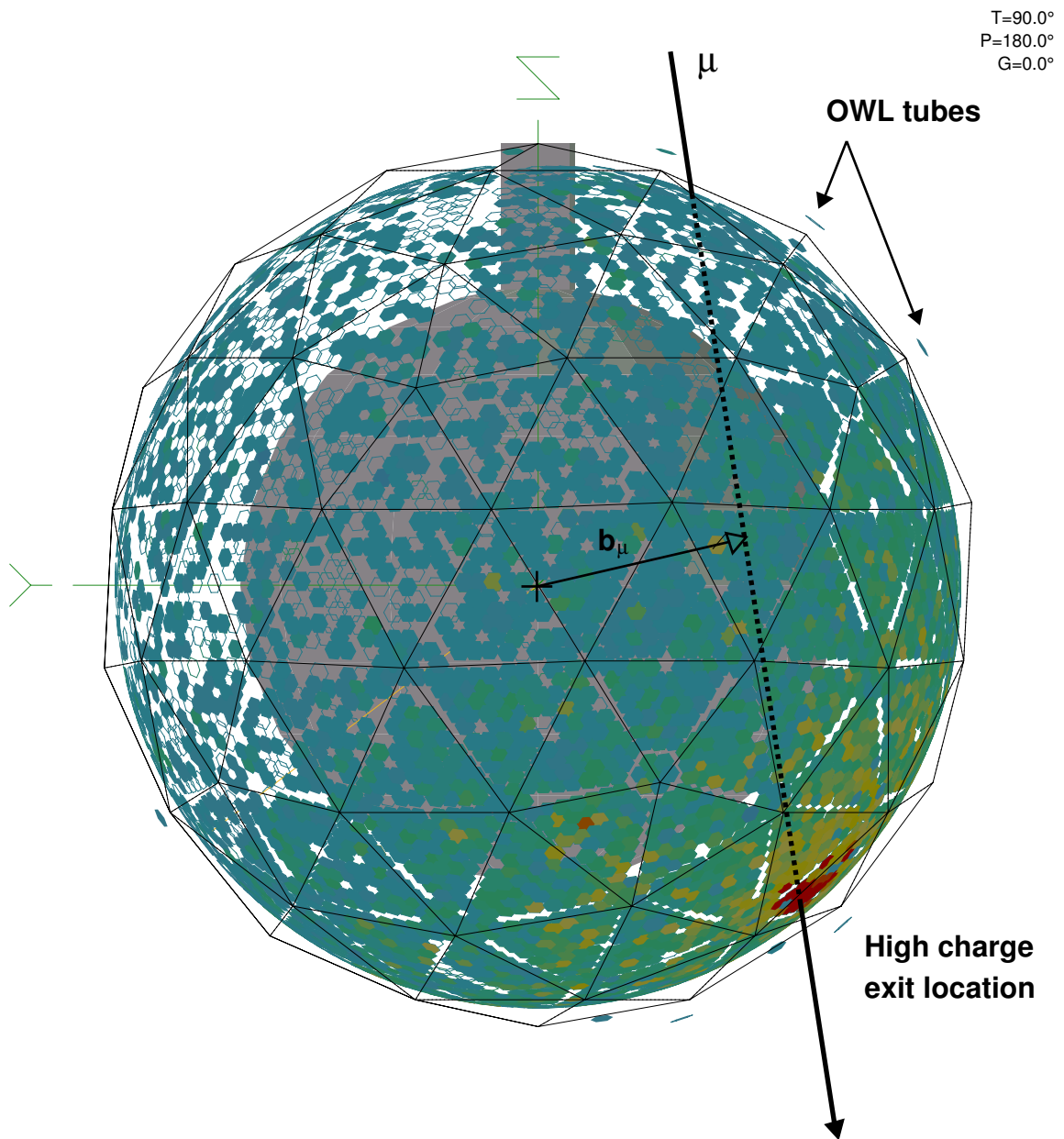
Figure 10.1: The estimated muon flux at SNO as a function the incident direction of the incoming muons. Figure taken from Ref. [201]. The ν_μ induced fluxes are drawn under two separate neutrino oscillation scenarios, as constrained by the Super-Kamiokande experiment. Super-Kamiokande results now favor the $\nu_\mu \rightarrow \nu_\tau$ oscillation model [101]. The γ value given for atmospheric muons is the choice used for a characteristic parameter in models of the muon flux.

Table 10.1: Classes of muon events at the Sudbury Neutrino Observatory. While deep inelastically scattered muons may actually survive and pass completely through the detector, these are a class of muon event to avoid in this study because of the hadronic showers produced in the detector.

Class Name	Muon(s)	Description	Used
Through-going	$\mu_{\text{atmo, induced}}^\pm$	Passes completely through interior of detector.	Yes
Decay	$\mu_{\text{atmo, induced}}^\pm$	Decays to Michel electron.	No
Stop & capture	$\mu_{\text{atmo, induced}}^-$	Captures on nuclei.	No
Deep inelastic scattering	$\mu_{\text{atmo, induced}}^\pm$	Muon creates high energy hadronic shower.	No
Partially contained	μ_{induced}^\pm	Muon begins in interior of detector and exits.	Yes
Fully contained	μ_{induced}^\pm	Muon begins in interior of detector and stops. See the stopped muon classes.	No

10.2 Muon Identification and Fitting

There are two methods for identifying muons in the SNO detector. One method's intention is to try to remove all muon candidate events. This method is referred to as the DAMN bit muon cut and is used to remove



Run: 15165 GTID: 488074 - Time: 02/23/2001 02:13:52.932298183 UTC

Figure 10.2: Example of a through-going muon. The muon's impact parameter is labeled as b_μ . The color represents the amount of charge deposited in the hit PMT.

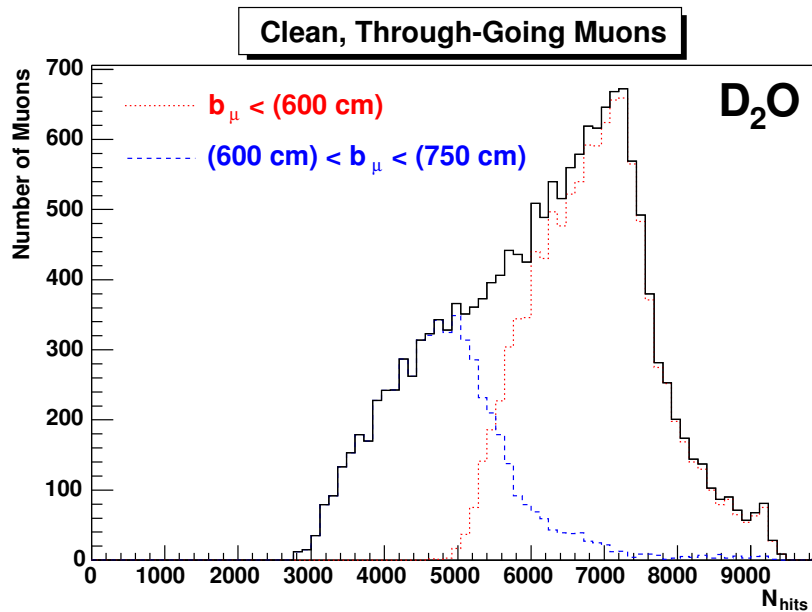


Figure 10.3: The clean, through-going muon N_{hit} spectrum in the Pure D_2O phase.

muons and their spallation products from the data sample used in SNO's solar neutrino analysis. The other method intends to provide a rudimentary fit to through-going muon's mean path through the detector. These are referred to as FTM muons. In the present analysis, both methods are used in unison to identify and select an unambiguous set of through-going muons.

10.2.1 A Simple Muon Identification - DAMN Muons

A DAMN muon is defined as any event that satisfies all the following criterion:

- The event contains 5 or more outward looking (OWL) photomultiplier tubes.
- The event contains 150 or more total photomultiplier tubes.
- The root mean square of the trigger times of the photomultiplier tubes in the event, is less than 90 ns.
- The event must *not* follow within $5 \mu s$ of any other event that has a combined total of OWL and BUTTS tubes greater than or equal to 3.
- The event must *not* fail a cut (the NECK cut) which is designed to eliminate events produced by light generation in the neck of the acrylic vessel. This NECK cut relies on the firing of 2 or more (out of 4) photomultiplier tubes situated in the neck of the acrylic vessel expressly for this purpose.

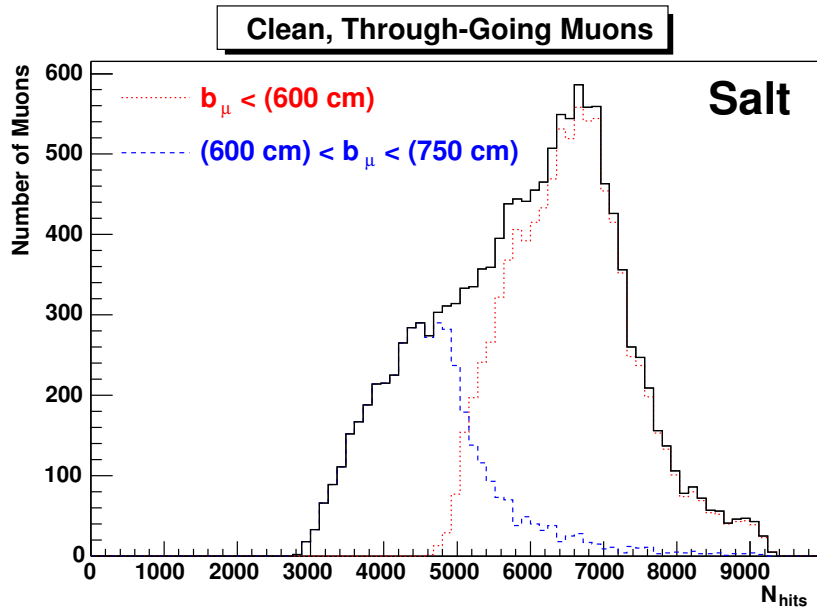


Figure 10.4: The clean, through-going muon N_{hit} spectrum in the Salt phase.

These muon identification criteria are successful and only have two known draw-backs. First, muons that produce few Čerenkov photons in the interior of the SNO detector will not be identified. This may happen if the muon is near or below Čerenkov threshold ($E_{\mu}^{\text{thresh.}} = 153.6 \text{ MeV}$) or if the muon only passes through the interior of the detector with a glancing, high impact parameter. The current analysis will focus on high energy through-going muons that pass through the acrylic vessel, thus these unidentified muons are of low interest for this analysis. Second, this identification criterion mis-identifies as muons other known instrumental background events, for example photomultiplier tubes which produce flashes of light. The contamination from instrumental backgrounds is addressed by the second muon identification method.

10.2.2 A Simple Muon Fitter - FTM Muons

A FTM muon candidate is defined as a muon which is successfully fit by the rudimentary muon fitter developed for muon analysis at SNO. The muon fitter is extensively discussed in N. Tagg's Doctoral thesis [201]. In simplified terms, the muon fitter begins by choosing the muon's likely exit location on the PSUP. This exit is determined from the center of a cluster of PMTs with high charge, relative to the mean charge per PMT in the event. Trial straight line tracks through the exit point are then used to model the expected geometrical and timing distribution of the muon's Čerenkov light. From these, the trial track producing (through a chi-squared minimization) the best model of the timing of the PMT hits is chosen as the best fit muon path through the detector.

To examine the quality of the fit provided by the above routine two parameters are determined. The first

parameter uses the geometry of the muon track to determine the ratio of the number of PMTs which should have detected prompt Čerenkov light from the muon given the fit track *and* did fire to the total number of PMTs which should have detected prompt Čerenkov light:

$$f_{\text{should}} = \frac{\text{Number of PMTs which should have fired and did fire.}}{\text{Number of PMTs which should have fired.}} \quad (10.1)$$

The second parameter uses a Monte Carlo generated probability density function of the PMTs' firing time residuals. The time residual is the actual time the PMT fired minus the time expected based upon a muon's modeled Čerenkov light from the fit track. The Monte Carlo provides knowledge of the actual simulated muon track, thus the probability density function is generated by calculating the time residuals from a simulated "perfect" fit. The probability density function is then used to calculate a weighted sum of the time residuals for the real fitting muon events. The negative log of the weight from the time residual probability density function is summed for all tubes and then divided by the total N_{hit} . This second quality-of-fit parameter is referred to as the LogPDF. The primary output of the muon fitter is the impact parameter of the through-going muon. Figure 10.5 shows the impact parameters of the muons which are used in the muon follower analysis in the latter half of this chapter.

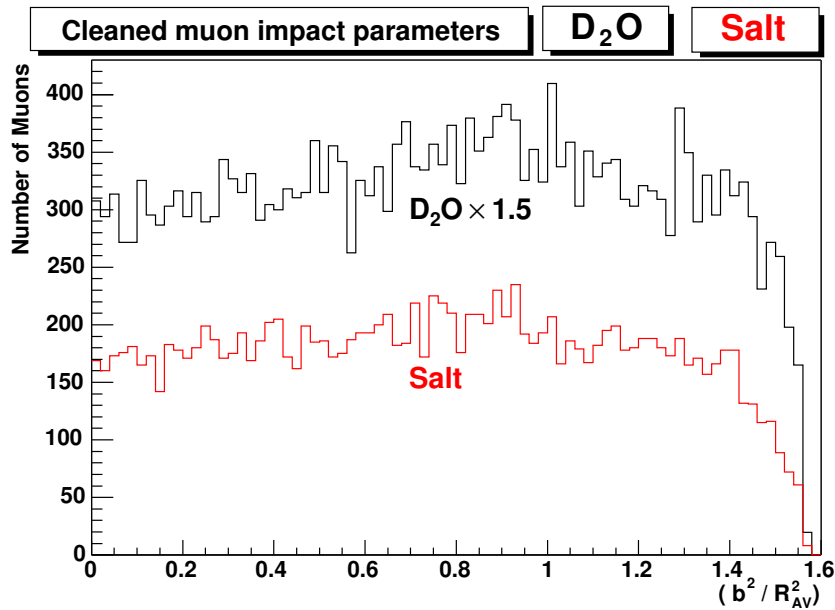


Figure 10.5: The impact parameter for clean, selected muons. The histogram of the Pure D₂O phase muons is multiplied by 1.5 to separate the two curves on the histogram.

The muon fitter is, by its design, mainly sensitive to through-going muons. In fact, the initial reliance on determination of a muon exit location means that the muon fitter does not do a good job handling muons

which stop in the detector. In this analysis it is important to select only through-going muons and to minimize contamination from muons which either stop in the detector or deep-inelastically scatter off nuclei. Thus, for this analysis, it is not a concern if the muon fitter fails to fit a muon that stops and decays. However, it will be necessary to further investigate candidate muons that pass the DAMN and FTM criterion for any signs that the muon does not pass entirely through the detector or deep-inelastically scatters.

10.2.3 Removing Muons with High Energy Followers

Q. R. Ahmad identifies 5 distinctive AV-going (DAG) muons as part of his dissertation work [8]. In that work it is speculated that these 5 events are muons accompanied by electromagnetic showering. Ahmad demonstrates that the energy response of the detector to DAG following events is slightly shifted away from the response expected from neutrons. The goal of this chapter is to select a sample of muon spallation *neutrons*. Thus, there is merit to investigating whether or not these distinctive muon events can be identified and thus eliminated from the muon sample.

Most generally, there is a range of possible interactions muons may have in the SNO detector beyond Čerenkov production:

- Real photo-disassociation of nuclei from bremsstrahlung radiation.
- Virtual photo-disassociation of nuclei (i.e. direct muon spallation).
- Decay $\mu^\pm \rightarrow e^\pm + \nu_e(\bar{\nu}_e) + \bar{\nu}_\mu(\nu_\mu)$.
- Pion production through inelastic scattering off heavy nuclei.
- Deep inelastic scattering.
- Negative muon capture: $\mu^- + {}^A_Z N \rightarrow \nu_\mu + {}^A_{Z-1} N^*$.

By requiring muons to satisfy both the DAMN and FTM criteria, many of these event classes are eliminated. For example, muons which stop in the interior of the detector should fail to be fit by the FTM muon fitter. Negative muon capture is an example of a muon that stops in the detector. In the case of deep inelastic scattering a muon can either pass entirely through the detector or produce a charged particle which will mimic the signature of the muon passing through the detector. The signature of deep inelastic scattering is a hadronic shower and the subsequent decay of the particle(s) produced and decay of the residual nucleus. Thus, to eliminate muons that either decay in the detector or deep-inelastically scatter off nuclei causing hadronic showering, the 11 μs after each candidate muon is investigated. Within 11 μs more than 99.3% of at rest muons will decay. Deep inelastic scattering and pion decay occurs on a shorter time scale.

For each event following within 11 μs of a candidate muon, the calibrated firing times of the hit tubes from -100 to 400 ns are histogrammed into single nanosecond bins. A constant (horizontal line) is fit to the histograms as a base value. A fitting procedure is then stepped over each histogram's 500 ns range in 16 three-quarters overlapping steps. In each step, an unconstrained Gaussian is fit to the range being stepped

over. Each step covers 100 ns - a time window which adequately contains all in-time light from a real Čerenkov event. If in any single fit:

The magnitude of the Gaussian fit is greater than 2.5 events (per nanosecond bin).

AND The magnitude of the Gaussian fit is greater than 1.5 times the magnitude of the line fit.

AND The mean of the Gaussian fit is within the fit's 100 ns range.

AND The integral of the histogram in the fit's 100 ns range contains ≥ 100 real PMTs.

then it is assumed that a decay or DIS Čerenkov ring has been found and the preceding muon is rejected. This procedure is visually outlined in Figure 10.6.

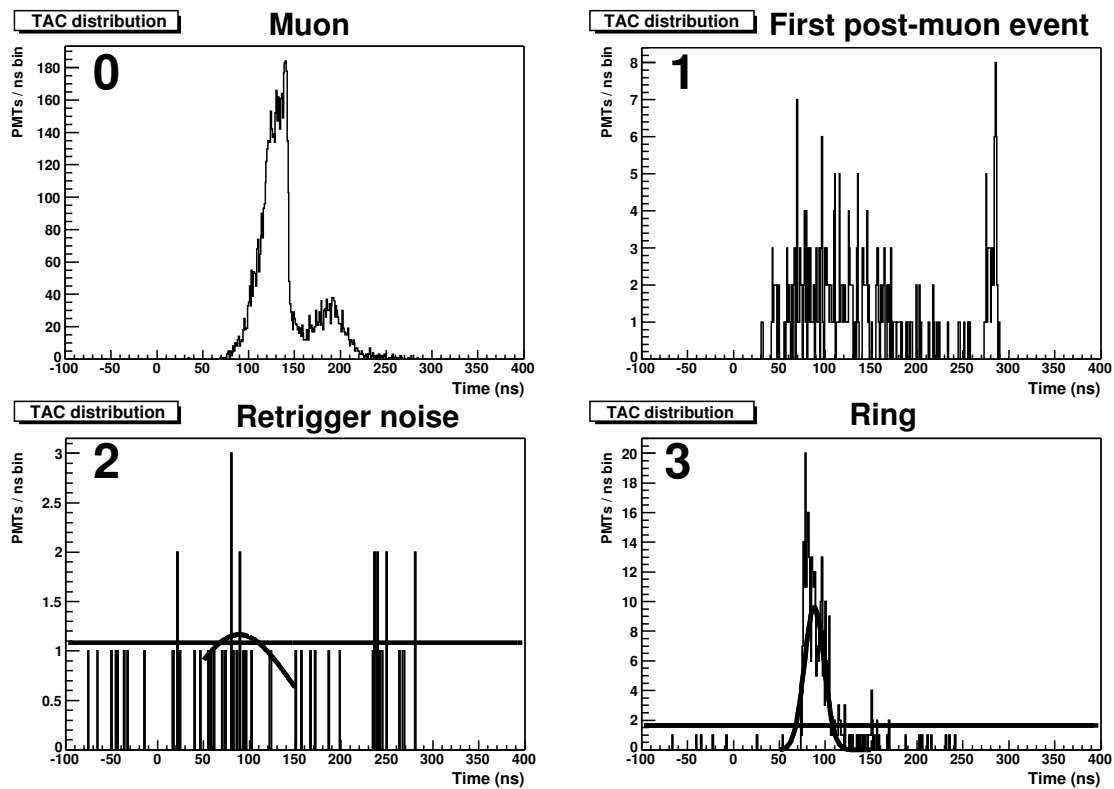


Figure 10.6: This sequence of four events beginning with a muon (0) shows how high energy rings are found during the “decay” period following within 11 μ s after a muon. Event (1) is not fit because the event 500 ns after the muon always has this distinctive shape. Event (2) is electronic after-pulsing noise. The fit in event (3) finds a Čerenkov signature and the muon is therefore rejected. This is a muon in run 10551 with a global trigger identification number of 3972171.

In passing, the five DAG events identified in Ahmad’s dissertation were properly eliminated from the set of muons used for the muon follower analysis presented later in this chapter. Table 10.2 lists the DAG events and why they were eliminated from the muon analysis chain presented in this chapter. A visual inspection of

Table 10.2: Distinctive AV-going (DAG) events and the reasons for their elimination as part of the analysis presented in this chapter. Either “No FTM fit” or “Failing the muon decay window test” will eliminate a muon from the muon follower analysis presented in this chapter. Note “No FTM fit” means either that the fit failed or gave a corrected impact parameter greater than 750 cm.

Run	Muon GTID	Reason
10008	1697058	No FTM fit. Passed the muon decay window test.
10549	3301460	No FTM fit. Failed the muon decay window test.
10946	299141	No FTM fit. Failed the muon decay window test.
11291	1015858	FTM fit muon. Failed the muon decay window test.
11347	92584	No FTM fit. Passed the muon decay window test.

the two events passing the muon decay window test, showed no evidence for rings following the muon. In other words, the muon decay test window test did what it was expected to do. This comparison to the DAG events also shows that the muon decay window test will find “interesting” events, which are otherwise ignored because they fail the FTM fitting routine. Unfortunately, a complete list of events failing the muon decay window test is of questionable value because such a list includes instrumental contamination (predominately wet end break down).

10.3 Muon Selection

In both the Pure D₂O and Salt phases of the experiment, a candidate muon must fulfill the criterion stated in Table 10.3 to become a muon used for the muon follower study. This set of selection criterion is designed to

Table 10.3: Criterion for muon selection in this study.

Satisfy the DAMN bit muon cut criterion.
Have a successful FTM fit with quality-of-fit parameters as suggested in Ref. [201] $f_{\text{should}} > 0.8$ & $\text{LogPDF} < 4.5$
FTM corrected impact parameter less than 750 cm.
Pass the decay window cut presented in Section 10.2.3.

produce a set of muons which are unambiguously through-going and have at most interacted in the detector via direct muon spallation or real photo-nuclear disassociation¹. Those muons satisfying all the criterion of Table 10.3 are succinctly referred to as “clean” muons.

¹There may also be pion production included in the muon events sample. See the footnote of Section 10.4.

10.3.1 Muon Selection in the Pure D₂O Phase

Muons are selected from the canonical 559 run data set used (Appendix A) with exceptions as noted in Table 10.4. After the exceptions are excluded, the total time the SNO detector was live to muons was 307.1 days.

Table 10.4: Runs excluded from the muon and muon follower analysis in the Pure D₂O phase. In all cases, these runs are not include in further analysis in this chapter.

Runs 10031 and 10038 were only partially processed.
Runs 10749, 11732, 11976, 15270 failed to be correctly processed.
Runs 10036 and 15611 did not have files usable for the decay window test.

Beginning with 17,145 FTM muons with corrected impact parameters less than 750 cm and satisfying the muon quality-of-fit tests, 328 were not used in this analysis because of the exceptions noted in Table 10.4. Of the remaining 16,817 fit muons, there were 49 FTM muons which did not satisfy the DAMN bit muon cut criterion. The decay window cut identified 131 FTM muons as having high energy events following within 11 μ s of the muon and were thus rejected. The 131 events rejected by the decay window cut are discussed in Appendix D. There were two pairs of muon events which overlapped within 0.5 seconds. These 4 muons were also rejected from the data set leaving a total of 16,633 muons from which spallation followers are extracted. Figures 10.3 & 10.5 show the N_{hit} and impact parameter distributions for these selected muons. The resultant rate of muons is 54.2 ± 0.4 selected muons/day for the selection criterion of Table 10.3. Tagg's result was 50.14 ± 0.7 muons/day in 175.5 m² effective area (nominally a corrected impact cut of < 750 cm). While Tagg's result used a slightly different muon selection criterion and was derived from a different data set, it is never-the-less unexpected to find the muon rate presented to be *larger* that Tagg's result.

10.3.2 Muon Selection in the Salt Phase

The canonical 697 run data set for the Salt phase (Appendix A) was used to select muons with the following exceptions:

- Runs 22734, 22735, and 22736 were not processed correctly (clock problems not fixed). This amounted to 84976.5 seconds of lost livetime.

After the exceptions, the total time the SNO detector was live to muons was 257.81 ± 0.01 days.

In the Salt phase the analysis was done by using the DAMN bit muon test as a filter, the results of which fed directly into the FTM muon fitting routine. The result of this procedure was 22,684 FTM muons before any quality-of-fit, impact parameter, or muon decay window cuts were applied. Applying the quality-of-fit tests and a impact parameter cut of less than 750 cm, 13,846 FTM muons remained. The muon decay window cut removed 83 muons (documented in Appendix D) leaving 13,763 muons. Due to the clock problems noted above, an additional 41 muons were not used in this analysis. The final selected muon set was thus composed of 13,722 clean, through-going muons giving a selected muon rate of 53.2 ± 0.5 selected muons/day, in

excellent agreement with the rate during the Pure D₂O phase. Figures 10.4 & 10.5 show the N_{hit} and impact parameter distributions for these selected muons.

10.4 Defining Muon Followers & Muon Predecessors

10.4.1 Muon Followers

Muon followers are loosely defined as those events which follow within a few seconds of the passage of a muon through the SNO detector. As already described in Section 10.2.3, muons which deep-inelastically scatter or decay are eliminated from the selected muon sample used for the muon follower analysis. The muons remaining in this clean, through-going muon sample are expected to potentially excite nuclei and spall or photo-disassociate nucleons from parent nuclei, or otherwise interact primarily electromagnetically². Figure 10.7 (from Ref. [222]) shows the relative weighting of the processes covered in this section. The figure is a general Monte Carlo and is not specific to the SNO experiment. Q. R. Ahmad's Doctoral thesis [8] and other SNO documents [152, 153] address in detail the full range of potential products produced by muons, specific to the SNO detector. This section exclusively focuses on processes where the passage of a muon generates free neutrons. It is possible to identify muon induced neutrons by their characteristic neutron capture time and neutron capture energy (N_{hit}) distribution. This muon induced neutron identification process mimics the identification process that is used in an electron antineutrino analysis which searches for a coincidence between an initial trigger event and a following neutron(s). The muon induced neutron analysis to is used to suggest cut parameters for the electron antineutrino analysis.

10.4.2 Muon Predecessors

Muon predecessors are those events which immediately precede the passage of a muon through the SNO detector. These events provide a "neutron signal-off" comparison to the muon followers.

10.5 Muon Follower & Muon Predecessor Selection

It is of paramount importance to treat the muon followers and predecessors identically. Practically, the focus on measuring the muon spallation neutrons (i.e. the followers) will determine the parameters which are then applied to the muon predecessors. The next two subsections discuss the selection process for the muon followers and it is implied that exactly the same process is being used on the muon predecessors unless otherwise stated.

²Inelastic pion production is an interesting case which straddles the region between pure electromagnetic interactions and deep inelastic scattering. If a pion is produced and decays more than 500 ns after the initial muon passes through the detector, the pion's decay muon or gamma pair will cause the muon decay window test to fail, thus eliminating the initial muon and its followers from the muon follower analysis. However, pions' proper lifetimes are sufficiently short so that a significant fraction will decay essentially immediately and can not be eliminated. This failure to eliminate inelastically produced pions doesn't appear to be a problem so long as the pion is not accompanied by a hadronic shower. The reason for this is that pions predominately create further spallation neutrons (and protons), exactly the kind of neutron followers this analysis is focused on [222, 120]. See Appendix D.

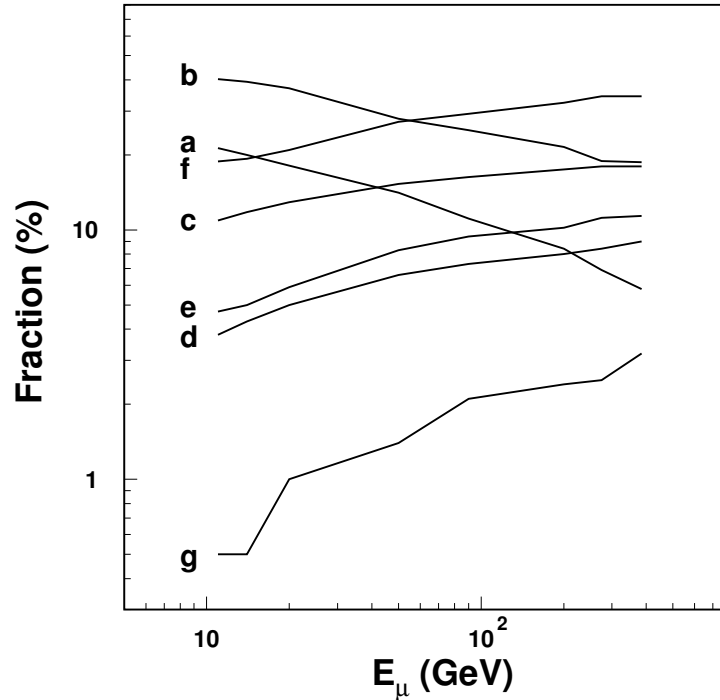


Figure 10.7: This figure, taken from Ref. [222], is a qualitative representation of the various neutron producing, muon spallation process expected in deep underground laboratories like SNO. The categories are (a) direct muon spallation, (b) real photo-nuclear disassociation, (c) neutron spallation, (d) proton spallation, (e) π^+ spallation, (f) π^- spallation and capture, and (g) others. This figure is for a simulation of a liquid scintillation detector composed of $C_{10}H_{22}$.

10.5.1 Follower/Predecessor Selection in the Pure D_2O Phase

The DAMN bit muon test was used to create a reduced data set for the muon follower and muon predecessor analysis. The reduced data is composed of events falling within 0.5 seconds before and 20 seconds after the DAMN bit muon. The DAMN bit muon event was always stored in the reduced data set. All other events were required to pass a set of instrumental background cuts (DAMN bit mask equal to 11628513) and have an N_{hit} value greater than 25. This reduced data set was the basis for further analysis.

The reduced data set was split into a muon follower set and a muon predecessor set. The time window around the muon was reduced to 500 ms and only the 16,633 clean, through-going muons were used. The next step applied an admittedly somewhat arbitrary cut on the muons used for the final muon follower and

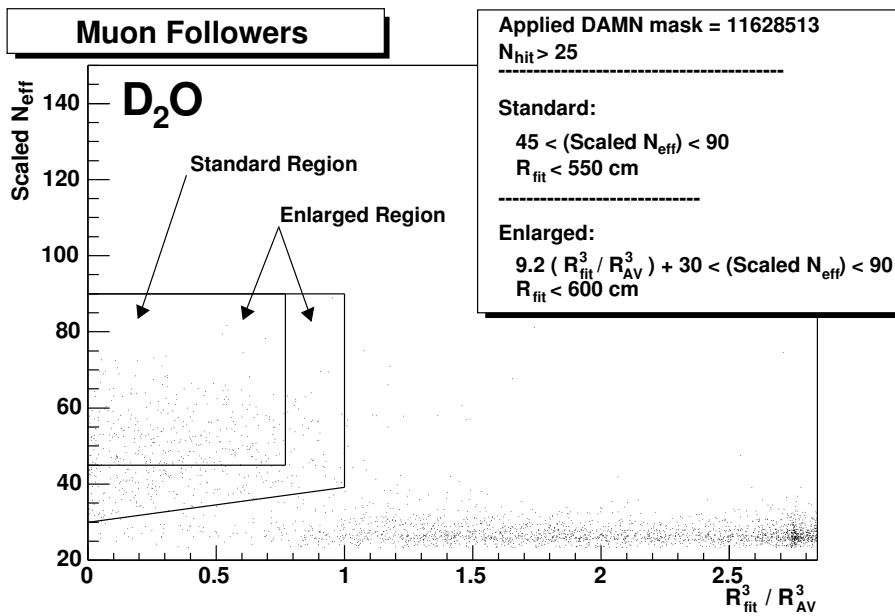


Figure 10.8: The N_{hit} vs. R_{fit} of muon followers in the Pure D₂O phase.

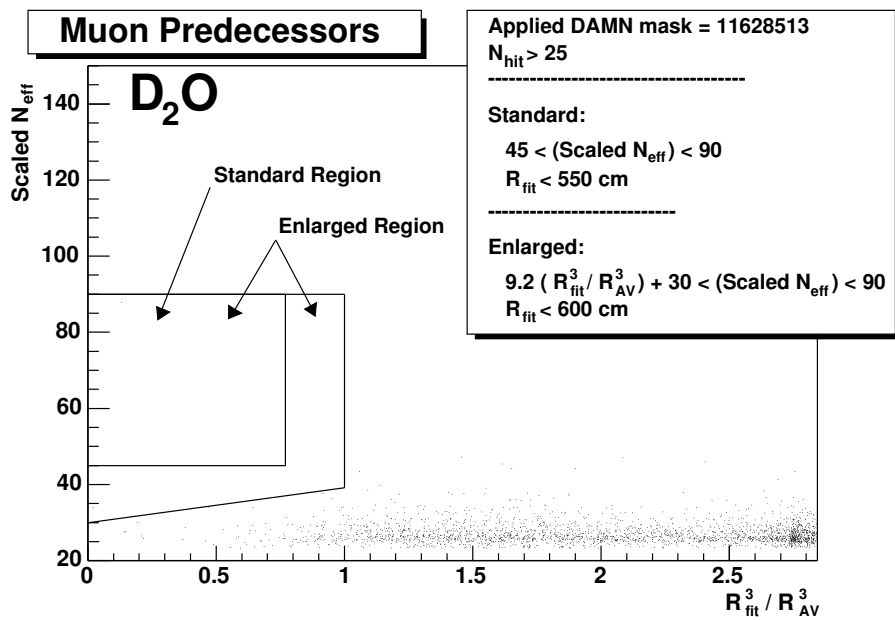


Figure 10.9: The N_{hit} vs. R_{fit} of muon predecessors in the Pure D₂O phase.

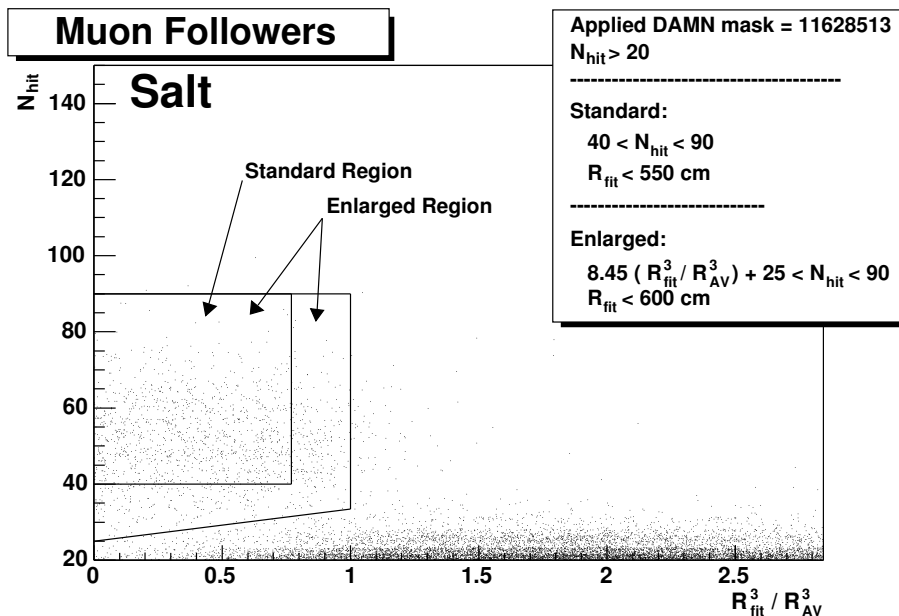
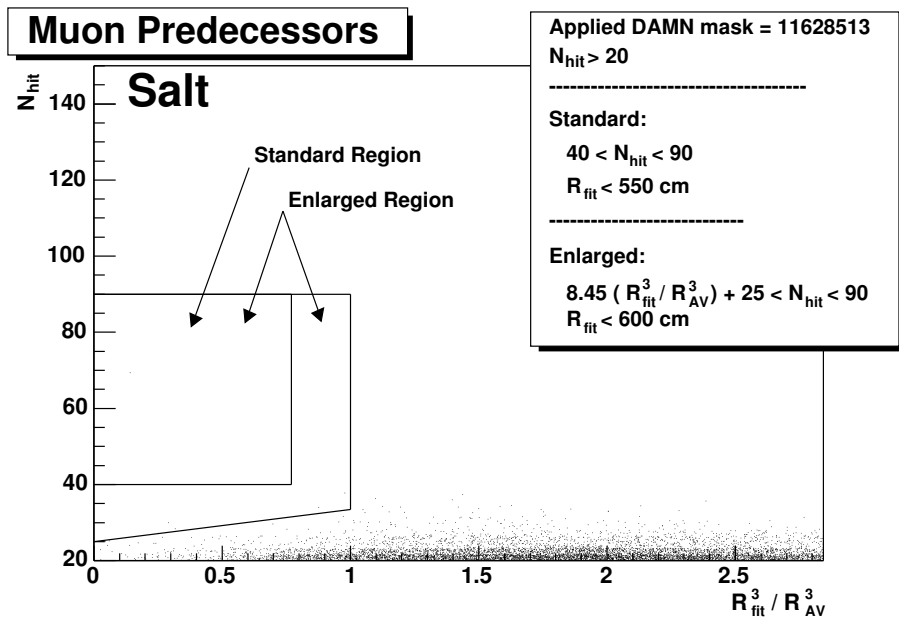
muon predecessor analysis. The muon followers and predecessors were drawn from cases where the muon had a corrected impact parameter of less than 600 cm. One could argue there is something to be learned from contrasting the muon follower signature from muons that do or do not pass through the heavy water. Since the heavy water is the active neutron target used for neutron detection, one could study neutron propagation into the heavy water from outside regions or learn about any mild sensitivity to neutrons in the light water region. The restriction to muons having a corrected impact parameter less than 600 cm is in essence focusing on the fact that the antineutrino analysis is primarily concerned with neutrons created and captured *inside* the D₂O volume.

The remaining events are plotted on a N_{hit} vs. reconstructed position phase space. Note that R_{fit} is the radial reconstructed position of the event and R_{AV} is the radial position (600 cm) of the acrylic vessel (AV), the edge of the heavy water region. Thus $R_{\text{fit}}^3/R_{\text{AV}}^3$ gives the correct volume weighting to show a uniform distribution of events throughout the detector volume. Figures 10.8 & 10.9 show the $N_{\text{hit}}-R_{\text{fit}}$ plots for the muon followers and muon predecessors. The Scaled N_{eff} parameter is a N_{hit} value that corrects for the drift in the energy scale of the detector in the Pure D₂O phase of the experiment. Notice the activity of the PMT support structure (PSUP) can be seen as the group of events $R_{\text{fit}}^3/R_{\text{AV}}^3 = 2.84$.

On each figure is draw two regions. Based on Monte Carlo simulations of neutrons (Chapter 16) neutron events are expected to populate these diagrams in the region $R_{\text{fit}}^3/R_{\text{AV}}^3 < 1$ and $25 < N_{\text{hit}} < 90$. The SNO Collaboration has previously published results [10, 11] using data that would populate the area labeled “Standard Region”. The area labeled “Enlarged Region” is meant to suggest how additional sensitivity to neutrons can be achieved by increasing the fiducial volume and lowering the energy (N_{hit}) threshold used in the analysis. Comparison between the muon follower Figure 10.8 and muon predecessor Figure 10.9 clearly shows an excess of events in the expected neutron region. To further compare the events in the Enlarged Region to the hypothesis of neutron events, Figures 10.12 & 10.13 are presented comparing muon follower and muon predecessor data to Monte Carlo neutrons. Please note that the choice of the parameters that define the Enlarged Region are justified in subsequent chapters.

10.5.2 Follower/Predecessor Selection in the Salt Phase

The DAMN bit muon test was used to create a reduced data set for the muon follower and muon predecessor analysis. The reduced data is composed of events falling within 0.5 seconds before and 0.5 seconds after the DAMN bit muon. The DAMN bit muon event was always stored in the reduced data set. All other events were required to have an N_{hit} value greater than 20. This reduced data set was the basis for further analysis. The reduced data set was then split into a muon follower set and a muon predecessor set using only the 13,722 clean, through-going muons. Once again a further restriction to muon having an impact parameter less than 600 cm was applied. The muon followers and predecessors are finally selected by removing events failing a set of instrumental background cuts (DAMN bit mask equal to 11628513). The remaining events are plotted on a $N_{\text{hit}}-R_{\text{fit}}$ phase-space in Figures 10.10 & 10.11.

Figure 10.10: The N_{hit} vs. R_{fit} of muon followers in the Salt phase.Figure 10.11: The N_{hit} vs. R_{fit} of muon predecessors in the Salt phase.

10.6 Conclusions from the Muon Follower Analysis

The conclusions one should draw from this chapter are entirely qualitative. Beyond demonstrating that it is possible to select a set of clean muons to use as a triggered source of spallation neutrons, it should be realized this is a method of determining how to define an optimal neutron selection window *in situ*. The $N_{\text{hit}}-R_{\text{fit}}$ plots clearly show backgrounds dominate at low energy and high radius. It is also clear that events located near the center of the D_2O volume are more likely to be neutrons of interest than events of the same N_{hit} value but near the edge of the acrylic vessel. This implies that an optimized neutron selection criterion should use a cut criterion relating N_{hit} and R_{fit} . The next several chapters will justify the choices of the parameters that define the Enlarged Region as it was presented in Figures 10.8, 10.9, 10.10, and 10.11.

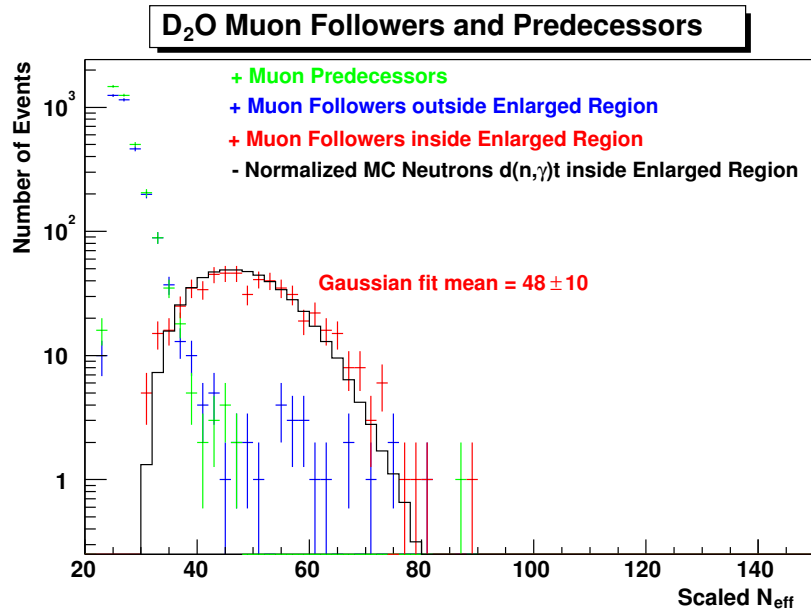


Figure 10.12: Pure D₂O phase N_{hit} distributions of muon followers, muon predecessors, and Monte Carlo neutrons. The fit is to the data inside the Enlarged Region presented in Figures 10.8 & 10.9.

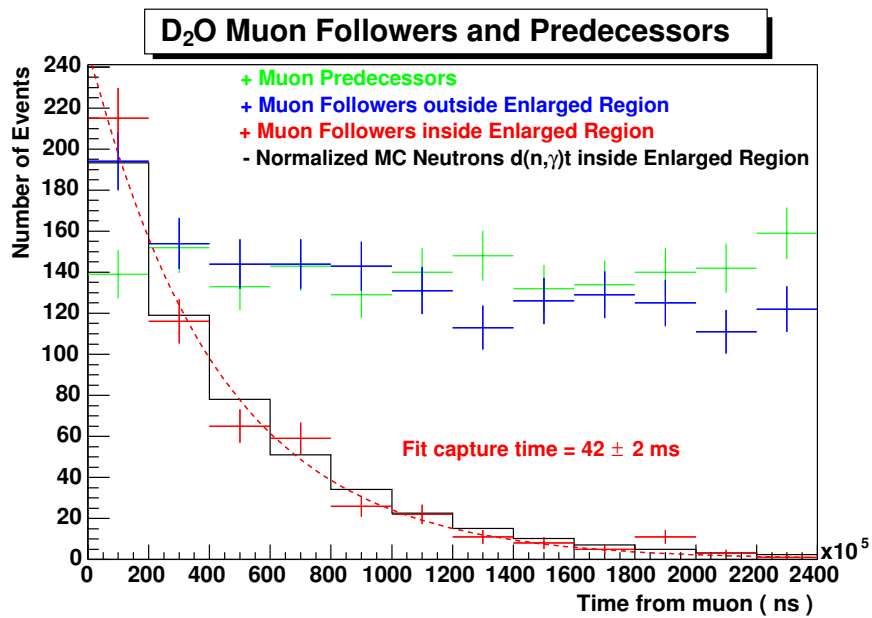


Figure 10.13: Pure D₂O phase Δt distributions of muon followers, muon predecessors, and Monte Carlo neutrons. The fit is the events inside the Enlarged Region presented in Figures 10.8 & 10.9.

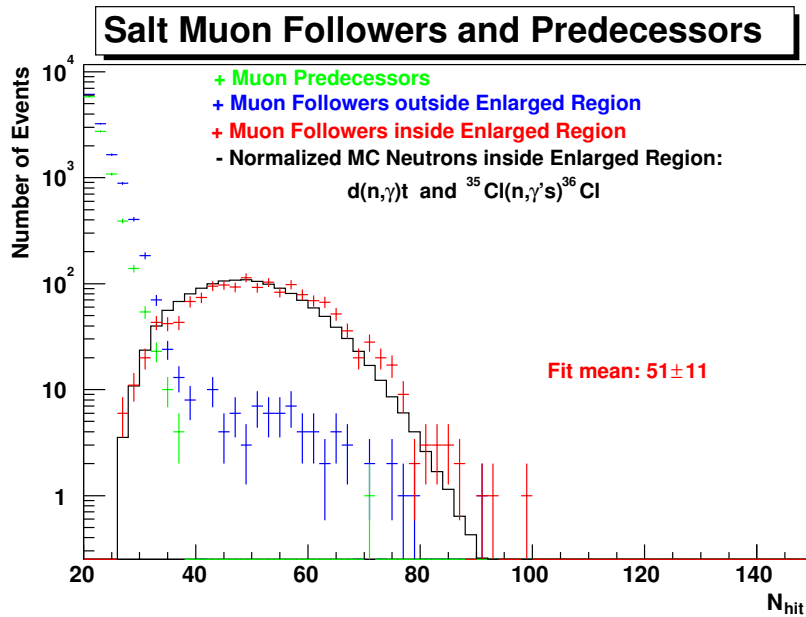


Figure 10.14: Salt phase N_{hit} distributions of muon followers, muon predecessors, and Monte Carlo neutrons. The fit is to the data inside the Enlarged Region presented in Figures 10.10 & 10.11.

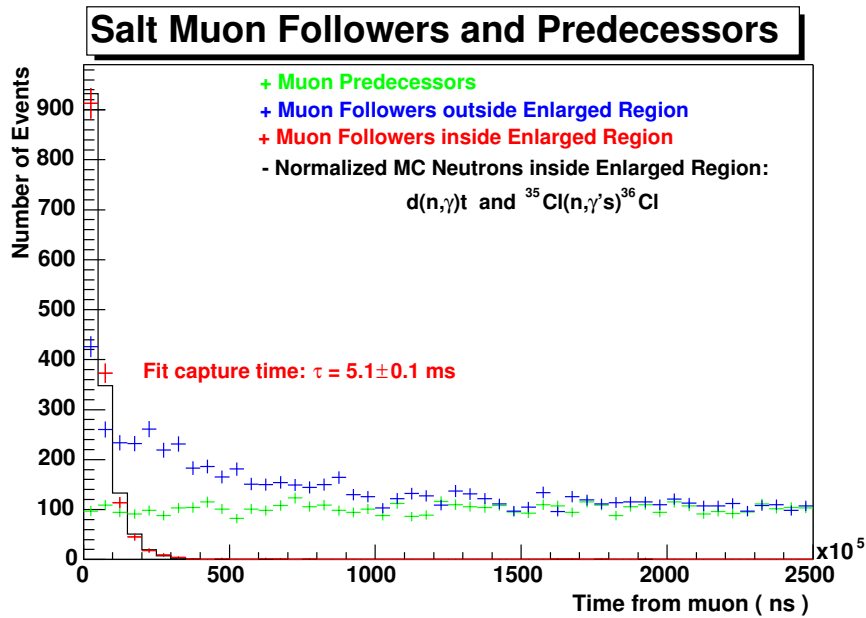


Figure 10.15: Salt phase Δt distributions of muon followers, muon predecessors, and Monte Carlo neutrons. The fit is the events inside the Enlarged Region presented in Figures 10.10.

Chapter 11

NEUTRON CAPTURE TIMES

11.1 Neutron Monte Carlo and Capture Times

To search for the coincidence of events indicative of $\overline{\text{CC}}$ interactions, one must choose a time window to define the meaning of “coincidence”. As the coincidence time window is necessary for nearly all further quantitative studies in the electron antineutrino search, this brief chapter presents and determines the widths of the coincidence time windows used throughout the rest of the analysis.

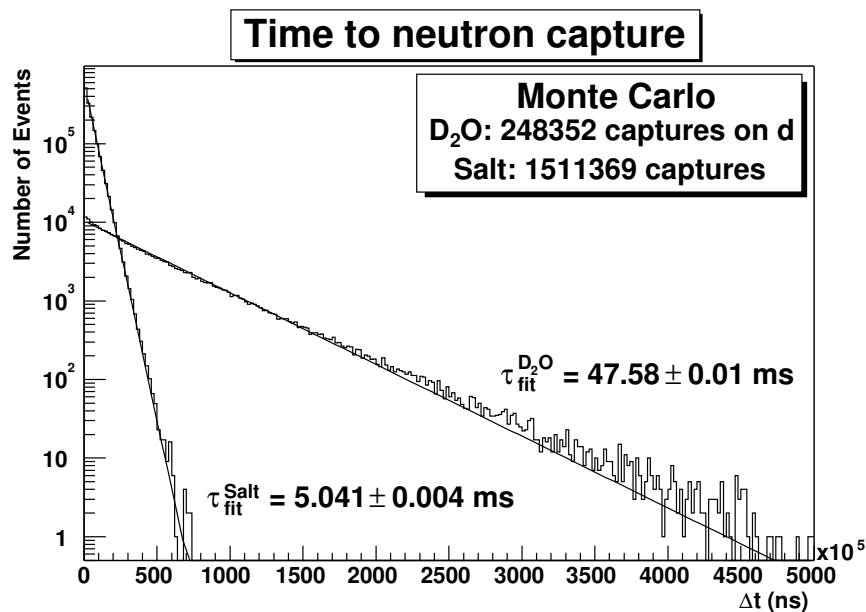


Figure 11.1: Monte Carlo neutron capture time for both the Pure D₂O and Salt phases. In the Pure D₂O phase it is required that the neutron capture on a deuteron as explained in the text. The number of events in each curve is only indicative of the number of neutrons in each of the Pure D₂O and Salt $\overline{\text{CC}}$ Monte Carlos.

The results needed are obtained from the $\overline{\text{CC}}$ Monte Carlos for the Pure D₂O and Salt phases which are described and used to their fullest potential in Chapter 16. In both Monte Carlos, neutrons are produced at a time zero, $t = 0$, and then random walk through the detector until they capture on nuclei at a time Δt . Plotted in Figure 11.1 is the time of capture relative to time zero. In the Pure D₂O phase only those

neutrons which capture on deuterons are included in the plot. If all captures are plotted then the capture time curve is dominated at early times by neutrons produced at large radius capturing on the protons in the acrylic vessel. Neutron capture on protons produces a 2.2 MeV gamma ray. The restriction to neutron capture on deuterons is an alternative to beginning to apply energy and fiducial volume cuts. For the Salt phase all neutron captures are plotted in Figure 11.1. In Chapter 16 the full suite of analysis cuts are used to analyze the Monte Carlo data. Again, the purpose of this section is merely to determine the mean capture time and choose a coincidence time window based upon the rough mean capture time.

11.2 Choice of the Coincidence Time Windows

Once the mean neutron capture time is known, the particular choice of the width of the coincidence time window depends on the goals of the analysis. The Standard and Enlarged analyses have already been introduced, defined, and distinguished by different choices of energy and fiducial volume analysis cuts. Additionally, these two types of analyses will have different coincidence time windows, because each analysis has a different goal. The Standard analysis, relying upon well studied analysis cuts from SNO's solar neutrino analyses, takes the obvious step of choosing a coincidence time window that attempts to maximize the signal-to-noise ratio [139]. To this end, it is assumed that 2% of the ^8B solar neutrinos are converted to electron antineutrinos. The mean event rate for events satisfying all the Standard analysis cuts is assumed to be 4×10^{-4} Hz (see Chapter 13). From these assumptions it can be shown [139] the optimal coincidence time window width is 150 ms. This dissertation will also follow this choice of a 150 ms coincidence time window for the Standard analysis as a check to the work done in Ref. [139].

The thrust of this dissertation, a high sensitivity electron antineutrino search, chooses the coincidence time window used to select candidate electron antineutrino events based on the following criterion:

- No sacrifice to the $\overline{\text{CC}}$ coincidence signal due to the size of the time window.
- A time window that does not bias a determination of the $\overline{\text{CC}}$ reaction's neutron capture time. For example if the time window was chosen as a *fraction* of the mean neutron capture time, then clearly one can not test to see if the events recorded in the detector have the correct mean capture time of neutrons!

Both of these items clearly argue for a coincidence time window that is large in comparison to the capture time of the neutrons in the given phase of the experiment. The first is a choice to not deliberately eliminate any true electron antineutrino events. The second is a choice based on the fact that, in the case of a large electron antineutrino signal, a neutron capture curve with the correct capture time is a very convincing sign that the candidate events are indeed electron antineutrino induced. Thus a coincidence window is chosen at approximately 6 times the mean capture time for neutrons in the given phase. These large coincidence time windows are used as part of the Enlarged analysis.

Table 11.1 lists the choices of coincidence time windows. The choice of the 20 ms coincidence time window for the Standard analysis in the Salt phase is chosen simply so that roughly the same fraction of the Enlarged coincidence time window is used as was the case in the Pure D_2O phase of the experiment.

Table 11.1: The coincidence time windows chosen for the electron antineutrino analysis for each phase of the experiment.

Phase	Analysis	Δt (ms)
Pure D ₂ O	Standard	150
	Enlarged	250
Salt	Standard	20
	Enlarged	35

The straight forward use of the Monte Carlo is supported by the work done on understanding the neutron response of the SNO detector for the primary neutral-current measurement of the total active solar neutrino flux. An early analytic calculation [166] provides a formula for calculating the mean neutron capture time (on deuterons). In this reference the mean neutron capture time for an infinitely large volume of heavy water (0.08% H₂O contamination) is determined to be $\tau_\infty = 72$ ms and the neutron diffusion length is $\ell = 123$ cm. To account for the acrylic vessel's absorption of neutrons, a mean lifetime reduction factor is calculated (formula (26) in Ref. [166]). This reduction factor is calculated for neutrons produced at a given radius, s , where the perfect absorber is at a radius, $R = 600$ cm. To determine the mean capture time for uniformly distributed neutrons the reduction factor should be weighted by the infinitesimal volume, $s^2 ds$, and integrated over from the origin to the radius of the absorber:

$$\tau = \tau_\infty \left[\frac{\int_0^R \left(1 + \frac{1}{2} \frac{R}{\ell} \frac{\cosh(R/\ell)}{\sinh(R/\ell)} - \frac{1}{2} \frac{R}{\ell} \frac{(\cosh(R/\ell) - \cosh(s/\ell))}{(\sinh(R/\ell) - (R/s)\sinh(s/\ell))} \right) s^2 ds}{\int_0^R s^2 ds} \right] \quad (11.1)$$

Equation 11.1 predicts a neutron capture time of $\tau_{\text{D}_2\text{O}} = 42$ ms in the Pure D₂O phase of the experiment. The primary study of neutrons (e.g. neutron detection efficiency) for the Pure D₂O solar neutrino results is given in Ref. [82]. Unfortunately, the neutron capture time is not determined or reported in that document. However, the document does show the Monte Carlo correctly simulates the ²⁵²Cf neutron calibration source, providing confidence in other neutron Monte Carlos such as the one used above. In the Salt phase of the experiment, the primary document studying neutrons [135] provides calculated neutron capture times based upon models of the ²⁵²Cf and AmBe neutron calibration sources. These capture times are $\tau_{\text{Salt}}^{252\text{Cf}} = 5.29$ ms and $\tau_{\text{Salt}}^{\text{AmBe}} = 5.31$ ms and the reported Monte Carlo neutron capture time is $\tau_{\text{Salt}}^{\text{MC}} = 5.40$ ms. Thus the straight forward use the neutron capture times derived from the $\overline{\text{CC}}$ Monte Carlo is acceptable for the purposes of choosing the coincidence time windows of Table 11.1.

Chapter 12

PULSE GLOBAL TRIGGER FOLLOWERS**12.1 Analysis Parameters and Accidental Coincidence Backgrounds**

The muon follower and muon predecessor analysis of Chapter 10 motivates developing the event selection parameterization in an energy response (N_{hit}) and reconstructed event position (fiducial volume) phase-space. The primary goal of this parameterization is to increase the detection efficiency while minimizing the background. In this case the one background we can control is the accidental coincidence rate. The accidental coincidence rate is simply the random time coincidence of two uncorrelated events within the chosen electron antineutrino analysis time window.

Q. R. Ahmad [8] showed it is possible to use Pulse Global Trigger (PulseGT) events to determine the accidental coincidence rate from the data. The Pulse Global Trigger is a trigger used in SNO to force the detector to “fire” at a minimum rate of 5 Hz. The PulseGT is the start event used to investigate the rate and type of events falling in the subsequent coincidence time window. This PulseGT followers method is used here to determine the values for the energy-volume parameterization used in the event selection. The determination of the accidental coincidence rate for the electron antineutrino analysis is done in Chapter 13 using methods based upon a full sampling of the data.

In this chapter the energy and volume event selection criterion are determined from the rate of all candidate events plotted in an energy and volume phase-space. Likewise, the selection of a specific energy and volume event selection window defines what the total detector event rate is within the event selection window. This total detector rate will then also determine the accidental coincidence rate.

12.2 Selecting m in $N_{\text{hit}}(R_{\text{fit}}) \geq m(R_{\text{fit}}/R_{\text{AV}})^3 + N_{\text{hit}}(0)$

The parameterization suggested by Chapter 10 takes the form

$$N_{\text{hit}}(R_{\text{fit}}) \geq m \left(\frac{R_{\text{fit}}}{R_{\text{AV}}} \right)^3 + N_{\text{hit}}(0) \quad (12.1)$$

Equation (12.1) states that events are selected when they have a given N_{hit} greater than or equal to a value that depends upon the event’s reconstructed position, R_{fit} . Thus the parameters to determine are m and $N_{\text{hit}}(0)$, the former being the “slope” of the parameterization and the latter being the minimum N_{hit} value for events at the center of the detector (i.e. $R_{\text{fit}} = 0$). This is demonstrated visually in Figure 12.1. Note that this is interpreted to mean that events which occur at the center of the vessel are considered more likely to be interesting physics events than those events which occur near the acrylic vessel.

The determination of the slope m is intuitively done by determining the rate at which events appear above the line in Figure 12.1 as the line is slid down the y-axis (i.e. lower the analysis energy threshold). The

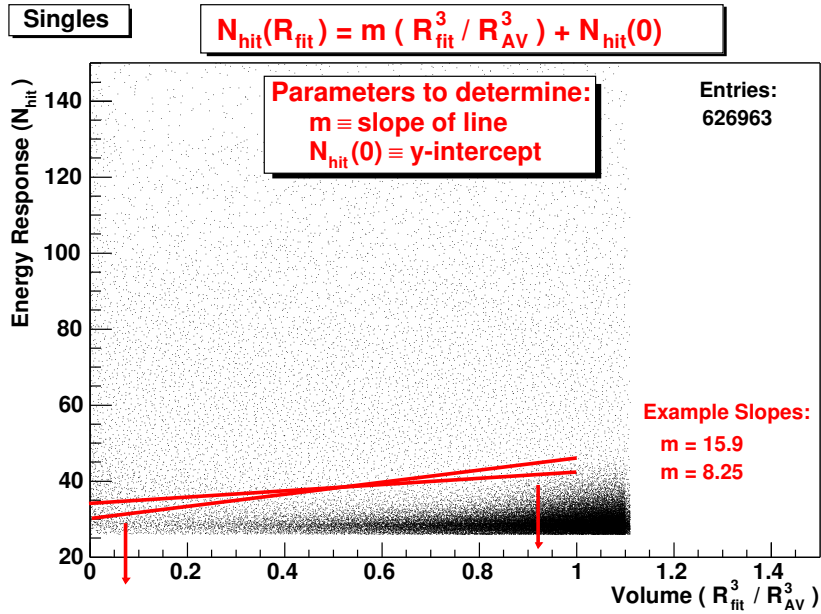


Figure 12.1: To determine the optimal parameters m and $N_{\text{hit}}(0)$ an imaginary line is slid down the y-axis (red sloping lines) and the *rate* of increase of events above the line is determined as a function of the volume variable (x-axis). The optimal slope is found when this rate is constant across along the line.

slope of the line is varied and the slope at which the rate of increase of events *along* the line is constant is the optimal slope.

This scheme was implemented with a simple algorithm. The normalized volume ($R_{\text{fit}}^3 / R_{\text{AV}}^3$) was divided into 4 bins (volume bins). Each volume bin was assigned an array, where each array element represented a different y-intercept value ($N_{\text{hit}}(0)$) used in equation (12.1). The content of each array element was the number of events satisfying equation (12.1) for the particular value of $N_{\text{hit}}(0)$ for that array element and a “given slope m ”. The rate, $r_i(m, N_{\text{hit}}(0))$, of events added to the normalized volume was then calculated by taking the difference between adjacent elements of the array (i.e. changes of the $N_{\text{hit}}(0)$ value). An average rate, $\langle r_i(m, N_{\text{hit}}(0)) \rangle$, for the four volume bins was calculated and the square deviation, $S(m)$, for each of the individual bins was calculated. The sum of the square of the deviations for each step along the array gives a measure of the relative increase in number of added events as the $N_{\text{hit}}(0)$ value is reduced. This sum, $S(m)$, becomes the statistic of merit for the “given slope m ”. This algorithm is represented by the following equations:

$$r_i(m, N_{\text{hit}}(0)) = N_i(m, N_{\text{hit}}(0)) - N_i(m, N_{\text{hit}}(0) + 1) \quad (12.2)$$

$$\langle r_i(m, N_{\text{hit}}(0)) \rangle = \frac{1}{4} \sum_{i=0}^4 r_i(m, N_{\text{hit}}(0)) \quad (12.3)$$

$$S(m) = \sum_{N_{\text{hit}}(0)=25}^{50} \left[\left(\sum_{i=0}^4 \left(r_i(m, N_{\text{hit}}(0)) - \langle r_i(m, N_{\text{hit}}(0)) \rangle \right) \right)^2 \right] \quad (12.4)$$

The procedure is repeated for a broad range of slope values and the summed square deviations is recorded. Figures 12.2 & 12.3 plot the summed square deviations for the Pure D₂O and Salt phases. The minimum value of these plots is where the relative increase in events contributing to the selection window is constant along the boundary line. This minimum is the choice of the slope. Note that a slope of 0.0 is a flat line which would decouple the N_{hit} selection parameter from the R_{fit} selection parameter. A slope of 15 directly translates into a difference of 15 N_{hit} between accepted events at the center of the vessel compared to the edge of the vessel.

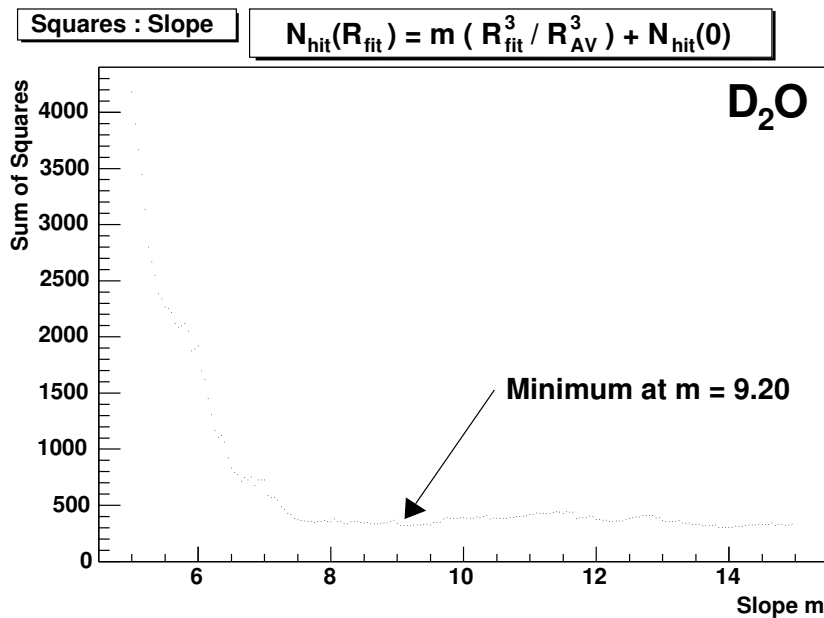


Figure 12.2: Choice of the slope parameter, m , in the Pure D₂O phase.

Figures 12.2 & 12.3 are initially less than convincing reasons for choosing a particular slope as there is not a minimum. Consider, however, that the shape of the curves is affected by the fact that there is a ultimate lower bound on the accessible N_{hit} values. In simple terms, this analysis was not able to use data lower than 25 or 20 N_{hit} for the Pure D₂O and Salt phases, respectively. Thus as the slope increases, the portion of the imaginary line near the center of the vessel is reaching into a N_{hit} region where there are no events, effectively setting the rate of increase in that volume bin to a constant of 0. In these cases the method outlined here produces *lower* summed square deviations. For example above a slope $m = 11.5$ in Figure 12.2, the value decreases. Thus the expected upturn of the plots at high slope is thwarted by the approach toward the minimum detector energy threshold.

A further defense of the choice of a particular slope value from Figures 12.2 & 12.3 comes from an

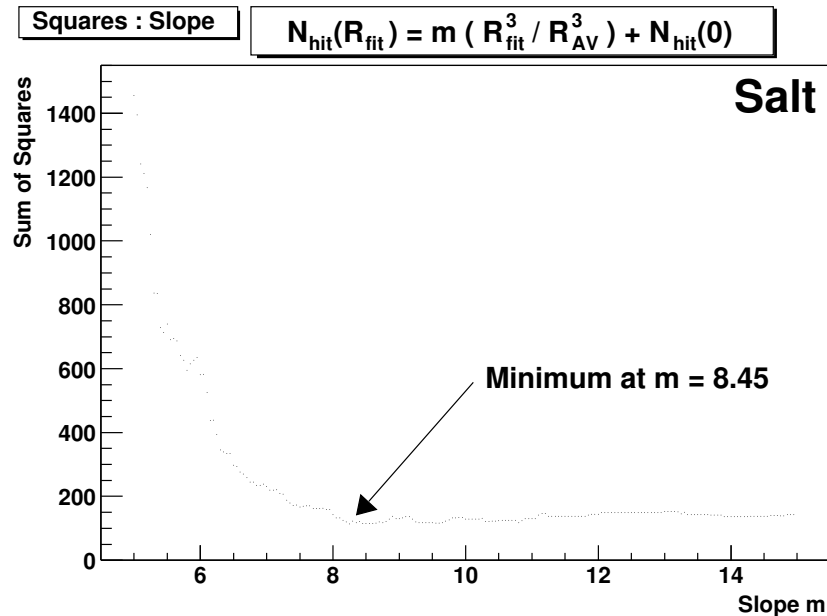


Figure 12.3: Choice of the slope parameter, m , in the Salt phase.

understanding of how the choice will affect the analysis. The choice of the slope *defines* the analysis region. Thus all detection efficiencies and background estimates are relative to this definition. A poor choice will reduce the signal to noise ratio. Clearly, if the background is *slowly* varying as a function of the chosen slope, then over this range the random background is *insensitive* to the particular choice of the slope. The net result is the realization that any slope value is acceptable in the slowly varying region with an eye on avoiding those slopes for which the background begins to vary rapidly (as a function of the slope).

12.3 Data Used in the Pulse Global Trigger Follower Analysis

In the Pure D₂O, after every 200th PulseGT event (once every 40 seconds) the half second following the PulseGT event was analyzed. Three cuts were applied: $N_{\text{hit}} < 80$, $R_{\text{fit}} < 600$ cm, and a cut to remove instrumental background events (DAMN mask of 11628513). The events remaining after these cuts were used to determine the $S(m)$ values plotted in 12.2. The minimum value of $N_{\text{hit}}(0)$ used was 25 in the Pure D₂O phase. In the Salt phase instead of using the PulseGT events as the initial trigger, the event times were used to select a half second of events out of every 40 seconds. This accomplishes the same task as the PulseGT method, but was computationally easier to implement. In the Salt phase the minimum value of $N_{\text{hit}}(0)$ was 20 and the other applied cuts were the same as in the Pure D₂O phase. In both the Pure D₂O and Salt phases the entire data sets were used.

Chapter 13

ACCIDENTAL COINCIDENCE BACKGROUND**13.1 Accidental Coincidences**

For any kind of occurrence which happens at random intervals, there is an analytically calculable probability that two occurrences of that kind will fall within a given time window. For example, even though volcanoes erupt infrequently, since different volcanic eruptions are unrelated, there is a certain probability that two different volcanoes will erupt simultaneously. This is termed an accidental coincidence, in this example, the accidental coincidence of two volcanic eruptions.

Accidental coincidences of SNO events can mimic the electron antineutrino signal. The size of this background is, however, under the control of the analyzer. Thus, in this section two important pieces of the electron antineutrino analysis are extracted from a single analysis of the mean rate of SNO events in an event selection window of interest. The two important pieces are the $N_{\text{hit}}(0)$ value for use in the equation $N_{\text{hit}}(R_{\text{fit}}) \geq m(R_{\text{fit}}/R_{\text{AV}})^3 + N_{\text{hit}}(0)$ and the expected number of accidental coincidences contributing as a background to the electron antineutrino analysis. Another way of looking at this is we want to calculate the accidental coincidence rates for a range of $N_{\text{hit}}(0)$ values and then choose the $N_{\text{hit}}(0)$ value that keeps the accidental coincidence background rate at an acceptable level.

13.2 The Theory of Accidental Coincidences

Knoll [133] gives an exposition of the theory of accidental coincidences of randomly occurring events. Knoll begins by discussing the accidental coincidence of two events which are drawn from distributions of randomly occurring events with given mean rates. Knoll refers to these as the mean singles rates r_1 and r_2 . At each starting pulse (i.e. one of the events from the first distribution), the probability that a time interval of length t will elapse without a stop pulse (i.e. an event from the second distribution) is given by e^{-tr_2} . Also, the differential probability of a stop pulse arriving within the next differential time dt is just $r_2 dt$. Since both of these two independent events must occur for there to be a coincidence, the overall differential probability of generating such an interval dt about t is $e^{-tr_2} \cdot r_2 dt$. The differential coincidence rate is then $r_1 \cdot e^{-tr_2} \cdot r_2 dt$. Thus for the coincidence of 2 events in a time window, t_w , the coincidence rate is

$$r_{\text{acc.,2}} = \int_0^{t_w} r_1 r_2 e^{-tr_2} dt \quad (13.1)$$

$$\rightarrow r_1 r_2 t_w \quad (\text{for } t_w r_2 \ll 1) \quad (13.2)$$

Knoll's formalism can be generalized to multiple event coincidences so long as the participating events occur independently of one another. The formula for a three fold event coincidence is

$$r_{\text{acc.,3}} = \int_0^{t_w^{(3)}} \left[\int_0^{t_w^{(2)}} r_1 r_2 e^{-t^{(2)} r_2} dt^{(2)} \right] r_3 e^{-t^{(3)} r_3} dt^{(3)} \quad (13.3)$$

$$\longrightarrow r_1 r_2 r_3 t_w^{(2)} t_w^{(3)} \quad \left(\text{for } t_w^{(2)} r_2 \ll 1, t_w^{(3)} r_3 \ll 1 \right) \quad (13.4)$$

The superscripts ⁽²⁾ and ⁽³⁾ distinguish the separate variables of integration of the two *independent* integrals. The independence of these integrals reflects the fact that the events are independent, being drawn from separate random distributions. It is clear that the integral inside of the brackets in equation (13.3) is just $r_{\text{acc.,2}}$ and acts like r_1 does in equation (13.1). It remains to be seen if the approximation $t_w r \ll 1$ will hold. With expected time windows of tenths to hundredths of a second and a detector rate of approximately 20 Hz, it is clear the approximation is invalid. However, if instrumental cuts on the data reduce the number of selected events down to the order of 10 thousand per live year, then the approximation will be adequate. Finally, in this analysis only a single time window, t_w , is used to extract coincidences from the data set, thus $t_w = t_w^{(2)} = t_w^{(3)}$ throughout.

13.3 Determining the Accidental Coincidence Rate and Selecting $N_{\text{hit}}(0)$

To apply the results of Section 13.2 several pieces of information are needed:

- Choose a value for the coincidence time window, t_w .
- Define the event selection criterion.
- Determine the rate of events *fulfilling* the event selection criterion.

The first item, a choice of t_w , was decided upon in Chapter 11 and presented in Table 11.1. For the second item, instead of choosing a single event selection criterion, three different event selection criteria are presented. The first of these three event selection criteria, the Standard analysis, is based upon the event selection criterion presented in SNO's published papers [10, 11]. The second and third event selection criteria are essentially the same Enlarged analysis that this dissertation is focused on presenting, the difference being whether or not the event selection is further narrowed to primarily identify neutrons. Thus these two slightly different Enlarged analyses are referred to as the e^+ -Enlarged and n -Enlarged event selection criteria. For the third item, the rate of events *fulfilling* the event selection criteria are determined by two methods for each phase of the experiment. The first method is simply the total number of events fulfilling the event selection criterion divided by the total time the experiment was live to electron antineutrinos (the livetime). The second method fits an exponential to the distribution of the time intervals between events fulfilling the event selection criterion, thus determining a mean event rate.

As already stated three different event selection criteria are presented here, namely the Standard analysis, the e^+ -Enlarged analysis, and the n -Enlarged analysis. To explicitly define the accidental coincidence rates

for these three analyses, define r_i as the experimentally determined rate of events fulfilling the event selection criterion for a given analysis, i , where i is one of the three analyses: (S \equiv Standard), (e^+ -E \equiv e^+ -Enlarged), or (n -E \equiv n -Enlarged)¹. The accidental coincidence rates for the three analyses are then written as

$$r_{\text{acc.,2}} = r_1 r_2 t_w \longrightarrow (r_S)^2 t_w \quad (13.5)$$

$$\longrightarrow (r_{e^+-E})^2 t_w \quad (13.6)$$

$$\longrightarrow (r_{e^+-E})(r_{n-E}) t_w \quad (13.7)$$

and

$$r_{\text{acc.,3}} = r_1 r_2 r_3 t_w^2 \longrightarrow (r_S)^3 t_w^2 \quad (13.8)$$

$$\longrightarrow (r_{e^+-E})^3 t_w^2 \quad (13.9)$$

$$\longrightarrow (r_{e^+-E})(r_{n-E})^2 t_w^2 \quad (13.10)$$

Finally, recall there are two methods used to determine the experimental mean event rate, r_i . The first method divides the total number of events fulfilling the selection criterion, N , by the total livetime, t_{live} , from which the events were chosen. The second method fits an exponential to the distribution of time intervals between events fulfilling the event selection criterion. This fitting method gives the mean rate, $\langle r_{\text{fit}} \rangle$. Thus r_i in equations (13.5) - (13.10) is replaced by either of two forms depending on the method used to determine the mean experimental rate:

$$r_i = \left[\frac{N}{t_{\text{live}}} \right]_i \pm \left[\frac{\sqrt{N}}{t_{\text{live}}} \right]_i \quad (13.11)$$

or

$$r_i = \langle r_{\text{fit}} \rangle_i \pm \sigma_{\langle r_{\text{fit}} \rangle_i} \quad (13.12)$$

The experimental errors are shown noting that the fitting routine provides $\sigma_{\langle r_{\text{fit}} \rangle_i}$.

13.3.1 The Accidental Coincidence Rate in the Pure D₂O Phase

The entire Pure D₂O phase data set (Appendix A) was analyzed to determine the total number of events, N , present in each of the three analysis selection windows from which a mean event rate is calculated, $r_i = [N/t_{\text{live}}]_i$. The parameters defining the presence of an event in any of the three analysis selection

¹ Please note the identifiers e^+ -Enlarged and n -Enlarged are used in two slightly different ways. Initially each refers to a different event selection criterion. For example, in general $r_{e^+-E} \neq r_{n-E}$. The r_i are then multiplied together to determine the accidental coincidence rates. It should be clear that a formula containing *only* r_{e^+-E} is referred to as a e^+ -Enlarged analysis value. However, an equation containing *both* r_{e^+-E} and r_{n-E} is referred to as a n -Enlarged analysis value to signify that the following events in the coincidence are required to be "most neutron like". Equation (13.7) is an example of a n -Enlarged analysis value. It is perhaps also useful to note that the events in a Standard analysis are a subset of those in a n -Enlarged analysis. Likewise the events in a n -Enlarged analysis are a subset of the events in a e^+ -Enlarged analysis.

windows is given in Table 13.1. The Standard window is based upon parameters used in the SNO Pure

Table 13.1: Event selection criterion for accidental coincidence rates in the Pure D₂O phase.

Analysis Type	Max R_{fit} (cm)	Max N_{hit}	Minimum N_{hit}	ITR Range	θ_{ij} Range
Standard	550	150	$N_{\text{hit}}(0)$	(0.55,0.95)	(0.75,1.45)
e^+ -Enlarged	600	150	$9.2 \left(\frac{R_{\text{fit}}}{R_{\text{AV}}}\right)^3 + N_{\text{hit}}(0)$	(0.55,0.95)	-
n -Enlarged	600	90	$9.2 \left(\frac{R_{\text{fit}}}{R_{\text{AV}}}\right)^3 + N_{\text{hit}}(0)$	(0.55,0.95)	-

D₂O publications. The e^+ -Enlarged and n -Enlarged windows are intended as optimized to detect positrons or neutrons, respectively, and are one of the main analysis focuses of this dissertation. A DAMN mask = 45182945 was used for all random rate analyses to remove instrumental events. The ITR and θ_{ij} analysis cuts are introduced and discussed in Chapter 14. The number of events satisfying each analysis window are presented as a function of $N_{\text{hit}}(0)$ in Table 13.2. As the number of events satisfying each analysis window

Table 13.2: The number of events satisfying the selection criterion in the Pure D₂O phase. Note that the “-” entries are not shown because they are not valid for all run ranges, as described in the text.

$N_{\text{hit}}(0)$	Standard	Enlarged		$N_{\text{hit}}(0)$	Standard	Enlarged	
		e^+	n			e^+	n
25	-	-	-	38	4242	4461	4055
26	-	-	-	39	4013	4281	3875
27	-	-	-	40	3816	4107	3701
28	47752	16435	16029	41	3660	3950	3544
29	31286	12849	12443	42	3502	3782	3376
30	21281	10214	9808	43	3368	3638	3232
31	14856	8500	8094	44	3248	3493	3087
32	10955	7284	6878	45	3133	3364	2958
33	8461	6412	6006	46	3035	3235	2829
34	6842	5794	5388	47	2921	3100	2694
35	5799	5309	4903	48	2822	2992	2586
36	5088	4959	4553	49	2719	2889	2483
37	4598	4675	4269	50	2616	2773	2367

were counted the time between accepted events was histogrammed. From these histograms the average event rate can be determined from a fit. A sub-set of these fits is presented in Figures 13.1, 13.2 & 13.3. To determine the number of accidental events present in the data set, the total time the detector was taking data is needed. The Pure D₂O phase data set presented here has a live time of $t_{\text{live}}^{\text{D}_2\text{O}} = 311.41$ days (312.93 raw days - (131305s + 37285000ns)) [156]. The time subtracted is due to dead time imposed by the analysis cut defined in Section 14.1.

From the results of Table 13.3 and the equations presented in Section 13.3, we can determine the accidental coincidence rate at each $N_{\text{hit}}(0)$ value. Recall from Chapter 11 that the coincidence time windows, t_w , are 150 ms and 250 ms for the Standard and Enlarged analyses, respectively. For brevity, only three accidental coincidence rates are reported here, one each for the Standard, e^+ -Enlarged, and n -Enlarged analyses. To determine the total number of accidental coincidences in the analyzed data set, simply multiply by the livetime of the data set. The results are given in Table 13.4.

Table 13.3: Mean event rates in the D₂O phase. See Section 13.3.3 for the error on the average rate.

Analysis	$N_{\text{hit}}(0)$	$[N/t_{\text{live}}]$ (mHz)	$\langle r_{\text{fit}} \rangle$ (mHz)	Average Rate (mHz)
Standard	45	0.1164 ± 0.0021	0.1207 ± 0.0038	0.1186 ± 0.0059
e^+ -Enlarged	30	0.3796 ± 0.0038	0.4232 ± 0.0056	0.4014 ± 0.0274
n -Enlarged	30	0.3645 ± 0.0037	0.4075 ± 0.0057	0.3860 ± 0.0272

Table 13.4: The accidental coincidence rates in the Pure D₂O phase. The values listed under (D₂O) are the actual number of expected coincidences in the Pure D₂O data set.

Analysis Type	Ave. Rate (mHz)	t_w (ms)	$r_{\text{acc.,2}}$ (nHz)	$r_{\text{acc.,3}}$ (nHz)	$N_{\text{acc.,2}}$		$N_{\text{acc.,3}}$	
					(yr ⁻¹)	(D ₂ O)	(yr ⁻¹)	(D ₂ O)
Standard	0.1186	150	2.110	$3.753 \cdot 10^{-5}$	0.067	0.057	$1.18 \cdot 10^{-6}$	$1.01 \cdot 10^{-6}$
e^+ -Enlarged	0.4014	250	40.28	$4.042 \cdot 10^{-3}$	1.27	1.08	$1.28 \cdot 10^{-4}$	$1.09 \cdot 10^{-4}$
n -Enlarged	0.3860	250	37.25	$3.595 \cdot 10^{-3}$	1.18	1.00	$1.13 \cdot 10^{-4}$	$0.97 \cdot 10^{-4}$

13.3.2 The Accidental Coincidence Rate in the Salt Phase

The entire first salt data set (Appendix A) is used in this analysis. The analysis regions presented for the Salt phase have similar definitions and goals as those described for the Pure D₂O phase as described in Section 13.3.1. The parameters defining the presence of an event in any of the three analysis selection windows is given in Table 13.5. The β_{14} analysis cut is introduced and discussed in Chapter 14. The Salt phase

Table 13.5: Event selection criterion for accidental coincidence rates in the Salt phase.

Salt Analysis Type	Max R_{fit} (cm)	Max N_{hit}	Minimum N_{hit}	ITR Range	β_{14} Range
Standard	550	150	$N_{\text{hit}}(0)$	(0.55,0.95)	(-0.12,0.95)
e^+ -Enlarged	600	150	$8.45 \left(\frac{R_{\text{fit}}}{R_{\text{AV}}}\right)^3 + N_{\text{hit}}(0)$	(0.55,0.95)	-
n -Enlarged	600	90	$8.45 \left(\frac{R_{\text{fit}}}{R_{\text{AV}}}\right)^3 + N_{\text{hit}}(0)$	(0.55,0.95)	-

Table 13.6: The number of events satisfying the selection criterion in the Salt phase.

$N_{\text{hit}}(0)$	Standard	Enlarged		$N_{\text{hit}}(0)$	Standard	Enlarged	
		e^+	n			e^+	n
25	82135	19572	19403	38	3884	4475	4306
26	48366	14645	14476	39	3763	4295	4126
27	29421	11481	11312	40	3630	4139	3970
28	18804	9519	9350	41	3517	3987	3818
29	12656	8135	7966	42	3406	3852	3683
30	9193	7168	6999	43	3281	3695	3526
31	7229	6477	6308	44	3171	3531	3362
32	6030	5972	5803	45	3071	3369	3200
33	5275	5610	5441	46	2978	3212	3043
34	4822	5295	5126	47	2863	3050	2881
35	4499	5066	4897	48	2758	2881	2712
36	4251	4846	4677	49	2638	2735	2566
37	4036	4656	4487	50	2517	2575	2406

event-to-event times are histogrammed in Figures 13.4, 13.5 & 13.6. From the results of Table 13.7 and the equations presented in Section 13.3, the accidental coincidence rate can be determined at each $N_{\text{hit}}(0)$ value. Recall from Chapter 11 that the coincidence time windows, t_w , are 20 ms and 35 ms for the Standard and Enlarged analyses, respectively. The Salt phase livetime is $t_{\text{live}}^{\text{Salt}} = 258.624$ days (258.792 raw days - (14501s + 631782500ns)) [107]. The time subtracted is due to dead time imposed by the analysis cut defined in Section 14.1. The results are given in Table 13.8.

Table 13.7: Mean event rates in the Salt phase. See Section 13.3.3 for the error on the average rate.

Analysis	$N_{\text{hit}}(0)$	$[N/t_{\text{live}}]$ (mHz)	$\langle r_{\text{fit}} \rangle$ (mHz)	Average Rate (mHz)
Standard	40	0.1625 ± 0.0027	0.1702 ± 0.0041	0.1663 ± 0.0080
e^+ -Enlarged	25	0.8759 ± 0.0063	0.8874 ± 0.0072	0.8817 ± 0.0129
n -Enlarged	25	0.8683 ± 0.0062	0.8800 ± 0.0073	0.8741 ± 0.0132

Table 13.8: The accidental coincidence rates in the Salt phase. The values listed under (Salt) are the actual number of expected coincidences in the Salt data set.

Analysis Type	Ave. Rate (mHz)	t_w (ms)	$r_{\text{acc.,2}}$ (nHz)	$r_{\text{acc.,3}}$ (nHz)	$N_{\text{acc.,2}}$		$N_{\text{acc.,3}}$	
					(yr^{-1})	(Salt)	(yr^{-1})	(Salt)
Standard	0.1663	20	0.553	$1.84 \cdot 10^{-6}$	0.0175	0.0124	$5.81 \cdot 10^{-8}$	$4.11 \cdot 10^{-8}$
e^+ -Enlarged	0.8817	35	27.2	$8.40 \cdot 10^{-4}$	0.859	0.608	$2.65 \cdot 10^{-5}$	$1.88 \cdot 10^{-5}$
n -Enlarged	0.8741	35	26.7	$8.18 \cdot 10^{-4}$	0.844	0.598	$2.58 \cdot 10^{-5}$	$1.83 \cdot 10^{-5}$

13.3.3 Disagreement Between the Event-Counting and Fit Detector Rates

The calculated average event rates and the event rates determined from fits to the event-to-event time separations presented in Tables 13.3 & 13.7 do not agree. As noted in the SNO Antineutrino Unified Document [139], the random rate of singles is time dependent during the Pure D₂O phase. In general the rate decreases over time. A slowly varying downward drift in the mean event rate will produce just the sort of non-exponential distribution seen in Figures 13.1 – 13.6. There are two ways to deal with this situation:

- Sub-divide the data set, determine rates and background counts per sub-division and add sub-division results to obtain a result for the data set.
- Determine a mean rate with an appropriately “large” error assignment.

A re-analysis was performed on the Pure D₂O phase by dividing the data into 31 sub-sets of approximately 10 days of detector “live” time (opposed to 10 calendar days). This revealed the time dependent rate previously indicated. Unfortunately the fits to event-to-event time separations were unreliable due to a low number of valid pairs of events. Dividing the Pure D₂O phase data set into fewer sub-sets would perhaps improve the fit results, though at the same time increasing the “live” duration of a particular sub-set also dilutes the fit because the rate *is* varying. In future studies it is recommended that mean detector event rate be determined by event counts solely and a total background rate determined for short “live” durations. The total background is then just the direct sum of the sub-set’s background counts.

In this study, the second method is used to convert the previously obtained data into a reasonable background estimate with uncertainty. Thus, the event rate used to determine the background rate of accidental coincidences is simply the average of the random rates determined by the two methods of event counting and fitting to event-to-event times. The uncertainty is determined by calculating the maximum spread allowed by the two event rate measurements. For example, from Table 13.3 for the Pure D₂O phase, the e^+ -Enlarged analysis has $[N/t_{\text{live}}] = 0.3796 \pm 0.0038$ and $\langle r_{\text{fit}} \rangle = 0.4232 \pm 0.0056$. The former value gives the lower bound $0.3796 - 0.0038 = 0.3758$ while the latter value gives the upper bound $0.4232 + 0.0056 = 0.4288$. The average value is 0.4014 thus the maximum spread is given by the upper bound $0.4288 - 0.4014 = 0.0274$. Thus, the Pure D₂O phase, e^+ -Enlarged analysis will assume a mean random event rate of 0.4014 ± 0.0274 . The average rates and uncertainties are reported in Tables 13.3 & 13.7. The largest uncertainty produced by this method is 7% of the average random event rate.

13.4 Conclusions

This chapter answered the following two questions with Tables 13.3, 13.4, 13.7, & 13.8 for each of the analyses and phases of the experiment.

- Determined the $N_{\text{hit}}(0)$ value for the Standard and Enlarged analyses.
- Determined the accidental coincidence rate for the Standard and Enlarged analyses.

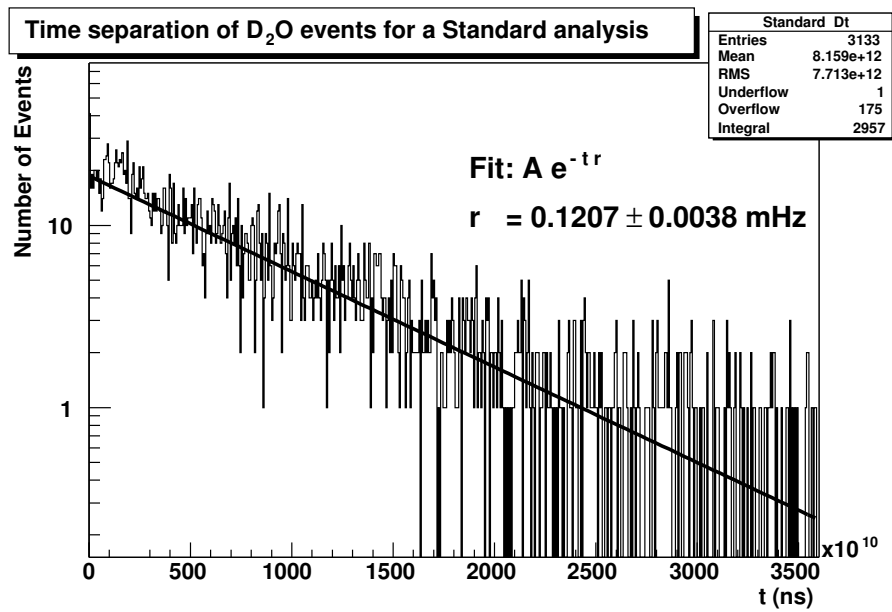


Figure 13.1: Fitting the mean event rate in the Pure D₂O phase Standard window.

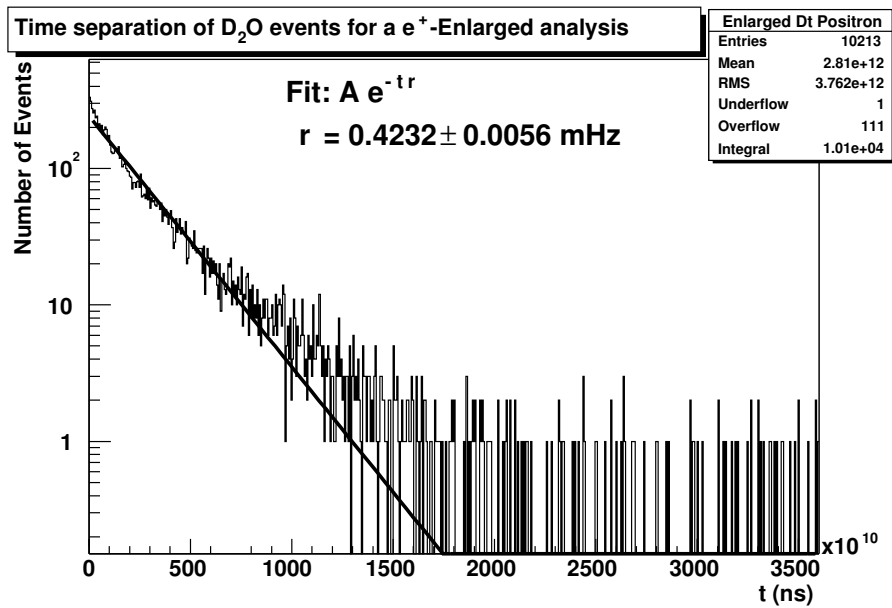


Figure 13.2: Fitting the mean event rate in the Pure D₂O phase e⁺-Enlarged window.

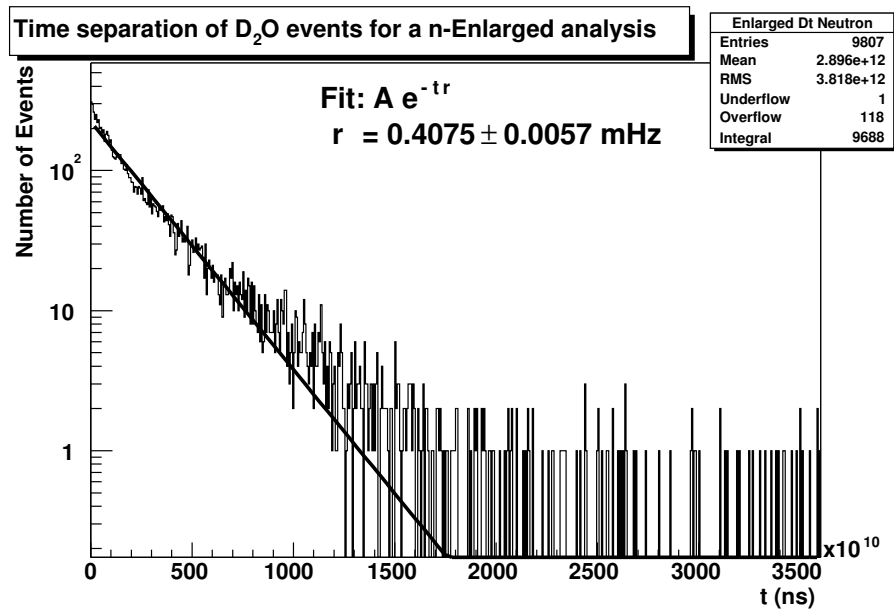


Figure 13.3: Fitting the mean event rate in the Pure D₂O phase *n*-Enlarged window.

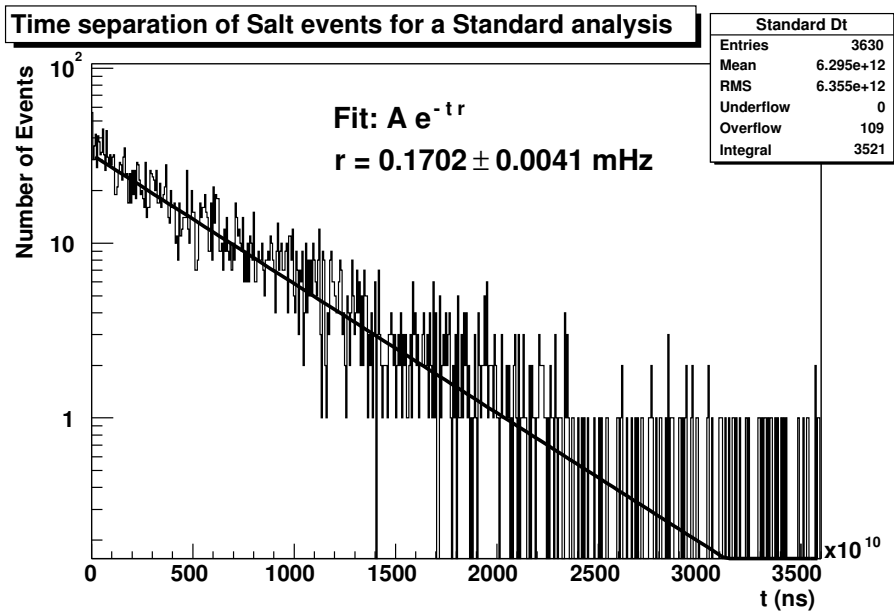


Figure 13.4: Fitting the mean event rate in the Salt phase Standard window.

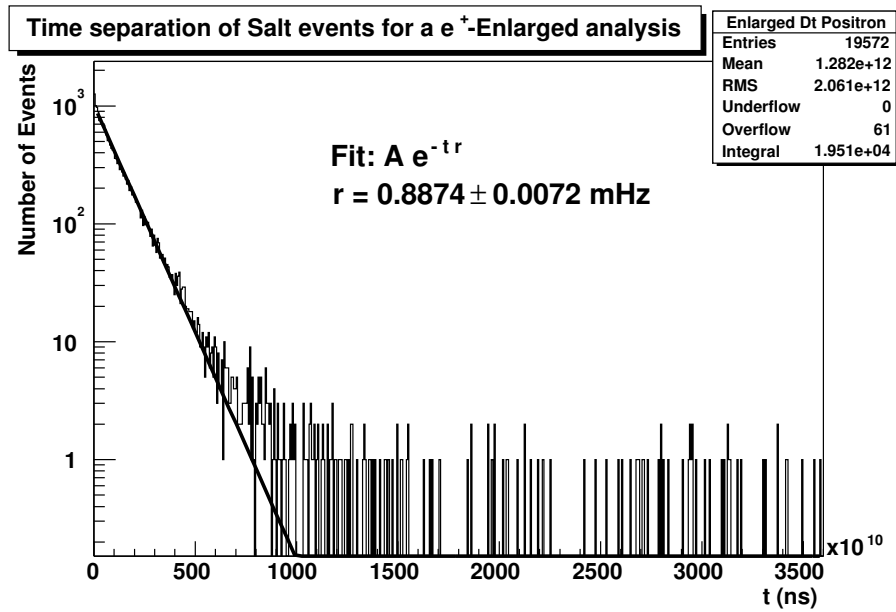


Figure 13.5: Fitting the mean event rate in the Salt phase e^+ -Enlarged window.

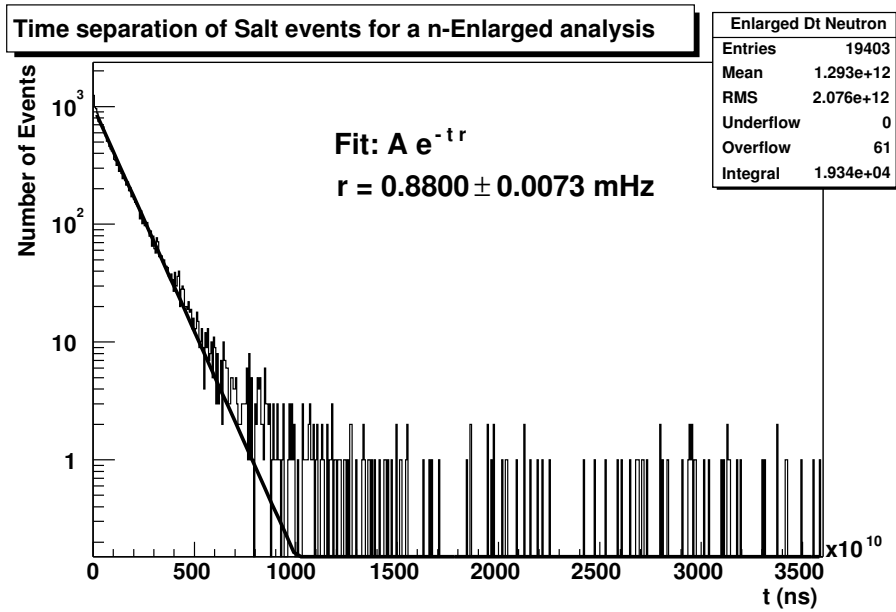


Figure 13.6: Fitting the mean event rate in the Salt phase n -Enlarged window.

Chapter 14

ADDITIONAL ANALYSIS CUTS

In the preceding chapters of Part III, a number of analysis cuts were developed for use in the electron antineutrino analysis. This section explains a few additional cuts used in the electron antineutrino analysis chosen to assist in the selection of Čerenkov events of interest to the electron antineutrino search.

14.1 A Maximum N_{hit} Value — $N_{hit} < 150$

As this dissertation is primarily focused on a search for *solar* electron antineutrinos, it is reasonable to impose a maximum event energy as well as a minimum event energy. This energy range is the window in which one would expect to find positrons produced by solar electron antineutrinos with a ${}^8\text{B}$ spectrum having an end point near 14 MeV. As is shown in Chapter 16 all positrons produced assuming a ${}^8\text{B}$ spectrum will have less than $150 N_{hit}$, which corresponds to an electron of ≈ 17.5 MeV [116]. Thus, in both the Pure D_2O and Salt phases, only events with less than $150 N_{hit}$ are considered as events possibly produced from a $\overline{\text{CC}}$ interaction in the SNO detector.

The choice of a maximum N_{hit} value of 150 has a second use and consequence. Since no positron is expected to have an N_{hit} value greater than 150, any case where there is an event with $N_{hit} > 150$ which is then followed (i.e. in coincidence) by additional physics events, should *not* be considered in the search for an *solar* electron antineutrino signal. Thus, when the extraction of coincidences from the data sets is done, all events following *any* event with more the 150 N_{hit} are excluded from consideration for the electron antineutrino analyses. The duration of time chosen for this exclusion period is twice that of the Enlarged coincidence window, or approximately 12 to 14 times the mean neutron capture time. The duration of the exclusion periods are 500 ms for the Pure D_2O phase and 70 ms for the Salt phase. These periods of exclusion eliminate coincidence backgrounds coming from cosmic-ray muons and atmospheric neutrino interactions in or around the SNO detector¹.

14.2 The Choice of R_{fit} — $R_{fit} < 550$ cm and $R_{fit} < 600$ cm

There are two analyses presented in this dissertation, the Standard Region and the Enlarged Region. The Standard Region only considers events with a reconstructed radial position, R_{fit} , less than 550 cm. This choice is made so that the Standard Region's analysis cuts are nearly the same as the analysis cuts of SNO's solar neutrino results [10, 12]. The choice of $R_{fit} < 550$ cm is based upon both background reduction and lowered systematic uncertainties coming from the reconstruction algorithms inside that radius. The $R_{fit} < 550$ cm requirement is the same for both the Pure D_2O and Salt phases of the SNO experiment.

¹Those familiar with SNO analyses should recognize this cut replaces the muon, muon follower, and missed muon follower cuts.

The Enlarged Region analysis, the thrust of this dissertation, takes the position that the coincidence detection nature of \overline{CC} interactions will allow a full use of the heavy water region as the analysis fiducial volume. Increasing the volume will significantly increase the detection efficiency of electron antineutrinos. This is demonstrated in the forthcoming Chapter 16. Thus, for the Enlarged analysis, those events with a reconstructed radial position, R_{fit} , less than 600 cm are considered in the search for \overline{CC} induced coincidences. The acrylic vessel separating the heavy water region from the light water region is located at 600 cm. It is expected that there is a systematic uncertainty of several percent in the reconstructed radial positions at these large radii. This difficulty is mitigated by the nature of the analysis presented. Once a maximum R_{fit} choice is made, all the detection efficiencies and background estimates are made with respect to that choice. Thus, the only way in which the analysis can fail is due to a degradation of the signal-to-background ratio.

14.3 “High-Level” Cuts — ITR , θ_{ij} , and β_{14}

Appendix B presents a suite of analysis cuts used to eliminate instrumental background events with low sacrifice of physics events of interest. A second class of analysis cuts were developed which attempted instead to select only those events which have a high likelihood of being true Čerenkov physics events. This second class of cuts is referred to as “high-level” cuts. This section briefly details only those high-level cuts used in the analyses presented in this dissertation.

14.3.1 The In-Time Ratio (ITR)

The In-Time Ratio (ITR) [116, 157] value is determined by taking the ratio of the number of PMTs firing in a time window, $[-2.5 \text{ ns}, +5 \text{ ns}]$, around the prompt light peak to the total number of PMTs firing in the event (485 ns long). If all the Čerenkov light produced by an event either fires a PMT or is absorbed (i.e. no reflections in the detector) the ITR value will nearly equal 1.0. That is, all the light is prompt light. The other extreme is produced by a constant light source in the detector. In this case the ITR value is approximately equal to the ratio of the widths of the time windows: $(7.5 \text{ ns}) / (485 \text{ ns}) \simeq 0.015$. In this way it is possible to distinguish real Čerenkov events from other light sources. Based upon the studies done for SNO’s solar neutrino analysis [9, 10, 11, 116, 157] every event considered for acceptance as a physics event must fulfill the following ITR criterion:

$$0.55 < ITR < 0.95 \tag{14.1}$$

14.3.2 Event Isotropy Measures — θ_{ij} and β_{14}

Another method for identifying events produced by real Čerenkov light is to consider the isotropy of the fired PMTs in the detector’s physical coordinate space. In other words, does the distribution of fired PMTs inside the detector resemble a Čerenkov light cone or is the light isotropically distributed and not projected in any one particular direction? The following two parameters, θ_{ij} and β_{14} , are used in the Pure D_2O and Salt phases of the experiment, respectively. Note that the event isotropy measures are only used in the Standard Analysis. The Enlarged analysis does not use event isotropy measures, because of concerns that the event isotropy distributions may change for events having “large” ($R_{\text{fit}} > 550 \text{ cm}$) radial fit positions.

θ_{ij} in the Pure D_2O Phase

One measure of an event's isotropy is to take a simple average, $\bar{\theta}$, of the angle between all pairs of fired PMTs in the event. This is defined via the equation

$$\bar{\theta} = \frac{1}{(N_{\text{hit}})^2} \sum_{i,j < i} \theta_{ij} \quad (14.2)$$

Note that while it is the value of $\bar{\theta}$ that is used to make analysis cuts on events, this parameter is *still* referred to as the θ_{ij} parameter. This should cause no confusion as the name " θ_{ij} " reminds us that this is "the average angle between all PMT pairs, i and j ". Based upon the studies done for SNO's solar neutrino analysis [9, 10, 11, 116, 157] every event considered for acceptance as a physics event *in the Pure D_2O phase* must fulfill the following θ_{ij} criterion:

$$0.75 < \bar{\theta} < 1.45 \quad (14.3)$$

 β_{14} in the Salt Phase

The β_{14} parameter is the name give to a particular linear combination of the discrete representations of the fired PMTs inside the detector using spherical harmonics, $Y_{l,m}$'s. The linear combination is

$$\beta_{14} \equiv \beta_1 + 4\beta_4 \quad (14.4)$$

where the discrete harmonic parameters β_1 and β_4 are described in Refs. [84, 83, 66]. Note that β_1 and β_4 are complicated functions of the cosine of the angle between pairs of fired PMTs, $\beta_1 \rightarrow \beta_1(\cos \theta_{ij})$ and $\beta_4 \rightarrow \beta_4(\cos \theta_{ij})$, where θ_{ij} is defined in the preceding paragraph. Based upon the studies done for SNO's solar neutrino analysis [12, 84, 83] every event considered for acceptance as a physics event *in the Salt phase* must fulfill the following β_{14} criterion:

$$-0.12 < \beta_{14} < 0.95 \quad (14.5)$$

Chapter 15

\overline{CC} DETECTION EFFICIENCY - THEORY

15.1 Introduction

This chapter presents the concepts needed to understand the \overline{CC} detection efficiency in the SNO experiment. The numerical detection efficiencies are calculated from Monte Carlo and discussed in Chapter 16. This chapter has two major goals. The first is to demonstrate the importance of understanding the effect of radial dependent detection efficiencies in *any* multi-particle analysis. The second is to present a general and expandable analytic approach to understanding and calculating the \overline{CC} detection efficiency based on the notion of an *outcome equation*. The utility provided in the latter is multi-fold as it allows one to calculate the \overline{CC} detection efficiency for different scenarios:

- When there are measured single-particle detection efficiencies (e.g. neutrons).
- When the radial dependence of the detection efficiency is unknown or is a minor effect.
- For quick mental calculations at the bar or on long runs.

15.2 Radius Dependent Detection Efficiencies

The efficiency for detecting any given particle generated in the SNO detector is a function of the radius at which the particle is generated. This effect is the greatest for neutrons because of the interplay between two features. First, neutrons random walk a distance before capturing on nuclei. Second, the acrylic vessel contains many protons and thus acts as an efficient neutron capture target. This induced radius dependent detection efficiency for neutrons impacts the consideration of \overline{CC} detection efficiencies.

Figure 15.1 shows three different functional dependencies of the detection efficiency on radius. The mean detection efficiencies for each curve are shown. Mean detection efficiencies are often used in SNO analyses to characterize the efficiency for detecting a given particle, usually neutrons.

15.2.1 Coincidence Detection and Radius Dependent Detection Efficiencies

Figure 15.2 shows the efficiency for detecting a coincidence of two of the same particles, generated at the same location. This is analogous to the two neutrons produced in a \overline{CC} reaction, but is also relevant for a process described by: ${}^A X(n, \gamma) {}^{A+1} X$ followed by a delayed decay ${}^{A+1} X \rightarrow {}^{A+1} Y + \beta^- + \bar{\nu}_e$. The mean coincidence detection efficiencies are reported alongside the curves on the figure. The important point is gained by comparing these mean coincidence detection efficiencies to the coincidence detection efficiencies *inferred* from the mean single-particle detection efficiencies. This quantitative comparison is facilitated by the

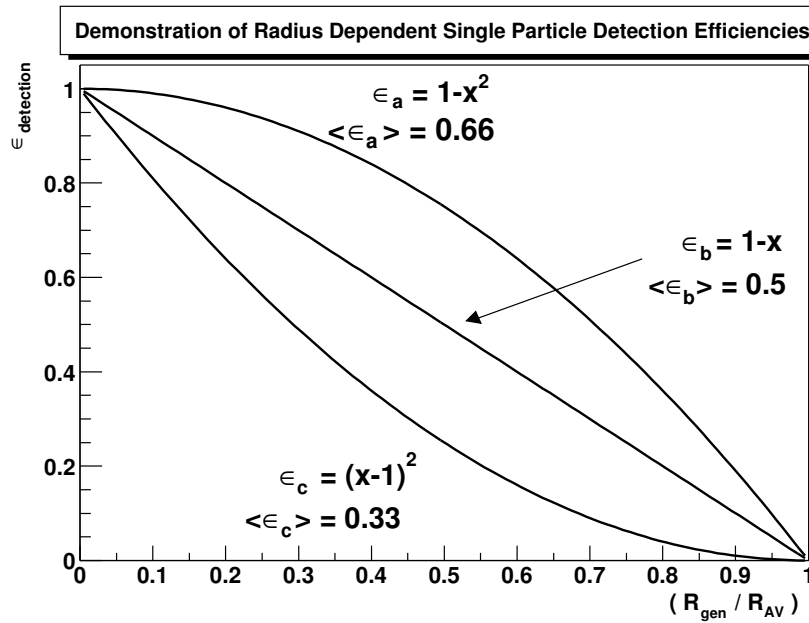


Figure 15.1: Different functional forms for radius-dependent, single-particle detection efficiencies.

values in the comparison box of Figure 15.2. These results demonstrate the importance of avoiding reliance on single particle detection efficiencies to infer coincidence detection efficiencies.

15.3 The Outcome Equation

Something must happen to each of the three particles produced in the $\overline{\text{CC}}$ interaction. Thus for a single $\overline{\text{CC}}$ interaction, $\mathbf{1}_{\overline{\text{CC}}}$, the outcome equation is

$$\mathbf{1}_{\overline{\text{CC}}} = \{\mathbf{1}_{e^+} \cdot \mathbf{1}_n \cdot \mathbf{1}_n\} \quad (15.1)$$

The bold $\mathbf{1}$'s are numerically equal to unity and represent all possible outcomes for each sub-scripted particle. By expanding each of these unitary "place holders" one is able to reliably extract the terms which contribute the total detection efficiency for the $\overline{\text{CC}}$ reaction. This methodical approach is applicable to dealing with any multi-particle event, simply by changing the subscripts and then expanding appropriately.

15.3.1 The Positron Outcome Equation

The positron will either be measured or not measured. Representing the positron detection efficiency by ϵ_{e^+} , the outcome equation for the positron is simple:

$$\mathbf{1}_{e^+} = \epsilon_{e^+} + (1 - \epsilon_{e^+}) \quad (15.2)$$

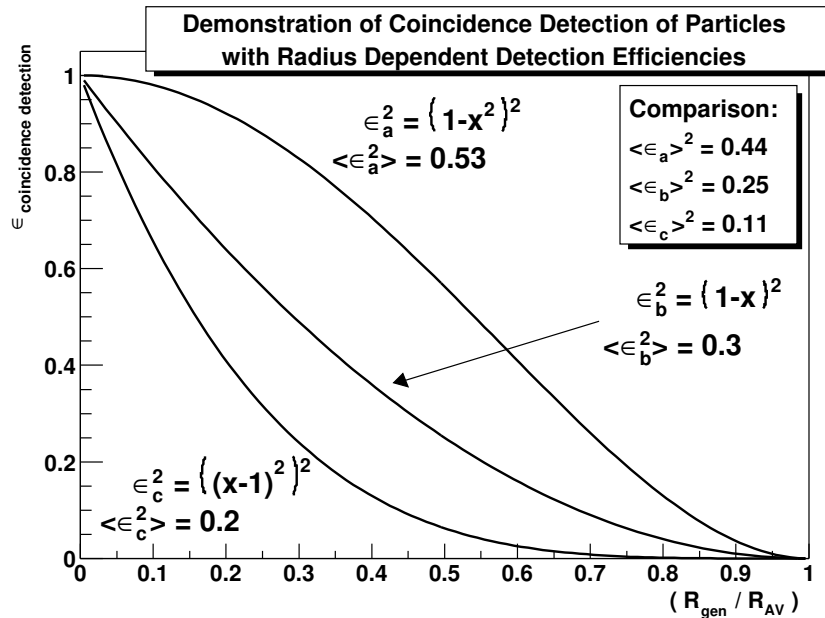


Figure 15.2: The effect of radius dependent single particle detection efficiencies on coincidence detection efficiencies. In all cases the actual coincidence detection efficiency is greater than the naive value inferred from the single particle detection efficiency.

The value of ε_{e^+} depends predominately on the electron antineutrino energy spectrum. Chapter 16 calculates ε_{e^+} for various analysis scenarios a solar ^8B neutrino spectrum is assumed for the electron antineutrinos.

15.3.2 The Neutron Outcome Equation

There are a great number of possible outcomes for a neutron produced in SNO's heavy water. Furthermore, a formulation is needed which is applicable to each of the three phases of the SNO experiment. Begin by considering the nuclei upon which neutrons may capture. There are three categories of nuclei in this regard:

- Neutron capture on deuterons.
- Neutron capture on some other nucleus *which can produce a measurable signal*.
- Neutron capture on nuclei which do not produce measurable signals.

This categorization is based upon separating which nuclei will allow SNO to detect the presence of a neutron from those which will not. The middle item thus accounts for either ^{35}Cl in the Salt phase or ^3He in the NCD phase. Each item is represented by a corresponding term in the outcome equation for the neutron:

$$\mathbf{1}_n = \varepsilon_n^{\text{cap,d}} + \varepsilon_n^{\text{cap,N}} + \left(1 - (\varepsilon_n^{\text{cap,d}} + \varepsilon_n^{\text{cap,N}})\right) \quad (15.3)$$

The term $\varepsilon_n^{\text{cap,d}}$ is the efficiency for a neutron generated in the heavy water volume to capture on a deuterium nucleus. The term $\varepsilon_n^{\text{cap,N}}$ is the efficiency for a neutron generated in the heavy water volume to capture on some other nucleus *which can produce a measurable signal*. That is, $\varepsilon_n^{\text{cap,N}}$ is the efficiency for the neutron to capture on ^{35}Cl or in the NCDs, depending on the phase of the SNO experiment. In the Pure D_2O phase $\varepsilon_n^{\text{cap,N}} = 0$.

Note in equation (15.3) that the last term, $(1 - (\varepsilon_n^{\text{cap,d}} + \varepsilon_n^{\text{cap,N}}))$, is the efficiency for the neutron to capture on a nucleus which does not produce a measurable signal. One example of this is the capture of neutrons on hydrogen nuclei. The capture of a neutron on a proton produces a 2.2 MeV gamma ray. This gamma-ray *does* actually produce measurable light in SNO. However, for this and many other cases, the signal produced is expected to be below the energy threshold imposed in the electron antineutrino analysis. Thus, capture on protons is included in this last term. It will, however, be important to return to this point later to determine if the neutron signal has any component not correctly accounted for in the above scheme.

Equation (15.4a) takes into account that once the neutron captures on a particular nucleus, there is an additional efficiency associated with the measurement of the capture.

$$\mathbf{1}_n = \varepsilon_n^{\text{cap,d}} \left(\varepsilon_n^{\text{meas,d}} + (1 - \varepsilon_n^{\text{meas,d}}) \right) + \varepsilon_n^{\text{cap,N}} \left(\varepsilon_n^{\text{meas,N}} + (1 - \varepsilon_n^{\text{meas,N}}) \right) + \left(1 - (\varepsilon_n^{\text{cap,d}} + \varepsilon_n^{\text{cap,N}}) \right) \quad (15.4a)$$

$$= \varepsilon_n^{\text{cap,d}} \varepsilon_n^{\text{meas,d}} + \varepsilon_n^{\text{cap,N}} \varepsilon_n^{\text{meas,N}} + \left(1 - (\varepsilon_n^{\text{cap,d}} \varepsilon_n^{\text{meas,d}} + \varepsilon_n^{\text{cap,N}} \varepsilon_n^{\text{meas,N}}) \right) \quad (15.4b)$$

In both the PMT and NCD analysis this efficiency is by-in-large due to the non-zero energy thresholds used for real data analysis. The term $\varepsilon_n^{\text{meas,d}}$ is the efficiency for measuring the signal produced when the neutron has captured on a deuteron. Likewise the term $\varepsilon_n^{\text{meas,N}}$ is the efficiency for measuring the signal produced by the neutron capturing either on ^{35}Cl or in the NCDs. Henceforth the quantities $(\varepsilon_n^{\text{cap,d}} \varepsilon_n^{\text{meas,d}})$ and $(\varepsilon_n^{\text{cap,N}} \varepsilon_n^{\text{meas,N}})$ in equation (15.4b) are referred to as the efficiencies for *detecting* a neutron by capture on deuterium nuclei or on ^{35}Cl or in the NCDs.

15.3.3 The Full Outcome Equation

The following definitions simplify future equations:

$$\overline{\varepsilon_{e^+}} = (1 - \varepsilon_{e^+}) \quad (15.5a)$$

$$\overline{\varepsilon_n^{\text{cap}}} = \left(1 - (\varepsilon_n^{\text{cap,d}} + \varepsilon_n^{\text{cap,N}}) \right) \quad (15.5b)$$

$$\overline{\varepsilon_n^{\text{meas,d}}} = (1 - \varepsilon_n^{\text{meas,d}}) \quad (15.5c)$$

$$\overline{\varepsilon_n^{\text{meas,N}}} = (1 - \varepsilon_n^{\text{meas,N}}) \quad (15.5d)$$

These definitions are all efficiencies for something to *not* occur. The efficiency for the positron to *not* be detected: $\overline{\varepsilon_{e^+}}$. The efficiency for the neutron to *not* capture on a nucleus which can generate a measurable signal: $\overline{\varepsilon_n^{\text{cap}}}$. The efficiency for the neutron to *not* be measured if it captures on a deuteron: $\overline{\varepsilon_n^{\text{meas,d}}}$. The efficiency for the neutron to *not* be measured if it captures either on ^{35}Cl or in the NCDs: $\overline{\varepsilon_n^{\text{meas,N}}}$. Using these

definitions and substituting equations (15.2) & (15.4a) into equation (15.1) one arrives at:

$$N_{\overline{\text{CC}}} = N_{\overline{\text{CC}}} \left\{ \varepsilon_{e^+} + \overline{\varepsilon_{e^+}} \right\} \left\{ \varepsilon_n^{\text{cap,d}} \left(\varepsilon_n^{\text{meas,d}} + \overline{\varepsilon_n^{\text{meas,d}}} \right) + \varepsilon_n^{\text{cap,N}} \left(\varepsilon_n^{\text{meas,N}} + \overline{\varepsilon_n^{\text{meas,N}}} \right) + \overline{\varepsilon_n^{\text{cap}}} \right\}^2 \quad (15.6a)$$

$$= N_{\overline{\text{CC}}} \left[\varepsilon_{e^+} \left(\varepsilon_n^{\text{cap,d}} \varepsilon_n^{\text{meas,d}} \right)^2 + \varepsilon_{e^+} \left(\varepsilon_n^{\text{cap,N}} \varepsilon_n^{\text{meas,N}} \right)^2 + 2\varepsilon_{e^+} \left(\varepsilon_n^{\text{cap,d}} \varepsilon_n^{\text{meas,d}} \right) \left(\varepsilon_n^{\text{cap,N}} \varepsilon_n^{\text{meas,N}} \right) \right]_{\text{3-fold}} \quad (15.6b)$$

$$+ N_{\overline{\text{CC}}} \left[2\varepsilon_{e^+} \left(\varepsilon_n^{\text{cap,d}} \varepsilon_n^{\text{meas,d}} \right) \left(\varepsilon_n^{\text{cap,d}} \overline{\varepsilon_n^{\text{meas,d}}} \right) + 2\varepsilon_{e^+} \left(\varepsilon_n^{\text{cap,d}} \varepsilon_n^{\text{meas,d}} \right) \left(\varepsilon_n^{\text{cap,N}} \overline{\varepsilon_n^{\text{meas,N}}} \right) + 2\varepsilon_{e^+} \left(\varepsilon_n^{\text{cap,d}} \varepsilon_n^{\text{meas,d}} \right) \left(\overline{\varepsilon_n^{\text{cap}}} \right) \right. \\ \left. + 2\varepsilon_{e^+} \left(\varepsilon_n^{\text{cap,N}} \varepsilon_n^{\text{meas,N}} \right) \left(\varepsilon_n^{\text{cap,N}} \overline{\varepsilon_n^{\text{meas,N}}} \right) + 2\varepsilon_{e^+} \left(\varepsilon_n^{\text{cap,N}} \varepsilon_n^{\text{meas,N}} \right) \left(\varepsilon_n^{\text{cap,d}} \overline{\varepsilon_n^{\text{meas,d}}} \right) + 2\varepsilon_{e^+} \left(\varepsilon_n^{\text{cap,N}} \varepsilon_n^{\text{meas,N}} \right) \left(\overline{\varepsilon_n^{\text{cap}}} \right) \right. \\ \left. + \overline{\varepsilon_{e^+}} \left(\varepsilon_n^{\text{cap,d}} \varepsilon_n^{\text{meas,d}} \right)^2 + \overline{\varepsilon_{e^+}} \left(\varepsilon_n^{\text{cap,N}} \varepsilon_n^{\text{meas,N}} \right)^2 + 2\overline{\varepsilon_{e^+}} \left(\varepsilon_n^{\text{cap,d}} \varepsilon_n^{\text{meas,d}} \right) \left(\varepsilon_n^{\text{cap,N}} \varepsilon_n^{\text{meas,N}} \right) \right]_{\text{2-fold}} \quad (15.6c)$$

$$+ N_{\overline{\text{CC}}} \left[\varepsilon_{e^+} \left(\varepsilon_n^{\text{cap,d}} \overline{\varepsilon_n^{\text{meas,d}}} \right)^2 + \varepsilon_{e^+} \left(\varepsilon_n^{\text{cap,N}} \overline{\varepsilon_n^{\text{meas,N}}} \right)^2 + 2\varepsilon_{e^+} \left(\varepsilon_n^{\text{cap,d}} \overline{\varepsilon_n^{\text{meas,d}}} \right) \left(\varepsilon_n^{\text{cap,N}} \overline{\varepsilon_n^{\text{meas,N}}} \right) \right. \\ \left. + 2\overline{\varepsilon_{e^+}} \left(\varepsilon_n^{\text{cap,d}} \varepsilon_n^{\text{meas,d}} \right) \left(\varepsilon_n^{\text{cap,d}} \overline{\varepsilon_n^{\text{meas,d}}} \right) + 2\overline{\varepsilon_{e^+}} \left(\varepsilon_n^{\text{cap,d}} \varepsilon_n^{\text{meas,d}} \right) \left(\varepsilon_n^{\text{cap,N}} \overline{\varepsilon_n^{\text{meas,N}}} \right) + 2\varepsilon_{e^+} \left(\varepsilon_n^{\text{cap,d}} \overline{\varepsilon_n^{\text{meas,d}}} \right) \left(\overline{\varepsilon_n^{\text{cap}}} \right) \right. \\ \left. + 2\overline{\varepsilon_{e^+}} \left(\varepsilon_n^{\text{cap,N}} \varepsilon_n^{\text{meas,N}} \right) \left(\varepsilon_n^{\text{cap,d}} \overline{\varepsilon_n^{\text{meas,d}}} \right) + 2\overline{\varepsilon_{e^+}} \left(\varepsilon_n^{\text{cap,N}} \varepsilon_n^{\text{meas,N}} \right) \left(\varepsilon_n^{\text{cap,N}} \overline{\varepsilon_n^{\text{meas,N}}} \right) + 2\varepsilon_{e^+} \left(\varepsilon_n^{\text{cap,N}} \overline{\varepsilon_n^{\text{meas,N}}} \right) \left(\overline{\varepsilon_n^{\text{cap}}} \right) \right. \\ \left. + 2\overline{\varepsilon_{e^+}} \left(\varepsilon_n^{\text{cap,d}} \varepsilon_n^{\text{meas,d}} \right) \left(\overline{\varepsilon_n^{\text{cap}}} \right) + 2\overline{\varepsilon_{e^+}} \left(\varepsilon_n^{\text{cap,N}} \varepsilon_n^{\text{meas,N}} \right) \left(\overline{\varepsilon_n^{\text{cap}}} \right) + \varepsilon_{e^+} \left(\overline{\varepsilon_n^{\text{cap}}} \right)^2 \right]_{\text{1-fold}} \quad (15.6d)$$

$$+ N_{\overline{\text{CC}}} \left[\overline{\varepsilon_{e^+}} \left(\varepsilon_n^{\text{cap,d}} \overline{\varepsilon_n^{\text{meas,d}}} \right)^2 + \overline{\varepsilon_{e^+}} \left(\varepsilon_n^{\text{cap,N}} \overline{\varepsilon_n^{\text{meas,N}}} \right)^2 + 2\overline{\varepsilon_{e^+}} \left(\varepsilon_n^{\text{cap,d}} \overline{\varepsilon_n^{\text{meas,d}}} \right) \left(\varepsilon_n^{\text{cap,N}} \overline{\varepsilon_n^{\text{meas,N}}} \right) \right. \\ \left. + 2\overline{\varepsilon_{e^+}} \left(\varepsilon_n^{\text{cap,d}} \overline{\varepsilon_n^{\text{meas,d}}} \right) \left(\overline{\varepsilon_n^{\text{cap}}} \right) + 2\overline{\varepsilon_{e^+}} \left(\varepsilon_n^{\text{cap,N}} \overline{\varepsilon_n^{\text{meas,N}}} \right) \left(\overline{\varepsilon_n^{\text{cap}}} \right) + \overline{\varepsilon_{e^+}} \left(\overline{\varepsilon_n^{\text{cap}}} \right)^2 \right]_{\text{0-fold}} \quad (15.6e)$$

The first set of bracketed terms (15.6b) is the efficiency for detecting a 3-particle coincidence (e^+ , n , n). The second set of bracketed terms (15.6c) is the efficiency for detecting a 2-particle coincidence. A 2-particle coincidence can be either of two types (e^+ , n) or (n , n). The third set of bracketed terms (15.6d) is the efficiency for detecting only 1 particle. These 1 particle detection outcomes will appear as backgrounds to the charged-current (CC) and neutral-current (NC) signals in the solar neutrino analysis of SNO data. Finally, the fourth set of bracketed terms (15.6e) is the efficiency for detecting none of the particles produced in the $\overline{\text{CC}}$ reaction.

To abbreviate further, (15.6b), (15.6c), (15.6d), and (15.6e) are denoted by N_3^{det} , N_2^{det} , N_1^{det} , and N_0^{det} , respectively. For coincidence based detection of $\overline{\text{CC}}$ events in SNO, N_3^{det} and N_2^{det} give the expected number of detected coincidences given a number of $\overline{\text{CC}}$ reactions, $N_{\overline{\text{CC}}}$. The total number of detected coincidences, N^{det} , is give by $N^{\text{det}} = N_3^{\text{det}} + N_2^{\text{det}}$.

15.3.4 Efficiency Inter-relationships

Section 15.3 defined N_2^{det} and N_3^{det} . These quantities are the empirically measurable quantities in the SNO experiment. Using the definitions from Section 15.3, it is possible to give a relationship between the two empirical quantities N_2^{det} and N_3^{det} . This relationship depends only on the detection efficiencies of the positron and the neutrons. Using lines 15.6b and 15.6c and by referring to the definitions 15.5a, the relationship is:

$$N_2^{\text{det}} = N_3^{\text{det}} \left[\frac{1}{\epsilon_{e^+}} + \frac{2}{\epsilon_n^{\text{cap,d}} \epsilon_n^{\text{meas,d}} + \epsilon_n^{\text{cap,N}} \epsilon_n^{\text{meas,N}}} - 3 \right] \quad (15.7)$$

This could be understood as a statement that a measurement of N_3^{det} predicts N_2^{det} (or vice versa). It might be possible to use this inter-relationship equation to determine if the empirically measured numbers of 3-particle coincidences and 2-particle coincidences are consistent with a $\overline{\text{CC}}$ production hypothesis.

Chapter 16

$\overline{\text{CC}}$ SIGNAL MONTE CARLO

16.1 The Monte Carlo Program

The SNO Collaboration uses a Monte Carlo program called SNOMAN [224] to simulate events in the interior heavy and light water regions of the SNO detector. The Monte Carlo program is written specifically to model and simulate the SNO detector incorporating the EGS4¹ [59] and MCNP² [63] Monte Carlo packages for particle transport. FLUKA³ [53] is a recent addition to the SNOMAN Monte Carlo package allowing for simulation of hadronic interactions and decays.

For the electron antineutrino analysis in the Pure D₂O and Salt phases of the experiment, $\overline{\text{CC}}$ reactions generating a positron and two neutrons were simulated for each run used in the analysis. These run-by-run simulations take into account the measured optical properties of the detector and the electronics configuration (i.e. which PMTs were on).

16.1.1 Electron Antineutrino Simulation in the Pure D₂O Phase

For the Pure D₂O phase, $\overline{\text{CC}}$ interactions were simulated from a flux of electron antineutrinos having the ⁸B solar neutrino energy spectrum and a total flux of 100 times the standard solar model ⁸B total electron neutrino flux: $100 \times \Phi_{\text{SSM}}^{\text{8B}} = 5.05 \times 10^8 \text{ cm}^{-2}\text{s}^{-1}$. This amounts to 423,900 generated $\overline{\text{CC}}$ interactions in the data set which is comparable to the calculations of Chapter 4 that predict 415,315 $\overline{\text{CC}}$ interactions for an equivalent exposure. Of the 423,900 generated events, 2974 were terminated due to geometry errors. These failures are treated as a systematic uncertainty as described in Section 16.3.1.

16.1.2 Electron Antineutrino Simulation in the Salt Phase

For the Salt phase, $\overline{\text{CC}}$ interactions were simulated from a flux of electron antineutrinos having the ⁸B solar neutrino energy spectrum and an undocumented total flux. The lack of a documented total flux is not a serious problem since only efficiencies are determined from the Monte Carlo and absolute normalizations are based upon the work done in Chapter 4. For the record, the Salt phase electron antineutrino Monte Carlo generated 859,670 $\overline{\text{CC}}$ interactions for a run time of 258.8 days which amounts to 1,213,271 $\overline{\text{CC}}/\text{kt} \cdot \text{yr}$. Compare this to the rate of 494,820 $\overline{\text{CC}}/\text{kt} \cdot \text{yr}$ used in the Monte Carlo of the Pure D₂O phase. Investigation of the log

¹EGS4 (Electron Gamma Shower 4) “is a general purpose package for the Monte Carlo simulation of the coupled transport of electrons and photons in an arbitrary geometry for particles with energies from a few keV up to several TeV.”

²“MCNP is a general-purpose Monte Carlo N-Particle code that can be used for neutron, photon, electron, or coupled neutron/photon/electron transport, including the capability to calculate eigenvalues for critical systems.”

³“FLUKA is a fully integrated particle physics Monte Carlo simulation package. It has many applications in high energy experimental physics and engineering, shielding, detector and telescope design, cosmic ray studies, dosimetry, medical physics and radio-biology”

files report “1355.50079 NU PER DAY” for the Pure D₂O phase Monte Carlo and “3329.82053 NU PER DAY” for the Salt phase Monte Carlo. These log file reports are consistent with the total number of generated events in either phase’s Monte Carlo. Of the 859,670 generated events, 9429 were terminated due to geometry errors. These failures are treated as a systematic uncertainty as described in Section 16.3.1.

16.2 Detector Response to $\overline{\text{CC}}$ Products

The detector response to $\overline{\text{CC}}$ interactions is divided into two categories. The first category is the response characteristics of the individual particles produced in a $\overline{\text{CC}}$ interaction. The characteristics are used to select events that will then be used to search for coincidences of events in the electron antineutrino search. The second category is composed of those characteristics which are intrinsic to the coincidence nature of the $\overline{\text{CC}}$ interaction. This second category provides a way to test if coincidences have a $\overline{\text{CC}}$ signature above and beyond the correct single particle characteristics.

16.2.1 Individual Particle Characteristics

The primary detector response of importance is the N_{hit} of a product particle from the $\overline{\text{CC}}$ interaction. Figures 16.1 & 16.2 show the Monte Carlo N_{hit} response of the positron, e^+ , and neutrons, n , in the Pure D₂O and Salt phases.

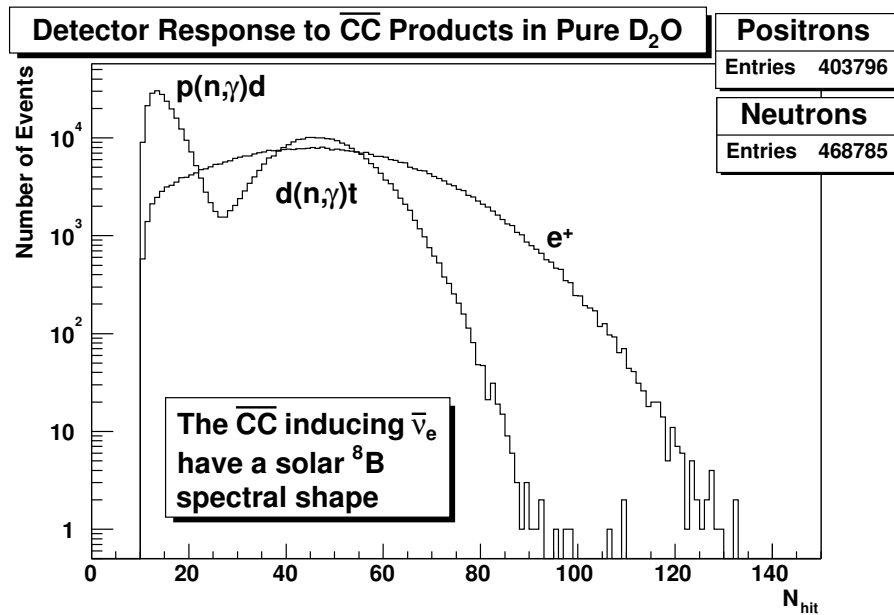


Figure 16.1: Monte Carlo N_{hit} response to $\overline{\text{CC}}$ products in the Pure D₂O phase.

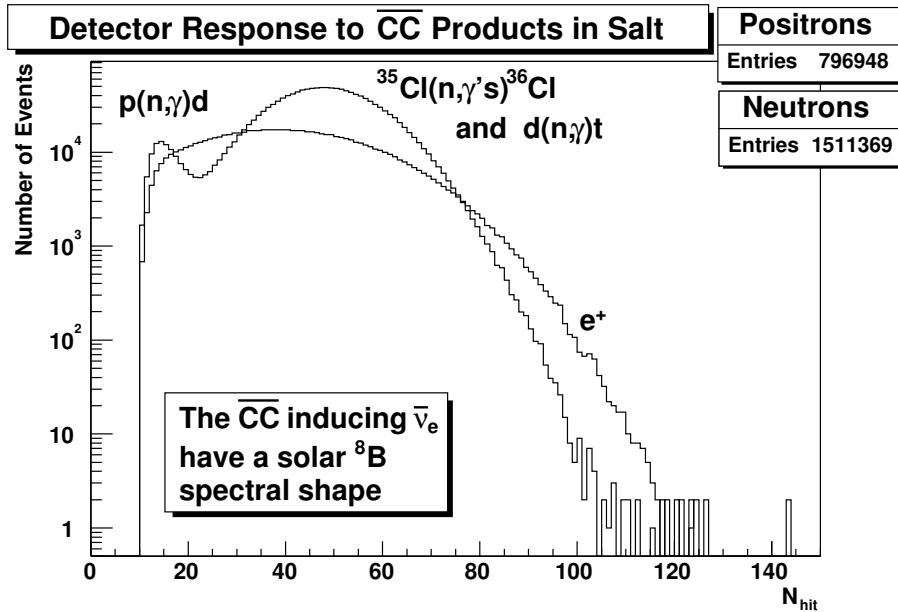


Figure 16.2: Monte Carlo N_{hit} response to \overline{CC} products in the Salt phase.

Positron Detection Efficiency as a Function of $\bar{\nu}_e$ Energy

As the electron antineutrino Monte Carlos are generated in such a way as to correctly account for the run-to-run detector configuration, they provide a resource for information on particle detection characteristics of value to studies related to the electron antineutrino analysis. One particular example is the detection efficiency of positrons as a function of the \overline{CC} inducing electron antineutrino's energy, $E_{\bar{\nu}_e}$. For both the Pure D_2O and Salt phase electron antineutrino Monte Carlos, out-going positrons were sorted into 0.1 MeV bins of electron antineutrino energy, $E_{\bar{\nu}_e}$. For each bin the detection efficiency was determined for the Standard and Enlarged analysis regions. Figure 16.3 presents these results. The Enlarged analysis is the entire D_2O volume while the Standard analysis is only 77% of the D_2O volume. As these plots are determined from a sample of $\bar{\nu}_e$'s with a ^8B spectrum, the scatter above 14 MeV is due to the reduced number of electron antineutrinos at these energies.

16.2.2 \overline{CC} Specific Characteristics

A \overline{CC} specific characteristic is defined as a parameter that is intrinsic to the coincidence nature of the three product particle final state containing a positron and two neutrons. For instant, the neutron capture time following a prompt Čerenkov signal from a positron, is a specific and distinguishing characteristic of \overline{CC} interactions. The neutron capture times for the Pure D_2O and Salt phases are discussed in Chapter 11 and are not repeated here, though one should keep in mind these remain an important handle on detecting neutrons in

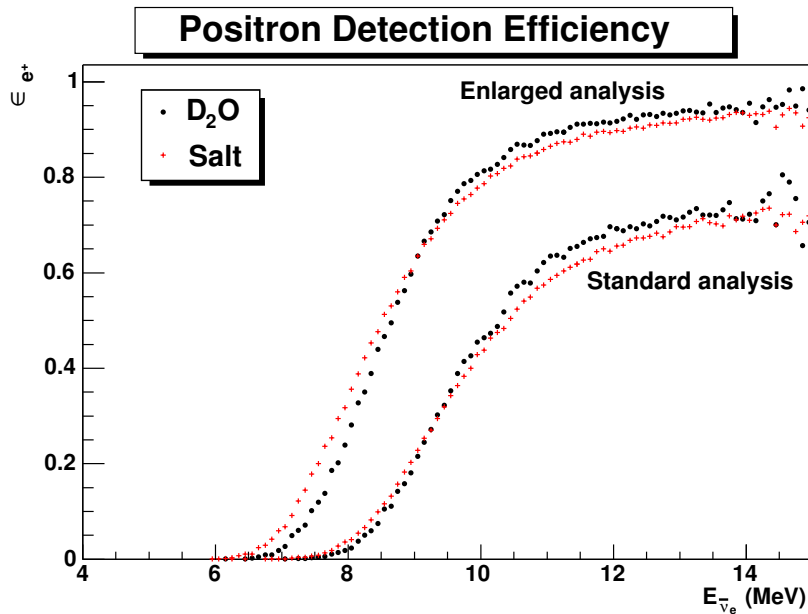


Figure 16.3: Monte Carlo positron detection efficiency in the Pure D_2O and Salt phase as a function of the electron antineutrino energy, $E_{\bar{\nu}_e}$.

coincidence with an initiating event that results in prompt Čerenkov light emission.

A second characteristic is the neutron capture distance. This is the distance between the location of a prompt Čerenkov signal from a positron to the location of the neutron capture. Alternatively, one can investigate the separation distance between the two neutron capture locations for those cases when the positron is below the analysis detection threshold. For the Pure D_2O phase, Figure 16.4 shows the distance separation between neutron captures on deuterium. No analysis cuts are applied to the Monte Carlo results shown in Figure 16.4 but a restriction to neutron capture on deuterons is made. The restriction to only considering neutron capture on deuterons eliminates contribution from neutron capture on protons in the acrylic vessel. This is reasonable because the detector response to the 2.2 MeV gamma-ray produced by neutron capture on protons is well below the analysis N_{hit} (energy) threshold at the radius of the acrylic vessel. For example, the Enlarged Region analysis cuts imply a minimum N_{hit} threshold of 39.2 (≈ 4.4 MeV) at a radius of 600 cm. Due to the low neutron capture fraction in the Pure D_2O phase, the distance between two neutron captures, Δr_n , is multiplied by 5 to clearly show the distribution. Figure 16.5 presents the neutron capture distance for the Salt phase. In the Salt phase, neutron capture on protons is again ignored. In the Pure D_2O phase the neutron capture distance is merely a distinguishing characteristic, however, in the Salt phase this characteristic is so pronounced that it may be considered as a new analysis cut to further eliminate backgrounds. This is not done in this dissertation in an attempt to keep the Pure D_2O and Salt phase analyses on-par and comparable. Another point is the neutron capture distance will not eliminate backgrounds that produce neutrons at a single,

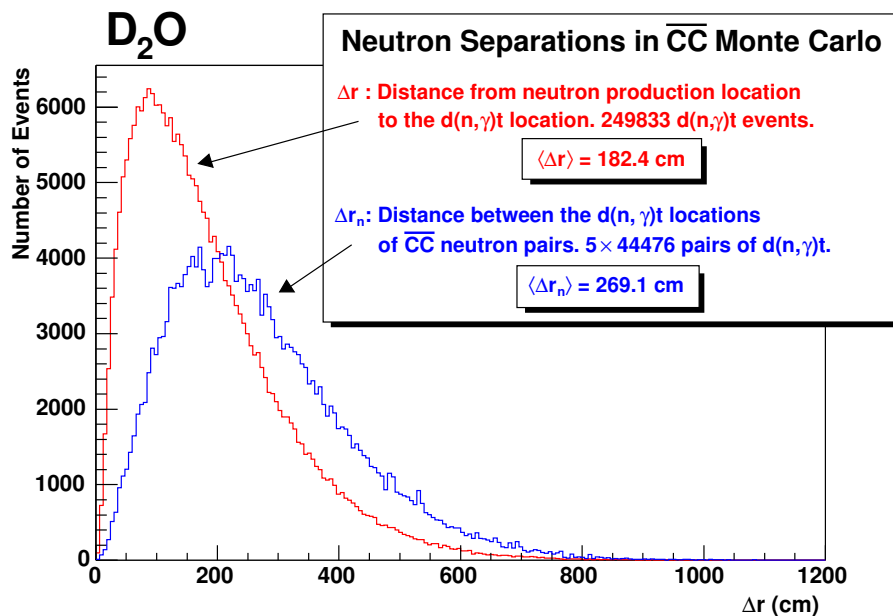


Figure 16.4: Monte Carlo neutron capture separation distances in the Pure D₂O phase.

initial location. Thus a neutron capture distance analysis cut could lower the accidental coincidence background (Chapter 13), but will not reduce backgrounds from spontaneous fission (Chapter 18) or atmospheric neutrinos (Chapter 19).

16.3 \overline{CC} Detection Efficiencies

The detection efficiencies are determined by applying all analysis cuts described in Chapters 11 – 14. The \overline{CC} detection efficiencies can be determined in two ways as described previously in Chapter 15. The individual particle detection efficiencies for the positron, e^+ , and the neutrons, n , can be determined and then combined analytically to determine a derived coincidence detection efficiency. The more correct method directly determines the number of coincidences found in the Monte Carlo data set divided by the number of possible coincidences. In both cases, the final value of interest is the total \overline{CC} detection efficiency which is the sum of the detection efficiencies for the three types of coincidences that can appear: (e^+, n, n) , (e^+, n) , and (n, n) . Tables 16.1 & 16.2 use these distinctions in reporting the \overline{CC} detection efficiencies for the Pure D₂O and Salt phases. In the Salt phase Monte Carlo, 841,205 \overline{CC} simulations resulted in 88 four-fold coincidences found in the Standard analysis and 849 in the Enlarged analysis. The Enlarged analysis had 4 cases of five-fold coincidences. These four and five-fold coincidences are primarily due to the secondary neutron production discussed in Chapter 21.

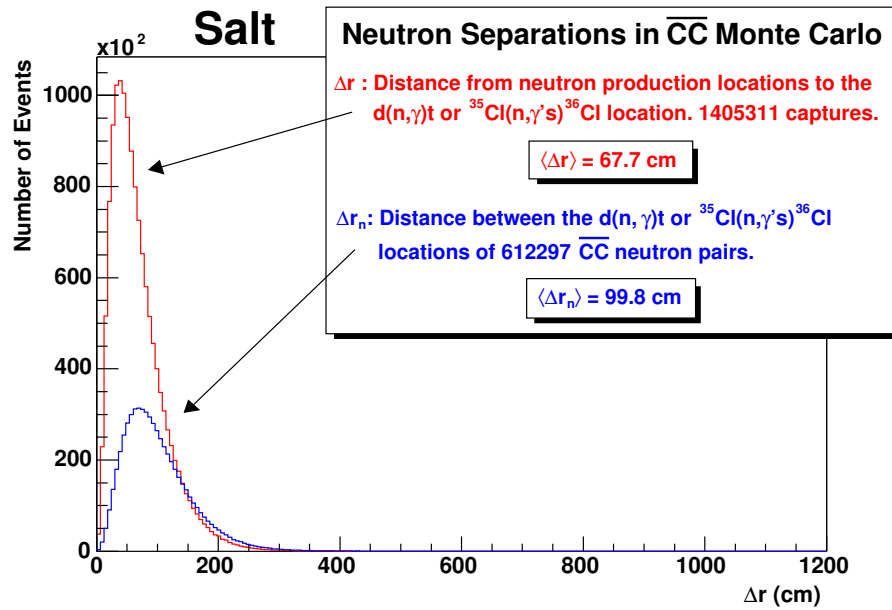


Figure 16.5: Monte Carlo neutron capture separation distances in the Salt phase.

Table 16.1: The Monte Carlo detection efficiency of $\bar{\nu}_e$ with a ^8B spectral shape in the Pure D_2O phase. The \overline{CC} detection efficiencies in the upper table are derived from the single particle detection efficiencies as explained in Chapter 15. The coincidence detection efficiencies in the lower table are the correct efficiencies to use in the electron antineutrino analysis.

Individual Particle Detection Efficiencies (%)			
Analysis	e^+	n	Derived Total \overline{CC}
Standard	$39.07 \pm 0.11^{+0.43}_{-0.27}$	$14.22 \pm 0.04^{+0.61}_{-0.10}$	$11.55 \pm 0.05^{+0.66}_{-0.13}$
Enlarged	$65.73 \pm 0.16^{+0.24}_{-0.46}$	$26.14 \pm 0.06^{+0.53}_{-0.19}$	$32.21 \pm 0.13^{+0.96}_{-0.39}$

Coincidence Detection Efficiencies (%)				
Analysis	(e^+, n, n)	(e^+, n)	(n, n)	Total \overline{CC}
Standard	$1.28 \pm 0.02^{+0.69}_{-0.01}$	$10.89 \pm 0.05^{+0.63}_{-0.08}$	$1.20 \pm 0.02^{+0.69}_{-0.01}$	$13.37 \pm 0.06^{+0.61}_{-0.09}$
Enlarged	$5.92 \pm 0.04^{+0.66}_{-0.04}$	$24.65 \pm 0.09^{+0.53}_{-0.17}$	$2.19 \pm 0.02^{+0.69}_{-0.02}$	$32.75 \pm 0.10^{+0.47}_{-0.23}$

16.3.1 Monte Carlo Detection Efficiency Uncertainties

The statistical and systematic uncertainties on the detection efficiencies presented in Tables 16.1 & 16.2 are determined solely from the Monte Carlo simulation and do not include systematic uncertainties due to the use of theoretical cross-sections etc. Statistical error is determined simply by a \sqrt{N} calculation. The systematic

Table 16.2: Monte Carlo detection efficiency of $\bar{\nu}_e$ with a ^8B spectral shape in the Salt phase. The $\overline{\text{CC}}$ detection efficiencies in the upper table are derived from the single particle detection efficiencies as explained in Chapter 15. The coincidence detection efficiencies in the lower table are the correct efficiencies to use in the electron antineutrino analysis.

Individual Particle Detection Efficiencies (%)			
Analysis	e^+	n	Derived Total $\overline{\text{CC}}$
Standard	$37.43 \pm 0.08^{+0.63}_{-0.38}$	$51.32 \pm 0.07^{+0.50}_{-0.52}$	$45.04 \pm 0.13^{+0.93}_{-0.95}$
Enlarged	$65.45 \pm 0.11^{+0.35}_{-0.66}$	$75.83 \pm 0.89^{+0.25}_{-0.77}$	$81.50 \pm 0.26^{+0.71}_{-2.20}$

Coincidence Detection Efficiencies (%)				
Analysis	(e^+, n, n)	(e^+, n)	(n, n)	Total $\overline{\text{CC}}$
Standard	$15.57 \pm 0.05^{+0.85}_{-0.16}$	$16.08 \pm 0.05^{+0.85}_{-0.16}$	$16.13 \pm 0.05^{+0.85}_{-0.16}$	$47.78 \pm 0.09^{+0.53}_{-0.48}$
Enlarged	$44.04 \pm 0.09^{+0.56}_{-0.44}$	$16.86 \pm 0.08^{+0.84}_{-0.17}$	$17.83 \pm 0.05^{+0.83}_{-0.18}$	$78.73 \pm 0.13^{+0.21}_{-0.79}$

uncertainty is due to the failure of the Monte Carlo to correctly process all events. The error estimation used here assumes that the Monte Carlo failures are *independent* of the type of particle, energy, or coincidence type. Thus, the efficiency is determined by dividing the number of events satisfying the analysis cuts, N_{out} , by the number of input events, N_{in} , minus the number of failed events, N_{fail} ,

$$\varepsilon = \frac{N_{\text{out}}}{N_{\text{in}} - N_{\text{fail}}} \quad \sigma_{\varepsilon}^{\text{stat}} = \sqrt{\frac{\varepsilon}{N_{\text{in}} - N_{\text{fail}}} \left(1 + \frac{\varepsilon(N_{\text{in}} + N_{\text{fail}})}{N_{\text{in}} - N_{\text{fail}}} \right)} \quad (16.1)$$

The statistical error is $\sigma_{\varepsilon}^{\text{stat}}$. The determination of the systematic error is *not* a Gaussian error bar. Instead the systematic error is the entire possible range allowed under minimal and maximal assumptions about the effect of N_{fail} . Thus, the systematic error range has variable upper and lower bounds. The maximum efficiency (i.e. upper systematic), ε^+ , is determined under the assumption that *all* N_{fail} events would contribute to the number of events satisfying the analysis cuts. The minimum efficiency (i.e. lower systematic), ε^- , is determined under the assumption that *all* N_{fail} events would *not* contribute to the number of events satisfying the analysis cuts.

$$\varepsilon^+ = \frac{N_{\text{out}} + N_{\text{fail}}}{N_{\text{in}}} \quad \varepsilon^- = \frac{N_{\text{out}}}{N_{\text{in}}} \quad (16.2)$$

The upper and lower systematic uncertainty ranges are then given as $\sigma_{\varepsilon}^{+\text{ syst}} = \varepsilon^+ - \varepsilon$ and $\sigma_{\varepsilon}^{-\text{ syst}} = \varepsilon - \varepsilon^-$, respectively. The efficiencies calculated are written in the form:

$$\varepsilon \pm \begin{matrix} \sigma_{\varepsilon}^{\text{stat}} + \sigma_{\varepsilon}^{+\text{ syst}} \\ -\sigma_{\varepsilon}^{-\text{ syst}} \end{matrix} \quad (16.3)$$

In the case of a derived efficiency, standard error propagation formulas must also be used. For example, the individual positron and neutron detection efficiencies are combined to determine a derive total $\overline{\text{CC}}$ detection

efficiency, as described in Chapter 15, and have errors given by

$$\sigma_{\overline{CC}} = \sqrt{\sigma_{e^+}^2 (2\varepsilon_n (1 - \varepsilon_n))^2 + \sigma_n^2 (2\varepsilon_{e^+} + 2\varepsilon_n)^2} \quad (16.4)$$

where σ_{e^+} & σ_n in equation (16.4) are replaced by the particles' statistical or systematic errors, depending on the type of error being calculated. It should be re-iterated that the error propagation formula (16.4) necessarily does not correctly account for particle-to-particle correlations present in \overline{CC} interactions. Chapter 15 details this complication and shows why the derived detection efficiencies are *not* relied upon for the results of an electron antineutrino analysis for the SNO detector data.

Chapter 17

DETECTION EFFICIENCY FOR NON-SOLAR SOURCES OF ELECTRON ANTINEUTRINOS

17.1 Review of Electron Antineutrino Sources

In Part II the electron antineutrino sources were discussed and the number of induced $\overline{\text{CC}}$ events per kt · yr was presented. This chapter takes the additional step of determining or estimating the detection efficiency for each of these sources of electron antineutrinos during the Pure D₂O and Salt phases of the SNO experiment. Table 17.1 reviews the results of Part II.

Table 17.1: Review of electron antineutrino sources as presented in Part II.

Known $\bar{\nu}_e$ Source		Rate		Note
Atmospheric		0.0012	$\overline{\text{CC}}/\text{kt} \cdot \text{yr}$	$4 < E_{\bar{\nu}_e} \text{ (MeV)} < 20$
Reactor	Pure D ₂ O	0.69	$\overline{\text{CC}}$	Actual number in SNO data sets.
	Salt	0.57	$\overline{\text{CC}}$	
Diffuse Supernova Neutrinos		0.03	$\overline{\text{CC}}/\text{kt} \cdot \text{yr}$	$4 < E_{\bar{\nu}_e} \text{ (MeV)} < 23$
Terrestrial Radioisotopes		0	$\overline{\text{CC}}/\text{kt} \cdot \text{yr}$	Below $\overline{\text{CC}}$ threshold

Hypothetical $\bar{\nu}_e$ Source		Rate		Note
Geo-Fission Reactor	Pure D ₂ O	0.54	$\overline{\text{CC}}$	Expected number in SNO data sets for an assumed 10 TW source.
	Salt	0.45	$\overline{\text{CC}}$	

17.2 Efficiencies to Detect Non-Solar Sources of Electron Antineutrinos

17.2.1 Hypothetical Geo-Fission Reactor and Nuclear Power Reactor Electron Antineutrinos

As the hypothetical geo-fission reactor discussed in Chapter 8 is an unenriched ²³⁸U reactor, it should have the same spectral properties of the CANDU nuclear power reactors discussed in Chapter 6. Thus the forthcoming results of this section can be applied to the hypothetical geo-fission reactor with the same caveats regarding the isotopic content differences between CANDU reactors and US light water reactors, as mentioned in Chapter 6. While the induced $\overline{\text{CC}}$ rate from a 10 TW geo-fission reactor is comparable to that of nuclear power reactors, the geo-fission reactor is a disfavored model of the Earth's core lacking a particular expectation for the thermal energy output, thus this potential source of electron antineutrinos is not considered further.

The reactor electron antineutrino induced \overline{CC} rate is the largest known electron antineutrino background in the SNO experiment. A detailed model of the detection efficiency for reactor electron antineutrinos is presented in this section. Chapter 6 presents the normalized reactor electron antineutrino spectrum in Figure 6.3. Chapter 16 presents the positron and neutron detection efficiencies. The neutron detection efficiency is independent of the energy of the $\bar{\nu}_e$ initiating the \overline{CC} reaction. The positron detection efficiency is presented in Figure 16.3 as a function of the $\bar{\nu}_e$ initiating the \overline{CC} reaction. An integration of the reactor spectrum times the positron detection efficiency from Figure 16.3 will give a positron detection efficiency for reactor electron antineutrino induced \overline{CC} reactions. These results are presented in the first line of Table 17.2.

As pointed out in Chapter 15, the detection efficiency for coincidences of particles will in general not be equal to the straight multiplication of the individual particle detection efficiencies. This is due to the radial dependence of the detection efficiencies. To account for this detail, as well as the run-by-run conditions of the Pure D₂O and Salt phases of the SNO experiment, the solar electron antineutrino Monte Carlo is used to determine the reactor $\bar{\nu}_e$ coincidence detection efficiency. This is accomplished by calculating the coincidence detection efficiencies in 0.1 MeV $\bar{\nu}_e$ energy bins. The 0.1 MeV wide bin coincidence detection efficiencies are then weighted by the reactor $\bar{\nu}_e$ spectrum of Figure 6.3 (taken in 0.1 MeV $\bar{\nu}_e$ energy bins). These results are presented in Table 17.2. The expected number of detected coincidences from electron antineutrinos from nuclear power reactors and the hypothetical geo-fission reactor are the product of the number of expected \overline{CC} interactions from Table 17.1 multiplied by the total coincidence detection efficiencies of Table 17.2.

Table 17.2: Nuclear reactor $\bar{\nu}_e$ induced \overline{CC} detection efficiencies.

Pure D₂O	Analysis		Salt	Analysis	
Particle	Standard	Enlarged	Particle	Standard	Enlarged
$\epsilon_{e^+}^{\text{det.}}$	2.1×10^{-3}	2.5×10^{-2}	$\epsilon_{e^+}^{\text{det.}}$	3.2×10^{-3}	4.1×10^{-2}
$\epsilon_n^{\text{det.}}$	1.4×10^{-1}	2.6×10^{-1}	$\epsilon_n^{\text{det.}}$	4.6×10^{-1}	7.6×10^{-1}
Coincidence	Standard	Enlarged	Coincidence	Standard	Enlarged
$\epsilon_{(e^+,n,n)}^{\text{det.}}$	7.7×10^{-5}	2.9×10^{-3}	$\epsilon_{(e^+,n,n)}^{\text{det.}}$	1.1×10^{-3}	3.1×10^{-2}
$\epsilon_{(e^+,n)}^{\text{det.}}$	6.2×10^{-4}	1.1×10^{-2}	$\epsilon_{(e^+,n)}^{\text{det.}}$	1.5×10^{-3}	8.7×10^{-3}
$\epsilon_{(n,n)}^{\text{det.}}$	2.7×10^{-2}	8.8×10^{-2}	$\epsilon_{(n,n)}^{\text{det.}}$	2.6×10^{-1}	6.1×10^{-1}
Total	2.8×10^{-2}	1.0×10^{-1}	Total	2.6×10^{-1}	6.5×10^{-1}

17.2.2 Atmospheric and Diffuse Supernova Background Electron Antineutrinos

The expected rate of \overline{CC} interactions induced by atmospheric electron antineutrinos below 20 MeV is a factor of 600 times less than the expected rate induced by reactor electron antineutrinos. Detection efficiencies further reduce this number. For these reasons the atmospheric $\bar{\nu}_e$ induced \overline{CC} rate is neglected from further study. However, a rough estimate of the atmospheric electron antineutrino detection efficiency is given by

assuming a 100 % positron detection efficiency and the neutron detection efficiencies from Tables 16.1 & 16.2 combined as described in Chapter 15.

The diffuse supernova background $\bar{\nu}_e$ induced $\overline{\text{CC}}$ rate is comparable to the expected rate induced by reactor electron antineutrinos. The neutron detection efficiencies are known (Chapter 16) and are independent of the $\overline{\text{CC}}$ inducing $\bar{\nu}_e$ energy. The positron detection efficiency is given as a function of the $\overline{\text{CC}}$ inducing $\bar{\nu}_e$ in Figure 16.3. Since the prediction for the diffuse supernova background neutrino rate is given for the energy range $4 < E_{\bar{\nu}_e} < 23$ (MeV), an extension of Figure 16.3 above $E_{\bar{\nu}_e} > 14$ MeV is needed. Based upon the trends on the Monte Carlo curves in Figure 16.3, the maximal positron detection efficiency is estimated for $\bar{\nu}_e$ above 14 MeV and presented in Table 17.3. To obtain a total integrated positron detection efficiency for the

Table 17.3: Estimated positron detection efficiency for $14 < E_{\bar{\nu}_e}$ (MeV) < 23 from Figure 16.3.

Phase	Analysis	
	Standard	Enlarged
Pure D ₂ O	0.72	0.95
Salt	0.70	0.92

diffuse supernova background neutrinos, parameterizations of Figure 16.3 are convolved with the normalized spectral yield given in Figure 7.1 from Ref. [129]. Note that while the yield-spectra from Ref. [129] is used (i.e. Figure 7.1), the absolute $\overline{\text{CC}}$ rate is taken from Ref. [31] as presented in Table 17.1. See Chapter 7 for more details. Table 17.4 gives the total integrated positron detection efficiency for the diffuse supernova background neutrinos in the energy range $4 < E_{\bar{\nu}_e}$ (MeV) < 23 . It is possible to estimate the total $\overline{\text{CC}}$ detection efficiency for diffuse supernova electron antineutrinos by combining the neutron detection efficiencies from Table 17.2 with the total integrated positron detection efficiencies estimated in Table 17.4 via the prescriptions of Chapter 15. The results are presented in Table 17.4. Recall that the total $\overline{\text{CC}}$ detection efficiency is the sum of the efficiencies to detect the three possible coincidence types: (e^+, n, n) , (e^+, n) , and (n, n) .

Table 17.4: Total positron and $\overline{\text{CC}}$ detection efficiencies for diffuse supernova background $\bar{\nu}_e$.

Diffuse Supernova $\bar{\nu}_e$'s $4 < E_{\bar{\nu}_e} < 23$				
Phase	Analysis			
	Standard		Enlarged	
	ε_{e^+}	$\varepsilon_{\overline{\text{CC}}}$	ε_{e^+}	$\varepsilon_{\overline{\text{CC}}}$
Pure D ₂ O	0.64	0.18	0.87	0.40
Salt	0.59	0.50	0.82	0.88

Chapter 18

SPONTANEOUS FISSION BACKGROUNDS

18.1 Spontaneously Fissioning Isotopes in SNO

Spontaneous fission of heavy nuclei is a potential background to an electron antineutrino analysis in SNO because multiple free neutrons are produced in the fission process [211]. The multiplicity of produced neutrons can mimic the coincidence signal used to identify $\overline{\text{CC}}$ events. Along with the multiple neutrons produced in the fission process, the fission fragments are generally neutron rich and are in excited nuclear states. Thus the fission fragments move toward nuclear stability via both beta decay and gamma-ray emission. This chapter discusses the relevant spontaneously fissioning isotopes and estimates the background to the $\overline{\text{CC}}$ signal.

The smallest nucleus known to spontaneously fission is ^{230}Th . Furthermore, ^{238}U is the largest, naturally occurring, nucleus known to spontaneously fission. SNO uses Cf as an encapsulated source of neutrons for calibration of the SNO detector. Thus, it is important to consider potential contamination from the ^{252}Cf , ^{250}Cf , and ^{249}Cf in the Cf calibration source. The Cf calibration source was deposited from a solution of ^{252}Cf and ^{249}Cf at a concentration ratio of $[\text{}^{252}\text{Cf}]/[\text{}^{249}\text{Cf}] = 36.3/3.2$ on January 15, 1998 [91]. Table 18.1 presents the six nuclei considered as potential spontaneous fission backgrounds in the SNO experiment.

For each of the nuclei listed in Table 18.1 the entire decay chains should be considered. In the case of the Cf source, it is possible to show under reasonable assumptions that the long half-lives of certain nuclei effectively limit the progression through the complete decay chains. Figures 18.1 & 18.2 show the relevant portions of the decay chains for the six nuclei listed in Table 18.1

18.1.1 ^{232}Th , ^{235}U , and ^{238}U in SNO

The uranium and thorium decay chains contain γ -decays with energies above the 2.22 MeV threshold energy for the photo-disintegration reaction $d(\gamma, n)p$. The neutron liberated in this photo-disintegration reaction is indistinguishable from a neutron produced by the neutral-current neutrino interaction, $\nu_\ell + d \rightarrow p + n + \nu_\ell$, of interest in the solar neutrino studies SNO was designed to address. Thus the SNO Collaboration actively pursues a monitoring program for the uranium and thorium concentrations in the detector volume.

There are two methods used to monitor the amount of uranium and thorium in the detector, known as the *in-situ* and *ex-situ* measurements. The *in-situ* measurements rely upon the Čerenkov light produced by the decays of ^{208}Tl and ^{214}Bi present in the uranium and thorium decay chains. The *ex-situ* measurements consist of three radio-chemical extraction techniques referred to as MnO_x [30], HTiO [29], and Rn Assay [147]. Figure 18.3 shows the published results for the uranium and thorium concentrations in the Pure D_2O phase of the experiment based upon each of these techniques. The Low Energy Background Group gives a recommended combined *in-situ* and *ex-situ* recommended value for the concentrations of U and Th in the heavy water volume. These results are recorded in Table 18.2 and shown graphically for the Pure D_2O phase in Figure 18.3.

Table 18.1: The six nuclei considered as potential spontaneous fission backgrounds to the electron antineutrino analysis. To avoid confusion with antineutrinos, \bar{n} is used to represent the mean number of neutrons produced in spontaneous fission (SF) rather than the symbol commonly used, $\bar{\nu}$. Half-life values and branching fractions come from Ref. [89] while \bar{n} values are cited separately. The \bar{n} value for ^{235}U is a thermal neutron induced multiplicity.

Nucleus	Half-Life	Note	Decay	Branching Fraction (%)	Product Nucleus
					Mean Neutrons, \bar{n}
^{232}Th	1.405×10^{10} y	100% natural abundance	α	≈ 100	^{228}Ra
			SF	1.8×10^{-9}	2.14 ± 0.2 [132]
^{235}U	7.038×10^8 y	0.72% natural abundance	α	≈ 100	^{231}Th
			SF	7×10^{-9}	2.4334 ± 0.0036 [132]
^{238}U	4.468×10^9 y	99.28% natural abundance	α	≈ 100	^{234}Th
			SF	5.45×10^{-5}	2.00 ± 0.02 [132]
^{249}Cf	351 y	Potential contaminant	α	≈ 100	^{245}Cm
			SF	4.4×10^{-7}	3.4 ± 0.4 [132]
^{250}Cf	13.08 y	Potential contaminant	α	99.923	^{246}Cm
			SF	0.077	3.53 ± 0.09 [211]
^{252}Cf	2.645 y	Potential contaminant	α	96.908	^{248}Cm
			SF	3.092	3.7676 ± 0.0047 [132]

Table 18.2: Concentrations of U and Th in the Pure D_2O and Salt phases.

Nucleus	Concentration g[X]/g D_2O	
	Pure D_2O [175]	Salt [174]
U	$(17.8^{+3.5}_{-4.3}) \times 10^{-15}$	$(8.67^{+2.62}_{-2.24}) \times 10^{-15}$
Th	$(1.61 \pm 0.56) \times 10^{-15}$	$(1.64 \pm 0.84) \times 10^{-15}$

One important point should be noted: in both the *in-situ* and *ex-situ* monitoring schemes, there is an implicit assumption that the nuclear decay chains for uranium and thorium are in secular equilibrium. This assumption is necessary to translate the actual physical measurements of the amount of daughter products in the detector back to the amount of uranium and thorium present. One could imagine a worst case scenario where-by one of the intermediate long-lived daughter nuclei is completely removed from the detector. In this worst case, the secular equilibrium condition is broken and it is then, in principle, possible to have a much greater amount of uranium or thorium in the water than the monitoring techniques will assert. However, the secular equilibrium condition provides the only handle on the uranium and thorium content of the detector

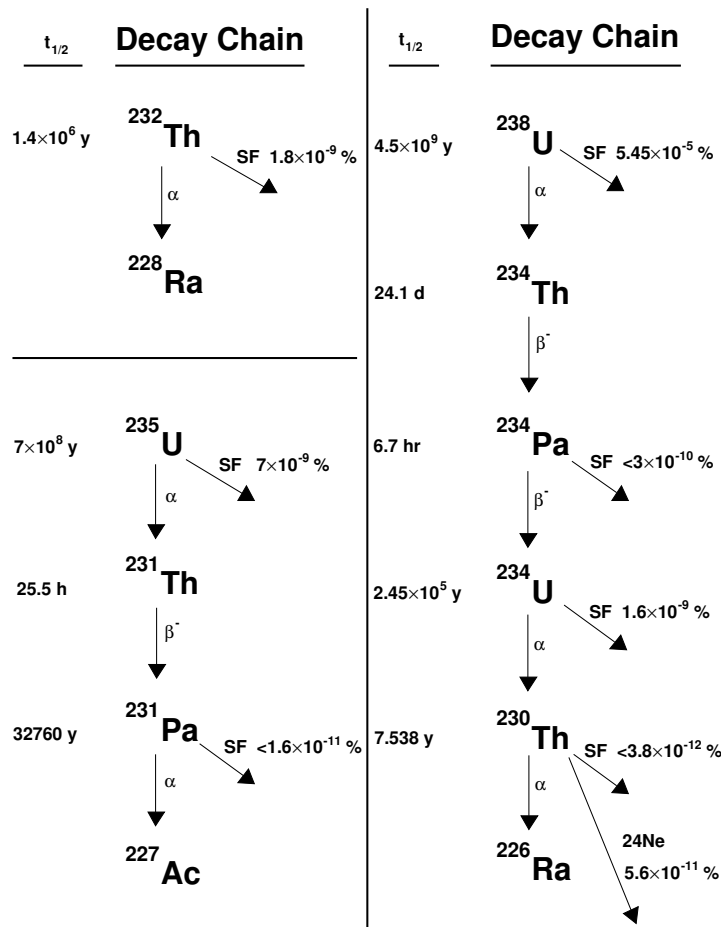


Figure 18.1: The decay chains for ^{232}Th , ^{235}U , and ^{238}U [89].

heavy water volume at the concentration levels desired.

Expected Number of Spontaneous Fissions from ^{232}Th , ^{235}U , and ^{238}U

A general equation relates the number of spontaneous fissions in the D_2O volume per year to the concentration of the particular isotope of interest, X:

$$N_{\text{SF},X} = \frac{\left([\text{X}] \frac{\text{gX}}{\text{gD}_2\text{O}} \right) \left(10^9 \frac{\text{gD}_2\text{O}}{\text{gD}_2\text{O}} \right) \left(1 \text{ yr} \right) \left(\frac{\ln 2}{t_{1/2}} \frac{\text{decay}}{\text{yr}} \right)}{\left(10^3 \frac{\text{gX}}{\text{kgX}} \right) \left(M_X \frac{\text{amu}}{\text{X}} \right) \left(1.66 \times 10^{-27} \frac{\text{kgX}}{\text{amu}} \right)} \left(B_X \frac{\text{SF}}{\text{decay}} \right) \quad (18.1)$$

$$= \left([\text{X}] \frac{\text{gX}}{\text{gD}_2\text{O}} \right) \left[\left(\frac{B_X}{t_{1/2} M_X} \right) 4.174 \times 10^{32} \frac{\text{gD}_2\text{O amu decay}}{\text{gX}} \right] \quad (18.2)$$

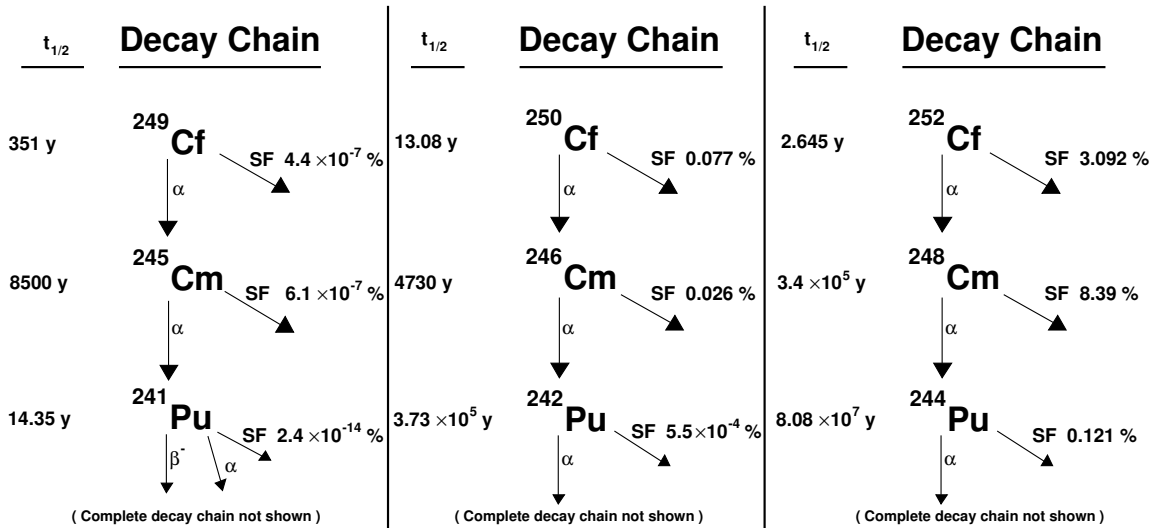


Figure 18.2: The decay chains for ^{249}Cf , ^{250}Cf , and ^{252}Cf [89].

Here $[X]$ is the concentration of nuclei X in the heavy water detector volume in $\text{gX/gD}_2\text{O}$, $t_{1/2}$ is the half-life of nuclei X measured in years, M_X in the mass of nuclei X in amu, and B_X is the spontaneous fission branching ratio. Note that $[X]$, the concentration of the *isotope* X , is usually not the reported quantity. Usually concentrations are reported for an atomic species, thus the isotopic abundance must also be taken into account. Table 18.3 gives the result of this calculation for ^{232}Th , ^{235}U , and ^{238}U . As only ^{238}U will prove a significant background to the electron antineutrino analysis, only this nuclei is investigated further in the following sections.

Table 18.3: The number of spontaneous fissions of ^{232}Th , ^{235}U , and ^{238}U calculated from (18.2) and using values from Table 18.1.

Nuclei	Phase	$[X] \frac{\text{gX}}{\text{gD}_2\text{O}}$	$N_{\text{SF}}/\text{kt} \cdot \text{yr}$
^{232}Th	D ₂ O	$(1.61 \pm 0.56) \times 10^{-15}$	$(3.71 \pm 1.29) \times 10^{-6}$
	Salt	$(1.64 \pm 0.84) \times 10^{-15}$	$(3.78 \pm 1.94) \times 10^{-6}$
^{235}U	D ₂ O	$(0.13 \pm 0.03) \times 10^{-15}$	$(2.29 \pm 0.53) \times 10^{-5}$
	Salt	$(0.06 \pm 0.02) \times 10^{-15}$	$(1.06 \pm 0.35) \times 10^{-5}$
^{238}U	D ₂ O	$(17.7^{+3.47}_{-4.27}) \times 10^{-15}$	$(3.79^{+0.74}_{-0.91})$
	Salt	$(8.61^{+2.60}_{-2.40}) \times 10^{-15}$	$(1.84^{+0.56}_{-0.51})$

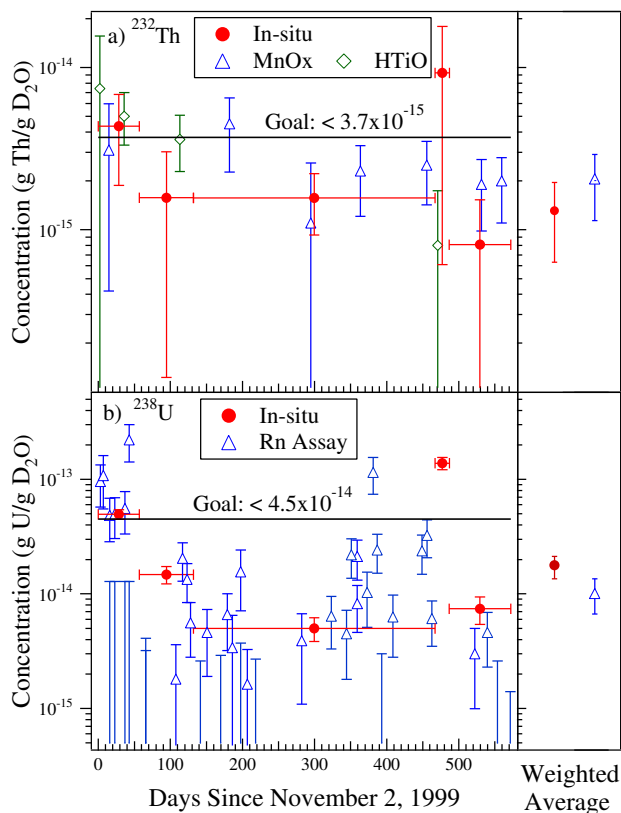


Figure 18.3: The U and Th concentrations in the Pure D₂O phase [10].

18.1.2 Potential Cf Contamination from the Neutron Calibration Source

The californium neutron calibration source is required to meet stringent requirements regarding potential contamination of the SNO detector due to release of ^{249}Cf or ^{252}Cf into the heavy water. The Cf is deposited onto a wire and then entirely encapsulated in acrylic. However, if ^{249}Cf or ^{252}Cf were released into the SNO detector, the spontaneous fission of these nuclei (or their α -decay progeny) would be a background to the $\overline{\text{CC}}$ signal. Under the assumption that only Cf atoms were deposited on encapsulated wire when the source was created (i.e. no progeny products present), then only the first few nuclei in the Cf decay chains are important. The 8500 year, 4730 year, and 3.4×10^5 year half-lives of ^{245}Cm , ^{246}Cm , and ^{248}Cm effectively inhibit significant production of nuclei lower in the decay chains. For the purposes of the electron antineutrino analysis, it is assumed that there is zero contamination of Cf in the SNO detector. However, as an example case, the effect of introduction of ^{252}Cf into the detector volume is investigated further in the following sections.

18.2 Spontaneous Fission Products

In the process of spontaneous fission the parent nucleus fissions into two nuclear fragments, multiple neutrons are released, and de-excitation gammas are present. Furthermore the neutron heavy fission fragments will move toward a stable state via beta decays with half-lives on the order of seconds to days. The greatest concern for the electron antineutrino analysis are the prompt neutrons and de-excitation gammas as their time coincidence will mimic the $\overline{\text{CC}}$ signal.

18.2.1 Neutron Multiplicities of Spontaneous Fission

There is a discrete distribution of neutrons produced during the spontaneous fission process. Table 18.4 presents the probability for a particular neutron multiplicity in the spontaneous fission of ^{238}U and ^{252}Cf .

Table 18.4: The neutron multiplicity probabilities for spontaneous fission of ^{238}U and ^{252}Cf .

	^{238}U [176]	^{252}Cf [211]
P_0	0.052 ± 0.010	0.00197 ± 0.00008
P_1	0.277 ± 0.030	0.02447 ± 0.00025
P_2	0.366 ± 0.035	0.1229 ± 0.0005
P_3	0.247 ± 0.030	0.2707 ± 0.0008
P_4	0.050 ± 0.010	0.3058 ± 0.0010
P_5	0.008 ± 0.003	0.1884 ± 0.0007
P_6		0.0677 ± 0.0006
P_7		0.016 ± 0.0003
P_8		0.0021 ± 0.0002

18.2.2 Prompt Gamma Emission in Spontaneous Fission

Measurements such as those in Figure 18.4 [212], show that a generic exponential can describe the prompt gamma-ray flux spectrum per fission. The prompt gamma-rays are produced on a time scale of 10^{-21} to 10^{-10} seconds after the fission begins [132]. This time scale is short compared to SNO's event times, thus we can consider the prompt gamma emission as a cascade of gamma-rays contained within a single SNO event.

To model this prompt fission, cascade gamma-ray flux spectrum per fission, a Monte Carlo was developed that generated a set of gamma-rays weighed exponentially, Ae^{-mx} with a total energy distributed around the measured mean values reported [132], as given in Table 18.5. A minimum gamma energy of 0.25 MeV was required and no gammas were allowed above 8.0 MeV. For any given spontaneous fission event the total energy in gammas was chosen from a Gaussian distribution around the measured mean value using a sigma of 0.5 MeV. This assumed sigma width is the most unreasonable estimate made in this calculation, however a true, measured distribution's width is strongly anti-correlated with the number of emitted neutrons [132]. This study does not take into account the correlation between the number of emitted neutrons and the total energy left available for gamma emission, thus using the mean total energy in gammas is appropriate. The

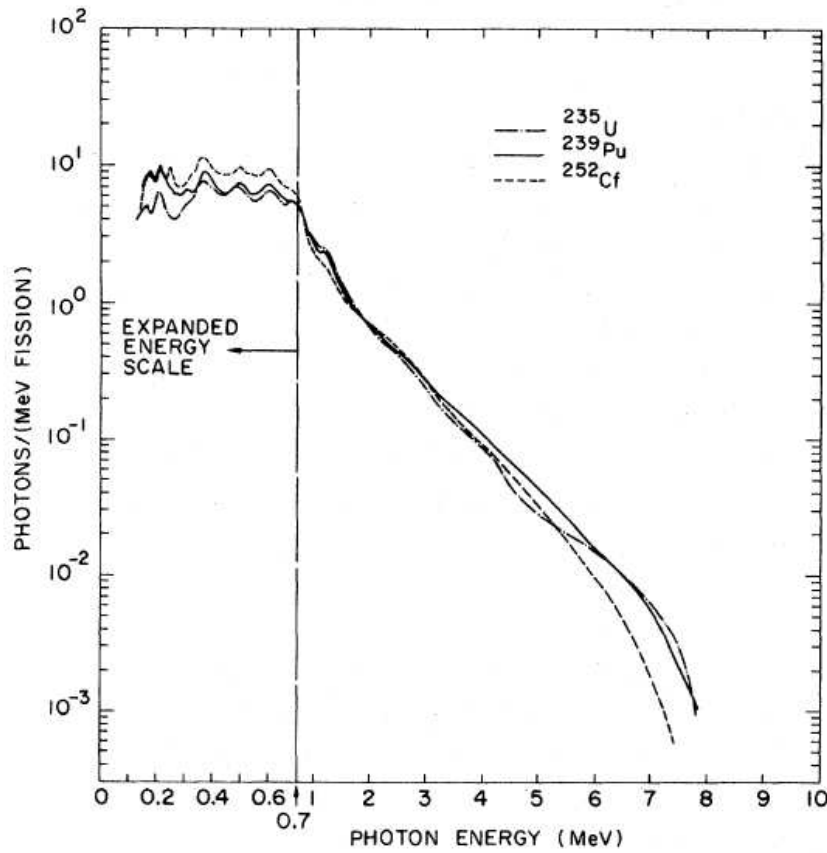


Figure 18.4: Prompt gamma-ray spectra for spontaneous fission. Figure taken from [212].

Table 18.5: The average total energy, average number of prompt gamma-rays, and average single gamma energy in spontaneous fission. All values from Ref. [132]

Isotope	$\langle \sum E_\gamma \rangle$ (MeV)	$\langle n_\gamma \rangle$	$\langle E_\gamma \rangle$ (MeV)
^{238}U	6.06 ± 0.03	6.36 ± 0.47	0.95 ± 0.07
^{252}Cf	6.95 ± 0.3	7.98 ± 0.4	0.87 ± 0.02

value A in the exponential was set to 10 in all cases to approximate the measured distributions. The value m in the exponential was adjusted so that using A , m , and $\langle \sum E_\gamma \rangle$ as input parameters for a given nucleus, the resultant Monte Carlo spectra nearly matched the measured values for $\langle n_\gamma \rangle$ and $\langle E_\gamma \rangle$. Figures 18.5 & 18.6 show the results of the Monte Carlo and the show the agreement achieved using the three input parameters to generate the gamma spectra with the correct characteristics.

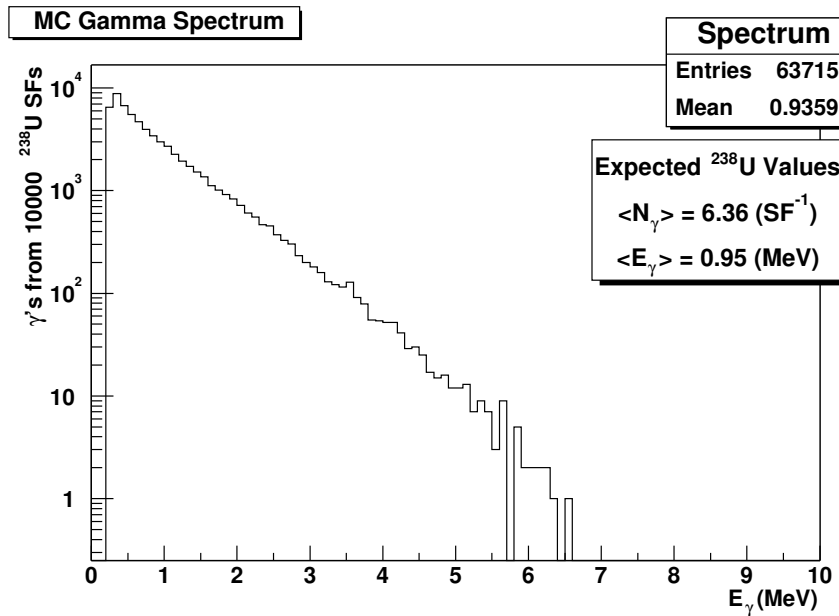


Figure 18.5: Monte Carlo of the prompt gamma-ray spectrum from spontaneous fission of ^{238}U . Comparing the number of entries divided by 10000 and the Mean to the expected values, shows the agreement achieved between the Monte Carlo and the measured spectrum characteristics.

18.2.3 Beta Decays of Spontaneous Fission Fragments

Fission fragments are generally neutron rich and thus are unstable to beta decay. In considering the beta decay of these fragments begin by noting that fission usually produces two initial fragments. Thus there are generally only two *chains* of beta decays to consider. Unlike the prompt gamma-rays, the beta decay half-lives are on the order of microseconds to days and thus are unlikely to overlap within a single SNO event. Thus each beta decay can be considered separately in determining the efficiency for creating a detected SNO event. One caveat is that these beta decays are often accompanied by a gamma-ray which will increase the produced Čerenkov light and thus increase the probability that SNO will register an event. Refs. [81, 194, 114] give examples of the beta spectrum, however this is currently not dealt with quantitatively. So long as the (weighted) majority of fission fragments have beta decay half-lives on the order of seconds, the results of this chapter will remain largely correct. A review of the most likely ^{238}U fission fragments ($A=92$ and $A=143$ with $\approx 39\%$ proton content) show this is a qualitatively correct supposition.

18.3 Efficiency to Detect Spontaneous Fission in SNO

The neutron multiplicity distributions of Section 18.2.1 and the sets of gamma-rays generated in the Monte Carlo of Section 18.2.2 were combined as inputs to the Monte Carlo of the SNO detector. Figure 18.7 shows

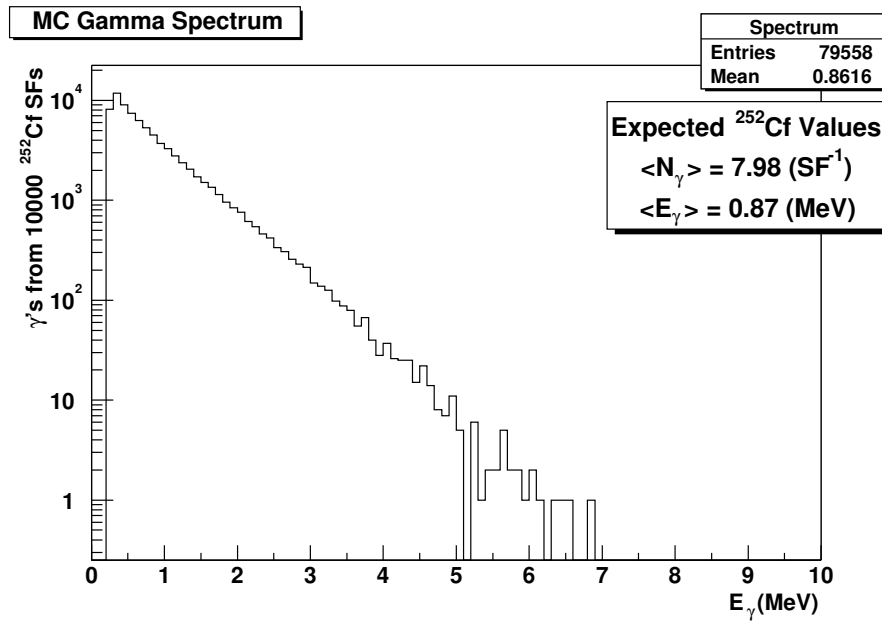


Figure 18.6: Monte Carlo of the prompt gamma-ray spectrum from spontaneous fission of ^{252}Cf . Comparing the number of entries divided by 10000 and the Mean to the expected values, shows the agreement achieved between the Monte Carlo and the measured spectrum characteristics.

the N_{hit} response of the detector to the gammas from spontaneous fission of ^{238}U and ^{252}Cf . The results of the Monte Carlo are the fraction of coincidence events detected within the signal region for spontaneous fissions. Tables 18.6, 18.7, 18.8, & 18.9 show the expected coincidence detection efficiency for ^{238}U and ^{252}Cf in the Pure D_2O and Salt phases of the SNO experiment.

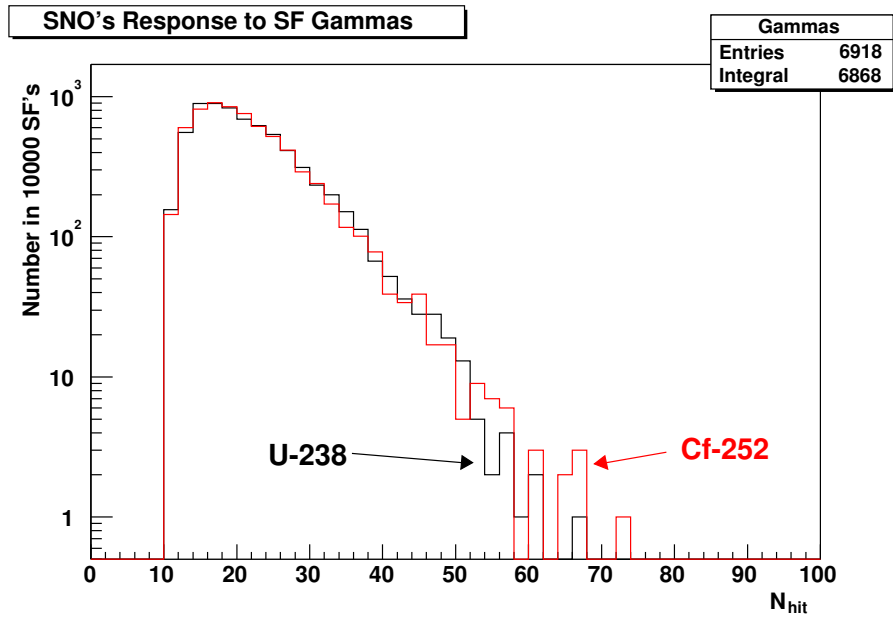


Figure 18.7: Monte Carlo response to prompt gamma-rays from spontaneous fission of ^{238}U & ^{252}Cf .

Table 18.6: Monte Carlo detection efficiency for ^{238}U spontaneous fission in the Pure D_2O phase. The top table is for the Standard signal region and the bottom table is for the Enlarged signal region.

$N_{hit}(0)$	0	1	2	3	4
25	0.5538	0.3226	0.1021	0.0201	0.0012
30	0.5885	0.3099	0.0865	0.0142	0.0007
35	0.6197	0.2941	0.0749	0.0110	0.0001
40	0.6598	0.2735	0.0596	0.0068	0.0001
45	0.7197	0.2360	0.0409	0.0032	0
25	0.5183	0.3431	0.1151	0.0214	0.0019
30	0.5566	0.3280	0.0979	0.0157	0.0016
35	0.6005	0.3090	0.0790	0.0107	0.0006
40	0.6650	0.2721	0.0566	0.0059	0.0002
45	0.7441	0.2219	0.0315	0.0022	0.0001

Table 18.7: Monte Carlo detection efficiency for ^{252}Cf spontaneous fission in the Pure D_2O phase. The top table is for the Standard signal region and the bottom table is for the Enlarged signal region.

$N_{\text{hit}}(0)$	0	1	2	3	4	5	6	7
25	0.3930	0.3347	0.1809	0.0731	0.0152	0.0022	0.0007	0
30	0.4155	0.3369	0.1698	0.0630	0.0123	0.0019	0.0004	0
35	0.4418	0.3325	0.1619	0.0527	0.0091	0.0015	0.0003	0
40	0.4824	0.3277	0.1430	0.0402	0.0058	0.0005	0.0002	0
45	0.5466	0.3181	0.1083	0.0241	0.0025	0.0002	0	0
25	0.3385	0.3426	0.2048	0.0870	0.0221	0.0039	0.0008	0.0001
30	0.3682	0.3438	0.1923	0.0749	0.0171	0.0030	0.0005	0
35	0.4135	0.3425	0.1712	0.0591	0.0114	0.0018	0.0003	0
40	0.4815	0.3337	0.1388	0.0386	0.0063	0.0008	0.0001	0
45	0.5884	0.2989	0.0923	0.0181	0.0019	0.0002	0	0

Table 18.8: Monte Carlo detection efficiency for ^{238}U spontaneous fission in the Salt phase. The top table is for the Standard signal region and the bottom table is for the Enlarged signal region.

$N_{\text{hit}}(0)$	0	1	2	3	4	5	6
25	0.2763	0.3420	0.2478	0.1071	0.0234	0.0030	0.0002
30	0.2910	0.3526	0.2415	0.0963	0.0166	0.0017	0.0001
35	0.3066	0.3618	0.2333	0.0832	0.0137	0.0011	0.0001
40	0.3305	0.3708	0.2178	0.0690	0.0110	0.0007	0
45	0.3691	0.3794	0.1928	0.0516	0.0066	0.0003	0
25	0.1457	0.3251	0.3126	0.1687	0.0419	0.0056	0.0002
30	0.1633	0.3446	0.3078	0.1481	0.0325	0.0034	0.0001
35	0.1923	0.3635	0.2914	0.1253	0.0251	0.0021	0.0001
40	0.2335	0.3856	0.2656	0.0976	0.0164	0.0011	0
45	0.3086	0.3982	0.2197	0.0643	0.0083	0.0007	0

Table 18.9: Monte Carlo detection efficiency for ^{252}Cf spontaneous fission in the Salt phase. The top table is for the Standard signal region and the bottom table is for the Enlarged signal region.

$N_{\text{hit}}(0)$	0	1	2	3	4	5	6	7	8
25	0.1453	0.1852	0.2317	0.2133	0.1468	0.0567	0.0172	0.0030	0.0006
30	0.1499	0.1954	0.2354	0.2123	0.1384	0.0515	0.0146	0.0019	0.0004
35	0.1574	0.2082	0.2413	0.2087	0.1270	0.0436	0.0117	0.0017	0.0002
40	0.1710	0.2262	0.2519	0.1986	0.1060	0.0372	0.0077	0.0010	0.0002
45	0.1988	0.2511	0.2629	0.1771	0.0811	0.0239	0.0042	0.0005	0.0002
25	0.0445	0.1078	0.2036	0.2577	0.2211	0.1156	0.0401	0.0082	0.0012
30	0.0516	0.1227	0.2185	0.2625	0.2036	0.1021	0.0321	0.0062	0.0005
35	0.0644	0.1439	0.2400	0.2627	0.1784	0.0832	0.0234	0.0036	0.0002
40	0.0872	0.1809	0.2672	0.2439	0.1477	0.0588	0.0120	0.0019	0.0002
45	0.1316	0.2359	0.2855	0.2081	0.1002	0.0317	0.0057	0.0010	0.0001

Chapter 19

ATMOSPHERIC NEUTRINO INDUCED BACKGROUNDS**19.1 Introduction and Review of Early Calculations**

As presented in Chapter 5, cosmic-ray interactions with the Earth's atmosphere generate neutrinos of the electron and muon flavors. Furthermore, Super-Kamiokande's atmospheric neutrino results imply muon neutrinos oscillate into tau neutrinos¹ [104, 105, 103, 106, 101]. Early studies by SNO Collaborators, suggested the atmospheric neutrino induced background rate was negligible for the primary solar neutrino analysis. However, the requirements for the electron antineutrino search are at the level of the estimated interaction rate. Atmospheric neutrino interactions are particularly troubling for the electron antineutrino analysis because neutral-current scattering events can break apart nuclei leaving free neutrons in the detector without a Čerenkov signature that can be used to veto the event. This chapter reviews the early calculations and then presents a more recent and improved treatment of atmospheric neutrino interactions in the SNO detector.

Table 19.1: The calculated quasi-elastic interaction rate in the SNO detector from various flavors of atmospheric neutrinos as provided by Ref. [97]. The oscillation calculation uses $\Delta m^2 = 3.2 \times 10^{-3} \text{ eV}^2$ and $\sin^2 2\theta_{\text{atmo.}} = 1$.

Neutrino	Flux (m^2yr^{-1})	Total CC Rate ($\text{kt} \cdot \text{yr}^{-1}$)	CC Rate w/ Osc. ($\text{kt} \cdot \text{yr}^{-1}$)	Total NC Rate ($\text{kt} \cdot \text{yr}^{-1}$)
ν_e	4851.8	47.75	47.75	17.42
$\bar{\nu}_e$	4303.2	14.35	14.35	7.25
ν_μ	9505.19	76.71	51.31	33.78
$\bar{\nu}_\mu$	9467.2	26.52	17.78	16.15

For the purposes of publication of the SNO Collaboration's Pure D₂O phase results, a number of efforts were mounted to determine the expected rate of neutrons generated by atmospheric neutrinos. This work culminated in Refs. [99, 97] and was largely supported by earlier work [221, 219, 220, 164]. The atmospheric neutrino, quasi-elastic, interaction rates were determined in Ref. [99] using Bartol Group [7] atmospheric neutrino fluxes for energy ranges 50 MeV to 10 GeV during the solar maximum (i.e. minimum cosmic ray flux). Table 19.1 presents the results of these quasi-elastic interaction rate calculations. The deep-inelastic scattering rate was considered in Refs. [219, 220], however it was not actually taken into account in the final neutron production rate estimation presented in [99]. In all cases it was reasonably assumed that only neutral-current processes would contribute untagged neutrons to the primary solar analysis. The conclusion was an

¹*CPT* is considered a good symmetry in this chapter.

expectation of 5.4 ± 1.0 neutrons / year that will be detected and are thus a background to the SNO solar neutrino analysis.

The efforts described above, unfortunately, lacked two important pieces, making an extension to a calculation of the expected background to the electron antineutrino analysis difficult. First, resonant, deep-inelastic, coherent, diffractive, and elastic scattering processes are ignored. These processes *will* produce a multiplicity of particles - the main concern for the electron antineutrino analysis. Second, knowledge of the final out-going particle states were not known. Knowing the distribution and energies of the product particles produced by an atmospheric neutrino interaction would allow simulation of the product particles in the SNO Monte Carlo program.

19.2 NUANCE and SNO's Monte Carlo Extension

The use of a public neutrino interaction generator called NUANCE [70], allows for the simulation of all atmospheric neutrino (quasi-elastic, resonance, deep-inelastic, coherent, diffractive, and elastic scattering) interactions *and* supplies the final particle states. The final particle states are essential to modeling the SNO detector's response and detection efficiencies using the SNO Monte Carlo program. NUANCE will simulate neutrino interactions from 50 MeV to several TeV.

19.2.1 NUANCE Input Parameters and Output Results

J. Formaggio and N. S. Oblath have been primarily responsible for implementing NUANCE with a SNO detector geometry. The input parameter information provided in this subsection is presented because future refinements of the method are expected. Further details on these parameters can be found in Ref. [98]. Table 19.2 provides the values used for the adjustable input parameters and the description of the target detector in the NUANCE neutrino simulator. The 850 cm radius is the entire region inside the array of photomultiplier tubes.

Provided with a target detector description, the NUANCE neutrino interaction simulator calculates the interaction rates and branching fractions for final states. The output consists of a record of all the neutrino interactions present and, most importantly, a list of all the particles present in the final state including individual particles with energies. Figure 19.1 displays the raw NUANCE multiplicities. Figure 19.1 shows that the vast majority of NUANCE events are best described as an out-going lepton plus other particles. The other particles are usually a single nucleon, a single gamma, and/or multiple pions. Pions are the reason for large multiplicities in the raw NUANCE output.

19.2.2 SNO Monte Carlo of NUANCE Events

The particle list generated for each NUANCE event was input into the SNO Monte Carlo. This allowed for the determination of the efficiency for detecting NUANCE events as either single or coincidence events. The FLUKA hadron package, implemented in the SNO Monte Carlo, handles free nucleon interactions for neutron and proton kinetic energies above 20 MeV. Additionally, this Monte Carlo will handle pion propagation, pion spallation, pion decay, muon propagation, muon spallation, muon decay, and negative muon capture. The processes specifically high-lighted above are the major processes of concern in a full atmospheric neutrino

Table 19.2: NUANCE input parameters used for atmospheric neutrino simulation and the description of the target SNO detector.

Physics Parameter	Setting
Vector & Axial Mass	0.84 GeV/c ² & 1.03 GeV/c ²
Atmospheric Flux < 10 GeV	1998 Bartol Group at Sudbury
Atmospheric Flux > 10 GeV	1996 Bartol Group at Sudbury
Energy Range	50 MeV to 200 GeV
Oscillation Parameters	
δm_{12}^2 δm_{32}^2 CP	5×10^{-5} 3×10^{-3} 0
θ_{12} θ_{23} θ_{13}	$\pi/4$ $\pi/4$ 0
Detector Parameter	Setting
Size	850 cm radius sphere
Depth Underground	2 km
Materials	D ₂ O, Acrylic (C ₂ O ₃ H ₂), H ₂ O
Fermi Momentum	225 MeV/c (O & C only)
Binding Energy	27 MeV/c (O & C only)

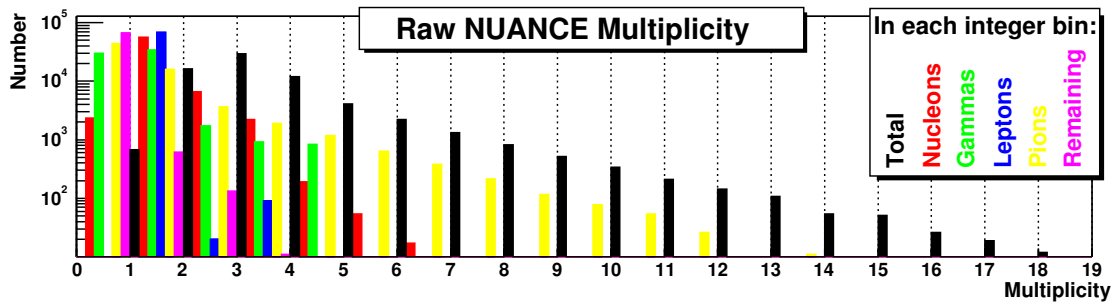


Figure 19.1: Raw NUANCE multiplicities for atmospheric neutrino interactions. The “Total” distribution will *always* include one out-going lepton and at least one other particle, hence the apparent +2 shift right.

simulation. Figures 19.2 & 19.3 present the SNO detector’s N_{hit} response to the particles produced by the NUANCE simulations.

Table 19.3 details the SNO Monte Carlo processing. There are five categories of Monte Carlo failure. To understand the nature of the failures and to account for the failures in the calculation of the electron antineutrino background each failure mode is reviewed and addressed.

The store full error is a over-flow of the (FORTRAN) Monte Carlo program’s allocated memory. It is expected that this failure mode is correlated with large numbers of particles and photons needing to be propagated. Thus store fulls are expected to have a correlation with high-energy neutrinos. There are a

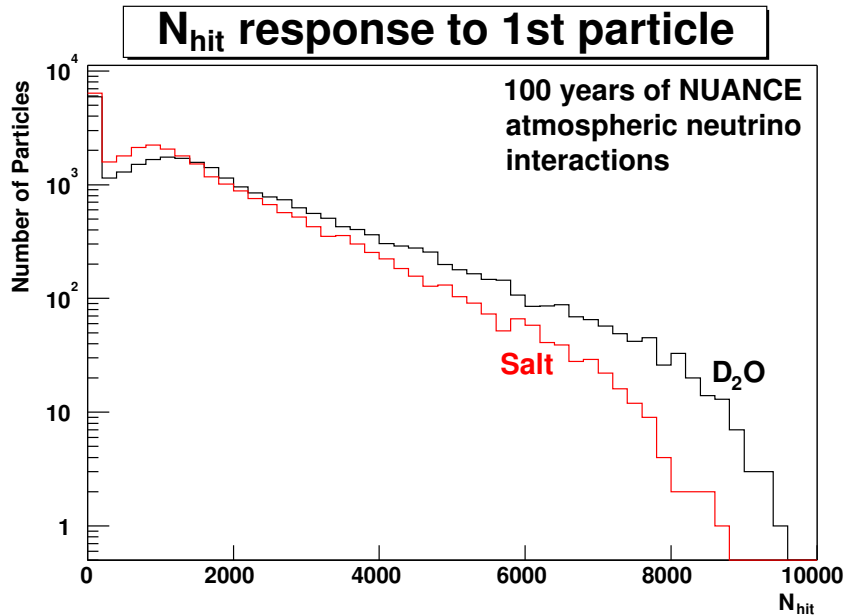


Figure 19.2: The N_{hit} response to the first particle from a atmospheric neutrino interaction. The 100 year sample was for atmospheric neutrino interactions inside a radius of 850 cm. The reduced N_{hit} response for the Salt phase is due to a known reduction from aging equipment and material in the water.

Table 19.3: Breakdown of Monte Carlo errors and output. The *a priori* cut eliminates NUANCE events prior to simulation in the SNO Monte Carlo based upon particular particles and their energies in the given events. See the detailed text in Section 19.2.2.

Events	Pure D ₂ O	Salt
Total NUANCE	45628	45628
Store full	183 $\xrightarrow{\text{a priori}}$ 0	52 $\xrightarrow{\text{a priori}}$ 0
Fatal geometry - Point outside region	165 \longrightarrow 0	154 \longrightarrow 0
Fatal geometry - PMT tracking	472 \longrightarrow 88	373 \longrightarrow 86
Fatal geometry - Error in primitive routine	6 \longrightarrow 3	2 \longrightarrow 1
Successful	44802	45047

number of geometry failure modes. Geometry errors are due to particles finding “holes” in the detector geometry descriptions, causing the event to fail. The exemplar of these failure modes is a single Čerenkov photon finding a “hole” in the geometry of the photomultiplier tube support structure which is composed of many (inhomogeneous) parts. For this reason, geometry errors are expected to be independent of the

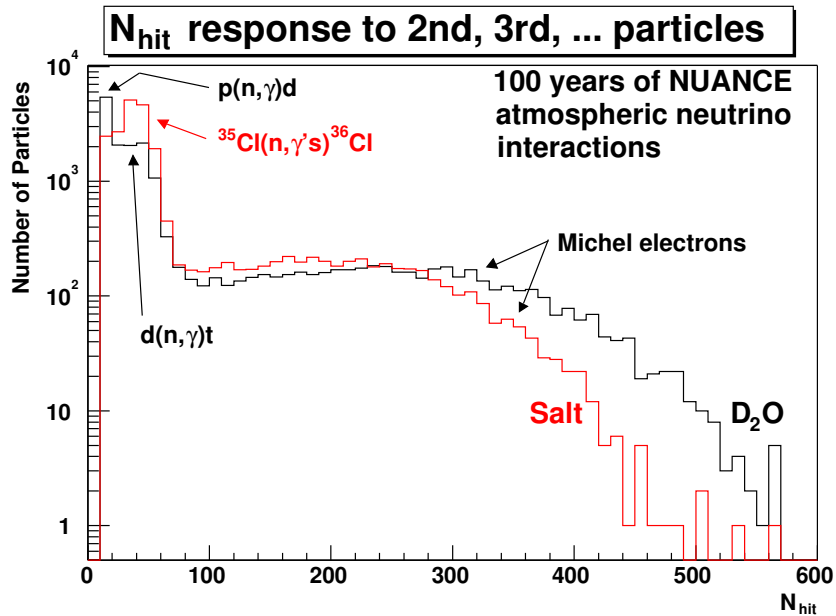


Figure 19.3: N_{hit} response to the second and later particles from a atmospheric neutrino interaction. See Figure 19.2 for details. Note one can see the effect on the neutron capture from the addition of salt.

NUANCE event that is input. However, there is a caveat. An event with 6000 Čerenkov photons is less likely to fail due to a geometry error than an event having 6,000,000 Čerenkov photons simply because the former has fewer photons that could potentially find a “hole” in the geometry description.

A Priori Elimination of NUANCE Events as Background Contributors

The difficulty in correctly simulating NUANCE events in the SNO Monte Carlo has motivated a set of studies aimed at circumventing complete reliance on the Monte Carlo program. Specifically, for the electron antineutrino analysis, a requirement that no event with greater than 150 N_{hit} appear before an $\overline{\text{CC}}$ candidate coincidence (Section 14.1). This upper limit on the N_{hit} value is based upon knowledge that positrons produced by $\overline{\text{CC}}$ reactions of electron antineutrinos in the ${}^8\text{B}$ energy range (< 15 MeV), will all fall below this N_{hit} value. It then becomes obvious that positrons (or electrons) above, say, 50 MeV will always be above this upper limit on the N_{hit} . The same is true for gamma-rays. To extend this rationale to other particles, two studies were made. The first study simulated 15,000, negative muons with energies of 500 MeV and produced inside a radius of 800 cm. This study showed that only 43 negative muons had a N_{hit} value less than 150. Of these 43 negative muons, 2 were generated at a radius ≈ 660 cm while the remaining 41 negative muons were all generated at a radius greater than 720 cm. Thus, it is concluded that, to good approximation, NUANCE events containing a charged muon at or above 500 MeV can *a priori* be eliminated from contributing to any

background to the electron antineutrino analysis. The second study simulated 6000, neutral pions, π^0 , with energies of 500 MeV and produced inside a radius of 800 cm. This study showed that only 29 neutral pions had a N_{hit} value less than 150. These 29 pions were all generated at a radius greater than 720 cm. Thus, it is concluded that, to good approximation, NUANCE events containing a neutral pion at or above 500 MeV can *a priori* be eliminated from contributing to any background to the electron antineutrino analysis. In both studies, the number of simulated particles was chosen to approximately equal the total number of that type of particle in the 100 year NUANCE event sample. Table 19.4 summarizes particles and energy thresholds that, if present in a NUANCE event, will eliminate the event as a potential background contributor to the electron antineutrino analysis. A cautionary note: charged pions do *not* appear to be candidates for this sort

Table 19.4: *A priori* elimination of atmospheric neutrino events as background contributors to the electron antineutrino analysis. A NUANCE event containing one of the following can be assumed to not contribute to the background of the electron antineutrino analysis.

Particle(s)	Energy (MeV)
$e^- e^+$	≥ 50
γ	≥ 50
$\mu^- \mu^+$	≥ 500
π^0	≥ 500

of *a priori* elimination. Small sample studies indicate charged pions can regularly appear below the 150 N_{hit} upper limit. It is speculated that strong interactions of charged pions with nuclei accounts for this and that the N_{hit} signature of neutral pions is due to their decay to gammas. In the future, this *a priori* elimination may be used to lessen the Monte Carlo over-head, but in this analysis it is only used to address the Monte Carlo failure modes. Another *a priori* way to eliminate failure modes is recognizing that failures increase as the simulated particles are located close to the photomultiplier tube support structure. Near the support structure, the events are located in the light water that surrounds the acrylic vessel. Studies have shown that 19 MeV neutrons produced in the light water travel no further than 10 - 20 cm before capturing on protons. Thus it is expected that NUANCE events occurring outside a radius of 650 cm will rarely contribute to the background of an electron antineutrino analysis. This expectation is confirmed by the results presented in Section 19.2.3. Thus one can consider limiting the fiducial volume simulated in atmospheric neutrino studies. In the present case, this additional *a priori* radial requirement eliminates Monte Carlo failures occurring outside a radius of 650 cm. The affect of these *a priori* requirements on the NUANCE and SNO Monte Carlo simulations is presented in Table 19.3.

19.2.3 Results: Backgrounds to the $\overline{\text{CC}}$ Signal

From the fully processed NUANCE events, the Standard and Enlarged analysis cuts developed in Chapters 11 – 14 are applied and coincidences are extracted. The results are presented in Tables 19.5 & 19.6. The background to the electron antineutrino analysis is given by dividing the entries in the summary tables by 100 years and multiplying by the live fraction of a year for each analysis phase.

Table 19.5: $\overline{\text{CC}}$ backgrounds in the Pure D₂O phase from 100 years of atmospheric neutrino interactions. The particle heading is the primary out-going lepton from the NUANCE interaction. Thus, charged leptons indicate charged-current interactions and neutrinos indicate neutral-current interactions. All numbers are reported as the number of events inside the acrylic vessel *plus* the number of events outside the acrylic vessel but within 250 cm of the acrylic vessel, $N_{r < (600 \text{ cm})} + N_{(600 \text{ cm}) < r < (850 \text{ cm})}$. The “S” and “E” headings stand for the Standard and Enlarged analyses. The results are given as a function of the multiplicity, \mathcal{M} .

\mathcal{M}	e^-		e^+		ν_e		$\bar{\nu}_e$	
	S	E	S	E	S	E	S	E
1	1+0	1+0			427+2	727+40	110+2	207+16
2					18+0	82+0	9+0	19+0
3					4+0	18+0	2+0	8+0
4						1+0		
5								
> 5								
\mathcal{M}	μ^-		μ^+		ν_μ		$\bar{\nu}_\mu$	
	S	E	S	E	S	E	S	E
1	61+2	92+5	8+3	14+5	422+9	713+53	197+5	321+23
2	3+1	6+1		1+0	25+0	75+0	20+0	46+1
3		2+0		1+0	4+0	14+0	2+0	13+0
4						4+0		1+0
5						0+0		1+0
> 5						1+0		
\mathcal{M}	τ^-		τ^+		ν_τ		$\bar{\nu}_\tau$	
	S	E	S	E	S	E	S	E
1					192+2	318+17	91+2	146+13
2					14+0	41+0	6+0	20+1
3					1+0	6+0	2+0	3+0
4						1+0		1+0
5								
5 >								
\mathcal{M}	Charged Currents		Neutral Currents		Total			
	S	E	S	E	S	E		
1	70+5	107+10	1329+22	2225+162	1399+27	2332+172		
2	3+1	7+1	83+0	264+2	86+1	271+3		
3		3+0	13+0	54+0	13+0	57+0		
4				8+0		8+0		
5				1+0		1+0		
> 5				1+0		1+0		

Table 19.6: \overline{CC} backgrounds in the Salt phase from 100 years of atmospheric neutrino interactions. See Table 19.5 for the table definitions.

\mathcal{M}	e^-		e^+		ν_e		$\overline{\nu}_e$	
	S	E	S	E	S	E	S	E
	5793+1493		1643+513		2060+3221		815+1226	
1	1+0	1+0	2+0	2+0	333+14	559+54	125+5	206+23
2		1+0			52+1	118+5	19+0	52+0
3					15+0	36+1	9+0	19+0
4					1+0	6+0	1+0	3+1
5					2+0	4+0	1+0	0+0
> 5						2+0		1+0

\mathcal{M}	μ^-		μ^+		ν_μ		$\overline{\nu}_\mu$	
	S	E	S	E	S	E	S	E
	7320+2366		2475+889		2886+4627		1309+2019	
1	83+2	121+10	22+3	27+6	408+11	697+66	196+9	293+28
2	16+0	27+0	3+0	11+1	87+0	176+9	54+0	96+3
3	0+0	7+0	1+0	1+0	14+0	63+2	10+0	33+0
4	1+0	5+0			5+0	16+0	2+0	16+0
5					0+0	2+0	1+0	3+0
> 5					1+0	4+0		2+0

\mathcal{M}	τ^-		τ^+		ν_τ		$\overline{\nu}_\tau$	
	S	E	S	E	S	E	S	E
	44+67		22+32		1267+2044		594+903	
1					204+12	325+31	107+1	159+15
2					38+0	86+3	20+0	50+1
3					13+0	30+0	7+0	18+0
4					2+0	10+0	1+0	6+0
5						3+0	0+1	1+0
> 5						1+0		1+1

\mathcal{M}	Charged Currents		Neutral Currents		Total	
	S	E	S	E	S	E
	17297+5360		8931+14040		26228+19400	
1	108+5	151+16	1373+52	2239+217	1481+57	2390+233
2	19+0	39+1	270+1	578+21	289+1	617+22
3	1+0	8+0	68+0	199+3	69+0	207+3
4	1+0	5+0	12+0	57+1	13+0	62+1
5			4+1	13+0	4+1	13+0
> 5			1+0	11+1	1+0	11+1

Corrections and Systematic Errors

Section 19.2.2 discusses failure modes of the SNO Monte Carlo in simulating NUANCE events. The results given in Tables 19.5 & 19.6 must be corrected for these simulation related failures. As discussed in Section 19.2.2, those failures arising from errors in the geometry are not expected to be biased to any class

of events. Thus the remaining 91 (D₂O) and 87 (Salt) Monte Carlo failures are treated as background contributors *in the same proportion as the successful events*. The contribution is, however, only in the positive direction. Thus a one sided (positive) uncertainty is assigned, $\sigma_{\text{fail}} = N_{\text{fail}} \times N_{\text{bkgrnd}} / N_{\text{successful}}$. It will turn out this is negligible in comparison to the atmospheric neutrino flux uncertainty.

N. S. Oblath has studied [168] the affect of varying the NUANCE input parameters on the expected interaction rate of atmospheric neutrinos in the SNO detector. The varied input parameters include neutrino oscillation parameters (θ_{12} , Δm_{12}^2 , θ_{23} , Δm_{23}^2), the axial mass, Pauli suppression, resonance uncertainty, and the total atmospheric neutrino flux. The total flux uncertainty dominates the derived systematic uncertainties of $\pm 27\%$ for charged-current (CC) interactions and $\pm 30\%$ for neutral-current (NC) interactions. The uncertainties were treated as independent. To determine the overall systematic error on the results obtained, the CC and NC event rates are individually varied and added together, rather than adding the errors in quadrature:

$$N_{\text{Total}}^{\pm} = (\pm 0.27)N_{\text{CC}} + (\pm 0.30)N_{\text{NC}} \quad (19.1)$$

Table 19.7 presents the estimated $\overline{\text{CC}}$ background counts from 100 years of atmospheric neutrino interactions taking into account the two uncertainties.

Table 19.7: Estimated $\overline{\text{CC}}$ backgrounds from 100 years of atmospheric neutrino interactions in SNO.

	Pure D ₂ O		Salt	
	Standard	Enlarged	Standard	Enlarged
Background counts $\Sigma_{\mathcal{M}=2,3}$	100	331	359	859
Failure mode systematic	+0.2	+0.7	+0.7	+1.6
CC Flux uncertainty	± 1.1	± 3.0	± 5.4	± 13.0
NC Flux uncertainty	± 28.8	± 96.0	± 101.7	± 240.3
Results	100 ± 30	331 ± 99	359 ± 107	859 ± 253

Chapter 20

BACKGROUNDS FROM (α, n) REACTIONS

During the construction phase of the SNO experiment the acrylic vessel was exposed to air containing radon. Radon (^{222}Rn) decaying via α emission becomes a negatively charged ion of polonium (^{218}Po). The polonium can electrostatically plate out on the acrylic vessel. Once situated on the acrylic vessel, the ^{218}Po will implant in the acrylic upon further decays. The ^{218}Po rapidly ($\sum_i (t_{1/2})_i \approx 50$ minutes) reaches ^{210}Pb , having a 19.4 year half-life. Two further β decays transforms ^{210}Pb into ^{210}Po . The 5.3 MeV α 's produced by ^{210}Po located on the surfaces of the acrylic vessel are a concern due to the possibility of their initiating (α, n) reactions on isotopes of carbon and oxygen.

The chemical composition of the acrylic vessel is $(\text{C}_5\text{H}_8\text{O}_2)_n$ having a molecular weight of 100.1. It is assumed that the acrylic is made from *naturally abundant* carbon, hydrogen and oxygen. Table 20.1 gives the isotopic content of the acrylic based upon this information.

Table 20.1: Elemental and mass fractions of isotopes in the acrylic vessel.

Isotope	Natural Abundance (%) [89]	Acrylic Mass Fraction
^{12}C	98.90(3)	0.5932
^{13}C	1.10(3)	0.0066
^{16}O	99.762(15)	0.3189
^{17}O	0.038(3)	0.0001
^{18}O	0.200(12)	0.0006

20.1 $^{13}\text{C}(\alpha, n)^{16}\text{O}$

The $^{13}\text{C}(\alpha, n)^{16}\text{O}$ reaction is of particular concern for the electron antineutrino analysis because 15.5% of the reactions leave the ^{16}O nucleus in an excited state which can decay by either e^+e^- pair emission from a 6.049 MeV state or γ emission from a 6.130 MeV state [154]. The Q-values to reach these two excited states are 5.014 and 5.095, respectively, just below the 5.3 MeV α decay energy of ^{210}Po . In Ref. [154] a ^{238}Pu α source was used induce the $^{13}\text{C}(\alpha, n)^{16}\text{O}$ reaction. The primary α decay energies of ^{238}Pu are 5.499 and 5.455. That work determined a 7:1 ratio of e^+e^- pair emission to γ emission.

For the primary solar neutrino analysis, the ingress of neutrons from regions and processes external to the heavy water volume was studied as a background to the NC signal. One of these studies [187] reports the total neutron rate from the acrylic vessel based upon a combined fit to the known solar neutrino induced

and background signals. Specifically, a probability density function for neutrons generated near the acrylic vessel was calculated via Monte Carlo. The magnitude of this probability density was allowed to float in a combined fit to the solar neutrino signals and other known backgrounds. The results from the Pure D₂O and Salt phase are $39.3 \pm 50.8^{+28.4}_{-29.3}$ and $84.5^{+34.5}_{-33.6}$ neutrons inside the published energy and fiducial volumes, Ref. [187] & [12], respectively. The errors reported for the Pure D₂O phase are statistical and systematic, respectively, while the Salt phase errors combine the statistical and systematic errors.

A second, related study determines the number of neutrons generated from deuteron photo-disintegration induced by gamma-rays from outside the D₂O volume (i.e. acrylic vessel, H₂O and PSUP). This analysis determines a neutron rate by looking at the Čerenkov signature of β and γ radiation in the H₂O and from the acrylic vessel [10, 92] (references for Pure D₂O and Salt phases, respectively). The results from the Pure D₂O and Salt phase are 27^{+8}_{-8} and 50^{+17}_{-20} neutrons inside the published energy and fiducial volumes. The neutrons accounted for by the processes in this second study are subtracted from the total neutron rate determined by the fit giving $12.3^{+58.7}_{-59.2}$ and $34.5^{+38.5}_{-39.1}$. These remaining neutrons are attributed to (α, n) reactions on the acrylic vessel. Clearly the attribution is not well determined and it may be most responsible to study the (α, n) rate assuming all the fit “external” neutrons come from (α, n) reactions. Either way, to determine the ¹³C (α, n) ¹⁶O rate a number of efficiencies are determined and used in combination with information on the acrylic vessel composition and reaction branching ratios.

20.1.1 A ¹³C (α, n) ¹⁶O Monte Carlo

A Monte Carlo of the 6.049 MeV e^+e^- pair emission from the ¹⁶O state produced in the ¹³C (α, n) ¹⁶O reaction was developed. It is assumed that these reactions take place on the inner and outer surfaces of the acrylic vessel. The angle, $\theta_{e^+e^-}$, between the e^+e^- pair directions was generated with a weighting $1 + \cos(\theta_{e^+e^-})$. The e^+e^- pair and a neutron were generated at time zero and coincidence detection efficiencies were determined using the Standard and Enlarged analyses’ cuts for both the Pure D₂O and Salt Phases. It has been noticed [187] that Monte Carlo events generated on or very near the acrylic vessel produce a significantly reduced simulated N_{hit} signature. To account for this reduction, a second Monte Carlo of just e^+e^- pairs produced at a radius of 500 cm was created. The N_{hit} distribution for the e^+e^- pairs at $R_{\text{gen}} = 500$ cm and $R_{\text{gen}} = 600$ cm are shown in Figures 20.1 & 20.2, for the Pure D₂O and Salt phases respectively. An average scaling factor of 1.24 is used as a multiplier whenever a calculation relies upon the e^+e^- pair’s N_{hit} value (e.g. coincidence efficiencies). The radial fit positions of the e^+e^- pairs and the neutrons are the dominate factor in determining which events will contribute a coincidence inside the Standard and Enlarged analyses. The radial fit positions of the e^+e^- pairs and the neutrons are shown in Figures 20.3 & 20.4. The neutron capture time, Figure 20.5, is also slightly reduced in comparison to uniformly distributed neutrons (Chapters 11 & 16) and could be used as another handle on this background.

The physically interesting quantities determined from this Monte Carlo are listed in Table 20.2. This includes the efficiencies for detecting a e^+e^- pair and neutron as a coincidence in the Standard and Enlarged analyses. The bottom portion of Table 20.2 presents the single neutron detection efficiencies inside the published analysis regions. These single neutron detection efficiencies are used to determine the rate of (α, n) reactions on the acrylic vessel, assuming one knows the fraction of external neutrons inside the published analysis regions that are due to (α, n) reactions.

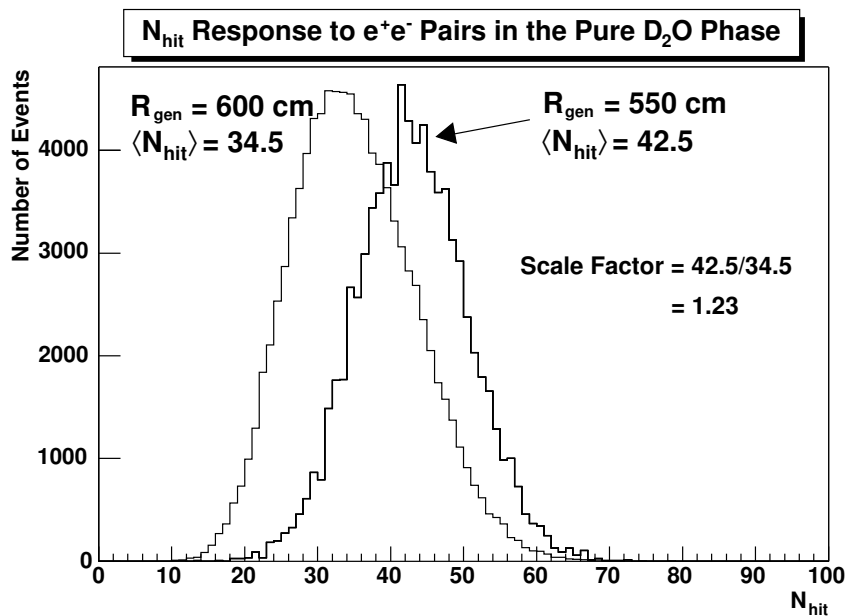


Figure 20.1: N_{hit} response to e^+e^- pairs in the Pure D_2O phase.

Table 20.2: Coincidence detection efficiencies for a e^+e^- pair and neutron produced at two radial positions. The number of significant figures on these results should not be taken as an indication of accuracy. The statistical errors on the efficiencies are given by $\sigma_i = (\varepsilon_i(1 + \varepsilon_i)/10^5)^{1/2}$. See the text for an explanation of the “Neutron” portion of the table.

	\mathcal{M}	Pure D_2O		Salt	
		Standard	Enlarged	Standard	Enlarged
$\varepsilon_{e^+e^-,n}^{\text{inner}}$	1	0.02924	0.29440	0.05904	0.34916
	2	0.00030	0.00954	0.00077	0.04435
	3		0.00002		0.00026
$\varepsilon_{e^+e^-,n}^{\text{outer}}$	1	0.01969	0.19467	0.03947	0.24049
	2	0.00010	0.00361	0.00037	0.01684
	3				0.00006

Neutrons	Pure D_2O	Salt
$\varepsilon_n^{\text{inner}}$	0.015	0.040
$\varepsilon_n^{\text{outer}}$	0.009	0.023

20.1.2 Estimate of the ^{13}C (α, n) ^{16}O Electron Antineutrino Background

The number of single neutrons detected, N_n^{det} , in the published SNO results from (α, n) reactions occurring on the inner and outer edges of the acrylic vessel is

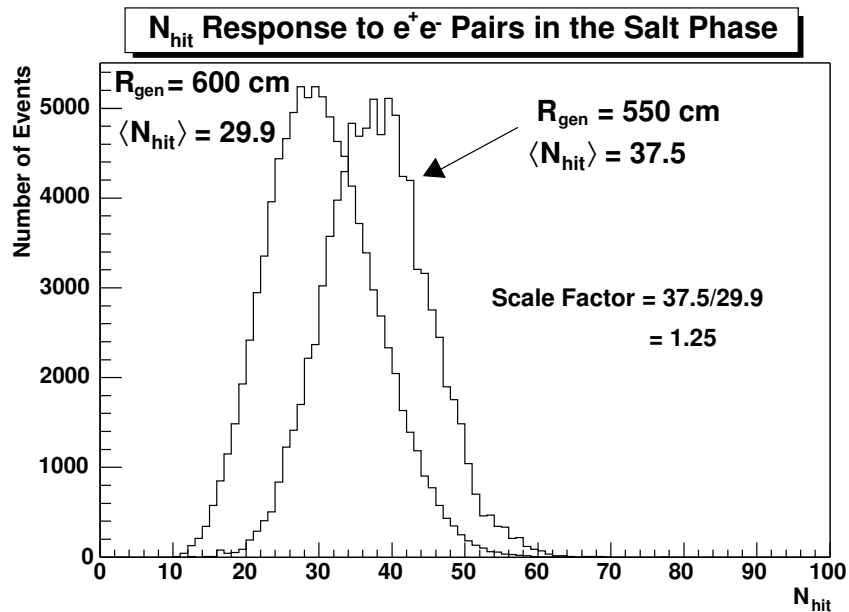


Figure 20.2: N_{hit} response to e^+e^- pairs in the Salt phase.

$$N_n^{det} = N_{(\alpha,n)}^{inner} \epsilon_n^{inner} + N_{(\alpha,n)}^{outer} \epsilon_n^{outer} \quad (20.1)$$

$$= N_{(\alpha,n)} (\epsilon_n^{inner} + \epsilon_n^{outer}) \quad \text{with} \quad N_{(\alpha,n)} = N_{(\alpha,n)}^{inner} = N_{(\alpha,n)}^{outer} \quad (20.2)$$

The simplifying second step is an assumption that the rate of (α, n) reactions is the same on the inner and outer edges of the acrylic vessel because equal quantities of radon daughters would have implanted on either side. The number of detected e^+e^- pair and neutron coincidences, $N_{e^+e^-,n}^{det}$, has a very similar formula

$$N_{e^+e^-,n}^{det} = N_{(\alpha,n)} f (\epsilon_{e^+e^-,n}^{inner} + \epsilon_{e^+e^-,n}^{outer}) \quad (20.3)$$

where the factor f accounts for:

- Relative fraction of neutrons from $^{nat}\text{C}(\alpha, n)$ as opposed to $^{nat}\text{O}(\alpha, n)$.
- Relative fraction of neutrons from $^{13}\text{C}(\alpha, n)^{16}\text{O}$ to the total $^{nat}\text{C}(\alpha, n)$.
- Branching ratios to the excited states in ^{16}O from $^{13}\text{C}(\alpha, n)^{16}\text{O}$ reactions.

In Ref. [188] it is reported that neutron yield from α bombardment of acrylic is $Y_{acrylic} = 0.512Y_C + 0.249Y_O$ and that the neutron yields from α bombardment of *naturally abundant* carbon and oxygen are 1.0×10^{-7}

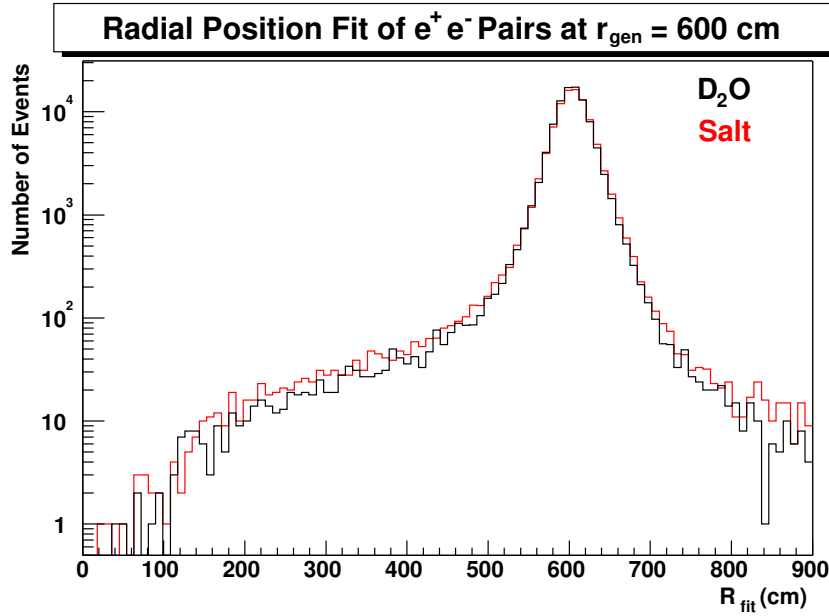


Figure 20.3: Radial fit position of e^+e^- pairs produced at $r = 600$ cm.

and 6.0×10^{-8} in units of neutrons per α . From this one can deduce that for every 100 neutrons that come from α bombardment of acrylic, 77.5 come from reactions with natural carbon and the remainder come from reactions with natural oxygen. Investigation shows α reactions with ^{12}C and ^{16}O are unlikely in the case studied here because

..., the fact that the spins of all nuclei concerned are zero and that at alpha-particle energies below 8 MeV the competing processes of proton and neutron emission are either excluded or extremely improbable because of the low available energy. [94]

For this reason it is assumed that 100% of the neutrons produced by α bombardment of *naturally abundant* carbon are due to reactions with ^{13}C . Finally, as already stated, only 15.5% of $^{13}\text{C} (\alpha, n) ^{16}\text{O}$ leave ^{16}O in an excited state. Of this 15.5%, the e^+e^- pair branch accounts for 7/8 of the decays. Thus the factor $f = 0.775 \times 1.0 \times 0.155 \times (7/8) = 0.1051$ is needed to correctly determine the e^+e^- pair rate from the total (α, n) rate. Combining equations (20.2) & (20.3) gives the e^+e^- pair and neutron coincidence detections based upon the total number of single neutrons detected in SNO's published results [10, 12]:

$$N_{e^+e^-,n}^{\text{det}} = N_n^{\text{det}} f \left(\frac{\mathcal{E}_{e^+e^-,n}^{\text{inner}} + \mathcal{E}_{e^+e^-,n}^{\text{outer}}}{\mathcal{E}_n^{\text{inner}} + \mathcal{E}_n^{\text{outer}}} \right) \quad (20.4)$$

Table 20.3 applies equation (20.4) and determines the number of e^+e^- pair and neutron coincidences that are a background to the electron antineutrino analysis. Note that the results of Table 20.3 assume that *all* neutrons

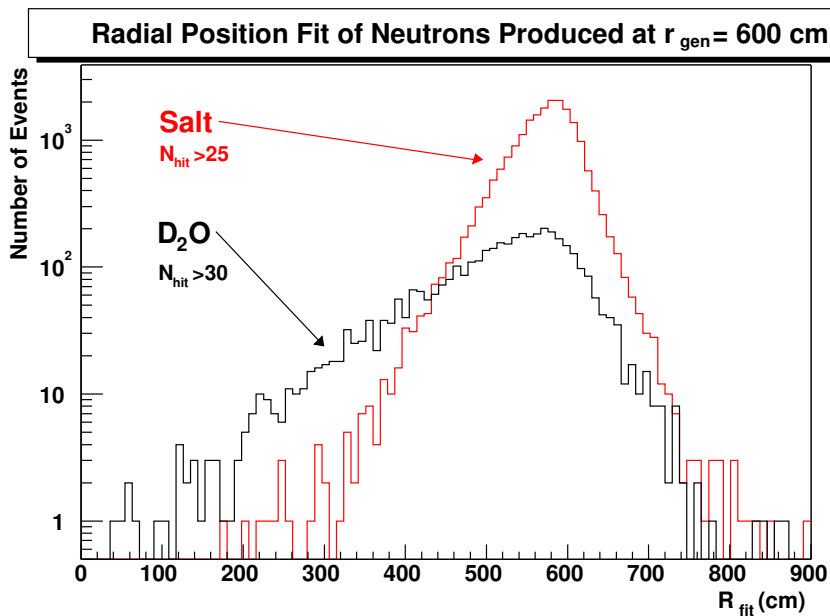


Figure 20.4: Radial fit position of neutrons produced at $r = 600$ cm.

Table 20.3: Backgrounds from $^{13}\text{C}(\alpha, n)^{16}\text{O}$ assuming all “external” neutrons reported in SNO’s published papers are due to (α, n) reactions.

Expected e^+e^- Pair and Neutron Coincidences		
Phase	Standard	Enlarged
Pure D ₂ O	0.07 ± 0.10	2.3 ± 3.4
Salt	0.16 ± 0.07	8.7 ± 3.5

attributed to the acrylic vessel and H₂O in the published results are due to (α, n) reactions. This assumption is a worst case scenario since it is expected that there are single neutrons generated just inside the acrylic vessel via photo-disintegration of deuterons. If one were to use the number of neutrons after the “external” photo-disintegration neutrons have been subtracted off, the results of Table 20.3 become those of Table 20.4.

20.2 $^{17,18}\text{O}(\alpha, n)^{20,21}\text{Ne}$

This (α, n) reaction should also represent a background to the electron antineutrino analysis in exactly the same way as the $^{13}\text{C}(\alpha, n)^{16}\text{O}$ reaction, studied in Section 20.1. However only 22.5% of the neutrons produced by α bombardment of acrylic are due to *naturally abundant* oxygen. This fact would reduce equation’s (20.3) factor f by a factor of $0.225/0.775 \approx 0.3$ in an analogous calculation. The (mass) ratio of ^{18}O

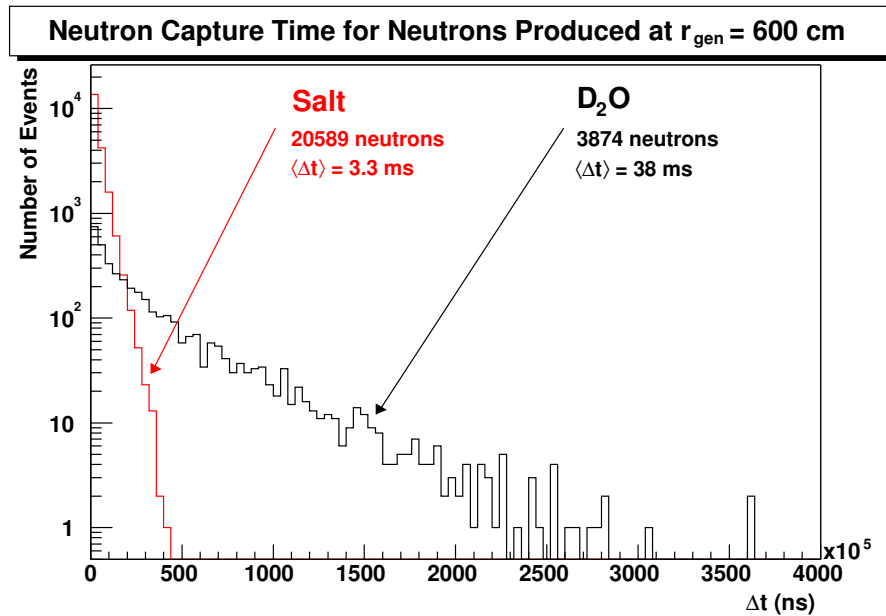


Figure 20.5: Capture time for neutrons produced at $r = 600 \text{ cm}$.

Table 20.4: Backgrounds from $^{13}\text{C} (\alpha, n) ^{16}\text{O}$ after subtraction of neutron attributed to photo-disintegration of deuterons by acrylic vessel activity.

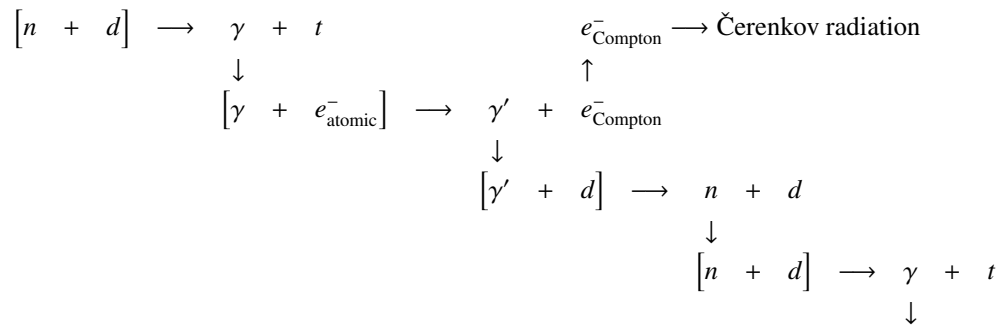
Expected e^+e^- Pair and Neutron Coincidences		
Phase	Standard	Enlarged
Pure D ₂ O	0.02 ± 0.10	0.71 ± 3.40
Salt	0.07 ± 0.07	3.54 ± 4.00

to ^{17}O is 5.3 and the product state of the $^{18}\text{O} (\alpha, n) ^{21}\text{Ne}$ reaction is a lower energy state. One reason these reactions may not contribute is that the excited states of ^{20}Ne & ^{21}Ne are closer to the ground state than in ^{16}O . This may imply the de-excitation gammas are below SNO's detection threshold. Clearly, this reaction has not been studied closely in the context of the electron antineutrino analysis, though it could contribute to the background.

Chapter 21

SECONDARY NEUTRONS**21.1 Secondary Neutrons**

Free neutrons in the SNO detector are measured in the Pure D₂O and Salt phases by their capture on nuclei which de-excite by gamma emission. The emitted gammas predominately Compton scatter atomic electrons producing the Čerenkov photons detected by the photomultiplier tubes. However, the de-excitation gammas may also photo-disintegrate deuterons (2.2 MeV binding energy). The secondary neutron produced by the photo-disintegration can capture creating a second Čerenkov signal in the photomultiplier tubes. In the Pure D₂O phase, this process is represented schematically (reactants are placed in square brackets):



The gamma-ray produced by neutron capture on deuterons has 6.25 MeV of energy. In the Salt phase, the primary neutron capture target is ³⁵Cl. Thus the sequence of secondary neutron production is the same as above with the replacement of deuteron's by ³⁵Cl. Neutron capture on ³⁵Cl produces a 8.6 MeV cascade of de-excitation gamma-rays. The higher energy and multiplicity of photons increases the frequency of secondary neutron production in the Salt phase. One important point, relevant to both phases of the experiment, is that in the cases where a gamma photo-disintegrates a deuteron, 2.2 MeV is absorbed and is not available to generate the full Čerenkov signal otherwise expected. Thus, it is expected that the first Čerenkov event will have a significantly reduced detector response. This reduced response is presented in Figures 21.1 & 21.2.

21.1.1 Secondary Neutrons in the Pure D₂O Phase

For the Pure D₂O, 10⁶ gammas of 6.25 MeV were simulated uniformly throughout the heavy water region. There were 4294 secondary neutrons generated by photo-disintegration. Table 21.1 shows the efficiency for detecting these 4294 neutrons in coincidence with the initial gamma-ray.

To calculate the number of coincidences in the data set used, the total neutron generation rate inside the D₂O volume is needed. This neutron generation rate is dominated by the solar neutrino NC reaction, $\nu_x + d \rightarrow$

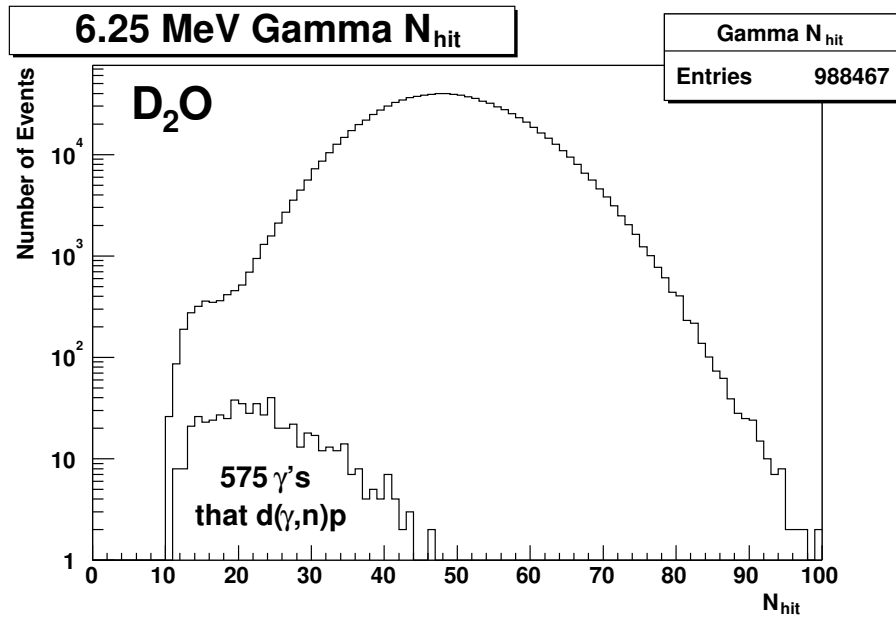


Figure 21.1: Monte Carlo of the N_{hit} response to 6.25 MeV gamma-rays from neutron capture on deuterons. The smaller curve is cases where a deuteron is photo-disintegrated by the gamma-ray.

Table 21.1: Secondary neutrons in the Pure D₂O phase and Salt phases. The efficiency, $\epsilon_{\gamma,n}$, for detecting a coincidence from secondary neutron production is given as a function of $N_{hit}(0)$. $N_{\gamma,n}$ is the number of coincidences in the Pure D₂O data set due to secondary neutron production.

D₂O		Standard Region		Enlarged Region	
$N_{hit}(0)$	$\epsilon_{\gamma,n} \times 10^6$	$N_{\gamma,n}$ in Data Set	$\epsilon_{\gamma,n} \times 10^6$	$N_{\gamma,n}$ in Data Set	
25	82	0.37 ± 0.03	68	0.31 ± 0.02	
30	43	0.20 ± 0.02	34	0.12 ± 0.01	
35	19	0.086 ± 0.007	10	0.045 ± 0.004	
40	6	0.027 ± 0.002	0	–	
45	0	–	0	–	

Salt		Standard Region		Enlarged Region	
$N_{hit}(0)$	$\epsilon_{\gamma,n} \times 10^5$	$N_{\gamma,n}$ in Data Set	$\epsilon_{\gamma,n} \times 10^5$	$N_{\gamma,n}$ in Data Set	
25	146	5.2 ± 0.4	132	4.7 ± 0.3	
30	97	3.5 ± 0.3	78	2.8 ± 0.2	
35	56	2.0 ± 0.1	39	1.4 ± 0.1	
40	27	0.97 ± 0.07	16	0.57 ± 0.04	
45	12	0.43 ± 0.03	6	0.21 ± 0.02	

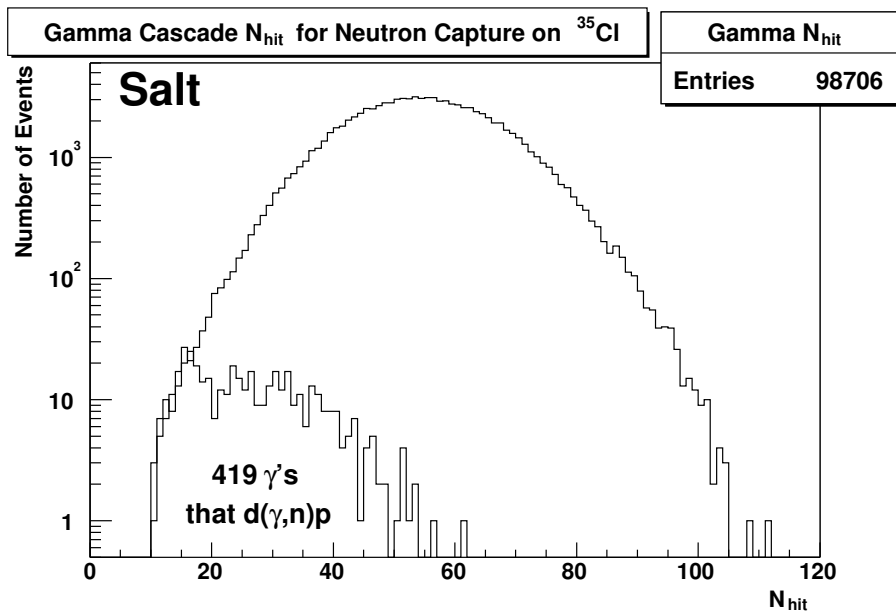


Figure 21.2: Monte Carlo of the N_{hit} response to the 8.6 MeV gamma cascade from neutron capture on ^{35}Cl . The smaller curve is cases where a deuteron is photo-disintegrated by the cascade.

$n + p$, with additional neutrons coming from radioactive elements in the detector materials. To estimate the neutron generation rate, the results from the SNO solar neutrino analysis are used [10]. SNO reports $576.5^{+49.5}_{-48.9}$ NC events (from a statistical separation) and 78 ± 12 background neutrons. The neutron detection efficiency quoted is $\epsilon_n = 0.144$. Combining these results, the estimated number of neutrons generated inside the D_2O volume is $N_n = 4545^{+354}_{-350}$. The number of coincidences expected is then given by $N_{\gamma,n} = \epsilon_{\gamma,n} N_n$ and is presented in Table 21.1.

21.1.2 Secondary Neutrons in the Salt Phase

For the salt phase, 10^5 gamma cascades from neutron capture on ^{35}Cl were simulated uniformly throughout the heavy water region. There were 717 secondary neutrons generated by photo-disintegration. Table 21.1 shows the efficiency for detecting these 717 neutrons in coincidence with the initial gamma cascade. The estimated total neutron rate is once again calculated from SNO's published results [12]. SNO reports, from a statistical separation, $1345.1^{+69.8}_{-69.0}$ NC events and $84.5^{+34.5}_{-33.6}$ background neutrons. The neutron detection efficiency quoted is $\epsilon_n = 0.399 \pm 0.0198$. Combining these results, the estimated number of neutrons generated inside the D_2O volume is $N_n = 3583^{+264}_{-262}$. The number of coincidences expected is then given by $N_{\gamma,n} = \epsilon_{\gamma,n} N_n$ and is presented in Table 21.1. Note there were 3 cases of (γ, γ, n) (i.e. tertiary neutrons) in the 10^5 Monte Carlo.

Chapter 22

OTHER BACKGROUNDS**22.1 “Sacrifice and Contamination”**

The terminology of “sacrifice and contamination” has a particular meaning in SNO analyses. Sacrifice is the loss of signal events due to the application of the instrumental background cuts described in Appendix B. Contamination is the appearance of instrumental events in the data sample due to the inefficiency of the same instrumental cuts. This discussion of sacrifice and contamination is implicitly referring to *single* SNO events. The signal in the electron antineutrino analysis is *coincidences* of single SNO events. This is an important distinction in what follows.

Sacrifice of single SNO events is as much of a concern for the electron antineutrino analysis as it is for the primary solar neutrino analysis. To this end sacrifice of single events was studied and shown to be less than 1% for instrumental cuts [157]. Since the $\overline{\text{CC}}$ interaction produces three detectable particles, the sacrifice of *coincidences* will be even less than this 1%. In the same study, the contamination was also found to be less than 1%. Contamination of single events is not a problem for the electron antineutrino analysis because these contaminating events contribute to the accidental coincidence rate which was measured in Chapter 13. The remaining category is instrumental contaminating *coincidences*. For this sort of contamination to occur the less than 1% of contaminating *single* events must also be correlated in time so as to mimic the $\overline{\text{CC}}$ time structure.

22.2 Yet More Minor Backgrounds

The SNO Antineutrino Unified Document [139], addresses a number of minor backgrounds which this analysis will rely upon as demonstrating they are not a concern. These backgrounds are specific U and Th chain decays.

^{214}Bi : $\beta - \gamma$ where the β gives a prompt Čerenkov signal and the γ photo-disintegrates a deuteron.

^{210}Tl : $\beta - n$ where the β gives a prompt Čerenkov signal followed by neutron capture.

^{208}Tl : $\beta - \gamma$ where the β gives a prompt Čerenkov signal and the γ photo-disintegrates a deuteron.

Table 22.1 presents the expected number of coincidences as determined in the Antineutrino Unified Document for a energy and fiducial volume analysis equivalent to the Standard analysis of this dissertation in the Pure D_2O phase. Each of these backgrounds is intrinsic to the heavy water volume and thus scales with the volume. These processes are primarily dependent on rates rather than on energy threshold.

Table 22.1: Other backgrounds taken from the Antineutrino Unified Document [139]. The number of coincidences is determined for an energy and fiducial volume analysis equivalent to the Standard analysis of this dissertation in the Pure D₂O phase.

Process	Number of Coincidences Pure D ₂ O (Standard)
²¹⁴ Bi: $\beta - \gamma$	7.6×10^{-5}
²¹⁰ Tl: $\beta - n$	$\simeq 10^{-8}$
²⁰⁸ Tl: $\beta - \gamma$	8.7×10^{-4}

22.3 A List of Other Potential Backgrounds Not Yet Addressed

The following is a list of backgrounds that have never been addressed, as far as the author knows.

- $\mu^- + d \rightarrow \nu_\mu + n + n$ in Reference [202]. Only possible for a small class of muons that enter or are produced in the detector below Čerenkov threshold.
- $\mu^- + {}^{16}\text{O} \rightarrow \nu_\mu + n + {}^{15}\text{N}^*$ where the ${}^{15}\text{N}^*$ de-excites via a gamma-ray of approximately what energy? This would be in the same small class of below Čerenkov threshold muons as the previous item.

Part IV

Electron Antineutrino Analysis

Chapter 23

CANDIDATE \overline{CC} EVENT SELECTION

23.1 Data Sets Used

A data set is defined as those data taking runs which were selected for solar neutrino analysis. Such runs are deemed to be of the highest quality and thus acceptable for physics analysis. The data sets used in this electron antineutrino analysis correspond to the same data as presented in the Pure D₂O phase result of Ref. [10] and the initial Salt phase result of Ref. [12]. The analysis cuts developed in Chapters 11 – 14 are applied to these data sets to extract the candidate coincidences. In fact, *all* coincidences are extracted and presented in this chapter. Based upon the Monte Carlo of Chapter 19 it is expected that coincidences of greater than three events will be found in the data sets. The technical details of how the data was processed, composed, manipulated, etc. is presented in Appendix A along with complete lists of runs used.

23.2 Extracting Candidate \overline{CC} Coincidences

It is worth noting that up until this point, the raw data need not have been inspected for candidate \overline{CC} coincidences. This shows that $\approx 90\%$ of the effort put forth for an electron antineutrino analysis is developing sensible analysis cuts and understanding the backgrounds.

23.2.1 Candidate \overline{CC} Coincidences in the Pure D₂O Phase

Table 23.1 presents the candidate coincidences for the Pure D₂O phase. There are eight distinct coincidences found. Upon visually inspecting these coincidences and the events occurring before them, it was determined that two coincidences were caused by processes other than a possible \overline{CC} interaction. The first of these is part of a “Flat TAC” episode. Flat TAC (time-to-analog converter) refers to a uniform distribution of PMT pulses in time. Real Čerenkov events have sharply peaked PMT time distributions in the tens of nanoseconds rather than spread out (flat) across the entire event’s 480 nanoseconds. The appearance of this coincidence in the candidate set demonstrates the selection criterion do not eliminate all instrumental backgrounds. The second visually rejected coincidence is assumed to be trailing events from a high energy muon passing through the detector 1.3 seconds prior to the coincidence. Of the remaining six coincidences there are three 2-fold, two 3-fold, and one 4-fold coincidences. The atmospheric neutrino studies of Chapter 19 predict 4-fold and higher coincidences to be detected. Thus the single 4-fold coincidence is dropped from consideration in the electron antineutrino analysis (\overline{CC} interactions only make three detectable particles). This leaves five (5) candidate \overline{CC} coincidences in the Pure D₂O data set for the Enlarged analysis. Upon careful examination of Table 23.1, one will determine there are three (3) candidate coincidences in the Standard analysis. Those coincidences satisfying the Standard analysis criterion are listed in short in Table 23.2.

Table 23.1: Pure D₂O phase, Enlarged region electron antineutrino candidate coincidences.

UTC Date & Time	Run	GTID	N_{hit}	R_{fit} (cm)	ITR	θ_{ij}	Δt (ms)	Δr (cm)	Δt to last ... (s)
1999/11/16 09:16:59	10142	1161995	37	276	0.71	1.10	0	0	$N_{\text{hit}} > 100$ -130
		1161996	35	403	0.76	1.10	67.3	130	OWL trig. -85
1999/11/16 13:02:23	10142	1406278	103	106	0.73	0.65	0	0	-
		1406296	147	231	0.64	0.81	1.6	330	-
The above events are part of a Flat TAC episode.									
2000/01/28 05:59:22	10946	299486	70	596	0.78	1.12	0	0	-
		299491	48	536	0.78	1.10	184.2	447	-
The above events follow a <i>highly</i> energetic muon at $\Delta t = -1.3$ s. Many, multiple rings seen.									
2000/06/30 14:43:02	12167	806727	83	283	0.64	1.35	0	0	$N_{\text{hit}} > 100$ -86
		806729	49	472	0.73	1.11	16.7	206	OWL trig. -802
		806730	49	349	0.76	1.10	20.3	118	
2000/07/06 12:49:41	12183	3084974	46	167	0.70	1.13	0	0	$N_{\text{hit}} > 100$ -51
		3084977	40	499	0.67	0.89	74.6	522	OWL trig. -977
2000/07/20 10:54:13	12233	2648588	51	458	0.73	1.20	0	0	$N_{\text{hit}} > 100$ -179
		2648590	47	245	0.70	1.23	32.6	340	OWL trig. -336
2000/11/24 09:19:39	14177	299927	54	430	0.70	1.27	0	0	$N_{\text{hit}} > 100$ -148
		299928	37	422	0.82	1.13	84.1	236	OWL trig. -161
		299929	59	506	0.81	0.96	88.9	81	
2001/04/30 06:40:25	15799	1133443	41	364	0.79	1.08	0	0	$N_{\text{hit}} > 100$ -852
		1133444	39	376	0.70	1.21	6.4	193	OWL trig. -3959
		1133446	63	194	0.73	0.98	26.9	414	
		1133450	53	520	0.73	1.25	127.9	293	

Table 23.2: Short list of Pure D₂O phase, Standard region $\overline{\text{CC}}$ candidate coincidences.

Run	GTID	Run	GTID	Run	GTID
12167	806727	12233	2648588	14177	299927
	806729		2648590		299929
	806730				

23.2.2 Candidate $\overline{\text{CC}}$ Events in the Salt Phase

Tables 23.3 & 23.4 present the twenty-five (25) candidate coincidences found in the Salt phase. Of these, one coincidence (run 26551) is rejected as a result of visual inspection showing it is composed of instrumental background events. The other commented coincidence (run 26066) is retained as it is unlikely a coincidence is produced by a high-energy event (of any sort) 27 seconds prior. Upon visual inspection two coincidences were found to have *additional* events. In both cases (runs 26609 and 26857) the additional event failed a cut criterion but appeared, visually, as a true Čerenkov physics event. In both cases these additional *events*

Table 23.3: Salt phase, Enlarged region \overline{CC} candidate coincidences – I.

UTC Date & Time	Run	GTID	N_{hit}	R_{fit} (cm)	ITR	β_{14}	Δt (ms)	Δr (cm)	Δt to last ... (s)
2001/09/28 06:47:17	21651	781020	50	294	0.69	0.26	0	0	$N_{\text{hit}} > 100$ -151.1
		781021	60	311	0.75	0.15	0.8	21	OWL trig. -4055.4
		781022	32	429	0.69	0.52	2.8	172	
		781023	49	396	0.69	0.32	9.6	105	
2001/09/28 13:47:55	21651	1213289	53	275	0.72	0.41	0	0	$N_{\text{hit}} > 100$ -64.2
		1213290	56	335	0.70	0.74	9.0	132	OWL trig. -3967.2
2001/09/29 06:21:10	21652	2249450	30	429	0.86	0.32	0	0	$N_{\text{hit}} > 100$ -19.4
		2249451	50	583	0.83	0.43	4.0	178	OWL trig. -882.6
2001/12/03 01:20:46	22444	579916	44	554	0.79	0.39	0	0	$N_{\text{hit}} > 100$ -150.3
		579919	46	494	0.69	0.34	7.4	173	OWL trig. -586.0
2002/01/09 12:00:32	22878	1028179	35	429	0.71	0.51	0	0	$N_{\text{hit}} > 100$ -416.1
		1028180	56	338	0.75	0.23	3.6	115	OWL trig. -770.6
2002/01/18 05:00:43	22997	595774	59	513	0.75	0.11	0	0	$N_{\text{hit}} > 100$ -136.6
		595775	52	578	0.82	0.32	2.2	81	OWL trig. -1987.9
		595776	44	461	0.90	0.31	3.4	75	
2002/01/26 11:33:33	23163	711142	59	543	0.72	0.46	0	0	$N_{\text{hit}} > 100$ -19.5
		711143	55	567	0.71	0.37	5.9	118	OWL trig. -1680.5
2002/02/21 14:11:55	23646	706423	45	567	0.82	1.22	0	0	$N_{\text{hit}} > 100$ -133.3
		706425	44	484	0.75	0.39	2.1	104	OWL trig. -335.8
2002/03/07 07:57:58	23780	426986	51	260	0.80	0.50	0	0	$N_{\text{hit}} > 100$ -569.4
		426987	54	411	0.80	0.29	1.8	220	OWL trig. -2584.7
2002/03/09 14:13:56	23826	1244632	55	579	0.85	0.56	0	0	$N_{\text{hit}} > 100$ -104.4
		1244633	44	528	0.81	0.28	8.1	160	OWL trig. -2153.8
2002/03/22 11:33:41	23932	3093065	29	262	0.67	0.72	0	0	$N_{\text{hit}} > 100$ -226.1
		3093066	38	331	0.73	0.32	2.3	461	OWL trig. -8696.6
2002/03/25 17:49:04	23965	1059906	51	507	0.71	0.38	0	0	$N_{\text{hit}} > 100$ -224.2
		1059907	38	545	0.75	0.62	6.1	81	OWL trig. -2512.0
2002/04/28 00:53:10	24520	742402	36	350	0.82	0.40	0	0	$N_{\text{hit}} > 100$ -183.5
		742403	57	378	0.78	0.18	4.2	93	OWL trig. -1851.1
2002/05/04 14:51:00	24583	1310960	65	502	0.82	0.00	0	0	$N_{\text{hit}} > 100$ -127.0
		1310964	47	380	0.72	0.71	7.5	167	OWL trig. -1138.1
		1310965	37	481	0.80	0.60	8.4	42	
		1310966	49	505	0.73	0.32	15.5	185	
2002/05/05 16:44:16	24590	870220	43	304	0.88	0.27	0	0	$N_{\text{hit}} > 100$ -186.1
		870221	32	220	0.76	0.20	5.7	117	OWL trig. -7220.8

are noted in the coincidence tables, but are otherwise not included in further analysis. That is to say, these *coincidences* are retained for further consideration but the additional *events* are ignored.

Of these twenty-four (24) remaining coincidences, four coincidences were 4-fold or higher (runs 21651,

Table 23.4: Salt phase, Enlarged region \overline{CC} candidate coincidences – II.

UTC Date & Time	Run	GTID	N_{hit}	R_{fit} (cm)	ITR	β_{14}	Δt (ms)	Δr (cm)	Δt to last ... (s)
2002/05/21 22:50:43	24888	2086896	53	469	0.80	0.24	0	0	$N_{hit} > 100$ -10928
		2086898	42	509	0.74	0.06	15.2	128	OWL trig. -1456
2002/06/30 15:28:21	25965	102996	72	509	0.81	0.17	0	0	$N_{hit} > 100$ -185
		102997	51	534	0.71	0.41	13.2	75	OWL trig. -2007
2002/07/09 20:33:05	26066	38045	48	479	0.86	0.47	0	0	$N_{hit} > 100$ -27
		38046	44	494	0.75	0.33	3.7	51	OWL trig. < -1641
The preceding $N_{hit} > 100$ event was a high-energy ring w/ followers.									
2002/08/23 21:46:13	26551	105317	45	587	0.71	0.29	0	0	
		105319	39	492	0.79	0.14	33.6	571	
These are instrumental background events.									
2002/09/01 16:44:53	26609	1777848	53	588	0.78	0.53	0	0	$N_{hit} > 100$ -374
		1777849	61						OWL trig. -92
		1777850	52	550	0.84	0.48	6.3	189	
2002/09/13 09:11:02	26726	339783	34	280	0.67	0.42	0	0	$N_{hit} > 100$ -13
		339784	46	141	0.75	0.39	3.1	198	OWL trig. -999
		339785	41	263	0.84	0.57	4.3	69	
		339786	59	224	0.74	0.33	5.3	210	
		339787	53	154	0.72	0.41	8.1	214	
339788	73	474	0.77	0.48	11.3	241			
2002/09/24 01:31:45	26857	169243	122				-2.8		
		169244	49	566	0.79	0.18	0	0	$N_{hit} > 100$ -699
		169245	63	550	0.79	0.37	7.5	263	OWL trig. -19
169246	40	518	0.72	0.24	13.3	164			
2002/09/24 22:02:51	26866	169338	61	319	0.82	0.36	0	0	$N_{hit} > 100$ -150
		169339	26	285	0.90	0.15	28.9	439	OWL trig. -3088
2002/09/26 02:01:07	26881	31944	89	567	0.71	0.18	0	0	$N_{hit} > 100$ -76
		31946	64	374	0.81	0.48	0.2	213	OWL trig. -1025
		31947	65	317	0.78	0.23	0.4	256	
		31948	46	535	0.77	0.05	0.8	36	
		31949	32	356	0.80	0.26	2.7	272	
		31950	59	318	0.84	0.27	3.6	328	
		31952	56	201	0.74	0.22	6.5	370	
		31953	50	352	0.73	0.16	8.9	237	
31954	50	223	0.83	0.21	15.4	448			
31955	57	367	0.71	0.34	23.3	386			
2002/09/26 04:03:26	26881	153629	51	590	0.81	0.28	0	0	$N_{hit} > 100$ -499
		153630	45	490	0.76	0.39	1.3	164	OWL trig. -254

24583, 26726, and 26881). Again it is assumed these high multiplicity coincidences are due to atmospheric neutrino interactions. Note that these four rejected high multiplicity coincidences do not include the coinci-

dence in run 26857 which may provide a concrete example of the sort of background that is addressed by the atmospheric neutrino calculations of Chapter 19. Thus it is finally determined that there are twenty (20) \overline{CC} candidate coincidences in the Enlarged analysis of the Salt phase. Careful examination of Tables 23.3 & 23.4 will reveal there are seven (7) \overline{CC} candidate coincidences for a Standard analysis of the Salt phase. Those coincidences satisfying the Standard analysis are listed in short in Table 23.5.

Table 23.5: Short list of Salt phase, Standard region \overline{CC} candidate coincidences.

Run	GTID	Run	GTID	Run	GTID	Run	GTID
21651	1213289	23780	426986	25965	102996	26857	169245
	1213290		426987		102997		169246
22997	595774	24888	2086896	26066	38045		
	595776		2086898		38046		

A particularly interesting result is the distribution of radial fit positions of the first event in 2-fold coincidences found in the Salt phase. Recall from Section 20.1 the discussion of the $^{13}\text{C}(\alpha, n)^{16}\text{O}$ background located at the acrylic vessel. The e^+e^- pair emitted from the 6.049 MeV state of ^{16}O should have a reconstructed position near the acrylic vessel. Figure 23.1 shows that the initial event of the 2-fold coincidences are *uniformly* distributed throughout the detector volume.

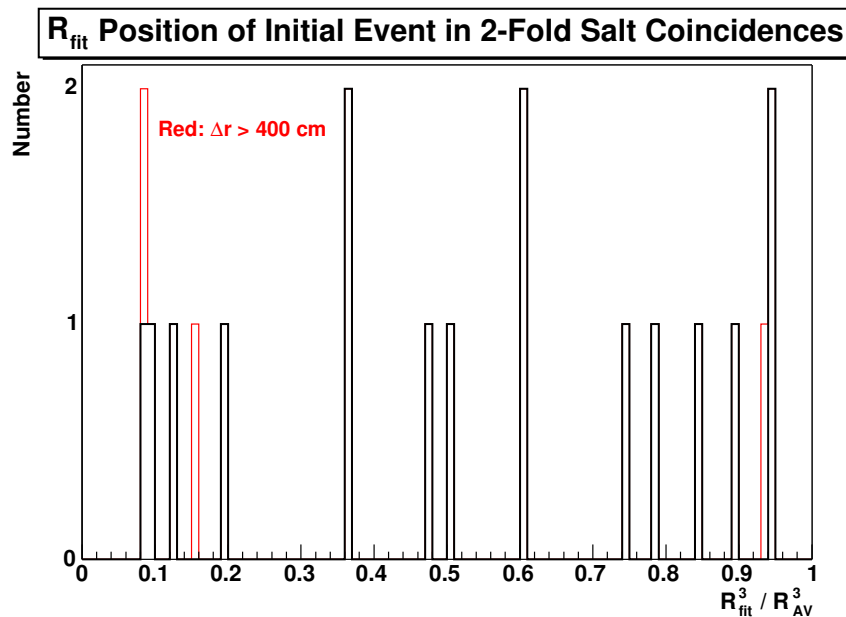


Figure 23.1: The radial fit position of the first event in 2-fold coincidences during the Salt phase.

Chapter 24

STATISTICAL TREATMENT AND PHYSICS RESULTS**24.1 The Feldman & Cousins Method**

The Feldman & Cousins method of classical (Neyman) confidence belt construction [93], has been adopted by the Particle Data Group [113] as the recommended method for presenting the results of experiments that measure small, Poisson event rates with known backgrounds. The results of the electron antineutrino analysis will rely on this method. It is worth noting that the Feldman & Cousins method presented in [93] does *not* incorporate systematic or statistical uncertainties on the estimation of the background. Imagine an example experiment that reports $n_0 = 0.0$ recorded events with an expected background of $b = 3.2^{+152.3}_{-3.1}$ events. The Feldman & Cousins method fails to account for the +152.3 error bar and gives the same confidence interval as a second experiment reporting $n_0 = 0.0$ recorded events with an expected background of $b = 3.2^{+0.2}_{-0.1}$ events. There are recent attempts [77, 121] to address this and other issues with the Feldman & Cousins method. A SNO Collaborator, N. McCauley, has developed a stand-alone code [155] implementing the ideas of Feldman & Cousins with the extensions presented in Refs. [77, 121]. This stand-alone code is used throughout to determine the confidence intervals reported in this electron antineutrino analysis.

24.1.1 A Lesson on Adhering to Confidence Intervals

In discussing a Poisson process with a known background, Feldman & Cousins make the following point regarding construction of confidence belt upper limits and confidence intervals:

Although the word “conservative” in this context may be viewed by some as desirable, in fact it is an undesirable property of a set of confidence intervals. Ideal intervals cover the unknown true value at exactly the stated confidence: 90% C.L. intervals should fail to contain the true value 10% of the time. If one desires intervals which cover more than 90% of the time, the solution is not to add conservatism to the intervals, but rather to choose a higher confidence level.

This quotation specifically addresses the integral nature of Poisson statistics. Feldman & Cousins then go on to note that it is the practicing physicist’s *choice* whether to construct *either* the confidence belt upper limit *or* a confidence interval. The Feldman & Cousins method provides both the correct coverage and eliminates the physicist’s choice to use either a confidence belt upper limit or a confidence interval. The physicist’s choice is eliminated by the Feldman & Cousins method since a confidence belt upper limit or a confidence interval is now merely a matter of the specific measured count rate and the known background count rate.

There is a broader lesson to learn from this. Strict adherence to the confidence intervals determined by the method, is crucial to maintaining the meaningfulness of the quoted confidence level. Practically speaking, in

using the Feldman & Cousins method, one is obligated to quote *either* a confidence interval *or* an upper limit in the case when the lower bound on the confidence interval is identically zero.

24.2 Background Counts

Table 24.1 collects the estimated number of background counts to the electron antineutrino analysis in both Pure D₂O and Salt phases for the Standard and Enlarged analyses this dissertation developed. The results

Table 24.1: Summary of expected background counts in the Pure D₂O and Salt phases.

Source	Pure D ₂ O		Salt		Note
	Standard	Enlarged	Standard	Enlarged	
Background Sources of Electron Antineutrinos					
Atmospheric	< 0.001		< 0.0008		$4 < E_{\bar{\nu}_e} \text{ (MeV)} < 20$
Reactor	0.019	0.069	0.148	0.371	
Diffuse Supernova Neutrinos	0.005	0.010	0.011	0.019	$4 < E_{\bar{\nu}_e} \text{ (MeV)} < 23$
Total	0.024	0.070	0.159	0.390	
Non-Electron Antineutrino Backgrounds					
Accidentals	0.057	1.08	0.012	0.608	$E_{\nu_e} > 50 \text{ MeV}$
Spontaneous Fission	0.143	0.367	0.374	0.627	
Atmospheric ν 's	0.85	2.82	2.54	6.08	
Secondary neutrons	< 0.027	0.12	0.97	4.7	
$^{13}\text{C}(\alpha, (n, e^+e^-))^{16}\text{O}$	0.02	0.71	0.07	3.54	d(γ, n)p subtracted
Total	1.07	5.10	3.97	15.56	
Grand Total	1.09	5.17	4.13	15.95	

presented in Table 24.1 are correctly adjusted to account for the livetime of the two phases of the experiment: $t_{\text{live}}^{\text{D}_2\text{O}} = 311.41$ days and $t_{\text{live}}^{\text{Salt}} = 258.624$ days. The upper limits on the number of atmospheric electron antineutrino induced $\overline{\text{CC}}$ interactions *merely* accounts for detector livetime and does *not* include detection efficiencies.

24.3 Limits on the Solar Electron Antineutrino Flux

A limit is derived as follows. The number of measured coincidences is taken from Section 23.2. Using the 90% confidence level tables in Feldman & Cousins [93]¹ match the number of measured coincidences (n_0 rows) and find the range under the appropriate background (b columns). When the lower value is 0.00, the upper value is then an upper limit. If both values are non-zero, then one is obligated to report a measured *signal* in the specific interval. This upper limit or signal range value, L , is the number of events to convert to a flux value. For example, an upper limit is divided by the total $\overline{\text{CC}}$ detection efficiency, $\varepsilon_{\overline{\text{CC}}}$, determined in

¹Since the background does not happen to have integer or half-integer values, a Feldman & Cousins implementation with extensions was provided by a SNO Collaborator, N. McCauley [155].

Table 24.2: Uncertainties on the \overline{CC} background estimates.

Source	Pure D ₂ O		Salt		Note
	Standard	Enlarged	Standard	Enlarged	
Uncertainties on Background Sources of Electron Antineutrinos					
Atmospheric	< 0.0003		< 0.0002		Ignored
Reactor	0.002	0.007	0.015	0.037	10%
Diffuse Supernova Neutrinos	0.001	0.002	0.002	0.004	Assumed 20%
Uncertainties on Non-Electron Antineutrino Backgrounds					
Accidentals	0.006	0.148	0.001	0.018	
Spontaneous Fission	0.031	0.080	0.114	0.182	
Atmospheric ν 's	0.26	0.84	0.76	1.79	
Secondary neutrons	0	0.01	0.4	0.3	
$^{13}\text{C}(\alpha, n, e^+e^-)^{16}\text{O}$	0.10	3.40	0.07	4.00	
Total Uncertainty in Quadrature	0.28	3.51	0.87	4.40	

Chapter 16, see Tables 16.1 & 16.2. The value is converted into an equivalent value for one kt · yr using each phase's livetime. Finally, this \overline{CC} per kt · yr value is scaled to a flux using Table 4.4. This is mathematically expressed as

$$\Phi_{\bar{\nu}_e}^{8\text{B}} = \frac{L(\overline{CC})}{\varepsilon_{\overline{CC}}} \left(\frac{365.25 \left(\frac{\text{days}}{\text{yr}} \right)}{t_{\text{live}} (\text{kt} \cdot \text{days})} \right) \left(\frac{10^5 \left(\frac{\bar{\nu}_e}{\text{cm}^2\text{s}} \right)}{96 \left(\frac{\overline{CC}}{\text{kt}\cdot\text{yr}} \right)} \right) \quad (24.1)$$

where L is the limit or value from the Feldman & Cousins method to be converted to an equivalent electron antineutrino flux assuming a ^8B spectrum, $\Phi_{\bar{\nu}_e}^{8\text{B}}$. The application of equation (24.1) is presented in Table 24.3.

Table 24.3: Limits on the flux of solar electron antineutrinos, $\Phi_{\bar{\nu}_e}^{8\text{B}}$.

Pure D ₂ O			
Standard Analysis 3 Coincidences	Background	1.09 ± 0.0	1.09 ± 0.28
	Flux (10 ⁴ /cm ² s) at 90% C.L.	< 5.8	< 5.8
Enlarged Analysis 5 Coincidences	Background	5.17 ± 0.0	5.17 ± 3.51
	Flux (10 ⁴ /cm ² s) at 90% C.L.	< 1.8	< 2.4
Salt			
Standard Analysis 7 Coincidences	Background	4.13 ± 0.0	4.13 ± 0.87
	Flux (10 ⁴ /cm ² s) at 90% C.L.	< 2.6	< 2.7
Enlarged Analysis 20 Coincidences	Background	15.95 ± 0.0	15.95 ± 4.40
	Flux (10 ⁴ /cm ² s) at 90% C.L.	< 2.3	< 2.8

Part V

Conclusion

Chapter 25

CONCLUDING REMARKS

The results of the search for an electron antineutrino signal in the Sudbury Neutrino Observatory are presented in Chapter 24, specifically Table 24.3. The present, concluding chapter, has three topics. First, it is useful to reflect more globally on the strengths and weaknesses of the analysis presented in this dissertation. Second, I wish to highlight some of the more important original work I have contributed to the Sudbury Neutrino Observatory experiment. This also provides an opportunity to point out work done not directly associated with the thesis of this dissertation. Third, I mention the Career Development Organization for Physicists and Astronomers, an activity I am particularly proud of and *do* believe is a valuable part of this process of becoming a practicing, professional physicist.

25.1 Strengths and Weaknesses of the Analysis Presented

The primary thrust of the analysis presented in this dissertation is to show that for a coincidence analysis, such as the electron antineutrino analysis, SNO can increase the fiducial volume beyond that defined by a $R_{\text{fit}} < 550$ cm cut. Increasing the fiducial volume to include the entire heavy water volume contained within a radius of 600 cm provides nearly a 30% increase in the target size and volume. Furthermore, this dissertation shows it is possible to reduce the analysis energy threshold below the level used in SNO's solar neutrino analyses. The increased detection efficiency and target exposure gained by these methods is the primary strength of the analysis presented in this dissertation.

There are additional methodological strengths. Chapters 10, 12, & 13 are effectively presenting a generic prescription for how to choose a set of energy and fiducial volume cuts. These choices are independent of any specific reconstruction algorithms or energy estimators. Another strength of this prescription for determining the energy and fiducial volume selection is that the choices are derived from real detector data. Moreover, these choices are made in such a way as to avoid allowing the analyzer to become biased by the results of a search for real coincidence events in the data sample. In other words, by using muon follower data and averages over the entire data set, one can develop the cuts and criterion for a coincidence search *without ever performing such a search*.

This section, however, is really meant to address what is lacking in the analysis presented. The reconstruction and energy estimators are all well studied inside the $R_{\text{fit}} < 550$ cm cut. One of the reasons why (besides elevated background counts) the $R_{\text{fit}} < 550$ cm cut was chosen is that it is known that the reconstruction and energy estimators behave poorly near the acrylic vessel (i.e. at a radius of 600 cm). This behavior is easy to understand. Čerenkov light produced very close to the acrylic vessel will have large angles of incidence on the acrylic. These large angles increase the reflection and refraction of the Čerenkov light thus changing the mean topology of the PMTs fired in a given event. It is for these reasons that one may be reluctant to accept

that the large fiducial volume analysis argued for in this dissertation is really an improvement. There are two responsible replies to this assertion:

1. Yes, the SNO Collaboration needs to show the extent to which the reconstruction and energy estimators are usable at high radius.
2. In analyses where only a “Yes, it was a Čerenkov event.” or “No, it was not.” distinction is needed, the requirements for precision and accuracy in event reconstruction and energy estimation are reduced.

Both of these points are open questions which could afford real a quantitative investigation that was not supplied by this dissertation.

Chapter 10 presented an investigation of muons and muon followers. One area not addressed in Chapter 10 is the sacrifice imposed by the use of Section 10.2.3’s muon cut based upon finding high energy events appearing in the following 11 microseconds. A high rate of sacrifice of muons (and their followers) is not a concern for the work presented in Chapter 10 because all that was needed was a high purity sample of spallation neutrons. However, if the cut detailed in Section 10.2.3 is used for further muon studies in particular, then such a study is necessary. For example, one may wish to use this cut to try to categorize muons into a “spallation” set and a “DIS+” set. This is an excellent goal requiring a more detailed study and perhaps tuning of the muon decay window cut of Section 10.2.3.

Another potential problem not addressed is the increased detection of neutron capture on the acrylic vessel as the fiducial volume is increased and the analysis energy threshold is reduced. It is an open question how far the energy threshold can be lowered before these neutron captures on protons become a *significant* fraction of the event rate.

25.2 My Contributions to the SNO Experiment

25.2.1 Electron Antineutrino Publication

The SNO Collaboration is preparing a report on an electron antineutrino analysis of the SNO detector data [13]. This publication in preparation is roughly equivalent to the Standard analysis of the Pure D₂O phase presented in this dissertation. The work presented here is an independent check and confirmation of the work that will be presented in the published report. More importantly however, the background studies done for this dissertation were used to determine the backgrounds for the coming publication. It is worth emphasizing that the original plan for the electron antineutrino publication was to assume a “conservative” background of 0.0 events. I worked to provide a set of reliable background estimates so that a true Feldman-Cousins unified calculation of the limit on the flux of solar electron antineutrinos could be presented in the publication.

25.2.2 Large Volume, Low Energy $\bar{\nu}_e$ Analysis

As already stated many times, SNO results published thus far [9, 10, 11, 12] have used a fiducial volume defined by $R_{\text{fit}} < 550$ cm and an energy threshold of 5.0 MeV kinetic or above. The 550 cm fiducial volume

leaves nearly 30% of the D₂O volume unanalyzed. The 5.0 MeV kinetic energy threshold is set just below the $d(n, \gamma)t$ peak at 6.25 MeV. In the electron antineutrino analysis presented here, I believe I have demonstrated that it is possible to increase the acceptance in both volume and energy.

The coincidence signature of the \overline{CC} signal helps to reduce the background but I believe it is also important to recognize that making the analysis energy threshold dependent on the event reconstruction position also reduces the background contamination. In effect, the large volume and low energy analysis I have developed for studying electron antineutrino signals says “The closer the event is to the center of the acrylic vessel, the more likely it really is a real physics event of interest.” I have shown how to select this energy (in this case N_{hit}) as a function of reconstructed position and, there-by, increase the over all neutron detection efficiency. This type of analysis is an original contribution on my part to the SNO experiment.

25.2.3 *Reactor Antineutrino Flux Calculation*

I have developed a calculation of the nuclear power reactor induced electron antineutrino flux at SNO from spectra and historical reactor power output data. This calculation is of primary importance for any electron antineutrino analysis that SNO attempts. Additionally, this calculation’s result will factor into every solar neutrino analysis SNO produces as a small but known background. All previous calculations have used the rated power output for the reactors. This calculation takes into account the actual reactor power output and reactor shutdown periods. This calculation also factors in the effect of neutrino oscillations. I believe this calculation is the most principled, precise, and accurate calculation of the reactor $\overline{\nu}_e$ flux at SNO that has ever been presented in literature or otherwise.

25.2.4 *Separation of Muon Spallation into Photo-Dissociative and “Other” Classes*

The neutrino physics community as well as other scientific disciplines who conduct research underground will continue to need to account for cosmic-ray muons and more importantly the spallation products that these muons create. SNO can and should provide a detailed report of the cosmogenic activity that is detected. These results will assist those in the community [222] who are actively trying to develop Monte Carlo methods for estimating and addressing cosmic-ray induced activity at underground research sites. In this dissertation I have demonstrated a means by which the spallation products in SNO can be subdivided for comparison to the models used in Monte Carlo schemes. This is a new analysis avenue that I have opened the door to and that I hope the SNO Collaboration will pursue.

25.2.5 *Electron Antineutrino Monte Carlo Work-Around*

One technical detail not covered in the body of this dissertation was the difficulty posed by the multi-particle Monte Carlo needed for the electron antineutrino analysis. The Monte Carlo program used by the SNO Collaboration can generate multiple particle events. However, the program design is such that it is not possible to simultaneously record the Monte Carlo generation information (i.e. “known” position, momentum, interactions, Čerenkov production, etc.) and the simulated detection information (i.e. “measured” N_{hit} , PMTs fired, etc). This separation of “known” verses “measured” information in the Monte Carlo allows for the Monte Carlo data and the *real* data to appear identical and can, thus, be analyzable with the same suite of analysis

tools. This is good in general, but has repeatedly proved a major obstacle in SNO analyses requiring the study of multi-particle events.

In the case of single particle physics events, it is unambiguous as to which Monte Carlo information corresponds to which simulated detection information. The problem in the multiple particle physics event case is the correspondence is lost. I developed a scheme where the Monte Carlo information of multiple particles is saved to one set of files and the simulated detection information is saved to a different set of files. I then used timing information and a couple other “identifying parameters” to resolve the ambiguity of which Monte Carlo information corresponds to which simulated detection information. Re-establishing this correspondence is critical for any multi-particle Monte Carlo study the SNO Collaboration under takes. I developed this method for the electron antineutrino analysis presented here, but the method is entirely general and is necessary and usable in any multi-particle physics analysis in the SNO experiment.

25.2.6 Chairperson of the Salt Phase Run Selection Committee

The Salt phase of the SNO experiment began in May of 2001 and continued until September of 2003. During this period I was the Chairperson of the Run Selection Committee. The Run Selection Committee is charged with determining the list of runs chosen for neutrino analysis and ensuring the data quality and integrity of the selected runs. As Chairperson I organized the Run Selection Committee’s activities and ensured that we provided timely information to the Collaboration regarding what runs should be used in SNO’s primary solar neutrino analysis.

The Run Selection Committee was composed of 4 graduate students from 4 different institutions. Assistance from other graduate students was greatly appreciated. A major time consuming job of the Run Selection Committee members was to read through all shift reports (3 per day) detailing the activity at the experiment. To make the fullest of this reading, it was necessary to hold conference calls every two weeks. This allowed us to contact detector operators and inquire further when we had difficulty understanding the state and/or configuration of the detector.

25.2.7 Qualified On-site Scientist-In-Charge

During the period of January of 2001 to the summer of 2002, I spent every other month on-site at the SNO detector in Sudbury, Ontario. During this period I not only operated the detector as detector operator, I gained enough experience with the daily and weekly operating activities to qualify as a Scientist-In-Charge (SIC). The SIC is on-call to respond to any unforeseen difficulties with the detector which operates 24 hours per day. The SIC is responsible for determining the data taking configuration of the SNO detector and must be capable of performing complete shut-down and start-up procedures of this multi-million dollar experiment.

25.3 The Career Development Organization for Physicists and Astronomers

The Career Development Organization (CDO) for Physicists and Astronomers is a Registered Student Organization (RSO) at the University of Washington. The CDO’s mission is:

...to assist physics and astronomy students in their career advancement by organizing career seminars, compiling relevant employment data and preparatory information, and offering networking opportunities. To remain competitive in the job market, physicists and astronomers need to augment their analytical and problem-solving skills with flexibility, leadership, and cross-disciplinary aptitude. The activities and services of the CDO are intended to inform students about these challenges, and to help them prepare for a successful transition to their next endeavor.

The CDO was founded in the Summer of 2000 by Hans Vija and other physics and astronomy graduate students, including myself. Initially we focused on developing a seminar series and gaining the support of the Department of Physics. In the second year, Theresa Bullard pioneered the UW Physics Networking Day, a one day event where employers are invited to visit our campus for the express purpose of interacting with physics and astronomy students. As the 2002-2003 CDO President, I continued the work started by Hans and Theresa, with a major focus on expanding and simplifying the process of running the Networking Day. I will be continuing these career oriented activities after graduation as an appointed member of the American Physical Society's Committee on Careers and Professional Development. I believe this work, while not research related, is a valuable addition to my Ph.D. because much of being a practicing physicist includes the ability to organize and work with one's peers toward a goal, scientific or otherwise.

Part VI

Bibliography and Appendices

BIBLIOGRAPHY

- [1] A. Acker, A. Joshipura, and S. Pakvasa, *A Neutrino Decay Model, Solar Antineutrinos and Atmospheric Neutrinos*, Phys. Lett. B **285**, 371 (1992).
- [2] A. Acker and S. Pakvasa, *Solar Neutrino Decay*, Phys. Lett. B **320**, 320 (1994).
- [3] A. Acker, S. Pakvasa, and J. Pantaleone, *Solar-Neutrino Problem: Some Old Solutions Reexamined*, Phys. Rev. D **43**, R1754 (1991).
- [4] A. Acker, S. Pakvasa, and J. Pantaleone, *Decaying Dirac Neutrinos*, Phys. Rev. D **45**, R1 (1992).
- [5] M. Aglietta *et al.*, *Limits on Low-Energy Neutrino Fluxes with the Mont Blanc Liquid Scintillator Detector*, Astropart. Phys. **1**, 1 (1992).
- [6] M. Aglietta *et al.*, *Upper Limit on the Solar Antineutrino Flux According to LSD Data*, Sov. Phys.-JETP **63**, 791 (1996).
- [7] V. Agrawal, T. K. Gaisser, P. Lipari, and T. Standev, *Atmospheric Neutrino Flux Above 1 GeV*, Phys. Rev. D **53**, 1314 (1996).
- [8] Q. R. Ahmad, *Muon Correlated Background at the Sudbury Neutrino Observatory*, PhD thesis, Brown University 2002.
- [9] Q. R. Ahmad *et al.*, *Measurement of the Rate of $\nu_e + d \rightarrow p + p + e^+$ Interactions Produced by ^8B Solar Neutrinos at the Sudbury Neutrino Observatory*, Phys. Rev. Lett. **87**, 071301 (2001).
- [10] Q. R. Ahmad *et al.*, *Direct Evidence for Neutrino Flavor Transformation from Neutral-Current Interactions in the Sudbury Neutrino Observatory*, Phys. Rev. Lett. **89**, 011301 (2002).
- [11] Q. R. Ahmad *et al.*, *Measurement of Day and Night Neutrino Energy Spectra at SNO and Constraints on Neutrino Mixing Parameters*, Phys. Rev. Lett. **89**, 011302 (2002).
- [12] S. N. Ahmed *et al.*, *Measurement of the Total Active ^8B Solar Neutrino Flux at the Sudbury Neutrino Observatory with Enhanced Neutral Current Sensitivity*, arXiv.org **nucl-ex**, 0309004 (2003), Accepted by Physical Review Letters.
- [13] S. N. Ahmed *et al.*, *Electron Antineutrino Search at the Sudbury Neutrino Observatory*, (2004), In preparation.

- [14] E. Kh. Akhmedov, *Resonance Enhancement of the Neutrino Spin Precession in Matter and the Solar Neutrino Problem*, Sov. J. Nucl. Phys. **48**, 382 (1988).
- [15] E. Kh. Akhmedov, *Resonant Amplification of Neutrino Spin Rotation in Matter and the Solar-Neutrino Problem*, Phys. Lett. B **213**, 64 (1988).
- [16] E. Kh. Akhmedov, *Mutual Influence of Resonant Spin-Flavor Precession and Resonant Neutrino Oscillations*, Sov. Phys.-JETP **68**, 690 (1989).
- [17] E. Kh. Akhmedov, *Antineutrinos from the Sun*, Phys. Lett. B **255**, 84 (1991).
- [18] E. Kh. Akhmedov, *Oscillations-Assisted Resonant Spin-Flavor Precession and Time Variations of the Solar-Neutrino Flux*, Phys. Lett. B **257**, 163 (1991).
- [19] E. Kh. Akhmedov *et al.*, *SNO and the Neutrino Magnetic Moment Solution of the Solar Neutrino Problem*, Phys. Lett. B **485**, 178 (2000).
- [20] E. Kh. Akhmedov and O. V. Bychuk, *Resonant Spin-Flavor Precession of Neutrinos and the Solar Neutrino Problem*, Sov. Phys.-JETP **68**, 250 (1989).
- [21] E. Kh. Akhmedov and M. Yu. Khlopov, *Resonant Amplification of Neutrino Oscillations in Longitudinal Magnetic Field*, Mod. Phys. Lett. A **3**, 451 (1988).
- [22] E. Kh. Akhmedov, P. I. Krastev, and A. Yu. Smirnov, *Resonant Neutrino Spin-Flip Transitions in Twisting Magnetic Fields*, Z. Phys. C **52**, 701 (1991).
- [23] E. Kh. Akhmedov, A. Lanza, and S. T. Petcov, *Implications of Gallium Solar Neutrino Data for the Resonant Spin-Flavor Precession Scenario*, Phys. Lett. B **303**, 85 (1993).
- [24] E. Kh. Akhmedov, A. Lanza, and S. T. Petcov, *Solar Neutrino Data, Neutrino Magnetic Moments and Flavor Mixing*, Phys. Lett. B **348**, 124 (1995).
- [25] E. Kh. Akhmedov, S. T. Petcov, and A. Yu. Smirnov, *Neutrinos with Mixing in Twisting Magnetic Fields*, Phys. Rev. D **48**, 2167 (1993).
- [26] E. Kh. Akhmedov, S. T. Petcov, and A. Yu. Smirnov, *Pontecorvo's Original Oscillations Revisited*, Phys. Lett. B **309**, 95 (1993).
- [27] E. Kh. Akhmedov and J. Pulido, *Solar Neutrino Oscillation and Bounds on Neutrinos Magnetic Moment and Solar Magnetic field*, Phys. Lett. B **553**, 7 (2003).

- [28] P. Aliani, V. Antonelli, M. Picariello, and E. Torrente-Lujan, *KamLAND, Solar Antineutrinos and Their Magnetic Moment*, J. High Energy. Phys. **02**, 025 (2003).
- [29] T. C. Andersen *et al.*, *A Radium Assay Technique Using Hydrous Titanium Oxide Adsorbent for the Sudbury Neutrino Observatory*, Nucl. Instrum. Methods **A501**, 386 (2003).
- [30] T. C. Andersen *et al.*, *Measurement of Radium Concentration in Water with Mn-Coated Beads at the Sudbury Neutrino Observatory*, Nucl. Instrum. Methods **A501**, 399 (2003).
- [31] S. Ando, K. Sato, and T. Totani, *Detectability of the Supernova Relic Neutrinos and Neutrino Oscillation*, Astropart. Phys. **18**, 307 (2003).
- [32] C. Aneziris and J. Schechter, *Neutrino "Spin Rotation" in a Twisting Magnetic Field*, Int. J. Mod. Phys. A **6**, 2375 (1991).
- [33] C. Aneziris and J. Schechter, *Three Majorana Neutrinos in a Twisting Magnetic Field*, Phys. Rev. D **45**, 1053 (1992).
- [34] C. Athanassopoulos *et al.*, *Evidence for $\bar{\nu}_\mu \rightarrow \bar{\nu}_e$ Oscillations from the LSND Experiment at the Los Alamos Meson Physics Facility*, Phys. Rev. Lett. **77**, 3082 (1996).
- [35] C. Avilez, G. Marx, and B. Fuentes, *Earth as a Source of Antineutrinos*, Phys. Rev. D **23**, 1116 (1981).
- [36] A. Ayala, J. C. D'Olivo, and M. Torres, *Bound on the Neutrino Magnetic Moment from Chirality Flip in Supernovae*, Phys. Rev. D **59**, 111901 (1999).
- [37] J. N. Bahcall, *Neutrino Astrophysics*, Cambridge University Press 1990.
- [38] J. N. Bahcall, M. H. Pinsonneault, and S. Basu, *Solar Models: Current Epoch and Time Dependences, Neutrinos, and Helioseismological Properties*, Astrophys. J. **555**, 990 (2001).
- [39] A. B. Balantekin *et al.*, *Consequences of Twisting Solar Magnetic Fields in Solar Neutrino Experiments*, Phys. Rev. D **48**, 5496 (1993).
- [40] A. B. Balantekin, P. J. Hatchell, and F. Loreti, *Matter-Enhanced Spin-Flavor Precession of Solar Neutrinos with Transition Magnetic Moments*, Phys. Rev. D **41**, 3583 (1990).
- [41] A. B. Balantekin and F. Loreti, *Solar and Supernova Neutrino Physics with Sudbury Neutrino Observatory*, Phys. Rev. D **45**, 1059 (1992).
- [42] A. Bandyopadhyay, S. Choubey, and S. Goswami, *MSW Mediated Neutrino Decay and the Solar Neutrino Problem*, Phys. Rev. D **63**, 113019 (2001).

- [43] R. Barbieri and G. Fiorentini, *The Solar Neutrino Puzzle and the $\nu_L \rightarrow \nu_R$ Conversion Hypothesis*, Nucl. Phys. B **304**, 909 (1987).
- [44] R. Barbieri, G. Fiorentini, G. Mezzorano, and M. Moretti, *Do $\bar{\nu}_e$ Come Out from the Sun?*, Phys. Lett. B **259**, 119 (1991).
- [45] G. Barenboim, J. F. Beacom, L. Borissov, and B. Kayser, *CPT Violation and the Nature of Neutrinos*, Phys. Lett. B **537**, 227 (2002).
- [46] G. Barenboim, L. Borissov, and J. Lykken, *CPT Violating Neutrinos in the Light of KamLAND*, arXiv.org **hep-ph**, 0212116 (2002).
- [47] G. Barenboim, L. Borissov, and J. Lykken, *Neutrinos that Violate CPT and the Experiments that Love Them*, Phys. Lett. B **534**, 106 (2002).
- [48] G. Barenboim, L. Borissov, J. Lykken, and A. Y. Smirnov, *Neutrinos as the Messengers of CPT Violation*, J. High Energy Phys. **10**, 001 (2002).
- [49] G. Barenboim and J. Lykken, *A Model of CPT Violation for Neutrinos*, Phys. Lett. B **554**, 73 (2003).
- [50] G. Barenboim and C. Quigg, *Neutrino Observatories Can Characterize Cosmic Sources and Neutrino Properties*, Phys. Rev. D **67**, 073024 (2003).
- [51] G. Barr, T. K. Gaisser, and T. Stanev, *Flux of Atmospheric Neutrinos*, Phys. Rev. D **39**, 3532 (1989).
- [52] J. Barranco, O. G. Miranda, T. I. Rashba, V. B. Semikov, and J. W. F. Valle, *Confronting Spin Flavor Solutions of the Solar Neutrino Problem with Current and Future Solar Neutrino Data*, Phys. Rev. D **66**, 093009 (2002).
- [53] G. Battistoni, A. Ferrari, T. Montaruli, and P. R. Sala, *The FLUKA Atmospheric Neutrino Flux Calculation*, Astropart. Phys. **19**, 269 (2003).
- [54] J. F. Beacom and N. F. Bell, *Do Solar Neutrinos Decay?*, Phys. Rev. D **65**, 113009 (2002).
- [55] J. F. Beacom and M. R. Vagins, *GADZOOKS! Antineutrino Spectroscopy with Large Water Čerenkov Detectors*, arXiv.org **hep-ph**, 0309300 (2003).
- [56] J. F. Beacom and P. Vogel, *Neutrino Magnetic Moments, Flavor Mixing, and the Super-Kamiokande Solar Data*, Phys. Rev. Lett. **83**, 5222 (1999).
- [57] C. Bemporad, G. Gratta, and P. Vogel, *Reactor-Based Neutrino Oscillation Experiments*, Rev. Mod. Phys. **74**, 297 (2002).

- [58] J. W. Bieber, D. Seckel, T. Stanev, and G. Steigman, *Search for Neutrinos from the Sun*, Nature **348**, 407 (1990).
- [59] A. F. Bielajew, H. Hirayama, Y. Namito, W. R. Nelson, and D. W. O. Rogers, *Electron Gamma Shower 4* 3rd edition 1997, NRC-PIRS-0436.
- [60] S. M. Bilenkya and C. Giunti, *A Model Independent Approach to Future Solar Neutrino Experiments*, Astropart. Phys. **2**, 353 (1994).
- [61] F. Boehm and P. Vogel, *Physics of Massive Neutrinos*, Cambridge University Press 2nd edition 1992.
- [62] J. Boger *et al.*, *The Sudbury Neutrino Observatory*, Nucl. Instrum. Methods **A449**, 172 (2000).
- [63] T. E. Booth *et al.*, *Monte Carlo N-Particle*, <http://laws.lanl.gov/x5/MCNP/index.html>.
- [64] M. G. Boulay, *Direct Evidence for Weak Flavour Mixing with the Sudbury Neutrino Observatory*, PhD thesis, Queen's University 2001.
- [65] J. J. Brehm and W. J. Mullin, *Introduction to the Structure of Matter*, John Wiley & Sons, Inc. 1989.
- [66] S. J. Brice, *Monte Carlo and Analysis Techniques for the Sudbury Neutrino Observatory*, PhD thesis, Balliol College, Oxford 1996.
- [67] Morgan Brown, P. Eng., Research Engineer, Chalk River Laboratories, A text file containing all the reactor electrical output data was supplied., e-mail: brownmj@aecl.ca.
- [68] C. P. Burgess, N. S. Dzhililov, T. I. Rashba, V. B. Semikoz, and J. W. F. Valle, *Resonant Origin for Density Fluctuations Deep within the Sun: Helioseismology and Magneto-gravity Waves*, Mon. Not. Roy. Astron. Soc. **348**, 609 (2004).
- [69] Scott Burnell, Public Affairs Officer, Nuclear Regulatory Commission, The ADAMS online document server was used to access required reactor monthly production reports. 2002, e-mail: SRB3@nrc.gov.
- [70] D. Casper, *The NUANCE Neutrino Physics Simulation, and the Future*, Nucl. Phys. B (Proc. Suppl.) **112**, 161 (2002).
- [71] B. C. Chauhan and J. Pulido, *Resonance Spin Flavor Precession of Solar Neutrinos after SNO Neutral Current Data*, Phys. Rev. D **66**, 053006 (2002).
- [72] B. C. Chauhan, J. Pulido, and E. Torrente-Lujan, *KamLAND and Solar Antineutrino Spectrum*, arXiv.org **hep-ph**, 0309068 (2003).

- [73] B. C. Chauhan, J. Pulido, and E. Torrente-Lujan, *KamLAND, Solar Antineutrinos and the Solar Magnetic Field*, Phys. Rev. D **68**, 033015 (2003).
- [74] H. H. Chen, *Direct Approach to Resolve the Solar-Neutrino Problem*, Phys. Rev. Lett. **55**, 1534 (1985).
- [75] S. Choubey, S. Goswami, and D. Majumdar, *Status of Neutrino Decay Solution to the Solar Neutrino Problem*, Phys. Lett. B **484**, 73 (2000).
- [76] A. Cisneros, *Effect of Neutrino Magnetic Moment on Solar Neutrino Observations*, Astrophys. Space Sci. **10**, 87 (1971).
- [77] J. Conrad, O. Botner, A. Hallgren, and C. Perez de los Heros, *Including Systematic Uncertainties in Confidence Interval Construction for Poisson Statistics*, Phys. Rev. D **67**, 012002 (2003).
- [78] R. Davis, *Solar Neutrinos. II. Experimental*, Phys. Rev. Lett. **12**, 303 (1964).
- [79] R. Davis, D. S. Harmer, and C. Kenneth, *Search for Neutrinos from the Sun*, Phys. Rev. Lett. **20**, 1205 (1968).
- [80] Y. Declais *et al.*, *Study of Reactor Antineutrino Interaction with Proton at BUGEY Nuclear Power Plant*, Phys. Lett. B **338**, 383 (1994).
- [81] J. K. Dickens, *Calculated Beta-Ray Spectra from Decay of Fission Products Produced by Thermal-Neutron Fission of ^{235}U* , Phys. Lett. B **113**, 201 (1982).
- [82] M. Dragowsky and A. Hime, *Neutron Response and Efficiency for the Pure-D₂O Phase in SNO*, Draft v1.1, Technical report April 2002, SNO Internal Report.
- [83] J. A. Dunmore, *Generation of Energy Dependent Beta Parameter PDFs*, Technical report August 2003, SNO Internal Report.
- [84] J. A. Dunmore, *The Beta Parameters*, Technical report January 2003, SNO Internal Report.
- [85] J. A. Dunmore, R. G. H. Robertson, *et al.*, *Background Neutron Sources to the Neutral-Current Signal in SNO*, Technical report December 1999, Internal SNO report.
- [86] K. Eguchi *et al.*, *First Results from KamLAND: Evidence for Reactor Antineutrino Disappearance*, Phys. Rev. Lett. **90**, 021802 (2003).
- [87] K. Eguchi *et al.*, *High Sensitivity Search for $\bar{\nu}_e$'s from the Sun and Other Sources at KamLAND*, Phys. Rev. Lett. **92**, 071301 (2004).

- [88] H. Ejiri *et al.*, *Limits on the Majorana Neutrino Mass and Right-Handed Weak Currents by Neutrinoless Double β Decay of ^{100}Mo* , Phys. Rev. C **63**, 065501 (2001).
- [89] L. P. Ekstrom and R. B. Firestone, WWW Table of Radioactive Isotopes, Database version 2/28/99, <http://ie.lbl.gov/toi/>.
- [90] P. Elmfors, K. Enqvist, G. Raffelt, and G. Sigl, *Neutrinos with Magnetic Moment: Depolarization Rate in Plasma*, Nucl. Phys. B **503**, 3 (1997).
- [91] G. Ewan, Source Strength of ^{252}Cf Calibration Neutron Sources by Gamma Counting, Technical report September 2000, SNO Internal Report.
- [92] J. Farine *et al.*, The Low Energy Background in the Salt Phase of the SNO Experiment, Technical report June 2003, SNO Internal Report.
- [93] G. J. Feldman and R. D. Cousins, *Unified Approach to the Classical Statistical Analysis of Small Signals*, Phys. Rev. D **57**, 3873 (1998).
- [94] A. J. Ferguson and L. R. Walker, *The Scattering of Alpha-Particles by Carbon and Oxygen*, Phys. Rev. **58**, 666 (1940).
- [95] G. Fiorentini and G. Mezzorani, *Solar Neutrinos, Sunspot Number and the Magnetic Field in the Convective Zone*, Phys. Lett. B **253**, 181 (1991).
- [96] G. Fiorentini, M. Moretti, and F. L. Villante, *Superkamiokande and Solar Antineutrinos*, Phys. Lett. B **413**, 378 (1997).
- [97] J. A. Formaggio, Invisibles from the Sky, Part II: Neutrino-Induced Sources, Technical report February 2002, SNO internal report.
- [98] J. A. Formaggio, One Hundred Years of Atmospheric Data: NUANCE Simulations of Atmospheric Neutrinos in SNO, Technical report 2003, Internal SNO Report.
- [99] J. A. Formaggio *et al.*, Neutron Cosmogenics: Summary of Backgrounds, Technical report April 2002, SNO internal report.
- [100] A. Friedland and A. Gruzinov, *A New Solution to the Solar Neutrino Deficit*, Astropart. Phys. **19**, 575 (2003).
- [101] S. Fukuda *et al.*, *Tau Neutrinos Favored over Sterile Neutrinos in Atmospheric Muon Neutrino Oscillations*, Phys. Rev. Lett. **85**, 3999 (2000).

- [102] Y. Fukuda *et al.*, *Solar Neutrino Data Covering Solar Cycle 22*, Phys. Rev. Lett. **77**, 1683 (1996).
- [103] Y. Fukuda *et al.*, *Evidence for Oscillation of Atmospheric Neutrinos*, Phys. Rev. Lett. **81**, 1562 (1998).
- [104] Y. Fukuda *et al.*, *Measurement of a Small Atmospheric ν_μ/ν_e Ratio*, Phys. Lett. B **433**, 9 (1998).
- [105] Y. Fukuda *et al.*, *Study of the Atmospheric Neutrino Flux in the Multi-GeV Energy Range*, Phys. Lett. B **436**, 33 (1998).
- [106] Y. Fukuda *et al.*, *Measurement of the Flux and Zenith-Angle Distribution of Upward Throughgoing Muons by Super-Kamiokande*, Phys. Rev. Lett. **82**, 2644 (1999).
- [107] B. Fulsom, N. McCauley, K. Miknaitis, S. Oser, C. Sims, and M. Wehrenberg, *Lifetime for the Salt Data Set*, Technical report June 2003, Internal SNO Report.
- [108] A. M. Gago *et al.*, *Global Analysis of the Post-SNO Solar Neutrino Data for Standard and Non-Standard Oscillation Mechanisms*, Phys. Rev. D **65**, 073012 (2002).
- [109] T. K. Gaisser and M. Honda, *Flux of Atmospheric Neutrinos*, Ann. Rev. Nucl. Sci. **52**, 153 (2002).
- [110] T. K. Gaisser, T. Stanev, and G. Barr, *Cosmic-Ray Neutrinos in the Atmosphere*, Phys. Rev. D **38**, 85 (1988).
- [111] Y. Gando *et al.*, *Search for $\bar{\nu}_e$ from the Sun at Super-Kamiokande-I*, Phys. Rev. Lett. **90**, 171302 (2003).
- [112] W. Grimus, M. Maltoni, T. Schwetz, M. A. Tortola, and J. W. F. Valle, *Constraining Majorana Neutrino Electromagnetic Properties from the LMA-MSW Solution of the Solar Neutrino Problem*, Nucl. Phys. B **648**, 376 (2003).
- [113] K. Hagiwara *et al.*, *Particle Data Group Review of Particle Physics*, Phys. Rev. D **66**, 1 (2002).
- [114] A. A. Hahn *et al.*, *Antineutrino Spectrum from ^{241}Pu and ^{239}Pu Thermal Neutron Fission Products*, Phys. Lett. B **218**, 365 (1989).
- [115] D. H. Hartmann and S. E. Woosley, *The Cosmic Supernova Neutrino Background*, Astropart. Phys. **7**, 137 (1997).
- [116] K. M. Heeger, *Model-Independent Measurement of the Neutral-Current Interaction Rate of Solar ^8B Neutrinos with Deuterium in the Sudbury Neutrino Observatory*, PhD thesis, University of Washington 2002.

- [117] K. M. Heeger, February 7, 2004, Private communication.
- [118] J. M. Herndon, *Substructure of the Inner Core of the Earth*, Proc. Nat. Acad. Sci. USA **93**, 646 (1996).
- [119] J. M. Herndon, *Nuclear Georeactor Origin of Oceanic Basalt $^3\text{He}/^4\text{He}$, Evidence, and Implications*, Proc. Nat. Acad. Sci. USA **100**, 3047 (2003).
- [120] R. Herrenberger, M. Chen, and B. L. Dougherty, *Muon-Induced Neutron and Pion Production in an Organic Liquid Scintillator at Shallow Depth*, Phys. Rev. C **52**, 3449 (1995).
- [121] G. C. Hill, *Comment on "Including Systematic Uncertainties in Confidence Interval Construction for Poisson Statistics"*, Phys. Rev. D **67**, 118101 (2003).
- [122] D. F. Hollenbach and J. M. Herndon, *Deep-Earth Reactor: Nuclear Fission, Helium, and the Geomagnetic Field*, Proc. Nat. Acad. Sci. USA **98**, 11085 (2001).
- [123] M. Honda, *Uncertainty of the Atmospheric Neutrino Fluxes*, Nucl. Phys. B (Proc. Suppl.) **77**, 140 (1999).
- [124] M. Honda, T. Kajita, K. Kasahara, and S. Midorikawa, *Calculation of the Flux of Atmospheric Neutrinos*, Phys. Rev. D **52**, 4985 (1995).
- [125] H. Ishino, *Measurement of the Solar Neutrino Energy Spectrum at Super-Kamiokande*, PhD thesis, University of Tokyo January 1999.
- [126] M. Jacobson and T. Ohlsson, *Extrinsic CPT Violation in Neutrino Oscillation in Matter*, Phys. Rev. D **69**, 013003 (2004).
- [127] A. S. Joshipura, E. Masso, and S. Mohanty, *Constraints on Decay Plus Oscillation Solutions of the Solar Neutrino Problem*, Phys. Rev. D **66**, 113008 (2002).
- [128] A. S. Joshipura and S. Mohanty, *Bounds on Neutrino Magnetic Moment Tensor from Solar Neutrinos*, Phys. Rev. D **66**, 012003 (2002).
- [129] M. Kaplinghat, G. Steigman, and T. P. Walker, *Supernova Relic Neutrino Background*, Phys. Rev. D **62**, 043001 (2000).
- [130] J. Klein, M. Neubauer, F. M. Newcomer, and R. Van Berg, *The SNO Trigger System*, Technical report October 1997, Internal SNO Report.
- [131] J. R. Klein, *Data Cleaning: An Analog Measurement Board Cut*, Technical report August 1999, SNO internal report.

- [132] H.-H. Knitter, U. Brosa, and C. Budtz-Jørgensen, Neutron and Gamma Emission in Fission, In C. Wagemans, editor, *The Nuclear Fission Process* chapter 11, page 497, CRC Press 1991.
- [133] G. F. Knoll, *Radiation Detection and Measurement*, John Wiley & Sons 2nd edition 1992.
- [134] M. Kobayashi, C. S. Lim, and M. M. Nojiri, *Economical Neutrino Oscillation*, Phys. Rev. Lett. **67**, 1685 (1991).
- [135] M. Kos, K. Graham, and A. Hime, Neutron Detection Efficiency During the Salt Phase of SNO, Technical report June 2003, Internal SNO Report.
- [136] P. I. Krastev and A. Yu. Smirnov, *Spin-Flavor Conversion and Time Variations of Solar Neutrino Signals*, Z. Phys. C **49**, 675 (1991).
- [137] L. M. Krauss, S. L. Glashow, and D. N. Schramm, *Antineutrino Astronomy and Geophysics*, Nature **310**, 191 (1984).
- [138] T. Kubota, T. Kurimoto, and E. Takasugi, *Seasonal Oscillation of the Solar Neutrino Flux: Effects of Twisting Toroidal Magnetic Fields in the Sun*, Phys. Rev. D **49**, 2462 (1994).
- [139] T. Kutter, Antineutrino Unified Document v0.9, Technical report October 2003, Internal SNO Report.
- [140] P. Langacker and J. Wang, *Neutrino-Antineutrino Transitions*, Phys. Rev. D **58**, 093004 (1998).
- [141] H. Lee and S. A. Bludman, *Low-Energy Atmospheric Neutrinos*, Phys. Rev. D **37**, 122 (1988).
- [142] H. B. Li *et al.*, *Limit on the Electron Neutrino Magnetic Moment from the Kuo-Sheng Reactor Neutrino Experiment*, Phys. Rev. Lett. **90**, 131802 (2003).
- [143] C. Lim and W. J. Marciano, *Resonant Spin-Flavor Precession of Solar and Supernova Neutrinos*, Phys. Rev. D **37**, 1368 (1988).
- [144] C. S. Lim, M. Mori, Y. Oyama, and A. Suzuki, *Correlation Between Solar Neutrino Flux and Solar Magnetic Activity for Majorana Neutrinos*, Phys. Lett. B **243**, 389 (1990).
- [145] P. Lipari, M. Lusignoli, and F. Sartogo, *The Neutrino Cross Section and Upward Going Muons*, Phys. Rev. Lett. **74**, 4384 (1995).
- [146] D. W. Liu *et al.*, *Limits on the Neutrino Magnetic Moment Using 1496 Days of Super-Kamiokande-I Solar Neutrino Data*, arXiv.org **hep-ex**, 0402015 (2004).

- [147] M. Liu, H. W. Lee, and A. B. McDonald, *^{222}Rn Emanation into Vacuum*, Nucl. Instrum. Methods **329**, 291 (1993).
- [148] Y. Liu, L. Derome, and M. Buenerd, *Atmospheric Muon and Neutrino Flux from 3-Dimensional Simulation*, Phys. Rev. D **67**, 073022 (2003).
- [149] F. N. Loreti and A. B. Balantekin, *Neutrino Oscillation in Noisy Media*, Phys. Rev. D **50**, 4762 (1994).
- [150] R. A. Malaney, *Evolution of the Cosmic Gas and the Relic Supernova Neutrino Background*, Astropart. Phys. **7**, 125 (1997).
- [151] M. Malek *et al.*, *Search for Supernova Relic Neutrinos at Super-Kamiokande*, Phys. Rev. Lett. **90**, 061101 (2003).
- [152] A. D. Marino, *Muon-Induced Spallation Products in the SNO Detector*, Technical report May 2000, Internal SNO Report.
- [153] A. D. Marino, *Muon-Induced Spallation Products in the Salt Phase of SNO*, Technical report April 2003, Internal SNO Report.
- [154] J. P. Mason, *A 6130 keV Gamma-Ray Source Using the $^{13}\text{C}(\alpha, n)^{16}\text{O}$ Reaction*, Nucl. Instrum. Methods **241**, 207 (1985).
- [155] N. McCauley, *Calculation of Confidence Limits Including Systematic Uncertainties for the HEP and Antineutrino Analyses*, Technical report March 2004, SNO Internal Report.
- [156] N. McCauley, S. Oser, J. L. Orrell, K. Schaffer, and M. Smith, *Livetime Status Report V*, Technical report December 2001, SNO Internal Report.
- [157] N. K. McCauley, *Producing a Background Free Data Set for Measurement of the Charge Current Flux and Day-Night Asymmetry at the Sudbury Neutrino Observatory*, PhD thesis, The Queen's College, Oxford 2001.
- [158] H. Minakata and H. Nunokawa, *Hybrid Solution of the Solar Neutrino Problem in Anticorrelation with Sunspot Activity*, Phys. Rev. Lett. **63**, 121 (1989).
- [159] H. Minakata and H. Nunokawa, *Time Variation of the Solar-Neutrino Flux and the Resonant Spin-Flavor Rotation Mechanism*, Phys. Rev. D **43**, R297 (1991).
- [160] O. G. Miranda, C. Pena-Garay, T. I. Rashba, V. B. Semikoz, and J. W. F. Valle, *A Non-Resonant Dark-Side Solution to the Solar Neutrino Problem*, Phys. Lett. B **521**, 299 (2001).

- [161] O. G. Miranda, C. Pena-Garay, T. I. Rashba, V. B. Semikoz, and J. W. F. Valle, *The Simplest Resonant Spin-Flavor Solution to the Solar Neutrino Problem*, Nucl. Phys. B **595**, 360 (2001).
- [162] R. Mohapatra and P. B. Pal, *Massive Neutrinos in Physics and Astrophysics*, World Scientific 2nd edition 1998.
- [163] S. Nakamura *et al.*, *Neutrino Deuteron Reactions at Solar Neutrino Energies*, Nucl. Phys. A **707**, 561 (2002).
- [164] C. W. Nally, Atmospheric Neutrino Induced Backgrounds in the Solar Neutrino Energy Range, Technical report 2000, SNO Internal Report.
- [165] M. S. Neubauer, *Evidence for Electron Neutrino Flavor Change Through Measurement of the ^8B Solar Neutrino Flux at the Sudbury Neutrino Observatory*, PhD thesis, University of Pennsylvania 2001.
- [166] B. G. Nickel and J. J. Simpson, The Efficiency and Lifetime of Neutrons in the SNO Detector, Technical report 2000, SNO Internal Report.
- [167] H. Nunokawa and H. Minakata, *Neutrino Flavor Mixing, Spin Precession and the Solar Neutrino Experiments*, Phys. Lett. B **314**, 371 (1993).
- [168] N. S. Oblath and J. Formaggio, NUANCE Systematics, Technical report November 2003, SNO Internal Report.
- [169] N. S. Oblath and C. E. Okada, Limits on the Antineutrino Flux at the Sudbury Neutrino Observatory, Technical report 2001, Internal SNO report.
- [170] L. B. Okun, *On the Electric Dipole Moment of the Neutrino*, Sov. J. Nucl. Phys. **44**, 546 (1986).
- [171] J. L. Orrell, Nuclear Reactor Power Data February 2003, SNO Internal Report, <http://manhattan.sno.laurentian.ca/sno/anoteb.nsf/URL/MANN-5VXTT4>.
- [172] E. A. Paschos *et al.*, *Neutrino Interactions in Oscillation Experiments*, Phys. Rev. D **65**, 033002 (2001).
- [173] V. Plyaskin, *Calculation of Atmospheric Neutrino Flux*, Phys. Lett. B **516**, 213 (2001).
- [174] A. W. P. Poon, Final (Post Box Opening) In-situ and Ex-situ Results, <http://manhattan.sno.laurentian.ca/sno/anoteb.nsf/URL/MANN-5QTK3R> July 27, 2003, Internal SNO Report.

- [175] A. W. P. Poon *et al.*, The Low Energy Background in the Pure D₂O Phase of the SNO Experiment, Technical report 2001, Internal SNO Report.
- [176] A. G. Popeko, V. I. Smirnov, G. M. Ter-Akopyan, B. V. Fefilov, and L. P. Chelnokov, *Multiplicity of Prompt Neutrons in Spontaneous Fission of ²³⁸U*, Sov. J. Nucl. Phys. **24**, 245 (1976).
- [177] G. Prezeau, M. Ramsey-Musolf, and P. Vogel, *Neutrinoless Double β Decay and Effective Field Theory*, Phys. Rev. D **68**, 034016 (2003).
- [178] J. Pulido, *The Solar Neutrino Problem and the Neutrino Magnetic Moment*, Phys. Rep. **211**, 167 (1992).
- [179] J. Pulido, *Neutrino Magnetic Moment Solution for the Solar Neutrino Problem and the SNO Experiment*, Nucl. Phys. B (Proc. Suppl.) **100**, 71 (2001).
- [180] J. Pulido and A. M. Mourao, *Neutrino Magnetic Moment Upper Bound from Solar Neutrino Observations*, Phys. Rev. D **57**, 1794 (1998).
- [181] G. G. Raffelt, *Limits on Neutrino Electromagnetic Properties - An Update*, Phys. Rep. **320**, 319 (1999).
- [182] R. S. Raghavan, *Detecting a Nuclear Fission Reactor at the Center of the Earth*, arXiv.org **hep-ex**, 0208038 (2002).
- [183] R. S. Raghavan, *A New Model of Solar Neutrinos in Manifest Violation of CPT Invariance*, J. Cosmo. Astro. Phys. **08**, 002 (2003).
- [184] R. S. Raghavan *et al.*, *Direct Tests for Solar-Neutrino Mass, Mixing and Majorana Magnetic Moment*, Phys. Rev. D **44**, 3786 (1991).
- [185] R. S. Raghavan *et al.*, *Measuring the Global Radioactivity in the Earth by Multidetector Antineutrino Spectroscopy*, Phys. Rev. Lett. **80**, 635 (1998).
- [186] R. S. Raghavan, X.-G. He, and S. Pakvasa, *Neutrino Decay Catalyzed by the Mikheyev-Smirnov-Wolfenstein Effect*, Phys. Rev. D **38**, 1317 (1988).
- [187] R. G. H. Robertson, *Coincidence Data from (α ,n) Reactions in the D₂O and Salt Phases*, Technical report August 2003, SNO Internal Report.
- [188] R. G. H. Robertson *et al.*, *"Other" Background Sources in the Salt Phase of SNO*, Technical report 2003, Internal SNO Report.

- [189] C. G. Rothschild, M. C. Chen, and F. P. Calaprice, *Antineutrino Geophysics with Liquid Scintillator Detectors*, *Geophys. Res. Lett.* **25**, 1083 (1998).
- [190] V. Rusu, *Energy Scale and Other Goodies from Muon Followers*, Technical report 2003, SNO Internal Report.
- [191] V. L. Rusu, *Measurement of the Total ^8B Solar Neutrino Flux at the Sudbury Neutrino Observatory*, PhD thesis, University of Pennsylvania 2003.
- [192] J. Schechter and J. W. F. Valle, *Majorana Neutrinos and Magnetic fields*, *Phys. Rev. D* **24**, 1883 (1981).
- [193] J. Schechter and J. W. F. Valle, *Erratum: Majorana Neutrinos and Magnetic fields*, *Phys. Rev. D* **25**, 283 (1982).
- [194] K. Schreckenbach, G. Colvin, W. Gelletly, and F. Von Feilitzsch, *Determination of the Antineutrino Spectrum from ^{235}U Thermal Neutron Fission Products up to 9.5 MeV*, *Phys. Lett. B* **160**, 325 (1985).
- [195] V. B. Semikoz, S. Pastor, and J. W. F. Valle, *Low-energy Anti-neutrinos from the Sun*, *Nucl. Phys. B (Proc. Suppl.)* **70**, 348 (1999).
- [196] N. Severijns *et al.*, *Limits on Right-Handed Charged Weak Currents from a Polarization-Asymmetry Correlation Experiment with ^{107}In* , *Phys. Rev. Lett.* **70**, 4047 (1993).
- [197] N. Severijns *et al.*, *Limits on Right-Handed Charged Weak Currents from a Polarization-Asymmetry Correlation Experiment with ^{107}In [Phys. Rev. Lett. 70, 4047 (1993)]*, *Phys. Rev. Lett.* **73**, 611 (1994), Errata.
- [198] X. Shi, D. N. Schramm, R. Rosner, and D. S. Dearborn, *On Using a Neutrino Magnetic Moment to Attack the Solar Neutrino Problem*, *Comments Nucl. Part. Phys.* **21**, 151 (1993).
- [199] S. Skadhauge, *Probing CPT Violation with Atmospheric Neutrinos*, *Nucl. Phys. B* **639**, 281 (2002).
- [200] A. Yu. Smirnov, *The Geometrical Phase in Neutrino Spin Precession and the Solar Neutrino Problem*, *Phys. Lett. B* **260**, 161 (1991).
- [201] N. Tagg, *The ^8Li Calibration Source and Through-Going Muon Analysis in the Sudbury Neutrino Observatory*, PhD thesis, University of Guelph 2001.
- [202] N. Tataru *et al.*, *Weak Interaction Processes on Deuterium: Muon Capture and Neutrino Reactions*, *Phys. Rev. C* **42**, 1694 (1990).

- [203] E. Torrente-Lujan, *Solar Antineutrinos from Fluctuating Magnetic Fields at Kamiokande*, Phys. Lett. B **441**, 305 (1998).
- [204] E. Torrente-Lujan, *Neutrino Spin Flavor Precession in Fluctuating Solar Magnetic fields*, Phys. Rev. D **59**, 093006 (1999).
- [205] E. Torrente-Lujan, *Bounds on the Solar Antineutrino Total Flux and Energy Spectrum from the SK Experiment*, Phys. Lett. B **494**, 255 (2000).
- [206] E. Torrente-Lujan, *KamLAND Bounds on Solar Antineutrinos and Neutrinos Transition Magnetic Moments*, J. High Energy. Phys. **04**, 054 (2003).
- [207] S. Toshev, *Resonant Neutrino "Spin-Rotation" in a Twisting Magnetic Field. Analytical Results*, Phys. Lett. B **271**, 179 (1991).
- [208] T. Totani and K. Sato, *Spectrum of the Relic Neutrino Background from Past Supernovae and Cosmological Models*, Astropart. Phys. **3**, 367 (1995).
- [209] I. S. Towner and J. C. Hardy, *Currents and Their Couplings in the Weak Sector of the Standard Model*, arXiv.org **nucl-th**, 9504015 (1995).
- [210] Y. Tserkovnyak, R. Komar, C. Nally, and C. Waltham, *A Three-Dimensional Calculation of Atmospheric Neutrino Fluxes*, Astropart. Phys. **18**, 449 (2003).
- [211] R. Vandenbosch and J. R. Huizenga, *Nuclear Fission*, Academic Press 1973.
- [212] V. V. Verbinski, H. Weber, and R. E. Sund, *Prompt Gamma Rays from $^{235}\text{U}(n,f)$, $^{239}\text{Pu}(n,f)$, and Spontaneous Fission of ^{252}Cf* , Phys. Rev. C **7**, 1173 (1973).
- [213] J. Vidal and J. Wudka, *Non-Dynamical Contributions to Left-Right Transitions in the Solar Neutrino Problem*, Phys. Lett. B **249**, 473 (1999).
- [214] P. Vogel, *Double Beta Decay: Theory, Experiment and Implications*, In D. O. Caldwell, editor, *Current Aspects of Neutrino Physics* chapter 8, page 177, Springer 2001, See Section 8.3.
- [215] P. Vogel, G. K. Schenter, F. M. Mann, and R. E. Schenter, *Reactor Antineutrino Spectra and Their Application to Antineutrino-Induced Reactions II*, Phys. Rev. C **24**, 1543 (1981).
- [216] M. B. Voloshin and M. I. Vysotskii, *The Neutrino Magnetic Moment and the Time Variation of the Solar Neutrino Flux*, Sov. J. Nucl. Phys. **44**, 544 (1986).

- [217] M. B. Voloshin, M. I. Vysotskii, and L. B. Okun, *Electromagnetic Properties of the Neutrino Possible Semiannual Variations of the Solar Neutrino Flux*, Sov. J. Nucl. Phys. **44**, 440 (1986).
- [218] M. B. Voloshin, M. I. Vysotskii, and L. B. Okun, *Neutrino Electrodynamics and Possible Consequences for Solar Neutrinos*, Sov. Phys.-JETP **64**, 446 (1986).
- [219] C. Waltham, Estimate of Neutral Current Atmospheric Neutrino Background, Technical report 2001, Internal SNO report.
- [220] C. Waltham, Silent Production of Neutrinos by Cosmic Ray Induced Events: A Compendium of Numbers, Technical report 2002, Internal SNO report.
- [221] C. Waltham and C. Nally, Atmospheric Neutrino Backgrounds to the Solar Neutrino Signal in SNO, Technical report 2001, Internal SNO report.
- [222] Y.-F. Wang *et al.*, *Predicting Neutron Production from Cosmic-Ray Muons*, Phys. Rev. D **64**, 013012 (2001).
- [223] J. Wentz *et al.*, *Simulation of Atmospheric Muon and Neutrino Fluxes with CORSIKA*, Phys. Rev. D **67**, 073020 (2003).
- [224] N. West *et al.*, The SNOMAN User's Manual Version 5.00, Technical report 2003, Internal SNO report.

Appendix A

DEFINING THE DATA SETS USED

A.1 The Pure D₂O Phase and Salt Phase Data Sets

The data sets used in this electron antineutrino analysis correspond to the same data as presented in the Pure D₂O phase result of Ref. [10] and the initial Salt phase result of Ref. [12]. A data set is defined as those data taking runs which were selected for solar neutrino analysis. This Appendix details *exactly* how those data sets were composed and prepared for the electron antineutrino analysis. Unfortunately, this composition was not as simple as copying the data files to a disk and then applying the analysis cuts, hence the necessity of this Appendix.

A.1.1 The Pure D₂O Phase Data Set

As part of the main solar neutrino analysis, the raw Pure D₂O data was reduced by requiring events to pass the following tests:

- For run numbers > 9999.5 and < 11479.5 , each event must have $N_{\text{hit}} > 27.5$.
- For run numbers > 11479.5 and < 14008.5 , each event must have $N_{\text{hit}} > 26.5$.
- For run numbers > 14008.5 and < 16013.5 , each event must have $N_{\text{hit}} > 25.5$.

Below these N_{hit} values the data is dominated by two kinds of events. The first is Pulse Global Trigger events (i.e. forced global triggers) with mean N_{hit} values of 2-3. The second is just above the self-generating global trigger threshold of approximately $20 N_{\text{hit}}$. The reduced data was then split into two categories, one referred to as the “clean” set and the other referred to as the “dirty” set¹. This division was defined by

- $(\text{DAMN} \wedge 15822821) == 0$

for an event to be considered clean. This set of instrumental cuts (i.e. DAMN mask 15822821) is not appropriate for an electron antineutrino analysis because it includes the Burst Cut and the N_{hit} Burst Cut (See Appendix B). These cuts remove a window of data defined by events in a time coincidence. This time coincidence is *precisely* the sort signal of interest in an electron antineutrino analysis, thus the “clean” and “dirty” data sets must be recombined for the electron antineutrino analysis. During the recombining of the data, it was checked that only events below the run number dependent N_{hit} values were missing and that the data was recombined in a time ordered fashion to facilitate finding electron antineutrino candidate coincidences. Thus, confidence is insured that the complete and correct data is used in this electron antineutrino analysis.

¹(surf)/bigdisk/analysis/sas/ver_oct01/pass_1/ntuples/clean/snocr_clean_00000xxxxx_yyy.ntp
(surf)/bigdisk/analysis/sas/ver_oct01/dirty/ntuples/snocr_dirty_00000xxxxx_yyy.ntp

A.1.2 The Salt Phase Data Set

During the Salt phase the raw Salt data was reduced in size by applying a global N_{hit} threshold of greater than or equal to $20 N_{\text{hit}}$. No division of “clean” and “dirty” data was made in this phase of the experiment. Thus in the Salt phase the electron antineutrino analysis was able to proceed directly on these reduced data sets. Precisely, the data analyzed were the Root trees of (primarily) MCPROD pass 2. The runs in the range 26xxx were part of MCPROD pass 3. All of these runs were processed before the run number bug was discovered in the QEvent class. This bug does not affect the analysis in anyway, but serves as a mental mile-marker for those intimate with SNO analysis.

A.2 Runs Used in the Pure D₂O Phase and Salt Phase

Tables A.2 & A.2 list all runs used in the electron antineutrino analysis presented in this dissertation.

Table A.1: The canonical 559 runs used in the Pure D₂O analysis.

1000	10189	10710	10811	10938	11347	11490	11655	11976	12237	13401	14190	14425	14970	15272	15657	15826
10002	10190	10714	10813	10939	11366	11493	11657	11977	12238	13405	14196	14429	15005	15276	15662	15828
10003	10197	10734	10815	10942	11368	11498	11676	11978	12240	13408	14252	14431	15012	15279	15669	15829
10005	10219	10735	10821	10943	11371	11502	11679	11985	12243	13415	14255	14438	15014	15309	15670	15830
10008	10221	10736	10826	10944	11377	11504	11681	11988	12257	13418	14264	14450	15018	15340	15671	15842
10015	10224	10737	10828	10946	11381	11506	11682	11990	12289	13421	14287	14451	15020	15352	15672	15843
10020	10236	10738	10836	10948	11383	11508	11730	11991	12290	13423	14291	14464	15021	15370	15673	15844
10023	10237	10739	10841	10949	11384	11510	11732	12038	12329	13428	14292	14466	15022	15538	15679	15862
10025	10534	10740	10843	10950	11389	11512	11733	12054	12330	13431	14293	14493	15025	15563	15684	15865
10030	10536	10741	10869	10951	11390	11525	11764	12059	12506	13432	14301	14495	15027	15567	15696	15869
10031	10549	10742	10871	10953	11393	11528	11783	12082	12568	13434	14304	14496	15028	15595	15698	15870
10034	10551	10743	10873	10954	11397	11530	11802	12150	12571	13441	14308	14677	15029	15598	15724	15871
10035	10554	10744	10876	10955	11399	11531	11805	12157	12575	13444	14311	14680	15034	15600	15745	15872
10036	10555	10747	10878	10956	11400	11532	11816	12159	12576	13446	14315	14684	15065	15601	15746	15873
10038	10638	10748	10879	10959	11402	11533	11819	12162	12577	13451	14316	14685	15067	15604	15747	15874
10040	10649	10749	10881	10961	11406	11537	11820	12167	12590	13746	14377	14757	15078	15610	15748	15877
10124	10650	10756	10882	10962	11407	11539	11824	12168	12598	13811	14378	14762	15083	15611	15750	15884
10125	10651	10762	10883	10963	11415	11541	11828	12172	12614	13874	14386	14768	15105	15612	15752	15905
10129	10655	10770	10884	10970	11417	11543	11829	12173	12615	13880	14388	14770	15111	15615	15755	15907
10130	10659	10773	10885	10972	11429	11544	11831	12178	12618	13882	14389	14773	15112	15617	15762	15941
10133	10675	10775	10886	10975	11431	11550	11859	12181	13121	13886	14390	14775	15117	15618	15767	15943
10141	10677	10776	10887	10976	11433	11553	11864	12183	13292	13895	14393	14777	15119	15620	15789	15947
10142	10678	10779	10891	11269	11436	11554	11867	12187	13294	14006	14394	14781	15120	15624	15791	15948
10149	10680	10781	10894	11271	11437	11561	11875	12190	13302	14008	14398	14782	15129	15640	15792	15949
10161	10686	10782	10922	11272	11443	11568	11890	12197	13331	14031	14404	14787	15132	15641	15794	15958
10162	10687	10783	10923	11281	11444	11570	11899	12207	13334	14033	14405	14807	15147	15643	15799	15978
10163	10700	10784	10924	11286	11446	11575	11901	12222	13338	14077	14409	14814	15165	15647	15802	15997
10169	10701	10797	10925	11289	11462	11579	11903	12224	13340	14078	14410	14878	15214	15651	15806	15998
10170	10704	10801	10927	11291	11466	11582	11911	12226	13341	14080	14411	14883	15228	15652	15808	16002
10171	10705	10803	10932	11303	11474	11591	11915	12227	13351	14083	14413	14958	15268	15653	15810	16003
10172	10706	10804	10933	11310	11479	11621	11919	12229	13389	14177	14415	14961	15269	15654	15819	16013
10174	10708	10805	10935	11312	11481	11650	11924	12233	13392	14185	14417	14962	15270	15655	15820	
10177	10709	10806	10936	11313	11489	11652	11925	12234	13396	14186	14422	14969	15271	15656	15821	

Appendix B

INSTRUMENTAL NOISE AND CUTS

B.1 Instrumental Noise and Cuts

Cuts are algorithms designed to identify (and thus remove) events which are produced by features of the electronics and PMTs that are *not* indicative of true Čerenkov light inside the detector volume. These cuts are:

- Retrigger - This cut flags any event occurring within $5 \mu\text{s}$ of the previous event. When this happens it indicates the detector electronics are spontaneously retriggering, usually due to large charge depositions in a preceding event.
- Q vs. T - The charge (Q) verse time (T) cut is designed to flag noise events where a single PMT produces a pulse of light which is then detected by PMTs across the detector - called “flasher” events. The charge verse time cut flags any event where the highest charge tube in the event occurs much earlier than the mean time of the other PMTs in the event.
- Q/N_{hit} - The charge divided by N_{hit} cut flags events with low charge to N_{hit} ratios. These events contain many PMTs with charge values less than one photo-electron and are thus not produced by true Čerenkov light inside the detector volume.
- Crate Isotropy - This cut flags events where more than 70% of the hit PMTs are located in a single electronics crate and localized to two adjacent electronics boards. This localization in electronics space is not repeated in PMT location in detector coordinates.
- AMB - The analog measurement board cut uses the peak and integral of a summation of Gaussian pulses from all fired PMTs. Each fired PMT contributes a Gaussian pulse normalized to it’s total charge. This cut discriminates real Čerenkov light producing events from noise events which have exceedingly high or low charge [131].
- FTS - The fitterless time spread cut is designed to remove “blind flashers” - flashers events where the flashing tube is missing. This situation is possible if a PMT has high voltage on, but is not set to be read out, a likely operator induced configuration error. This cut flags events that have large average time separations for pairs of PMTs within 3 m of each other.
- OWL - The outward looking PMT cut flags events when more than three PMTs on the outside of the PSUP fire. This acts like a standard cosmic-ray veto shield.

- **Junk** - The junk cut removes events where either the same PMT is included more than once, the event contains electronics calibration flags, or the PMTs are “orphaned”. Orphaned PMTs do not have an assigned global trigger ID number that corresponds to any global trigger ID numbers produced by the master trigger card, thus the PMT is not identified as belonging to a particular event.
- **Neck** - The neck cut flags events that include PMTs located in the neck of the acrylic vessel. It is observed that light produced in the neck of the acrylic vessel will trigger the neck tubes and fire PMTs at the bottom of the detector. This light is not associated with physics events of interest.
- **E Sum** - Whereas the Q/N_{hit} cut flags events with low charge and high N_{hit} , the energy summation cut flags events with high charge and low N_{hit} . The proto-typical E Sum flagged event contains only a few PMTs of which one or two have very high charge.
- **Q Cluster** - Is yet another cut designed to flag flasher events. The Q Cluster cut searches for a cluster (within 1 m) of fired PMTs which contain at least one PMT with extremely high charge.
- **In-Time Channel** - The in-time channel cut flags events where fewer than 60% of the PMTs are within a 93 ns coincidence. True physics events produce a prompt Čerenkov signal with all PMTs well within the coincidence window.
- **Flasher Geometry** - This flasher cut searches for a cluster of fired PMTs like the Q Cluster cut. The average distance from all the PMTs *inside* the cluster to all the PMTs *outside* the cluster is calculated. For flasher events, this calculated distance is large because the majority of the light is projected across the 17 m diameter PSUP.
- **OWL Trigger** - Similar to the OWL cut, the OWL trigger cut flags events where outward looking tubes have caused a global trigger of the detector. This trigger identifies high energy external events.
- **Zero Zero** - The zero zero cut is similar in purpose to the junk cut. The zero zero cut flags events with global trigger ID numbers that have the lowest 8 bits set to zero. These events can potentially “adopt” orphaned PMT information which would have otherwise appeared in an orphan event.

B.2 Muon and Muon Spallation Cuts

As discussed in detail in Chapter 10, muons passing through the SNO detector can generate spallation neutrons or short-lived radioactive nuclei. To eliminate these muons and their spallation products from the data set there is one muon identification algorithm and four cuts designed to provide different levels of protection against muon spallation products. The “Missed Muon” cuts are an extra level of protection that flag any potential low energy muons.

- **Muon Cut** - This identifies muons by the presence of OWL tubes in the event and over 150 total N_{hit} .

- Muon Follower Short - Flags all events following 20 s after an event flagged by the Muon Cut.
- Muon Follower Long - Flags all events following 60 s after an event flagged by the Muon Cut.
- Missed Muon Follower Short - Flags all events 250 ms after *any* event with $N_{\text{hit}}^{\text{D}_2\text{O}} \geq 60$ or $N_{\text{hit}}^{\text{Salt}} \geq 150$.
- Missed Muon Follower Long - Flags all events 500 ms after *any* event with $N_{\text{hit}}^{\text{D}_2\text{O}} \geq 60$ or $N_{\text{hit}}^{\text{Salt}} \geq 150$.

B.3 Blindness “Cuts”

For the Salt phase of the SNO experiment a blindness scheme was implemented where a fraction of the events that would normally be flagged by the Muon Follower Cuts are allowed to slip through, unflagged. This introduces an unknown number of neutrons into the solar neutrino analysis thus making preliminary results “blind” to the actual neutral-current flux. The events which are allowed to slip through the Muon Follower Cuts are flagged by the Blindness “Cut”.

Appendix C

REACTOR THERMAL TO ELECTRICAL EFFICIENCY DETERMINATION***C.1 Reactor Thermal to Electrical Efficiency***

Approximately one-third of US nuclear reactors reported *both* thermal and electrical energy outputs to the NRC. This information is used to determine an average thermal to electrical conversion efficiency for all reactors. Table C.1 lists the details of this estimation. The number of reports that give both the thermal and electrical energy outputs is listed in the right most columns of Table C.1. Note, however, that each reactor is given equal weight in the final determination of the average of all reactors' thermal to electrical efficiency.

Table C.1: The average thermal to electric conversion efficiencies for select US nuclear reactors.

Unit	ϵ	Reports	Unit	ϵ	Reports
Arkansas Nuclear One	$0.327 \pm (3 \cdot 10^{-3})$	5	Monticello	$0.33 \pm (2 \cdot 10^{-3})$	29
Callaway	$0.324 \pm (1 \cdot 10^{-3})$	3	North Anna	$0.320 \pm (5 \cdot 10^{-4})$	59
Catawba	$0.340 \pm (5 \cdot 10^{-4})$	52	Oconee	$0.332 \pm (6 \cdot 10^{-4})$	69
Clinton	$0.318 \pm (1 \cdot 10^{-4})$	34	Palisades	$0.313 \pm (9 \cdot 10^{-4})$	25
Comanche Peak	$0.325 \pm (3 \cdot 10^{-5})$	59	Pilgrim	$0.335 \pm (6 \cdot 10^{-4})$	23
Donald C. Cook	$0.308 \pm (1 \cdot 10^{-3})$	26	Point Beach	$0.332 \pm (4 \cdot 10^{-3})$	55
Duane Arnold	$0.319 \pm (2 \cdot 10^{-3})$	24	Prairie Island	$0.326 \pm (8 \cdot 10^{-5})$	65
Fitz Patrick	$0.328 \pm (6 \cdot 10^{-4})$	27	Quad Cities	$0.31 \pm (6 \cdot 10^{-4})$	42
Grand Gulf	$0.325 \pm (5 \cdot 10^{-4})$	10	Sequoyah	$0.333 \pm (1 \cdot 10^{-3})$	23
Indian Point	$0.322 \pm (2 \cdot 10^{-3})$	65	Surry	$0.325 \pm (6 \cdot 10^{-5})$	70
Kewaunee	$0.317 \pm (1 \cdot 10^{-4})$	24	Vermont Yankee	$0.326 \pm (3 \cdot 10^{-3})$	27
McGuire	$0.333 \pm (1 \cdot 10^{-3})$	44	Waterford	$0.323 \pm (1 \cdot 10^{-3})$	35
Millstone	$0.33 \pm (2 \cdot 10^{-3})$	31	Watts Bar	$0.333 \pm (1 \cdot 10^{-3})$	14

Overall (unweighted) ϵ	$0.325 \pm (8 \cdot 10^{-3})$
---------------------------------------------------	-------------------------------

Appendix D

MORE ON MUON FOLLOWERS

Physics research located in underground laboratories has been an important component of neutrino science. The discovery of neutrino mass has enticed the physics community to propose and request new funding for neutrino research. The underground facilities used by neutrino experiments are also used for dark matter searches, can be used for astro-particle physics, and are required for implementation of any ultra low background experiment. For these reasons it is expected that underground science will continue to grow in the early part of the 21st century. To take full advantage of the low background underground facilities it is important to measure and understand any remaining cosmic-ray interactions that take place deep underground. Articles such as Ref. [222] begin the process of providing an understanding of the atmospheric muon induced backgrounds. The Sudbury Neutrino Observatory can give a detailed example of the muon rate at depth as well as an analysis of the muon induced background. This appendix provides an incomplete analysis of the muons and their induced backgrounds. As the muon induced background has been studied in a number of other documents [8, 152, 153, 190], this appendix merely reports values derivable from the muon and muon follower study of Chapter 10. These values were not studied in-depth, but serve as a comparison to techniques used in other SNO documents.

D.1 Measured Neutron Production Rate

For the Pure D₂O phase, DAMN + FTM muon sample, there were 973 “neutrons” found in the Enlarged Region ($\epsilon_n = 0.2614$) in 307.1 live-days. This measured muon-induced neutron rate is $R_n^{\text{D}_2\text{O}} = (973/0.2614) \times (365/307.1) = 4424$ neutrons / kt · yr. If the decay ring test is applied the number is reduced to 546 neutrons. This gives a rate of $R_n^{\text{D}_2\text{O}} = 2482$ neutrons / kt · yr. Q. R. Ahmad presents similar results in his dissertation [8]. While similar, the results are not directly comparable. Ahmad removes his so-called DAG events from consideration of the total neutron rate. The muon sample presented in this dissertation (DAMN + FTM + decay ring test) was also shown to *not* use the DAG events. However, this dissertation went further and systematically removed muons with DAG like characteristics (See Section 10.2.3). Thus Ahmad’s measured value is expected to lie between the two muon-induced neutron rates reported above. The experimentally measured value presented by Ahmad is $R_n^{\text{D}_2\text{O}} = 365 \times (10.03 \pm 0.64)$ n/day/kt = 3650 ± 234 neutrons / kt · yr. For a comparison to the literature, Ahmad gives an expected muon-induced neutron rate of $R_n^{\text{D}_2\text{O}} = 3920 \pm 405$ neutrons / kt · yr.

For the Salt phase, DAMN + FTM muon sample, there were 1828 “neutrons” found in the Enlarged Region ($\epsilon_n = 0.7583$) in 257.8 live-days. This measured muon-induced neutron rate is $R_n^{\text{Salt}} = (1828.0/0.7583) \times (365/257.8) = 3413$ neutrons / kt · yr. If the decay ring test is applied the number is reduced to 1495 neutrons. This gives a rate of $R_n^{\text{Salt}} = 2791$ neutrons / kt · yr. There have not been any other calculations of the

muon-induced neutron rate during the Salt phase, even though these events have been studied and used by at least a half-dozen students.

D.2 Muon Follower Multiplicities

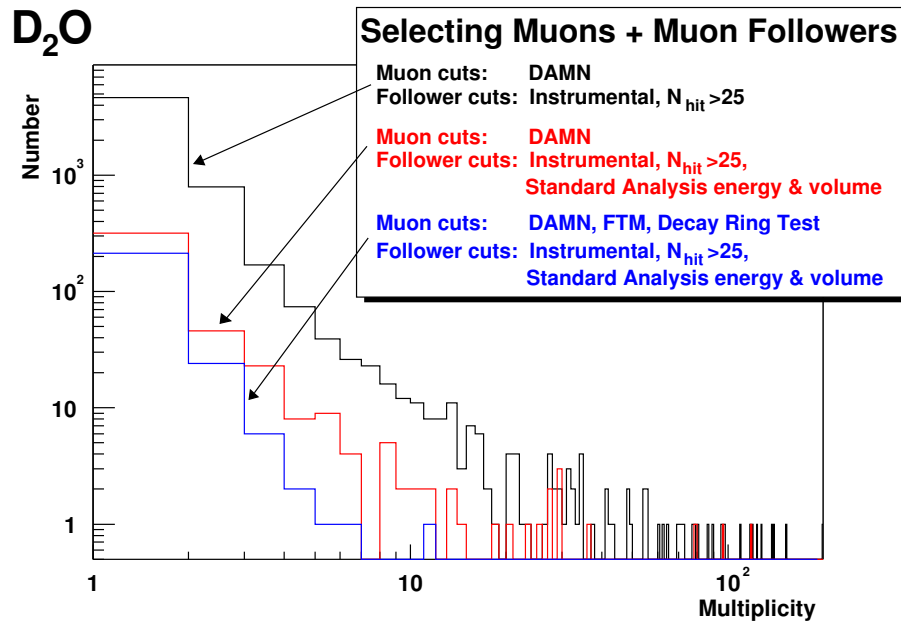
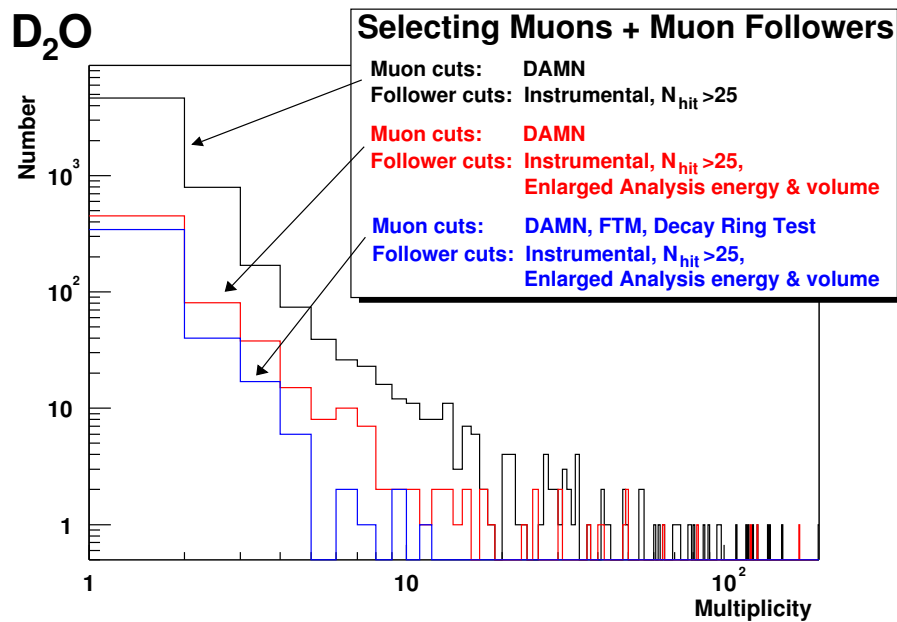
Figures D.1 & D.2 present the Pure D₂O phase muon follower multiplicities for the Standard and Enlarged analyses, respectively. The comparable Salt phase plots are presented in Figures D.3 & D.4. The highest, black histograms show only the simple muon selection and removal of instrumental events. The lower, red histograms show the result of applying energy and fiducial volume requirements to the muon followers. The lowest, blue histogram applies the muon fitter and the decay ring finder test. Reminder, the multiplicities determined here and those presented in V. Rusu's Doctoral dissertation [191] are *not* drawn from the same data sample. Rusu's analysis uses a much less restrictive definition of a muon such that muons which stop inside the detector are included in his sample. The result is the higher multiplicities seen in his presentation.

D.3 Muons Followed by High-Energy Čerenkov Rings

Table D.1 presents a list of those muon events which are:

- Flagged as a muon by the DAMN muon test.
- Have a FTM, corrected impact parameter of less than 750 cm.
- Fail the muon decay ring test.

These tests are presented in Chapter 10. The events are listed here because they should provide a sample of muon decay and muon deep-inelastic scattering candidates.

Figure D.1: Muon follower multiplicities in a Pure D₂O phase Standard analysis.Figure D.2: Muon follower multiplicities in a Pure D₂O phase Enlarged analysis.

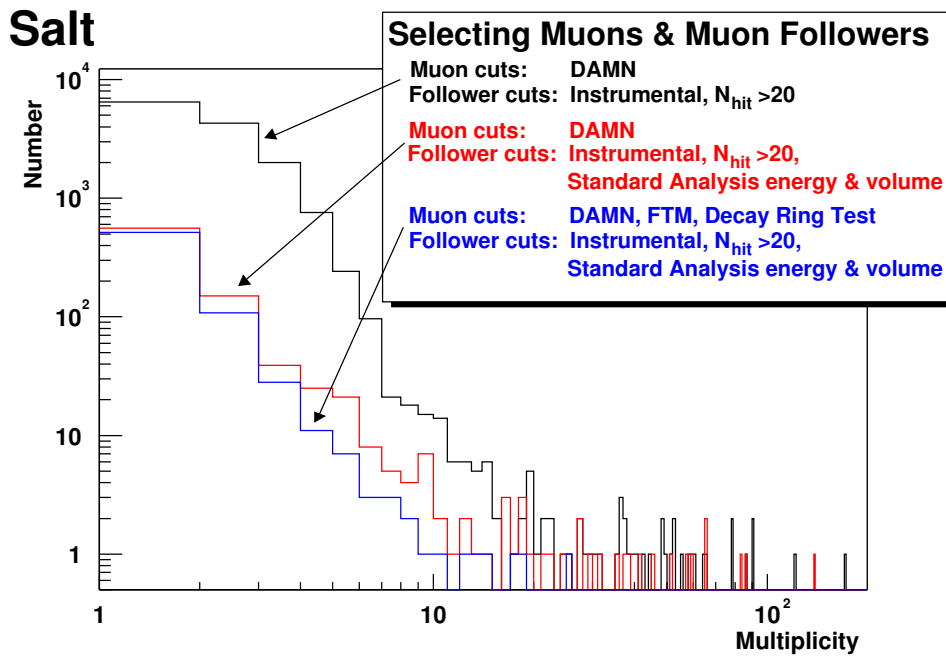


Figure D.3: Muon follower multiplicities in a Salt phase Standard analysis.

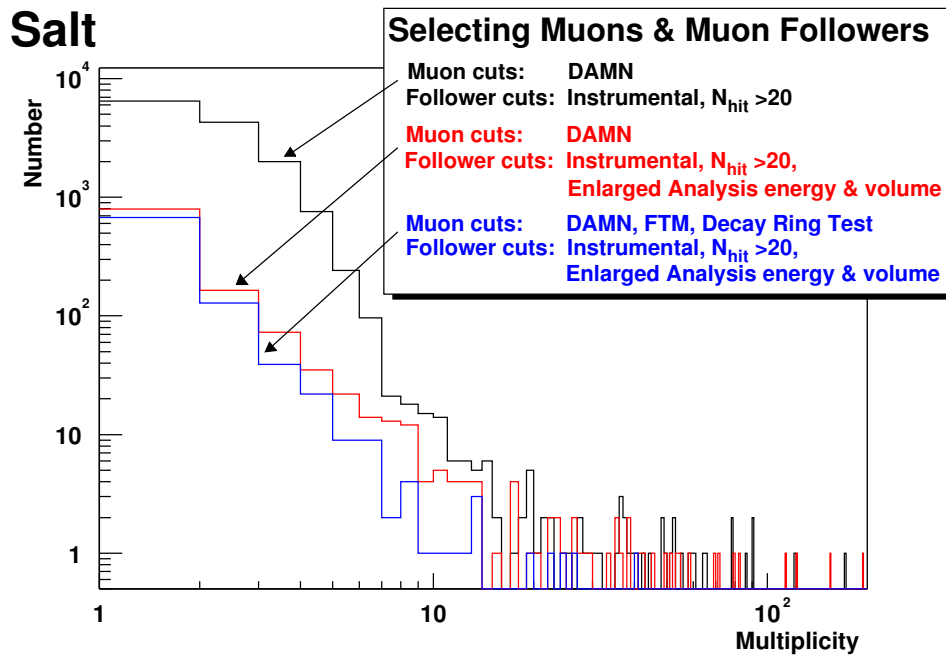


Figure D.4: Muon follower multiplicities in a Salt phase Enlarged analysis.

Table D.1: Muons (DAMN + FTM) that fail the muon decay ring test in the Pure D₂O & Salt phases.

Run	GTID	Run	GTID	Run	GTID	Run	GTID	Run	GTID
10133	56628	10948	1798194	11681	4413472	13302	1257787	14969	1547366
10162	848126	10948	2525941	11802	216324	13338	77695	15028	13847
10174	2761489	10975	2877852	11802	319479	13341	700347	15028	277589
10177	628792	10975	3363076	11802	892384	13351	850612	15112	1359116
10189	583712	11291	456887	11819	2695868	13351	1178838	15147	124259
10237	1565889	11291	1015858	11911	1245260	13389	149046	15165	983592
10551	3972171	11291	1099105	11911	3915658	13392	1724733	15269	2003845
10659	1016917	11310	356563	11925	1964774	13401	2674171	15279	6970143
10659	1626688	11312	2913329	12157	54709	13401	3088287	15352	773174
10687	1611648	11313	98663	12167	409767	13408	238470	15612	2156030
10687	1641713	11347	59917	12172	1030853	13423	2466735	15618	5346812
10687	3150544	11399	2401545	12181	1382093	13431	11218827	15752	1206447
10706	3940359	11399	3471122	12181	1510146	14008	7909159	15792	4218051
10706	4306002	11400	8117725	12183	2489402	14185	1272688	15802	340477
10738	4627499	11436	4690580	12183	2550562	14186	1992547	15820	1508391
10743	7619905	11437	6003975	12187	3777721	14255	566088	15830	8009057
10747	453575	11437	6369795	12187	5083127	14304	5068952	15862	780389
10748	725324	11437	8321589	12187	5704538	14311	6568638	15873	1585176
10784	8461768	11474	627902	12229	110759	14315	7337079	15877	324841
10815	1718581	11510	2236810	12229	661893	14316	8474135	15907	2649232
10815	2237201	11539	197292	12233	4905999	14393	38881	15941	2935644
10871	1360263	11539	1087343	12257	1088642	14394	3713035	15948	1830106
10885	463367	11561	3710664	12257	1172646	14417	6477675	15948	2841051
10885	2069647	11650	519748	12576	317499	14431	3733547		
10886	2225325	11679	8198	12577	1124049	14464	577886		
10886	2618291	11681	261068	12590	438262	14495	5178864		
10887	4617318	11681	1950713	12615	499707	14496	7971468		
Run	GTID	Run	GTID	Run	GTID	Run	GTID	Run	GTID
20773	56603	22527	2446600	23726	182426	24776	897924	26384	3479418
20807	886422	22538	1511985	23726	488804	24778	2784725	26385	5007710
20911	979765	22625	1735638	23734	1246895	24782	398374	26416	1283435
20937	298652	22736	5245691	23900	1393123	25555	928644	26583	3224072
20967	198435	22783	434373	23901	1647197	25555	1488593	26591	626071
20967	890640	22817	432566	23948	1361828	25569	580316	26609	1748595
21707	4288125	22901	131029	23950	273958	25569	673513	26623	845412
21711	5339455	22901	534227	24005	1162065	25646	963906	26628	7618
21740	1076607	23037	1159118	24018	4654574	25692	5479243	26649	4053241
21807	1025061	23164	2873736	24053	4651425	25701	372518	26753	258928
21809	152226	23164	3231189	24329	1042205	25954	1175641	26779	713339
21911	558975	23178	355509	24367	237805	25983	311000	26814	1252454
22030	2408193	23200	763517	24379	196558	25997	1054860	26818	2228585
22030	3406739	23208	275027	24399	367035	26022	379073	26882	1521431
22078	135297	23221	14536	24414	598550	26026	263680	26994	445392
22418	290758	23646	633044	24530	732489	26068	2044954		
22521	5340728	23664	2655057	24538	215972	26110	386837		

VITA

John Laurence Orrell

Education

University of Washington, Seattle, WA

- Doctor of Philosophy, Experimental Nuclear Physics (March 2004)
Title: *A Search for an Electron Antineutrino Signal in the Sudbury Neutrino Observatory*
- Master of Science, Physics (August 2001)

Rensselaer Polytechnic Institute, Troy, NY

- Bachelor of Science, *cum laude*, Physics (August 1998)
- Bachelor of Science, *cum laude*, Philosophy (August 1998)

Professional Profile

Leadership

Career Development Organization (CDO) for Physicists & Astronomers

- Founding member.
- **President** of this UW Registered Student Organization dedicated to facilitating the career advancement of physics & astronomy students.
- Organized career seminars, workshops, and networking opportunities for students.
- Led execution of the 2003 UW Physics Networking Day, showcasing student's work to employers.

Pi Kappa Alpha Fraternity, Gamma Tau Chapter

- President of a 100+ man chapter.
- Offices held: **President, Internal Vice-President, and Treasurer.**
- Developed goals for the Brotherhood in the areas of community service, academic excellence, and new member recruitment while maintaining a responsible, respectable, and lively social agenda.
- Maintained the solvency of the organization and its housing on a dues based, annual budget of \$160,000.

Communication

- Obtained Networking Day Sponsorships from participating companies and national laboratories.
- Gained support and funding from the UW Department of Physics for the CDO's programs.
- Recipient of two speaking awards for scientific presentations given at regional physics conferences.
- Achieved a 3.92 GPA in 12 philosophy courses while attending Rensselaer Polytechnic Institute, exemplifying skillful written communication.

Responsibility

*Qualified **Scientist-In-Charge** at the Sudbury Neutrino Observatory*

- Charged with maintaining day-to-day detector operation.
- Decided detector configuration and running conditions.
- Performed start-ups and shut-downs of the SNO detector.
- On-call to respond to electronics difficulties or unforeseen circumstances.

Team Work

- Worked in the CLAS, HERMES, and SNO international physics collaborations.
- Maintained the SNO detector in conjunction with the on-site staff members and scientists.
- Worked with graduate student peers to achieve the CDO's career advancement oriented goals.
- Integrated the CDO's goals and activities with those of the UW Department of Physics.

Honors and Awards

Appointed to the APS Committee on Careers and Professional Development (2004-2007).

Two *Best Graduate Student Talk* awards at annual meetings of the NW Section of APS:

- 2002 - High Energy Physics Session, May 17 - 18, Banff, Alberta.
- 2001 - Nuclear Physics Session, May 25 - 26, Seattle, WA.

Initiate of the National Order of Omega, the Greek Leadership Honor Society.

Dean's List all 8 semesters while attending Rensselaer Polytechnic Institute.

Experience

Research Assistant	University of Washington, Seattle, WA	1/99 - 1/04
	<ul style="list-style-type: none"> • Performed data analysis for the Sudbury Neutrino Observatory (SNO). • Qualified for on-site, Scientist-In-Charge duties at SNO. • Chairperson of the Run Selection Committee during the salt phase of SNO. • Trained operator of UW's Tandem Van de Graaff, particle accelerator. 	
Teaching Assistant	University of Washington, Seattle, WA	10/98 - 1/99
	<ul style="list-style-type: none"> • TA for two sections of the introductory classical mechanics laboratory. • Assistant TA for two sections of the introductory classical mechanics tutorial. 	
Research Intern	Argonne National Laboratory, Chicago, IL	5/98 - 8/98
	<ul style="list-style-type: none"> • Studied electron response of the HERMES Čerenkov for electron/pion separation. • Wrote report on the response of the HERMES Čerenkov for ANL. 	
Research Intern	Argonne National Laboratory, Chicago, IL	5/97 - 8/97
	<ul style="list-style-type: none"> • Authored programs to analyze and correct the HERMES Čerenkov counter's response to electrons as a function of track position and time. • Wrote simulation of the PMT light acceptance efficiency for a proposed HERMES Ring Imaging Čerenkov counter. 	
Lab Developer	Advanced Undergraduate Laboratory, RPI, Troy, NY	1/97 - 5/97
	<ul style="list-style-type: none"> • Built and tested a "Hall Effect in Bi" experiment for use in undergraduate physics labs. • Work used in-part in Section 2.3 of "Experiments in Modern Physics", 3rd Ed. by A. Melissinos and J. Napolitano. 	
Lab Technician	T. J. National Accelerator Facility, Newport News, VA	7/96 - 8/96
	<ul style="list-style-type: none"> • Installed and aligned mirrors in the CLAS Collaboration Čerenkov detectors. • Tested for and repaired gas & light leaks in completed Čerenkov detectors. 	
Lab Technician	Photomultiplier Test Lab, RPI, Troy, NY	9/95 - 7/96
	<ul style="list-style-type: none"> • Tested 5" photomultiplier tubes for the CLAS Collaboration Čerenkov detectors. • Analyzed test results to obtain relative efficiency and dark noise at a specified gain. • Trained other students in testing procedures. 	

Professional Affiliations

American Physical Society
 APS Division of Nuclear Physics
 APS Northwest Section Member
 Philosophy of Science Association

Publications

- S. N. Ahmed *et al.*, *Electron Antineutrino Search at the Sudbury Neutrino Observatory*, (2004) In preparation.
- S. N. Ahmed *et al.*, *Measurement of the Total Active ^8B Solar Neutrino Flux at the Sudbury Neutrino Observatory with Enhanced Neutral Current Sensitivity*, (2004) Accepted by Physical Review Letters.
- S. N. Ahmed *et al.*, *Constraints on Nucleon Decay via Invisible Modes from the Sudbury Neutrino Observatory*, Physical Review Letters **92** (2004) 102004.
- J. L. Orrell for the SNO Collaboration, " $\bar{\nu}_e$ and the Sudbury Neutrino Observatory", In Z. Parsa, editor, *Eighth Conference on the Intersections of Particle and Nuclear Physics: CIPANP2003*, AIP Conf. Proc. 698, pg 275, AIP New York 2003.
- Q. R. Ahmad *et al.*, *Measurement of Day and Night Neutrino Energy Spectra at SNO and Constraints on Neutrino Mixing Parameters*, Physical Review Letters **89** (2002) 011302.
- Q. R. Ahmad *et al.*, *Direct Evidence for Neutrino Flavor Transformation from Neutral-Current Interactions in the Sudbury Neutrino Observatory*, Physical Review Letters **89** (2002) 011301.
- Q. R. Ahmad *et al.*, *Measurement of the Rate of $\nu_e + d \rightarrow p + p + e^-$ Interactions Produced by ^8B Solar Neutrinos at the Sudbury Neutrino Observatory*, Physical Review Letters **87** (2001) 071301.